East European Journal of Physics. 3. 179–197 (2026)
DOI: 10.26565/2312-4334-2026-3-15 ISSN 2312-4334

# MULTIFORM SOLITARY WAVE STRUCTURES AND BIFURCATION ANALYSIS OF AN EXTENDED MODIFIED (3+1)-DIMENSIONAL KADOMTSEV–PETVIASHVILI EQUATION VIA HYBRID ANALYTICAL APPROACHES

**Ibrahim Saber**[1,2*], **Hamdy M. Ahmed**[3], **Niveen Badra**[1], **Islam Samir**[1]
[1]*Department of Physics and Mathematics Engineering, Faculty of Engineering, Ain Shams University, Cairo, Egypt*
[2]*Faculty of Artificial Intelligence, Egyptian Russian University, Cairo, Egypt*
[3]*Department of Physics and Engineering Mathematics, Higher Institute of Engineering, El Shorouk Academy, Cairo, Egypt*
[*]*Corresponding Author e-mail: ibrahim-saber@eru.edu.eg*
Received June 2, 2026; revised August 21, 2026; accepted August 26, 2026

This work presents the derivation of exact analytical solutions for a (3+1)-dimensional modified Kadomtsev–Petviashvili equation using two effective analytical schemes, namely the Improved Simple Equation Method and the exponential expansion approach. The considered model is relevant for describing complex nonlinear wave propagation in incompressible fluid environments, where dispersive and nonlinear effects are strongly coupled. The implemented techniques yield a rich variety of wave structures with distinct physical characteristics, including singular and non-singular localized formations, periodic patterns, and exponentially decaying profiles. In addition, hyperbolic and trigonometric configurations are obtained, reflecting different propagation regimes of the system. The qualitative behavior of these solutions is further clarified through three-dimensional surface representations and contour mappings. Furthermore, a bifurcation analysis is carried out for the reduced traveling-wave ordinary differential equation to investigate the equilibrium points, their stability properties, and the critical conditions associated with stability exchange. This analysis provides a complementary dynamical-systems perspective on the obtained wave structures and clarifies the influence of the governing parameters on the qualitative behavior of the model.

**Keywords:** *Nonlinear dispersive systems; Multidimensional nonlinear waves; Exact analytical solutions*

## 1. INTRODUCTION

In the realm of nonlinear scientific studies, nonlinear evolutionary systems (NLEEs) hold a considerable position. They serve as powerful mathematical tools for describing diverse and intricate phenomena such as fluid flow dynamics, nonlinear processes, and the distribution of electromagnetic fields in plasma physics. [1–9]. With ongoing research for NLEEs, a growing variety of exact analytical solutions have been identified and analyzed, offering deeper insights into the behavior of nonlinear phenomena in natural systems. Multiple highly effective methodologies have been developed to acquire precise analytical forms of equations describing nonlinear dynamic evolution (NLEEs), for instance, the inverse scattering transform [10], techniques such as a transformation approach derived from Bäcklund's concept [11], and a transformation method based on Darboux's framework [12], the algebraic–geometric technique [13] and an approach utilizing Hirota's bilinear formalism [14]. These methods not only enable the precise determination of solutions but also facilitate the study of complex solution structures.

During the late 1970s, Novikov's research group [15–19]. achieved notable advancements in the development of inverse spectral Paradigm and an approach based on algebraic geometry. These techniques were initially employed to analyze the KdV model, originally formulated by Diederik Korteweg and Gustav de Vries, leading to the derivation of quasiperiodic wave solutions, commonly referred to as algebraic–geometric solutions. Such solutions are defined by physical parameters including the wave number, phase velocity, and interaction amplitude, all determined on a compact, orientable Riemann surface. Although the technique grounded in algebraic geometry offers an analytical framework for constructing quasiperiodic wave solutions, the direct determination of key quantities for instance, wave numbers and phase shifts remains challenging, and frequencies remains difficult.

To address this, Nakamura introduced a direct approach combining the bilinear formalism in conjunction with the theta function introduced by Riemann has been employed to formulate solutions exhibiting quasiperiodic waves for both the KdV and Boussinesq equations [20, 21]. This method provides a more direct approach and offers a clearer understanding of the relationship between the solutions and their characteristic parameters. Subsequent extensions of this technique to Investigations into superintegrable and discrete integrable systems have been carried out by fan and colleagues [22–29]. Overall, nakamura's approach has considerably enhanced the comprehension related to solutions exhibiting quasi-periodicity and their function in the representation of nonlinear waves and examination of dynamical systems [30–33], yielding new insights into complex system dynamics as well as the appearance of chaotic behavior.

A nonlinear version of the Kadomtsev–Petviashvili equation (KPE) [34], this nonlinear evolution equation, incorporating two spatial coordinates and a single time variable, was designed to capture the dynamics of slowly varying long nonlinear waves in the transverse direction. By loosening the restriction by extending beyond one-dimensional wave

***Cite as:*** I. Saber, H.M. Ahmed, N. Badra, I. Samir, East Eur. J. Phys. 3, 179 (2026), https://doi.org/10.26565/2312-4334-2026-3-15

dynamics, Kadomtsev and Petviashvili introduced the fully integrable KP equation . This formulation is suitable for long shallow water waves propagating predominantly in one direction in scenarios where surface tension and viscosity are insignificant. The extended Kadomtsev–Petviashvili equation in (3 + 1) dimensions has, in recent years, garnered significant interest in both fluid mechanics and plasma physics research [35]. The proposed equation is expressed as follows:

$$u_{\mathrm{xxxy}} + 3\left(u_{\mathrm{x}}u_{\mathrm{y}}\right)_{\mathrm{x}} + \beta u_{\mathrm{xxxz}} + 3\beta\left(u_{\mathrm{x}}u_{\mathrm{z}}\right)_{x} + \rho_1 u_{\mathrm{xt}} + \rho_2 u_{\mathrm{yt}} + \rho_3 u_{\mathrm{zt}} + \omega_1 u_{\mathrm{xz}} + \omega_2 u_{\mathrm{yz}} + \omega_3 u_{\mathrm{zz}} = 0. \tag{1}$$

Here, $u = u(x, y, z, t)$ corresponds to the waveform, which depends on three uncorrelated coordinates $x$, $y$ and $z$, as well as a single temporal coordinate t. The coefficients $\rho_j$, $\omega_j$ and $\beta$ are nonzero fixed parameters where $j = 1, 2, 3$.

This work employs the Improved Simple Equation Method (ISEM) and the Exponential Method to derive exact explicit solutions of the generalized Kadomtsev–Petviashvili equation in (3+1) dimensions. By introducing a suitable wave transformation and balancing the nonlinear and highest derivative terms, several classes of explicit wave structures are obtained. These include exponential-type waves, dark solitons, singular solitons, trigonometric solutions, hyperbolic solutions, and singular periodic wave patterns. The derived results enrich the analytical framework of KP-type models and provide deeper physical insight into nonlinear wave propagation and interactions in multidimensional fluid systems. The effectiveness and simplicity of the adopted method confirm its applicability to a broader variety of nonlinear evolutionary equations.

Modified (3+1)-dimensional KP equation considered in the present work has not yet been investigated through the combined implementation of the Improved Simple Equation Method and the Exponential Expansion Method. Furthermore, most existing studies focus on obtaining individual classes of exact solutions without performing a systematic comparison between different analytical approaches. Therefore, the present study aims to bridge this gap by deriving several new exact wave structures using two complementary analytical schemes, followed by graphical visualization to evaluate their physical significance. In addition, all obtained analytical solutions are verified by direct substitution into the governing equation using symbolic computation to ensure their mathematical correctness.

Beyond the derivation of exact analytical solutions, the qualitative dynamical behavior of the reduced traveling-wave equation is also investigated through bifurcation analysis. This approach enables the identification of equilibrium points of the associated planar dynamical system, the examination of their local stability, and the determination of critical parameter conditions under which changes in the qualitative structure of the phase plane occur. Consequently, the bifurcation analysis complements the analytical solution procedures by providing deeper insight into the dynamical mechanisms governing the emergence and stability of the obtained nonlinear wave structures.

This paper is organized as follows. Section 2 presents the mathematical methodologies employed in this work, including the Improved Simple Equation Method and the Exponential Expansion Method. In Section 3, these techniques are systematically applied to derive a broad spectrum of exact analytical solutions for the extended modified (3+1)-dimensional Kadomtsev–Petviashvili equation. Section 4 is devoted to the bifurcation analysis of the reduced traveling-wave system, where the equilibrium points, their stability properties, and the associated critical bifurcation condition are investigated. Section 5 presents three-dimensional surface and contour visualizations to provide further insight into the qualitative and dynamical behavior of the obtained wave solutions. Finally, Section 6 summarizes the main results and highlights their significance in understanding nonlinear wave propagation and the underlying dynamical behavior of the model.

## 2. THE OUTLINED TECHNIQUES

Here, we present the methodology used for Equation (1), including the Improved Simple Equation and the Exponential Methods.

### 2.1. Improved Simple Equation Scheme

Here, an outline of the Improved Simple Equation Scheme is briefly discussed [36–38], which serves as the primary approach employed in the current study.
We examine the following expressed as a partial differential equation with nonlinear characteristics (NLPDE):

$$F\left(u, u_{xt}, u_{xy}, u_{xz}, u_{xt}, u_{xx}, u_{xxx}, \ldots\right) = 0. \tag{2}$$

The fundamental approaches to the Improved Simple Equation Scheme (ISEM) are condensed described below:
**Step 1**: Initially, the partial differential equation with nonlinear characteristics (NLPDE) presented in Eq(2) is mapped converted into an ordinary differential equation (ODE) through the following transformation:

$$u(x, y, z, t) = u(\xi); \quad \xi = x + z + y - c\,t; \quad c \neq 0, \tag{3}$$

here $c$ corresponds to the wave velocity. Accordingly, Equation(2) takes the following form:

$$H\left(u, u', u'', u''', \ldots.\right) = 0. \tag{4}$$

**Step 2**: The derived solution for the Equation (4) is presumed to take the following form:

$$u(\xi) = \sum_{j=-N}^{N} a_j z^j(\xi), \tag{5}$$

here $a_j$ represent coefficients required to be evaluated, while $z(\xi)$ is governed by the differential equation presented here:

$$z'(\xi) = d_0 + d_1 z(\xi) + d_2 z^2(\xi). \tag{6}$$

**Step 3**: In order to identify the quantity of $N$, the highest-order derivative term is balanced with the highest-order nonlinear term according to the balancing principle.
**Step 4**: By substituting the assumed solution given in Equation (5) into Equation (4), and using the differential relation in Equation (6), the resulting expression reduces to a polynomial in $z(\xi)$.
**Step 5**: By gathering that the coefficients of $z^j$ in the polynomial generated from Step (4) , one obtains a system composed of algebraic relations, the solution of that can serve as derived with the aid of numerical computing platforms like *Mathematica* for the purpose of determine the parameters to be determined.
**Step 6**: By assigning various values to $d_0$, $d_1$ and $d_2$, several families of general solutions for Equation (6) can provide different types of solutions as follows:
**First Family**: $d_2 = 0$

$$z(\xi) = \frac{\exp(d_1\xi)}{d_1} - \frac{d_0}{d_1}.$$

**Second Family**: $d_1 = 0$

$$z(\xi) = -\sqrt{-\frac{d_0}{d_2}}\tanh\left(\sqrt{-d_0 d_2}\xi\right), \quad d_0 d_2 < 0,$$
$$z(\xi) = \sqrt{\frac{d_0}{d_2}}\tan\left(\sqrt{d_0 d_2}\xi\right), \quad d_0 d_2 > 0.$$

**Third Family**: $d_0 = 0$

$$z(\xi) = \frac{d_1\exp(d_1\xi)}{1 - d_2\exp(d_1\xi)},$$
$$z(\xi) = \frac{-d_1\exp(d_1\xi)}{1 + d_2\exp(d_1\xi)}.$$

**Fourth Family**: $d_0, d_1, d_2 \neq 0$
When $d_1^2 > 4d_0d_2$ :

$$z(\xi) = -\frac{\sqrt{d_1^2-4d_0d_2}\tanh\left(\frac{1}{2}\sqrt{d_1^2-4d_0d_2}\xi\right)+d_1}{2d_2},$$
$$z(\xi) = -\frac{\sqrt{d_1^2-4d_0d_2}\coth\left(\frac{1}{2}\sqrt{d_1^2-4d_0d_2}\xi\right)+d_1}{2d_2},$$
$$z(\xi) = \frac{\frac{\sqrt{\left(d_1^2-4d_0d_2\right)\left(A^2+B^2\right)}-A\sqrt{d_1^2-4d_0d_2}\cosh\left(\sqrt{d_1^2-4d_0d_2}\xi\right)}{A\sinh\left(\sqrt{d_1^2-4d_0d_2}\xi\right)+B} - d_1}{2d_2}.$$

where $A, B \neq 0$

$$z(\xi) = \frac{2d_0\cosh\left(\frac{1}{2}\sqrt{d_1^2-4d_0d_2}\xi\right)}{\sqrt{d_1^2-4d_0d_2}\sinh\left(\frac{1}{2}\sqrt{d_1^2-4d_0d_2}\xi\right) - d_1\cosh\left(\frac{1}{2}\sqrt{d_1^2-4d_0d_2}\xi\right)},$$
$$z(\xi) = \frac{2d_0\sinh\left(\frac{1}{2}\sqrt{d_1^2-4d_0d_2}\xi\right)}{\sqrt{d_1^2-4d_0d_2}\cosh\left(\frac{1}{2}\sqrt{d_1^2-4d_0d_2}\xi\right) - d_1\sinh\left(\frac{1}{2}\sqrt{d_1^2-4d_0d_2}\xi\right)}.$$

When $d_1^2 < 4d_0d_2$ :

$$z(\xi) = \frac{\sqrt{4d_0d_2-d_1^2}\tan\left(\frac{1}{2}\sqrt{4d_0d_2-d_1^2}\xi\right) - d_1}{2d_2},$$

$$z(\xi) = -\frac{\sqrt{4d_0d_2-d_1^2}\cot\left(\frac{1}{2}\sqrt{4d_0d_2-d_1^2}\,\xi\right)+d_1}{2d_2},$$

$$z(\xi) = \frac{\frac{\sqrt{\left(4d_0d_2-d_1^2\right)\left(A^2-B^2\right)}-A\sqrt{4d_0d_2-d_1^2}\cos\left(\sqrt{4d_0d_2-d_1^2}\,\xi\right)}{A\sin\left(\sqrt{4d_0d_2-d_1^2}\,\xi\right)+B}-d_1}{2d_2}.$$

with A and B being nonzero constants that satisfy the condition, $B^2 < A^2$.

$$z(\xi) = -\frac{2d_0\cos\left(\frac{1}{2}\sqrt{4d_0d_2-d_1^2}\xi\right)}{\sqrt{4d_0d_2-d_1^2}\sin\left(\frac{1}{2}\sqrt{4d_0d_2-d_1^2}\xi\right)+d_1\cos\left(\frac{1}{2}\sqrt{4d_0d_2-d_1^2}\xi\right)},$$

$$z(\xi) = \frac{2d_0\sin\left(\frac{1}{2}\sqrt{4d_0d_2-d_1^2}\xi\right)}{\sqrt{4d_0d_2-d_1^2}\cos\left(\frac{1}{2}\sqrt{4d_0d_2-d_1^2}\xi\right)-d_1\sin\left(\frac{1}{2}\sqrt{4d_0d_2-d_1^2}\xi\right)}.$$

By inserting the evaluated constants $c$ and $a_j$ as well as the general solutions of Equation (6) into the assumed form of Equation (5), an ensemble of exact solutions for the differential equation is obtained.

### 2.2. Exponential Scheme

This section provides a concise overview of the newly developed Exponential Expansion scheme. The nonlinear evolution equation (NLEE) under consideration is given by:

$$F\left(u, u_{xt}, u_{xy}, u_{xz}, u_{xt}, u_{xx}, u_{xxx}, \ldots\right) = 0. \tag{7}$$

where $F$ denotes a function depending on $u, u_{xt}, u_{xy}, u_{xz}, u_{xt}, u_{xx}, u_{xxx}$ and the subscripts indicate partial derivatives of u(x,t) with respect to the variables x and t.

Assume that u(x,t) = u($\xi$), $\xi = x - c\,t$, where $c$ represents the wave propagation speed. Under this transformation, Eq. (7) reduces to a nonlinear ordinary differential equation (ODE) for u=u($\xi$):

$$U(u, u', u'', u''', \ldots.) \tag{8}$$

where U depends on $u, u', u'', u''', \ldots.$ and the prime symbol denotes ordinary differentiation with respect to $\xi$. We assume that the traveling wave solution of Eq. (8) can be represented in the following form:

$$\sum_{i=0}^{N} a_i(\exp(-z(\xi)))^i,\ a_n \neq 0. \tag{9}$$

where the coefficients $A_i (0 \leq i \leq N)$ are unknown constants to be determined and $z = z(\xi)$ satisfies the following three auxulary equations every one gives its own system a nonlinear ordinary differential equation of first order:

$$z'(\xi) = \mu\ exp(z(\xi)) + exp(-z(\xi)) + \lambda \tag{10}$$

where $\lambda\ \ and\ \ \mu$ represent constants with arbitrary values.

The positive integer parameter $N$ is obtained by equating the highest-order derivative terms having the highest-order nonlinear contributions appearing in Eq. (8). Substituting Eq. (9) into Eq. (8), together with Eq. (10) when necessary, leads to a system of algebraic equations for the unknown parameters $A_i (0 \leq i \leq N),\ \lambda\ and\ \mu$. By employing symbolic computation software, such as Mathematica, this algebraic system can be solved to obtain the corresponding values of $A_i,\ \lambda\ and\ \mu$ It is worth mentioning that Eq. (10) admits five distinct classes of general solutions. [39–41]:

$$z(\xi) = \ln\left[\frac{-\sqrt{\lambda^2-4\mu}\tanh\left(\sqrt{\lambda^2-4\mu}\,(\xi+V_0)\right)-\lambda}{2\mu}\right],\ \mu \neq 0,\ \lambda^2-4\mu > 0.$$

$$z(\xi) = \ln\left[\frac{\sqrt{-\lambda^2+4\mu}\tanh\left(\sqrt{-\lambda^2+4\mu}\,(\xi+V_0)\right)-\lambda}{2\mu}\right],\ \mu \neq 0,\ \lambda^2-4\mu < 0.$$

$$z(\xi) = -\ln\left[\frac{\lambda}{\exp\left(\lambda\left(\xi + V_0\right)\right) - 1}\right],\ \mu = 0,\ \lambda \neq 0,\ \lambda^2 - 4\mu > 0.$$

$$z(\xi) = \ln\left(-\frac{2\left(\lambda\left(\xi + V_0\right) + 2\right)}{\lambda^2\left(\xi + V_0\right)}\right),\ \mu = 0,\ \lambda \neq 0.$$

$$z(\xi) = \ln\left[\xi + V_0\right],\ \mu = 0,\ \lambda = 0.$$

here $V_0$ represents the integration constant. Thus, multiple explicit solutions of the nonlinear evolution equation (7) can be obtained. Again, let us assume that Eq. (8) admits a solution expressed as in Eq. (9), where $z = z(\xi)$ fulfills a separate first-order nonlinear ordinary differential equation:

$$z'(\xi) = -\lambda \exp(z(\xi)) - \mu \exp(-z(\xi)),\ \mu,\ \lambda \in \mathbb{R}. \tag{11}$$

By substituting Eq.(9) into Eq.(8) and applying Eq.(11), by performing this procedure repeatedly, we derive a system of algebraic equations for $A_i(0 \leq i \leq N)$,as well as $\lambda\ and\ \mu$. Using symbolic computation tools such as Mathematica, this system can be solved to determine the values of $A_i(0 \leq i \leq N),\ \lambda\ and\ \mu$. It is noteworthy that Eq. (11) admits the general solutions given below:

$$z(\xi) = -\ln\left(\sqrt{\frac{\lambda}{\mu}}\tan\left(\sqrt{\lambda\mu}\left(-ct + V_0 + x + y + z\right)\right)\right),\ \lambda\mu > 0.$$

$$z(\xi) = -\ln\left(-\sqrt{\frac{\lambda}{\mu}}\cot\left(\sqrt{\lambda\mu}\left(-ct + V_0 + x + y + z\right)\right)\right),\ \lambda\mu > 0.$$

$$z(\xi) = -\ln\left(\sqrt{-\frac{\lambda}{\mu}}\tanh\left(\sqrt{-\lambda\mu}\left(-ct + V_0 + x + y + z\right)\right)\right),\ \lambda\mu < 0.$$

$$z(\xi) = \ln\left(\sqrt{-\frac{\lambda}{\mu}}\coth\left(\sqrt{-\lambda\mu}\left(-ct + V_0 + x + y + z\right)\right)\right),\ \lambda\mu < 0.$$

$$z(\xi) = -\ln\left(-\frac{1}{\mu\left(-ct + V_0 + x + y + z\right)}\right),\ \mu > 0,\ \lambda = 0.$$

where $V_0$ is the integrating constant. Finally, we obtain the new multiple explicit solutions of NLEE EQ(7).

## 3. DERIVATION OF EXACT SOLUTIONS

This part aims to clarify the application of the mathematical methods previously presented to the equation under investigation, along with a detailed discussion of the results obtained from each method. The findings demonstrate the effectiveness of these methods in obtaining exact solutions that contribute to a deeper understanding of the physical and mathematical properties of the equation.

### 3.1. Improved Simple Equation scheme

In the subsequent portion, the Improved Simple equation-based method is utilized to formulate closed-form solutions of the KPE.

Initially, through an appropriate transformation, the nonlinear evolution (PDE) (1) is reformulated as (ODE) through the wave transformation defined in Equation (3). Consequently, Equation (1) takes the following form:

$$\left(-c(\rho_1 + \rho_2 + \rho_3) + \omega_1 + \omega_2 + \omega_3 + 6(1 + \beta)u'\right)u'' + (1 + \beta)u'''' = 0, \tag{12}$$

Performing a single integration of Equation (12) gives:

$$\left(-c(\rho_1 + \rho_2 + \rho_3) + \omega_1 + \omega_2 + \omega_3\right)u' + 3(1 + \beta)\left(u'\right)^2 + (1 + \beta)u''' = 0, \tag{13}$$

the analytical solution of Equation (13) is capable of being represented as given below:
For employing the proposed technique, it is first crucial for specifying the integer $N$ must first be identified. The value of $N = 1$. This value is obtained by equating the principal derivative term $u'''$ paired with the nonlinear contribution $(u')^2$ in Equation (13), leading to the conclusion that the solution corresponding to Equation (1) takes as illustrated below:

$$u(\xi) = a_0 + a_1 z(\xi) + \frac{b_1}{z(\xi)}. \tag{14}$$

Substituting Equations (14) and (6) into Equation (13) yields:

$$\begin{gathered}
z^4\left(6a_1(\beta+1)b_1d_2 + a_1c\rho_1 + a_1c\rho_2 + a_1c\rho_3 - 3a_1^2(\beta+1)d_0\right) \\
+z^4\left(a_1(-\beta-1)d_1^2 - 2a_1(\beta+1)d_0d_2 - a_1\omega_1 - a_1\omega_2 - a_1\omega_3\right) \\
+z^2\left(6a_1(\beta+1)b_1d_0 + b_1\left(-c(\rho_1+\rho_2+\rho_3) + (\beta+1)d_1^2 + \omega_1+\omega_2+\omega_3\right) - 3(\beta+1)b_1^2d_2 + 2(\beta+1)b_1d_0d_2\right) + \\
6a_1(\beta+1)b_1d_1z^3 + z^6\left(-3a_1^2(\beta+1)d_2 - 6a_1\beta d_2^2 - 6a_1d_2^2\right) + z^5\left(-3a_1^2(\beta+1)d_1 - 6a_1(\beta+1)d_1d_2\right) + \\
6(\beta+1)b_1d_0^2 - 3(\beta+1)b_1^2d_0 + z\left(6(\beta+1)b_1d_0d_1 - 3(\beta+1)b_1^2d_1\right) = 0.
\end{gathered} \tag{15}$$

Through comparing the coefficients of $z^j$ taken as zero produces a collection of algebraic relations, which are subsequently solved using Mathematica.
The solutions obtained are summarized below:
**Family 1**: When $d_2 = 0$, we have

$$a_1 = 0;\;\; d_0 = \frac{b_1}{2};\;\; d_1 = \sqrt{\frac{c\rho_1 + c\rho_2 + c\rho_3 - \omega_1 - \omega_2 - \omega_3}{\beta+1}}.$$

Consequently, the subsequent dark-type soliton solution is computed:

$$u(x,y,z,t) = a_0 + \frac{2b_1\sqrt{-\frac{-c(\rho_1+\rho_2+\rho_3)+\omega_1+\omega_2+\omega_3}{\beta+1}}}{2\exp\left((-ct+x+z+y)\sqrt{-\frac{-c(\rho_1+\rho_2+\rho_3)+\omega_1+\omega_2+\omega_3}{\beta+1}}\right) - b_1},$$

$$\frac{-c(\rho_1+\rho_2+\rho_3)+\omega_1+\omega_2+\omega_3}{\beta+1} < 0 \;\; \beta \neq -1. \tag{16}$$

**Family 2**:When $d_1 = 0$, the results can be expressed as follows:

**SET I:**

$$a_1 = 0;\;\; d_0 = \frac{b_1}{2};\;\; d_2 = \frac{-c\rho_1 - c\rho_2 - c\rho_3 + \omega_1 + \omega_2 + \omega_3}{4\beta d_0 + 4d_0}.$$

**SET II:**

$$d_2 = -\frac{a_1}{2};\;\; b_1 = 0;\;\; d_0 = \frac{-c\rho_1 - c\rho_2 - c\rho_3 + \omega_1 + \omega_2 + \omega_3}{4\beta d_2 + 4d_2}.$$

**SET III:**

$$a_1 = -2d_2;\;\; d_0 = \frac{b_1}{2};\;\; d_2 = \frac{-c\rho_1 - c\rho_2 - c\rho_3 + \omega_1 + \omega_2 + \omega_3}{16\beta d_0 + 16d_0}.$$

Based on Set I, the following solutions, singular periodic solution, is derived:

$$u(x,y,z,t) = a_0 + \frac{\sqrt{2}b_1\cot\left(\frac{(-ct+x+y+z)\sqrt{\frac{b_1(-c\rho_1-c\rho_2-c\rho_3+\omega_1+\omega_2+\omega_3)}{2\beta b_1+2b_1}}}{\sqrt{2}}\right)}{\sqrt{\frac{b_1(2\beta b_1+2b_1)}{-c\rho_1-c\rho_2-c\rho_3+\omega_1+\omega_2+\omega_3}}},\;\; \beta \neq -1,$$

$$\frac{b_1(-c\rho_1 - c\rho_2 - c\rho_3 + \omega_1 + \omega_2 + \omega_3)}{2\beta b_1 + 2b_1} > 0. \tag{17}$$

In accordance with Set II, singular periodic structures is determined as presented below:

$$u(x,y,z,t) = a_0 + \sqrt{2}a_1\sqrt{-\frac{-c\rho_1 - c\rho_2 - c\rho_3 + \omega_1 + \omega_2 + \omega_3}{a_1\left(-2a_1\beta - 2a_1\right)}} * \tan\left(\frac{(-ct + x + y + z)\sqrt{-\frac{a_1(-c\rho_1 - c\rho_2 - c\rho_3 + \omega_1 + \omega_2 + \omega_3)}{-2a_1\beta - 2a_1}}}{\sqrt{2}}\right),$$
$$\frac{a_1(-c\rho_1 - c\rho_2 - c\rho_3 + \omega_1 + \omega_2 + \omega_3)}{-2a_1\beta - 2a_1} < 0, \quad \beta \neq -1. \tag{18}$$

Referring to Set III, the corresponding singular periodic solution is presented below:

$$u(x,y,z,t) = a_0 + \frac{b_1\left(\cot\left(\frac{1}{4}(-ct + x + y + z)\sqrt{\frac{-c(\rho_1+\rho_2+\rho_3)+\omega_1+\omega_2+\omega_3}{\beta+1}}\right) - \tan\left(\frac{1}{4}(-ct + x + y + z)\sqrt{\frac{-c(\rho_1+\rho_2+\rho_3)+\omega_1+\omega_2+\omega_3}{\beta+1}}\right)\right)}{2\sqrt{\frac{(\beta+1)b_1^2}{-c(\rho_1+\rho_2+\rho_3)+\omega_1+\omega_2+\omega_3}}},$$
$$\frac{-c(\rho_1 + \rho_2 + \rho_3) + \omega_1 + \omega_2 + \omega_3}{\beta + 1} > 0, \quad \beta \neq -1. \tag{19}$$

**Family 3**: When $d_0 = 0$, we have

$$d_2 = -\frac{a_1}{2}; \quad b_1 = 0; \quad d_1 = \sqrt{\frac{c\rho_1 + c\rho_2 + c\rho_3 - \omega_1 - \omega_2 - \omega_3}{\beta + 1}}.$$

Consequently, the following exponential-type solutions are derived:

$$u(x,y,z,t) = a_0 + \frac{2a_1\sqrt{-\frac{-c(\rho_1+\rho_2+\rho_3)+\omega_1+\omega_2+\omega_3}{\beta+1}}\exp\left((-ct + x + y + z)\sqrt{-\frac{-c(\rho_1+\rho_2+\rho_3)+\omega_1+\omega_2+\omega_3}{\beta+1}}\right)}{a_1\exp\left((-ct + x + y + z)\sqrt{-\frac{-c(\rho_1+\rho_2+\rho_3)+\omega_1+\omega_2+\omega_3}{\beta+1}}\right) + 2},$$
$$\frac{-c(\rho_1 + \rho_2 + \rho_3) + \omega_1 + \omega_2 + \omega_3}{\beta + 1} < 0, \quad \beta \neq -1. \tag{20}$$

$$u(x,y,z,t) = a_0 + \frac{2a_1\sqrt{-\frac{-c(\rho_1+\rho_2+\rho_3)+\omega_1+\omega_2+\omega_3}{\beta+1}}\exp\left((-ct + x + y + z)\sqrt{-\frac{-c(\rho_1+\rho_2+\rho_3)+\omega_1+\omega_2+\omega_3}{\beta+1}}\right)}{a_1\exp\left((-ct + x + y + z)\sqrt{-\frac{-c(\rho_1+\rho_2+\rho_3)+\omega_1+\omega_2+\omega_3}{\beta+1}}\right) - 2},$$
$$\frac{-c(\rho_1 + \rho_2 + \rho_3) + \omega_1 + \omega_2 + \omega_3}{\beta + 1} < 0, \quad \beta \neq -1. \tag{21}$$

**Fourth Family**: When $d_0, d_1, d_2 \neq 0$, we have

**SET I:**

$$a_1 = 0; \quad d_0 = \frac{b_1}{2}; \quad d_2 = \frac{-c\rho_1 - c\rho_2 - c\rho_3 + \beta d_1^2 + d_1^2 + \omega_1 + \omega_2 + \omega_3}{4(\beta + 1)d_0}.$$

**SET II**

$$a_1 = -2d_2;\;\; b_1 = 0;\;\; d_2 = \frac{c\rho_1 + c\rho_2 + c\rho_3 - \beta d_1^2 - d_1^2 - \omega_1 - \omega_2 - \omega_3}{-4\beta d_0 - 4d_0}.$$

Utilizing Set I, the following solutions are constructed: $\beta \neq -1$.

$$u(x,y,z,t) = a_0 - \frac{-c(\rho_1+\rho_2+\rho_3) + (\beta+1)d_1^2 + \omega_1 + \omega_2 + \omega_3}{(\beta+1)\left(\sqrt{-\frac{-c(\rho_1+\rho_2+\rho_3)+\omega_1+\omega_2+\omega_3}{\beta+1}}\tanh\left(\frac{1}{2}(-ct+x+y+z)\sqrt{-\frac{-c(\rho_1+\rho_2+\rho_3)+\omega_1+\omega_2+\omega_3}{\beta+1}}\right) + d_1\right)},$$

$$\frac{-c(\rho 1+\rho 2+\rho 3)+\omega 1+\omega 2+\omega 3}{\beta+1} < 0,\;\; \beta \neq -1. \tag{22}$$

$$u(x,y,z,t) = a_0 - \frac{-c(\rho_1+\rho_2+\rho_3) + (\beta+1)d_1^2 + \omega_1 + \omega_2 + \omega_3}{(\beta+1)\left(\sqrt{-\frac{-c(\rho_1+\rho_2+\rho_3)+\omega_1+\omega_2+\omega_3}{\beta+1}}\coth\left(\frac{1}{2}(-ct+x+y+z)\sqrt{-\frac{-c(\rho_1+\rho_2+\rho_3)+\omega_1+\omega_2+\omega_3}{\beta+1}}\right) + d_1\right)},$$

$$\frac{-c(\rho 1+\rho 2+\rho 3)+\omega 1+\omega 2+\omega 3}{\beta+1} < 0,\;\; \beta \neq -1. \tag{23}$$

$$u(x,y,z,t) = a_0 + \frac{\left(A\sinh\left(\sqrt{M}(-ct+x+y+z)\right)+B\right)\left(-c(\rho 1+\rho 2+\rho 3)+(\beta+1)d_1^2+\omega 1+\omega 2+\omega 3\right)}{(\beta+1)\left(\sqrt{M\left(A^2+B^2\right)} - d_1\left(A\sinh\left(\sqrt{M}(-ct+x+y+z)\right)+B\right) - A\sqrt{M}\cosh\left(\sqrt{M}(-ct+x+y+z)\right)\right)},$$

$$M = -\frac{-c(\rho_1+\rho_2+\rho_3)+\omega_1+\omega_2+\omega_3}{\beta+1},\;\; M > 0,\;\; \beta \neq -1. \tag{24}$$

$$u(x,y,z,t) = a_0 - d_1 + \sqrt{-\frac{-c(\rho_1+\rho_2+\rho_3)+\omega_1+\omega_2+\omega_3}{\beta+1}}\tanh\left(\frac{1}{2}(-ct+x+z+y)\sqrt{-\frac{-c(\rho_1+\rho_2+\rho_3)+\omega_1+\omega_2+\omega_3}{\beta+1}}\right),$$

$$-\frac{-c(\rho_1+\rho_2+\rho_3)+\omega_1+\omega_2+\omega_3}{\beta+1} > 0,\;\; \beta \neq -1. \tag{25}$$

$$u(x,y,z,t) = a_0 - d_1 + \sqrt{-\frac{-c(\rho_1+\rho_2+\rho_3)+\omega_1+\omega_2+\omega_3}{\beta+1}}\coth\left(\frac{1}{2}(-ct+x+z+y)\sqrt{-\frac{-c(\rho_1+\rho_2+\rho_3)+\omega_1+\omega_2+\omega_3}{\beta+1}}\right),$$

$$\frac{-c(\rho_1+\rho_2+\rho_3)+\omega_1+\omega_2+\omega_3}{\beta+1} < 0,\;\; \beta \neq -1. \tag{26}$$

The solutions in Equations (22), (23) and(26) correspond to singular solitons, Eq.(25) correspond to dark soliton solution, Eq(24) is obtained hyperbolic solution.

$$u(x,y,z,t) = a_0 - \frac{-c(\rho_1+\rho_2+\rho_3) + (\beta+1)d_1^2 + \omega_1 + \omega_2 + \omega_3}{(\beta+1)\left(d_1 - \sqrt{\frac{-c(\rho_1+\rho_2+\rho_3)+\omega_1+\omega_2+\omega_3}{\beta+1}}\tan\left(\frac{1}{2}(-ct+x+z+y)\sqrt{\frac{-c(\rho_1+\rho_2+\rho_3)+\omega_1+\omega_2+\omega_3}{\beta+1}}\right)\right)},$$

$$\frac{-c(\rho_1+\rho_2+\rho_3)+\omega_1+\omega_2+\omega_3}{\beta+1} > 0,\;\; \beta \neq -1. \tag{27}$$

$$u(x,y,z,t) = a_0 - \frac{-c(\rho_1+\rho_2+\rho_3) + (\beta+1)d_1^2 + \omega_1 + \omega_2 + \omega_3}{(\beta+1)\left(\sqrt{\frac{-c(\rho_1+\rho_2+\rho_3)+\omega_1+\omega_2+\omega_3}{\beta+1}}\cot\left(\frac{1}{2}(-ct+x+z+y)\sqrt{\frac{-c(\rho_1+\rho_2+\rho_3)+\omega_1+\omega_2+\omega_3}{\beta+1}}\right) + d_1\right)},$$

$$\frac{-c(\rho_1+\rho_2+\rho_3)+\omega_1+\omega_2+\omega_3}{\beta+1}>0,\ \ \beta\neq-1. \tag{28}$$

$$u(x,y,z,t)=a_0+$$
$$\frac{\left(A\sin\left(\sqrt{F}(-ct+x+z+y)\right)+B\right)\left(-c(\rho_1+\rho_2+\rho_3)+(\beta+1)d_1^2+\omega_1+\omega_2+\omega_3\right)}{(\beta+1)\left(\sqrt{F\left(A^2-B^2\right)}-d_1\left(A\sin\left(\sqrt{F}(-ct+x+z+y)\right)+B\right)-A\sqrt{F}\cos\left(\sqrt{F}(-ct+x+z+y)\right)\right)},$$
$$F=\frac{-c(\rho_1+\rho_2+\rho_3)+\omega_1+\omega_2+\omega_3}{\beta+1},\ \ \beta\neq-1. \tag{29}$$

$$u(x,y,z,t)=a_0+d_1$$
$$+\sqrt{\frac{-c(\rho_1+\rho_2+\rho_3)+\omega_1+\omega_2+\omega_3}{\beta+1}}\tan\left(\frac{1}{2}(-ct+x+z+y)\sqrt{\frac{-c(\rho_1+\rho_2+\rho_3)+\omega_1+\omega_2+\omega_3}{\beta+1}}\right),$$
$$\frac{-c(\rho_1+\rho_2+\rho_3)+\omega_1+\omega_2+\omega_3}{\beta+1}>0,\ \ \beta\neq-1. \tag{30}$$

$$u(x,y,z,t)=a_0-d_1$$
$$+\sqrt{\frac{-c(\rho_1+\rho_2+\rho_3)+\omega_1+\omega_2+\omega_3}{\beta+1}}\cot\left(\frac{1}{2}(-ct+x+z+y)\sqrt{\frac{-c(\rho_1+\rho_2+\rho_3)+\omega_1+\omega_2+\omega_3}{\beta+1}}\right),$$
$$\frac{-c(\rho_1+\rho_2+\rho_3)+\omega_1+\omega_2+\omega_3}{\beta+1}>0,\ \ \beta\neq-1. \tag{31}$$

Equations (27), (28), (30) and (31) generate singular periodic wave structures, Eq.(29) trigonometric solution is obtained. In accordance with Set II, the explicit solutions are constructed in the manner described below:

$$u(x,y,z,t)=a_0+$$
$$\frac{-\sqrt{M\left(A^2+B^2\right)}+d_1\left(A\sinh\left(\sqrt{M}(-ct+x+z+y)\right)+B\right)+A\sqrt{M}\cosh\left(\sqrt{M}(-ct+x+z+y)\right)}{A\sinh\left(\sqrt{M}(-ct+x+z+y)\right)+B},$$
$$M=-\frac{-c(\rho1+\rho2+\rho3)+\omega1+\omega2+\omega3}{\beta+1},\ \ M>0,\ \ \beta\neq-1. \tag{32}$$

$$u(x,y,z,t)=a_0-\frac{\cosh\left(\frac{1}{2}\sqrt{M}(-ct+x+y+z)\right)\left(-c(\rho_1+\rho_2+\rho_3)+(\beta+1)d_1^2+\omega_1+\omega_2+\omega_3\right)}{(\beta+1)\left(\sqrt{M}\sinh\left(\frac{1}{2}\sqrt{M}(-ct+x+y+z)\right)-d_1\cosh\left(\frac{1}{2}\sqrt{M}(-ct+x+y+z)\right)\right)},$$
$$M=-\frac{-c(\rho_1+\rho_2+\rho_3)+\omega_1+\omega_2+\omega_3}{\beta+1},\ \ M>0,\ \ \beta\neq-1. \tag{33}$$

$$u(x,y,z,t)=a_0-\frac{\sinh\left(\frac{1}{2}\sqrt{M}(-ct+x+z+y)\right)\left(-c(\rho_1+\rho_2+\rho_3)+(\beta+1)d_1^2+\omega_1+\omega_2+\omega_3\right)}{(\beta+1)\left(\sqrt{M}\cosh\left(\frac{1}{2}\sqrt{M}(-ct+x+z+y)\right)-d_1\sinh\left(\frac{1}{2}\sqrt{M}(-ct+x+z+y)\right)\right)},$$
$$M=-\frac{-c(\rho_1+\rho_2+\rho_3)+\omega_1+\omega_2+\omega_3}{\beta+1},\ \ M>0,\ \ \beta\neq-1. \tag{34}$$

Equations (32), (33), and (34) describe hyperbolic solutions.

$$u(x,y,z,t)=a_0+$$
$$\frac{-\sqrt{F\left(A^2-B^2\right)}+Ad_1\sin\left(\sqrt{F}(-ct+x+y+z)\right)+A\sqrt{F}\cos\left(\sqrt{F}(-ct+x+y+z)\right)+Bd_1}{A\sin\left(\sqrt{F}(-ct+x+y+z)\right)+B},$$

$$F = \frac{-c(\rho_1+\rho_2+\rho_3)+\omega_1+\omega_2+\omega_3}{\beta+1}, \quad F>0, \quad \beta \neq -1. \tag{35}$$

$$u(x,y,z,t) = a_0 - \frac{\cos\left(\frac{1}{2}\sqrt{F}(-ct+x+z+y)\right)\left(-c(\rho_1+\rho_2+\rho_3)+(\beta+1)d_1^2+\omega_1+\omega_2+\omega_3\right)}{(\beta+1)\left(d_1\cos\left(\frac{1}{2}\sqrt{F}(-ct+x+z+y)\right)+\sqrt{F}\sin\left(\frac{1}{2}\sqrt{F}(-ct+x+z+y)\right)\right)},$$
$$F = \frac{-c(\rho_1+\rho_2+\rho_3)+\omega_1+\omega_2+\omega_3}{\beta+1}, \quad F>0, \quad \beta \neq -1. \tag{36}$$

$$u(x,y,z,t) = a_0 - \frac{\sin\left(\frac{1}{2}\sqrt{F}(-ct+x+z+y)\right)\left(-c(\rho_1+\rho_2+\rho_3)+(\beta+1)d_1^2+\omega_1+\omega_2+\omega_3\right)}{(\beta+1)\left(\sqrt{F}\cos\left(\frac{1}{2}\sqrt{F}(-ct+x+z+y)\right)-d_1\sin\left(\frac{1}{2}\sqrt{F}(-ct+x+z+y)\right)\right)},$$
$$F = \frac{-c(\rho_1+\rho_2+\rho_3)+\omega_1+\omega_2+\omega_3}{\beta+1}, \quad F>0, \quad \beta \neq -1. \tag{37}$$

Eqs(35), (36) and (37)are trigonometric solutions.

### 3.2. Calculation of exponential Scheme

This section presents the application of the proposed exponential expansion method to find the more general and exact traveling wave solutions to the ODE at Eq. (13). Upon Inserting Eqs. (9) and (10) into Eq. (13) results in the following first system:

$$\begin{cases} -3a_1\beta - 3a_1 + 6\beta + 6 = 0, \\ -6a_1\beta\lambda - 6a_1\lambda + 12\beta\lambda + 12\lambda = 0, \\ -3a_1\beta\lambda^2 - 6a_1\beta\mu - 3a_1\lambda^2 - 6a_1\mu + 7\beta\lambda^2 + 8\beta\mu - c\rho 1 - c\rho 2 - c\rho 3 + 7\lambda^2 + 8\mu + \omega 1 + \omega 2 + \omega 3 = 0, \\ -6a_1\beta\lambda\mu - 6a_1\lambda\mu + \beta\lambda^3 + 8\beta\lambda\mu - c\lambda\rho 1 - c\lambda\rho 2 - c\lambda\rho 3 + \lambda^3 + 8\lambda\mu + \lambda\omega 1 + \lambda\omega 2 + \lambda\omega 3 = 0, \\ -3a_1\beta\mu^2 - 3a_1\mu^2 + \beta\lambda^2\mu + 2\beta\mu^2 - c\mu\rho 1 - c\mu\rho 2 - c\mu\rho 3 + \lambda^2\mu + 2\mu^2 + \mu\omega 1 + \mu\omega 2 + \mu\omega 3 = 0. \end{cases}$$

By solving the system the results can be raised;
**Set I:**

$$a_1 = 2; \lambda = \sqrt{\frac{4\beta\mu + c\rho 1 + c\rho 2 + c\rho 3 + 4\mu - \omega 1 - \omega 2 - \omega 3}{\beta+1}}.$$

**Set II:**

$$a_1 = 2; \lambda = 0; \mu = \frac{c\rho_1 + c\rho_2 + c\rho_3 - \omega_1 - \omega_2 - \omega_3}{-4\beta - 4}$$

**First case**
Based on Set I, we obtained;

$$u(x,y,z,t) = a_0 + \frac{4\mu}{-\sqrt{G-4\mu}\tanh\left(0.5\sqrt{G-4\mu}\,(-ct+V_0+x+y+z)\right)-\sqrt{G}}, \quad G-4\mu>0,$$
$$G = \frac{4\beta\mu + c\rho 1 + c\rho 2 + c\rho 3 + 4\mu - \omega 1 - \omega 2 - \omega 3}{\beta+1} > 0, \beta \neq -1. \tag{38}$$

Based on Set II, we obtained;

$$u(x,y,z,t) = a_0 - \frac{2\,(c\rho_1 + c\rho_2 + c\rho_3 - \omega_1 - \omega_2 - \omega_3)\coth\left(\sqrt{-\frac{c\rho_1+c\rho_2+c\rho_3-\omega_1-\omega_2-\omega_3}{-4\beta-4}}\,(-ct+V_0+x+y+z)\right)}{(-4\beta-4)\sqrt{-\frac{c\rho_1+c\rho_2+c\rho_3-\omega_1-\omega_2-\omega_3}{-4\beta-4}}},$$
$$\frac{c\rho_1 + c\rho_2 + c\rho_3 - \omega_1 - \omega_2 - \omega_3}{-4\beta - 4} < 0, \beta \neq -1. \tag{39}$$

**Second case**

Based on Set I, we obtained;

$$u(x,y,z,t) = a_0 + \frac{4\mu}{\sqrt{4\mu - G}\tan\left(0.5\sqrt{4\mu - G}\,(-ct + V_0 + x + y + z)\right) - \sqrt{G}}, \quad 4\mu - G > 0,$$
$$G = \frac{4\beta\mu + c\rho1 + c\rho2 + c\rho3 + 4\mu - \omega1 - \omega2 - \omega3}{\beta + 1} > 0, \beta \neq -1. \tag{41}$$

Based on Set II, we obtained;

$$u(x,y,z,t) = a_1\sqrt{\mu}\cot\left(\sqrt{\mu}\,(-ct + V_0 + x + y + z)\right) + a_0, \quad \mu > 0. \tag{42}$$

Based on Set III, we obtained;

$$u(x,y,z,t) = a_0 + \frac{2\,(c\rho_1 + c\rho_2 + c\rho_3 - \omega_1 - \omega_2 - \omega_3)\cot\left(1.\sqrt{\frac{c\rho_1 + c\rho_2 + c\rho_3 - \omega_1 - \omega_2 - \omega_3}{-4\beta - 4}}\,(-ct + V_0 + x + y + z)\right)}{(-4\beta - 4)\sqrt{\frac{c\rho_1 + c\rho_2 + c\rho_3 - \omega_1 - \omega_2 - \omega_3}{-4\beta - 4}}},$$
$$\frac{c\rho_1 + c\rho_2 + c\rho_3 - \omega_1 - \omega_2 - \omega_3}{-4\beta - 4} > 0, \beta \neq -1. \tag{43}$$

**Third case**

**Set I:**

$$a_1 = 2; \lambda = \sqrt{\frac{c\rho_1 + c\rho_2 + c\rho_3 - \omega_1 - \omega_2 - \omega_3}{\beta + 1}}.$$

Based on Set I, we obtained;

$$u(x,y,z,t) = a_0 + \frac{2\sqrt{\frac{c\rho_1 + c\rho_2 + c\rho_3 - \omega_1 - \omega_2 - \omega_3}{\beta+1}}}{\exp\left(\sqrt{\frac{c\rho_1 + c\rho_2 + c\rho_3 - \omega_1 - \omega_2 - \omega_3}{\beta+1}}\,(-ct + V_0 + x + y + z)\right) - 1},$$
$$\frac{c\rho_1 + c\rho_2 + c\rho_3 - \omega_1 - \omega_2 - \omega_3}{\beta + 1} > 0, \beta \neq -1. \tag{44}$$

**fourth case**

**Set I:**

$$a_1 = 2; \lambda = \sqrt{\frac{4\beta\mu + c\rho1 + c\rho2 + c\rho3 + 4\mu - \omega1 - \omega2 - \omega3}{\beta + 1}}$$

**Set II:**

$$\mu = 0; \beta = -1; \omega3 = c\rho1 + c\rho2 + c\rho3 - \omega1 - \omega2.$$

**Set III:**

$$a_1 = 2; \lambda = \sqrt{\frac{c\rho_1 + c\rho_2 + c\rho_3 - \omega_1 - \omega_2 - \omega_3}{\beta + 1}}; \mu = 0.$$

Based on Set I, we obtained;

$$u(x,y,z,t) = a_0 - \frac{(4\beta\mu + c\rho_1 + c\rho_2 + c\rho_3 + 4\mu - \omega_1 - \omega_2 - \omega_3)\,(-ct + V_0 + x + y + z)}{(\beta + 1)\left(\sqrt{\frac{4\beta\mu + c\rho_1 + c\rho_2 + c\rho_3 + 4\mu - \omega_1 - \omega_2 - \omega_3}{\beta+1}}\,(-ct + V_0 + x + y + z) + 2\right)},$$
$$\frac{4\beta\mu + c\rho_1 + c\rho_2 + c\rho_3 + 4\mu - \omega_1 - \omega_2 - \omega_3}{\beta + 1} > 0, \beta \neq -1. \tag{45}$$

Based on Set II, we obtained;

$$u(x,y,z,t) = a_0 - \frac{a_1\lambda^2\,(-ct + V_0 + x + y + z)}{2\,(\lambda\,(-ct + V_0 + x + y + z) + 2)}. \tag{46}$$

Based on Set III, we obtained;

$$u(x,y,z,t) = a_0 - \frac{(c\rho_1 + c\rho_2 + c\rho_3 - \omega_1 - \omega_2 - \omega_3)\,(-ct + V_0 + x + y + z)}{(\beta+1)\left(\sqrt{\frac{c\rho_1+c\rho_2+c\rho_3-\omega_1-\omega_2-\omega_3}{\beta+1}}\,(-ct + V_0 + x + y + z) + 2\right)},$$
$$\frac{c\rho_1 + c\rho_2 + c\rho_3 - \omega_1 - \omega_2 - \omega_3}{\beta+1} > 0, \beta \neq -1. \tag{47}$$

Upon substituting Eq (9), Eq (12) into Eq(8) the following system is obtained;

$$\begin{cases} 3a_1\beta\mu^2 + 3a_1\mu^2 + 6\beta\mu^3 + 6\mu^3 = 0, \\ 3a_1\beta\lambda^2 + 3a_1\lambda^2 + 2\beta\lambda^2\mu - c\lambda\rho_1 - c\lambda\rho_2 - c\lambda\rho_3 + 2\lambda^2\mu + \lambda\omega_1 + \lambda\omega_2 + \lambda\omega_3 = 0, \\ 6a_1\beta\lambda\mu + 6a_1\lambda\mu + 8\beta\lambda\mu^2 - c\mu\rho_1 - c\mu\rho_2 - c\mu\rho_3 + 8\lambda\mu^2 + \mu\omega_1 + \mu\omega_2 + \mu\omega_3 = 0. \end{cases}$$

By solving the system the result can be raised;
**set I**

$$\mu = -\frac{a_1}{2}; \lambda = \frac{c\rho_1 + c\rho_2 + c\rho_3 - \omega_1 - \omega_2 - \omega_3}{2a_1\beta + 2a_1}.$$

$$u(x,y,z,t) = a_0 + \sqrt{2}a_1\sqrt{-\frac{c\rho_1 + c\rho_2 + c\rho_3 - \omega_1 - \omega_2 - \omega_3}{a_1\,(2a_1\beta + 2a_1)}} *$$
$$\tan\left(\frac{\sqrt{-\frac{a_1(c\rho_1+c\rho_2+c\rho_3-\omega_1-\omega_2-\omega_3)}{2a_1\beta+2a_1}}\,(-ct + V_0 + x + y + z)}{\sqrt{2}}\right), -\frac{c\rho_1 + c\rho_2 + c\rho_3 - \omega_1 - \omega_2 - \omega_3}{a_1\,(2a_1\beta + 2a_1)} > 0, \beta \neq -1. \tag{48}$$

$$u(x,y,z,t) = a_0 - \sqrt{2}a_1\sqrt{-\frac{c\rho_1 + c\rho_2 + c\rho_3 - \omega_1 - \omega_2 - \omega_3}{a_1\,(2a_1\beta + 2a_1)}}$$
$$\cot\left(\frac{\sqrt{-\frac{a_1(c\rho_1+c\rho_2+c\rho_3-\omega_1-\omega_2-\omega_3)}{2a_1\beta+2a_1}}\,(-ct + V_0 + x + y + z)}{\sqrt{2}}\right), \frac{c\rho_1 + c\rho_2 + c\rho_3 - \omega_1 - \omega_2 - \omega_3}{a_1\,(2a_1\beta + 2a_1)} < 0, \beta \neq -1. \tag{49}$$

$$u(x,y,z,t) = a_0 + \sqrt{2}a_1\sqrt{\frac{c\rho_1 + c\rho_2 + c\rho_3 - \omega_1 - \omega_2 - \omega_3}{a_1\,(2a_1\beta + 2a_1)}}$$
$$\tanh\left(\frac{\sqrt{\frac{a_1(c\rho_1+c\rho_2+c\rho_3-\omega_1-\omega_2-\omega_3)}{2a_1\beta+2a_1}}\,(-ct + V_0 + x + y + z)}{\sqrt{2}}\right), \frac{c\rho_1 + c\rho_2 + c\rho_3 - \omega_1 - \omega_2 - \omega_3}{a_1\,(2a_1\beta + 2a_1)} > 0, \beta \neq -1. \tag{50}$$

$$u(x,y,z,t) = a_0 + \sqrt{2}a_1\sqrt{\frac{c\rho_1 + c\rho_2 + c\rho_3 - \omega_1 - \omega_2 - \omega_3}{a_1\,(2a_1\beta + 2a_1)}}$$
$$\coth\left(\frac{\sqrt{\frac{a_1(c\rho_1+c\rho_2+c\rho_3-\omega_1-\omega_2-\omega_3)}{2a_1\beta+2a_1}}\,(-ct + V_0 + x + y + z)}{\sqrt{2}}\right), \frac{c\rho_1 + c\rho_2 + c\rho_3 - \omega_1 - \omega_2 - \omega_3}{a_1\,(2a_1\beta + 2a_1)} > 0, \beta \neq -1. \tag{51}$$

**Set II** When $\lambda = 0, \mu > 0$

$$\mu = -\frac{a_1}{2}; \omega_3 = c\rho_1 + c\rho_2 + c\rho_3 - \omega_1 - \omega_2.$$

$$u(x,y,z,t) = a_0 + \frac{2}{-ct + V_0 + x + y + z}. \tag{52}$$

## 4. BIFURCATION ANALYSIS

In this section, the bifurcation analysis is applied to the reduced ordinary differential equation obtained from the traveling-wave transformation of the modified (3 + 1)-dimensional KP equation, [42–46] given by

$$Au' + 3B(u')^2 + Bu''' = 0, \tag{53}$$

where

$$A = -c(\rho_1 + \rho_2 + \rho_3) + \omega_1 + \omega_2 + \omega_3, \qquad B = 1 + \beta.$$

Thus, the above third-order nonlinear ODE is the equation considered in the present bifurcation analysis. By introducing the transformation

$$v = u',$$

Eq. (53) is reduced to

$$v'' = Mv - 3v^2,$$

where

$$M = \frac{c(\rho_1 + \rho_2 + \rho_3) - (\omega_1 + \omega_2 + \omega_3)}{1 + \beta}.$$

This reduced ODE is then used to construct the corresponding planar dynamical system and investigate the bifurcation behavior of its equilibrium points. Introducing

$$w = v',$$

gives the planar dynamical system

$$\begin{cases} v' = w, \\ w' = Mv - 3v^2. \end{cases}$$

The equilibrium points are obtained from $w = 0$ and $Mv - 3v^2 = 0$:

$$E_1 = (0, 0), \qquad E_2 = \left(\frac{M}{3}, 0\right).$$

The Jacobian matrix is

$$J(v, w) = \begin{pmatrix} 0 & 1 \\ M - 6v & 0 \end{pmatrix}.$$

At $E_1 = (0, 0)$,

$$\lambda^2 = M.$$

Hence

$$\begin{cases} M > 0: & E_1 \text{ is a saddle (unstable)}, \\ M < 0: & E_1 \text{ is a center (neutrally stable)}, \\ M = 0: & \text{the linearization is degenerate}. \end{cases}$$

At $E_2 = (M/3, 0)$,

$$\lambda^2 = -M.$$

Therefore

$$\begin{cases} M < 0: & E_2 \text{ is a saddle (unstable)}, \\ M > 0: & E_2 \text{ is a center (neutrally stable)}, \\ M = 0: & E_1 = E_2 = (0, 0). \end{cases}$$

Thus, the two equilibrium branches intersect at the critical condition

$$M = 0,$$

that is,

$$c(\rho_1 + \rho_2 + \rho_3) = \omega_1 + \omega_2 + \omega_3.$$

For $\rho_1 + \rho_2 + \rho_3 \neq 0$, the corresponding critical wave speed is

$$c = \frac{\omega_1 + \omega_2 + \omega_3}{\rho_1 + \rho_2 + \rho_3}.$$

When $M$ changes sign through zero, the equilibrium points coalesce and exchange their local stability types: the origin changes between center and saddle, while the second equilibrium does the opposite. Therefore, the reduced traveling-wave system exhibits a stability-exchange bifurcation at $M = 0$.

## 5. GRAPHICAL DEPICTION OF THE SOLUTIONS

Graphical depictions of various solutions are presented in this section to demonstrate their characteristics. The 3D and contour visualizations of the dark-type soliton solution derived from Equation (16) are presented in Figure (1) with $c = 1.5,\ \rho_1 = \rho_2 = \rho_3 = \omega_1 = \omega_2 = \omega_3 = \beta = a_0 = -2,\ d_1 = -1,\ y = 2,\ z = 0.5$. The singular periodic wave solution of Equation (17) is demonstrated through its 3D and contour profiles in Figure (2) with $c = b_1 = -0.5,\ \rho_1 = \rho_2 = \rho_3 = \omega_1 = \omega_2 = \omega_3 = \beta = a_0 = -2,\ y = z = 0.75$. The dark wave solution of Equation (25), obtained for particular parameter settings, is displayed through 3D and contour plots in Figure (3) with $c = 2,\ d_1 = \rho_1 = \rho_2 = \rho_3 = \omega_1 = \omega_2 = \omega_3 = \beta = a_0 = -2,\ y = z = 0$. Figure (4) presents three-dimensional and contour visualizations of the soliton exhibiting singular behavior solution associated with Equation (26) with $d_1 = \ \rho_1 = \rho_2 = \rho_3 = \omega_1 = \omega_2 = \omega_3 = a_0 = -2,\ \beta = 2,\ y = 1,\ c = z = 0$.Figure (5): Presents the 3D and contour plot of the singular periodic solution corresponding to Equation (48) with $c = -0.03, \beta = a_0 = a_1 = \rho_1 = \rho_2 = \rho_3 = \omega_1 = \omega_2 = \omega_3 = V_0 = y = z = -2$. Figure (6) Presents the 3D of the singular soliton corresponding to Equation (51), with $c = -0.1, \beta = y = 2, a_0 = a_1 = \rho_1 = \rho_2 = \rho_3 = \omega_1 = \omega_2 = \omega_3 = V_0 = z = -2$. Figure (7): Presents the 3D and contour profiles of the dark-type solution corresponding to Equation (50) with $c = -0.8, \beta = 0.885, a_0 = a_1 = \rho_1 = \rho_2 = \rho_3 = \omega_1 = \omega_2 = \omega_3 = V_0 = -2, y = z = 0$. Figure (8): Phase portraits of the reduced KP system around the equilibrium point $(0, 0)$, showing its transition between a saddle for $M > 0$ and a center for $M < 0$. Figure (9): Phase portraits of the reduced KP system around the equilibrium point $(M/3, 0)$, showing its transition between a saddle for $M > 0$ and a center for $M < 0$.

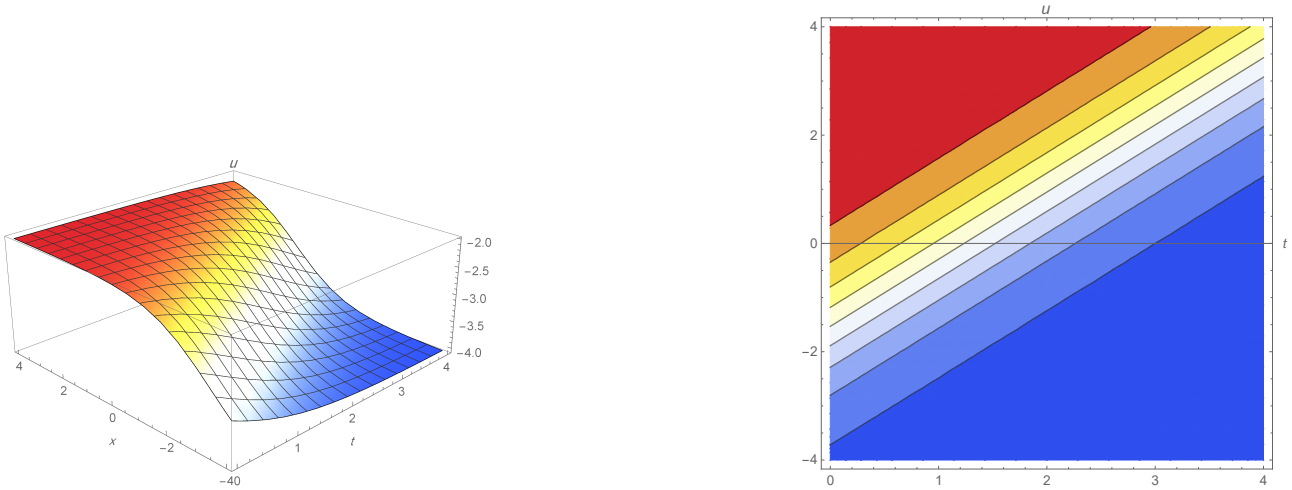


**Figure 1.** Provides the 3D and contour visualizations illustrating the dark-type soliton solution related to Equation (16)

.

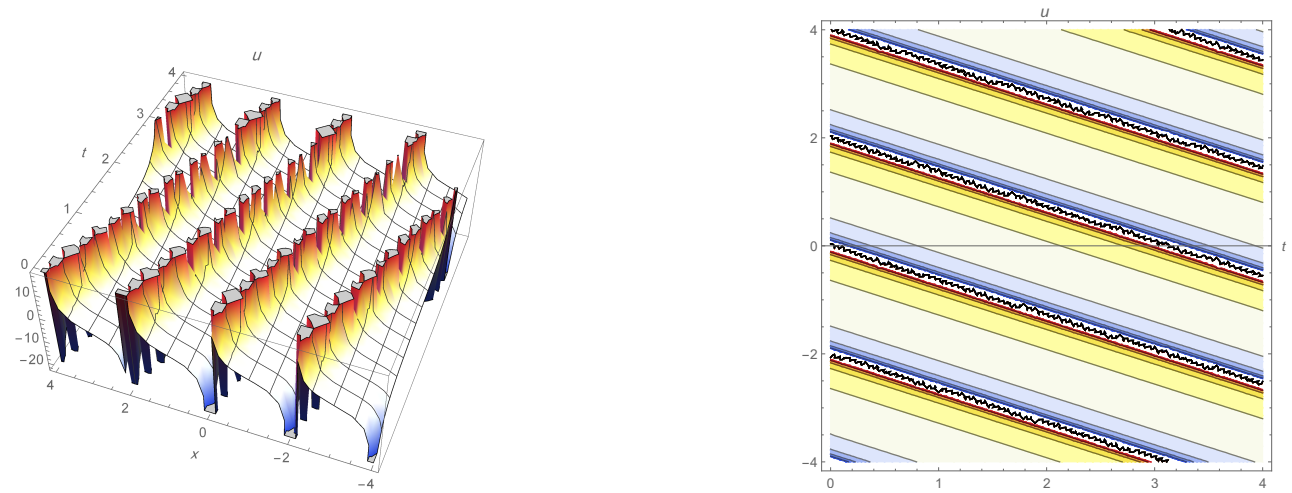


**Figure 2.** Provides the 3D and contour visualizations illustrating the periodic structures exhibiting singular behavior wave solution related to Equation (17)

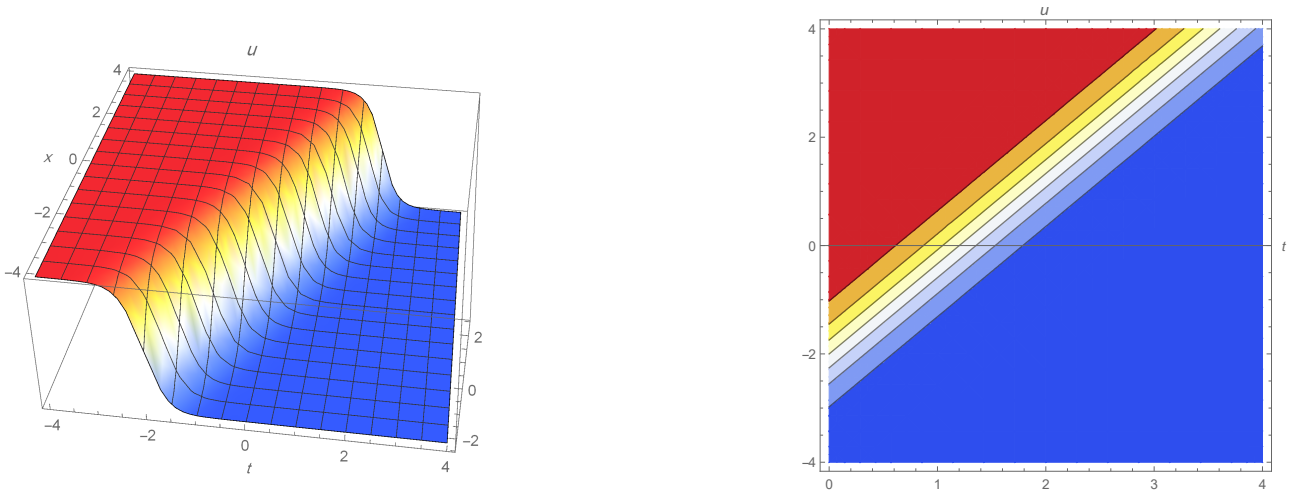


**Figure 3.** Presents the 3D and contour profiles of the dark-type solution corresponding to Equation (25)

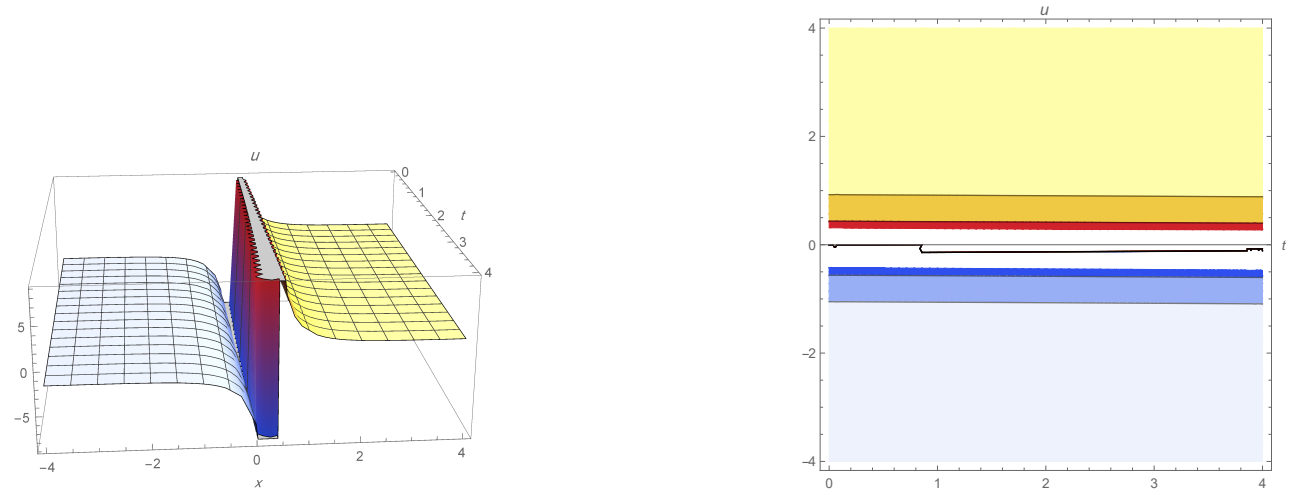


**Figure 4.** Depicts the 3D and contour views of the soliton exhibiting singular behavior solution associated with Equation (26)

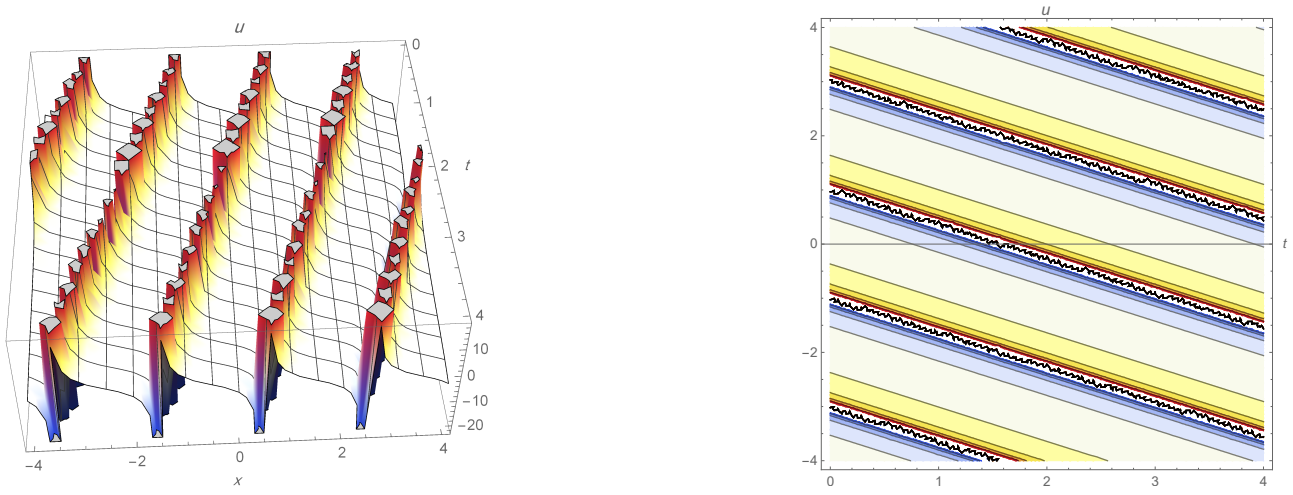


**Figure 5.** Presents the 3D and contour plot of the singular periodic solution corresponding to Equation (48)

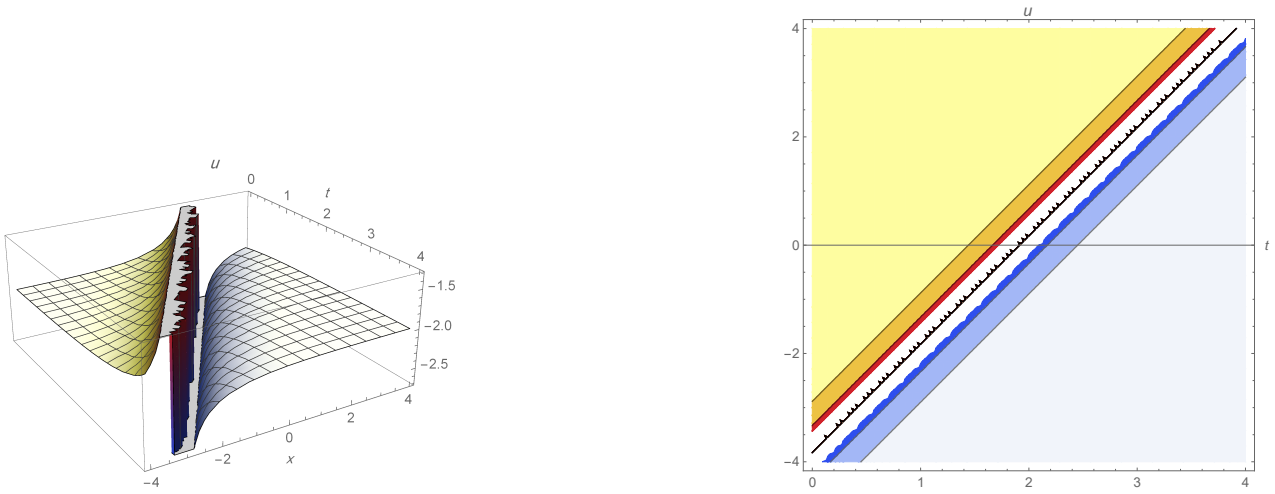


**Figure 6.** Presents the 3D and contour plot of the singular soliton corresponding to Equation (51)

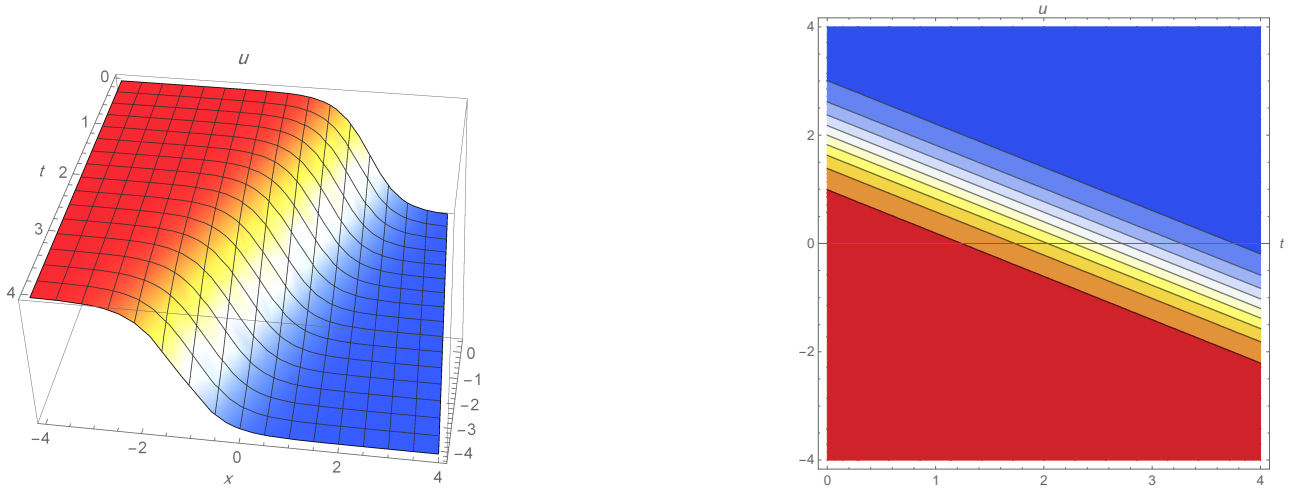


**Figure 7.** Presents the 3D and contour profiles of the dark-type solution corresponding to Equation (50)

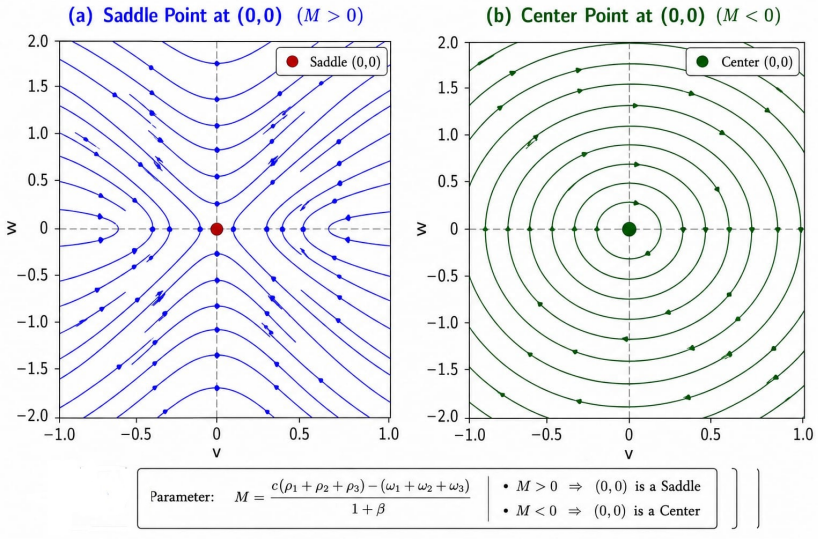


**Figure 8.** Phase portraits of the reduced KP system around the equilibrium point $(0, 0)$, showing its transition between a saddle for $M > 0$ and a center for $M < 0$

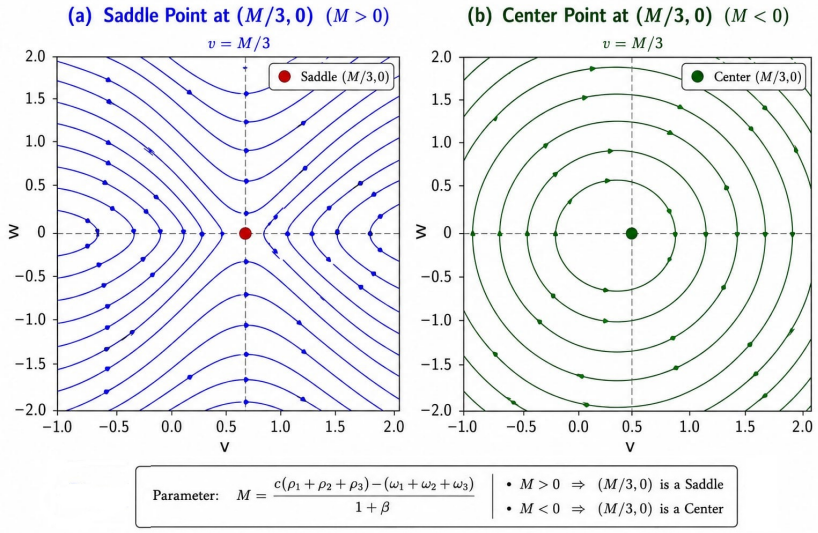


**Figure 9.** Phase portraits of the reduced KP system around the equilibrium point $(M/3, 0)$, showing its transition between a saddle for $M > 0$ and a center for $M < 0$

## CONCLUSIONS

In the present work, the (3+1)-dimensional generalized Kadomtsev–Petviashvili equation, which characterizes wave spread in incompressible fluids, is analytically investigated using the Improved Simple Equation Method (ISEM) and Exponential Method These methods are employed to construct several classes of exact wave solutions, including exponential-type solutions, dark-type soliton solutions, exhibiting singular solution, singular periodic patterns, as well as hyperbolic forms. Furthermore, three-dimensional representations along with contour plots are provided to visualize and analyze the dynamic and physical characteristics of the obtained solutions. Moreover, the bifurcation analysis of the reduced traveling-wave system provides a dynamical interpretation of the obtained nonlinear wave structures. The equilibrium points and their stability properties are examined, revealing a critical condition at which the equilibrium branches coalesce and exchange their stability characteristics. This bifurcation behavior clarifies how variations in the governing parameters influence the qualitative dynamics of the modified (3+1)-dimensional KP equation. Therefore, the combination of exact analytical solution methods and bifurcation analysis offers a more comprehensive understanding of both the explicit wave structures and their underlying dynamical behavior.

## ORCID

**Ibrahim Saber**, https://orcid.org/0009-0000-4262-3271; **Hamdy M. Ahmed**, https://orcid.org/0000-0001-8772-3663; **Niveen Badra**, https://orcid.org/0000-0002-8831-0577; **Islam Samir**, https://orcid.org/0000-0002-8172-3782

## REFERENCES

[1] Feng L, and Zhu Z. "Darboux transformation and soliton solutions for a nonlocal two-component complex mKdV equation," J. Nonlinear Math. Phys. **30**, 112–128 (2023). https://doi.org/10.1007/s44198-023-00112-w

[2] Alraddadi I, and Alsharif F. "Innovative soliton solutions for a (2+1)-dimensional generalized KdV equation using two effective approaches," AIMS Math. **9**, 1664–1685 (2024). https://doi.org/10.3934/math.2024082

[3] Alam N., Ullah M.S., Nofal T.A., Ahmed H.M., Ahmed K.K., and Al-Nahhas M.A. "Novel dynamics of the fractional KFG equation through the unified and unified solver schemes with stability and multistability analysis," Nonlinear Eng. **13**, 20240034 (2024). https://doi.org/10.1515/nleng-2024-0034

[4] Liao S. "A new non-perturbative approach in quantum mechanics for time-independent Schrödinger equations," Sci. China Phys. Mech. Astron. **63**, 234612 (2020). https://doi.org/10.1007/s11433-019-9430-4

[5] Ahmed K.K., Ahmed H.M., Badra N.M., Mirzazadeh M., Rabie W.B., and Eslami M. "Diverse exact solutions to Davey–Stewartson model using modified extended mapping method," Nonlinear Analysis: Modelling and Control. **29**(5), 983-1002 (2024). https://doi.org/10.15388/namc.2024.29.36103

[6] Biswas A, Vega-Guzman J, Kara A, Qin Z, Ekici M, Yıldırım Y, Alshehri H, and Belic M. "Conservation laws for solitons in magneto-optic waveguides with dual-power law nonlinearity," Phys Lett. A, **416**, 127667 (2021). https://doi.org/10.1016/j.physleta.2021.127667

[7] Samir I., Abd-Elmonem A., and Ahmed H.M. "General solitons for eighth-order dispersive nonlinear Schrödinger equation with ninth-power law nonlinearity using improved modified extended tanh method," Optical and Quantum Electronics, **55**(5), 470 (2023). https://doi.org/10.1007/s11082-023-04753-5

[8] Horikis T, Frantzeskakis D, and Smyth N. "Extended shallow water wave equations," Wave Motion, **112**, 102934 (2022). https://doi.org/10.1016/j.wavemoti.2022.102934

[9] Khalifa A.S., Ahmed H.M., Badra N.M., and Rabie W.B. "Exploring solitons in optical twin-core couplers with Kerr law of nonlinear refractive index using the modified extended direct algebraic method," Optical and Quantum Electronics, **56**(6), 1060 (2024). https://doi.org/10.1007/s11082-024-06882-x

[10] Shakeel K, et al. "Construction of soliton solutions of time-fractional CDGSK equation with Painlevé analysis in plasma physics." Symmetry, **16**, 824 (2024). https://doi.org/10.3390/sym16070824

[11] Alharbi M., Elmandouh A., and Elbrolosy M. "Soliton, bifurcation, and quasi-periodic behaviour in fractional coupled Schrödinger equations," Mathematics, **13**, 3174 (2025). https://doi.org/10.3390/math13193174

[12] Yao F., and Younas U. "Dynamics of soliton solutions to nonlinear dynamical equations via neural-symbolic methods," Mathematics, **13**, 3546 (2025). https://doi.org/10.3390/math13213546

[13] Chen, X., Xia, T., and Zhu, L., "A (2+1)-Dimensional Integrable Breaking Soliton Equation and Its Algebro-Geometric Solutions," Mathematics, **12**(13), 2034 (2024). https://doi.org/10.3390/math12132034

[14] Zhang Y, and Chen S. "Advanced Hirota bilinear approach for multi-component integrable systems," Appl Math Comput. **455**, 128123 (2024). https://doi.org/10.1016/j.amc.2023.128123

[15] Novikov, S. P., "The Periodic Problem for the Korteweg–de Vries Equation", Functional Analysis and Its Applications, **8**(3), 236–246 (1974). https://doi.org/10.1007/BF01075697

[16] Dubrovin, B. A., Matveev, V. B., and Novikov, S. P., "Nonlinear Equations of Korteweg–de Vries Type, Finite-Zone Linear Operators, and Abelian Varieties", Russian Mathematical Surveys, **31**(1), 59–146 (1976). https://doi.org/10.1070/RM1976v031n01ABEH001446

[17] Krichever, I. M., "Methods of Algebraic Geometry in the Theory of Nonlinear Equations", Russian Mathematical Surveys, **32**(6), 185–213 (1977). https://doi.org/10.1070/RM1977v032n06ABEH003862

[18] Dubrovin, B. A., "Theta Functions and Nonlinear Equations", Russian Mathematical Surveys, **36**(2), 11–92 (1981). https://doi.org/10.1070/RM1981v036n02ABEH002596

[19] Belokolos, E. D., Bobenko, A. I., Enolskii, V. Z., Its, A. R., and Matveev, V. B., *Algebro-Geometric Approach to Nonlinear Integrable Equations*, (Springer Series in Nonlinear Dynamics, Springer, Berlin, 1994). https://doi.org/10.1007/978-3-662-02973-2

[20] Nakamura, A., "A Direct Method of Calculating Periodic Wave Solutions to Nonlinear Evolution Equations. I", Journal of the Physical Society of Japan, **47**(5), 1701–1705 (1979). https://doi.org/10.1143/JPSJ.47.1701

[21] Nakamura, A., "A Direct Method of Calculating Periodic Wave Solutions to Nonlinear Evolution Equations. II", Journal of the Physical Society of Japan, **48**(4), 1365–1370 (1980). https://doi.org/10.1143/JPSJ.48.1365

[22] Hon, Y. C., Fan, E. G., and Qin, Z., "A Kind of Explicit Quasi-Periodic Solution and Its Limit for the Toda Lattice Equation", Modern Physics Letters B, **22**(8), 547–553 (2008). https://doi.org/10.1142/S0217984908015097

[23] Fan, E. G., and Chow, K. W., "On the Periodic Solutions for Both Nonlinear Differential and Difference Equations: A Unified Approach", Physics Letters A, **374**(35), 3629–3634 (2010). https://doi.org/10.1016/j.physleta.2010.07.005

[24] Hon, Y. C., and Fan, E. G., "Super Quasiperiodic Wave Solutions and Asymptotic Analysis for N = 1 Supersymmetric KdV-Type Equations", Theoretical and Mathematical Physics, **166**(3), 317–336 (2011). https://doi.org/10.1007/s11232-011-0026-x

[25] Fan, E. G., Chow, K. W., and Li, J. H., "On Doubly Periodic Standing Wave Solutions of the Coupled Higgs Field Equation", Studies in Applied Mathematics, **128**(1), 86–105 (2012). https://doi.org/10.1111/j.1467-9590.2011.00531.x

[26] Tian, S. F., and Zhang, H. Q., "Riemann Theta Function Periodic Wave Solutions and Rational Characteristics for Nonlinear Evolution Equations", Journal of Mathematical Analysis and Applications, **371**(2), 585–608 (2010). https://doi.org/10.1016/j.jmaa.2010.05.070

[27] Ahmed M.S., Zaghrout A.A., and Ahmed H.M. "Exploration new solitons in fiber Bragg gratings with cubic–quartic dispersive reflectivity using improved modified extended tanh-function method," The European Physical Journal Plus, **138**(1), 32 (2023). https://doi.org/10.1140/epjp/s13360-023-03666-2

[28] Su, Y. Q., "Theta Function Solutions of the (3+1)-Dimensional Jimbo–Miwa Equation", Mathematical Problems in Engineering, **2017**, 2924947 (2017). https://doi.org/10.1155/2017/2924947

[29] Zhao, S., Wang, H., and Wang, Y., "Quasiperiodic-to-Soliton Conversions and Their Mechanisms of the (3+1)-Dimensional Generalized Kadomtsev–Petviashvili Equation", Wave Motion, **134**, 103505 (2025). https://doi.org/10.1016/j.wavemoti.2025.103505

[30] Pu J., and Chen Y. "Integrability and exact solutions of the (2+1)-dimensional KdV equation with Bell polynomials approach," Acta Math. Appl. Sin. Engl. Ser. **38**, 861–881 (2022). https://doi.org/10.1007/s10255-022-1020-9

[31] Raut S., Barman R., and Sarkar T. "Integrability, breather, lump and quasi-periodic waves of non-autonomous Kadomtsev–Petviashvili equation based on Bell-polynomial approach," Wave Motion, **119**, 103125 (2023). https://doi.org/10.1016/j.wavemoti.2023.103125

[32] Kumar S, and Mann N. Dynamic study of qualitative analysis, traveling waves, solitons, bifurcation, quasiperiodic, and chaotic behavior of integrable Kuralay equations," Opt. Quantum Electron. **56**, 859 (2024). https://doi.org/10.1007/s11082-024-06701-3

[33] Juan Y, Zhao Z, and Wazwaz A. "Solitons, nonlinear wave transitions and characteristics of quasi-periodic waves for a (3+1)-dimensional generalized Calogero–Bogoyavlenskii–Schiff equation," Chin. J. Phys. **89**, 896–929 (2024). https://doi.org/10.1016/j.cjph.2024.03.034

[34] Kadomtsev, B. B., and Petviashvili, V. I., "On the Stability of Solitary Waves in Weakly Dispersive Media", Soviet Physics Doklady, **15**(6), 539–541 (1970). https://www.mathnet.ru/eng/dan35739

[35] Guan X, Liu W, Zhou Q, and Biswas A. "Some lump solutions for a generalized (3+1)-dimensional Kadomtsev–Petviashvili equation," Appl. Math. Comput. **366**, 124757 (2020). https://doi.org/10.1016/j.amc.2019.124757

[36] Zada A. "Applications of extended simple equation method to modern nonlinear Schrödinger-type equations," Optik, **271**, 170334 (2023). https://doi.org/10.1016/j.ijleo.2022.170334

[37] Khan Z. "Modulation instability and soliton dynamics for dual-power-law nonlinear Schrödinger models," Optik, **266**, 169789 (2023). https://doi.org/10.1016/j.ijleo.2022.169789

[38] Yildirim S. "Dispersive traveling waves in modified EW-type systems using updated analytical schemes," Results Phys. **43**, 106210 (2023). https://doi.org/10.1016/j.rinp.2023.106210

[39] Al-Amry M.S.A., and Al-Abdali E.F.A. "Exact soliton solutions for new (4+1)-dimensional NLDEs by a new exp-expansion method," Int. J. Theor. Appl. Math. **11**, 26–33 (2025). https://doi.org/10.11648/j.ijtam.20251101.14

[40] Abu-Alhamed S.F., and Elboree M.K. "Investigation of soliton solutions for some important nonlinear evolution equations via exp-expansion method," SVU Int. J. Basic Sci. **2**, 37–47 (2025). https://doi.org/10.21608/SVUIJBS.2025.322864.1006

[41] Borhan J.R., et al. "Exploring new traveling wave solutions to nonlinear integro-partial differential equations with generalized expansion methods," Math. J. **12**, 2023–2024 (2023). https://doi.org/10.3390/math11092023

[42] Yang D., and Zhang J. "The soliton wave solutions and bifurcations of the (2+1)-dimensional dissipative long wave equation," J. Nonlinear Math. Phys. **29**, 659–677 (2022). https://doi.org/10.1007/s44198-022-00055-8

[43] El-Ajou A., Zedan H.A., Alquran M., et al. "Investigation of the analytical and numerical solutions with bifurcation analysis for the (2+1)-dimensional Bogoyavlenskii-Kadomtsev-Petviashvili equation," Opt. Quantum Electron. **55**, (2023). https://doi.org/10.1007/s11082-023-04848-z

[44] Wang Y., Xu H., and Sun Q. "New groups of solutions to the Whitham-Broer-Kaup equation," Appl. Math. Mech. **41**, 1735–1746 (2020). https://doi.org/10.1007/s10483-020-2683-7

[45] Uecker H. "Continuation and bifurcation in nonlinear PDEs – algorithms, applications, and experiments," Jahresber Dtsch. Math-Ver. **124**, 43–80 (2022). https://doi.org/10.1365/s13291-021-00241-5

[46] Alam N., Ullah M.S., Manafian J., Mahmoud K.H., Alsubaie A.S., Ahmed H.M., Ahmed K.K., et al., "Bifurcation analysis, chaotic behaviors, and explicit solutions for a fractional two-mode Nizhnik-Novikov-Veselov equation in mathematical physics," AIMS Mathematics, **10**(3), 4558-4578 (2025). https://doi.org/10.3934/math.2025211

## БАГАТОФОРМНІ ОДИНОКІ ХВИЛЬОВІ СТРУКТУРИ ТА БІФУРКАЦІЙНИЙ АНАЛІЗ РОЗШИРЕНОГО МОДИФІКОВАНОГО (3+1)-ВИМІРНОГО РІВНЯННЯ КАДОМЦЕВА-ПЕТВІАШВІЛІ ЗА ДОПОМОГОЮ ГІБРИДНИХ АНАЛІТИЧНИХ ПІДХОДІВ

**Ібрагім Сабер**[1,2], **Хамді М. Ахмед**[3], **Нівін Бадра**[1], **Іслам Самір**[1]

[1]*Кафедра фізики та математики, Інженерний факультет, Університет Айн-Шамс, Каїр, Єгипет*

[2]*Факультет штучного інтелекту, Єгипетський російський університет, Каїр, Єгипет*

[3]*Кафедра фізики та інженерної математики, Вищий інженерний інститут, Академія Ель-Шорук, Каїр, Єгипет*

У цій роботі представлено виведення точних аналітичних розв'язків для (3+1)-вимірного модифікованого рівняння Кадомцева-Петвіашвілі рівняння з використанням двох ефективних аналітичних схем, а саме: покращеного методу простих рівнянь та підходу експоненціального розкладання. Розглянута модель є актуальною для опису поширення складних нелінійних хвиль у нестисливих рідинних середовищах, де дисперсійні та нелінійні ефекти сильно пов'язані. Застосовані методи дають багату різноманітність хвильових структур з різними фізичними характеристиками, включаючи сингулярні та несингулярні локалізовані утворення, періодичні структури та експоненціально спадаючі профілі. Крім того, отримані гіперболічні та тригонометричні конфігурації, що відображають різні режими поширення системи. Якісна поведінка цих рішень додатково уточнюється за допомогою тривимірних поверхневих представлень та контурних відображень. Крім того, проведено біфуркаційний аналіз для редукованого звичайного диференціального рівняння біжучої хвилі для дослідження точок рівноваги, їх властивостей стійкості та критичних умов, пов'язаних з обміном стійкістю. Цей аналіз забезпечує додаткову перспективу динамічних систем на отримані хвильові структури та уточнює вплив керівних параметрів на якісну поведінку моделі.

**Ключові слова:** *нелінійні дисперсійні системи; багатовимірні нелінійні хвилі; точні аналітичні рішення*

East European Journal of Physics. 3. 198–211 (2026)
DOI: 10.26565/2312-4334-2026-3-16 ISSN 2312-4334

# ACCELERATING FIVE-DIMENSIONAL BIANCHI TYPE-I COSMOLOGY IN SAEZ–BALLESTER THEORY WITH HYPERBOLIC EXPANSION

**Jagat Daimary**[1], **Rajshekhar Roy Baruah**[2*]
[1]*Department of Mathematics, Gyanpeeth Degree College, Nikashi, Baksa, Assam - 781372, India*
[2]*Department of Mathematical Sciences, Bodoland University, Kokrajhar, Assam - 783370, India*
[*]*Corresponding Author e-mail: rsroybaruah55@gmail.com*
Received June 6, 2026; revised August 20, 2026; accepted August 25, 2026

We present a five-dimensional anisotropic Bianchi type-I cosmological model in Saez–Ballester scalar–tensor theory employing the hyperbolic expansion law $a(t) = \sinh^{\alpha}(\beta t)$. Exact solutions of the field equations are derived and their cosmological behavior is examined. The model evolves from an initial singular state to a late-time accelerated phase, with anisotropy diminishing and isotropization achieved asymptotically. The deceleration parameter approaches $(q = -1)$, while $(\omega_{de} \approx -1.308)$ indicates phantom dark-energy behavior. The null, weak, and dominant energy conditions remain satisfied, whereas the strong energy condition is violated, supporting the observed cosmic acceleration. Furthermore, the statefinder and Om diagnostics reveal that the model asymptotically approaches the ΛCDM scenario.

**Keywords:** *Saez–Ballester theory; Bianchi type-I universe; Higher-dimensional cosmology; Hyperbolic expansion law; Dark energy; Cosmic acceleration*

## 1. INTRODUCTION

The discovery of the late-time accelerated expansion of the Universe through observations of type Ia supernovae revolutionized modern cosmology and established the existence of an exotic cosmic component known as dark energy [1, 2]. Subsequent observations of the cosmic microwave background radiation, baryon acoustic oscillations, and large-scale structure surveys have further confirmed this accelerating scenario and constrained the cosmological parameters with remarkable precision [3]. Within the framework of the standard cosmological model, the accelerated expansion is attributed to the cosmological constant Λ. Although the ΛCDM model successfully explains a wide range of observational data, it suffers from the well-known fine-tuning and coincidence problems, thereby motivating the exploration of alternative descriptions of dark energy and gravity [4, 5].

In recent years, modified theories of gravity have emerged as promising candidates for explaining the accelerated expansion of the Universe without introducing an ad hoc cosmological constant. Extensive investigations have been carried out in $f(R)$ gravity, scalar–tensor theories, teleparallel gravity, and other geometrically modified frameworks [6–10]. These theories provide richer gravitational dynamics and often admit cosmological solutions capable of describing both the early inflationary epoch and the present accelerated phase. Among the various alternatives to Einstein's theory, scalar–tensor theories occupy a central position because scalar fields naturally arise in higher-dimensional theories, supergravity, and string-inspired models. One particularly interesting scalar–tensor formulation is the Saez–Ballester theory proposed by Saez and Ballester [11]. This theory introduces a dimensionless scalar field coupled to gravity through a non-standard kinetic term and has been employed to study several cosmological scenarios. Owing to its mathematical simplicity and physical richness, the theory has attracted considerable attention in investigations of anisotropic universes, exact cosmological solutions, and dark-energy dynamics [12–15].

Anisotropic cosmological models play an important role in understanding the early stages of cosmic evolution. Although present observations indicate that the Universe is highly isotropic on large scales, it is plausible that anisotropies existed during the primordial epoch. The study of anisotropic space-times therefore provides valuable insight into the isotropization process and the dynamical behaviour of the Universe at early times [16–18]. In this context, Bianchi cosmological models have proved particularly useful because they represent homogeneous but anisotropic generalizations of the Friedmann–Lemaître–Robertson–Walker geometry. Among them, the Bianchi type-I model is the simplest anisotropic cosmological model and has been extensively employed in the study of dark energy, scalar fields, and modified gravity theories [19, 20]. Another important development in modern cosmology is the investigation of higher-dimensional space-times. The concept of extra dimensions originated from the pioneering works of Kaluza and Klein [21, 22] and subsequently became an important ingredient of unified field theories. Higher-dimensional cosmological models naturally arise in string theory, supergravity, and braneworld scenarios, providing a broader framework for investigating gravitational interactions and the large-scale dynamics of the Universe [23, 24]. In such models, the additional dimension can introduce

***Cite as:*** J. Daimary, R. Roy Baruah, East Eur. J. Phys. 3, 198 (2026), https://doi.org/10.26565/2312-4334-2026-3-16

extra geometric degrees of freedom and modify the effective four-dimensional gravitational dynamics obtained after dimensional reduction. Depending on the underlying higher-dimensional framework, these effects may manifest themselves through modifications of the effective energy density and pressure, the evolution of the scale factors, the gravitational coupling, or additional scalar-field-like degrees of freedom [25, 26]. Consequently, extra-dimensional models can provide alternative mechanisms for influencing the expansion history of the Universe and the evolution of primordial anisotropies. Recent investigations of higher-dimensional and braneworld cosmologies have demonstrated that their parameters can be constrained using cosmological observations, including Hubble-rate measurements, Type Ia supernovae, baryon acoustic oscillations, Big Bang nucleosynthesis, and the growth of large-scale structure [27, 28].

The physical verification of extra-dimensional effects, however, remains challenging because the additional dimension may be compactified at a scale beyond the direct reach of current experiments or may interact only weakly with ordinary matter. Nevertheless, possible signatures of extra dimensions can be investigated indirectly through precision tests of gravity and cosmological observations. In particular, laboratory experiments searching for deviations from Newton's inverse-square law at submillimetre scales provide constraints on possible compact extra dimensions and other short-range gravitational modifications [29]. Cosmological observations can provide complementary constraints, since extra-dimensional scenarios may modify the expansion history or introduce additional effective components that leave signatures in the cosmic microwave background, baryon acoustic oscillations, Type Ia supernovae, Big Bang nucleosynthesis, and the growth of cosmic structure [27, 30]. Such observations can therefore be used to place constraints on extra-dimensional scenarios, although the resulting signatures are generally model-dependent and may be degenerate with those arising from dark energy or other modified-gravity mechanisms. In this context, five-dimensional cosmological models provide a relatively tractable framework for studying the possible dynamical consequences of an additional dimension while retaining sufficient mathematical simplicity for obtaining and analyzing exact cosmological solutions. A five-dimensional Bianchi type-I space-time is particularly useful for examining the interplay between anisotropic expansion, higher-dimensional geometry, and scalar-field dynamics.

To obtain exact solutions of the nonlinear gravitational field equations, it is often necessary to impose physically motivated constraints on the cosmic dynamics. One useful approach is the adoption of specific expansion laws capable of describing realistic cosmological evolution. Hyperbolic expansion laws have received significant attention because they naturally describe a transition from an early decelerating phase to a late-time accelerating epoch. Such behaviour is consistent with observational evidence and has been successfully employed in a variety of cosmological investigations [31]. Furthermore, these expansion laws often lead to exact analytical solutions, enabling a detailed examination of the evolution of physical and geometrical parameters.

Motivated by the above considerations, we investigate a five-dimensional anisotropic Bianchi type-I cosmological model in the framework of Saez–Ballester scalar–tensor theory by adopting the hyperbolic expansion law $a(t) = \sinh^{\alpha}(\beta t)$, where $\alpha$ and $\beta$ are positive constants. Exact solutions of the field equations are obtained and the resulting cosmological behaviour is analyzed through the evolution of the Hubble parameter, expansion scalar, shear scalar, anisotropy parameter, energy density, pressure, and equation-of-state parameter. The physical viability of the model is further examined through the energy conditions, while statefinder and Om diagnostics are employed to characterize the dark-energy dynamics and assess the asymptotic behaviour of the model relative to the standard $\Lambda$CDM cosmology.

The paper is organized as follows. In Section 2, the field equations of the Saez–Ballester theory for a five-dimensional Bianchi type-I space-time are presented. Exact solutions are obtained in Section 3. The physical properties and cosmological implications of the model are discussed in subsequent sections. Finally, the main conclusions are summarized in the last section.

## 2. SAEZ–BALLESTER THEORY AND FIELD EQUATIONS

We consider the five-dimensional anisotropic Bianchi type-I space-time described by the line element

$$ds^2 = -dt^2 + A^2(dx^2 + dy^2) + B^2dz^2 + C^2d\psi^2, \tag{1}$$

where the metric potentials $A(t)$, $B(t)$, and $C(t)$ depend only on the cosmic time $t$. The coordinates $(x, y, z)$ represent the ordinary spatial dimensions, while $\psi$ denotes the additional spatial dimension. The model is spatially homogeneous but anisotropic and reduces to the spatially flat Friedmann–Robertson–Walker (FRW) universe in the isotropic limit $A = B = C$.

The gravitational dynamics are governed by the Saez–Ballester scalar–tensor theory, whose action is given by

$$S = \int \sqrt{-g}\left[R - \omega\phi^m g^{ij}\phi_{,i}\phi_{,j} + L_m\right] d^5x, \tag{2}$$

where $R$ is the Ricci scalar, $\phi$ is a dimensionless scalar field, $\omega$ and $m$ are coupling constants, and $L_m$ denotes the matter Lagrangian density. Throughout this work, geometrized units are adopted such that $8\pi G = c = 1$.

Variation of the action (2) with respect to the metric tensor $g_{ij}$ yields the gravitational field equations

$$R_{ij} - \frac{1}{2}g_{ij}R - \omega\phi^m\left(\phi_{,i}\phi_{,j} - \frac{1}{2}g_{ij}\phi_{,k}\phi^{,k}\right) = -T_{ij}, \tag{3}$$

where $T_{ij}$ is the energy–momentum tensor of the cosmic fluid.
Similarly, variation of the action with respect to the scalar field $\phi$ gives the scalar field equation

$$2\phi^m\phi^{,i}_{;i} + m\phi^{m-1}\phi_{,k}\phi^{,k} = 0 \tag{4}$$

The matter content of the Universe is assumed to be a perfect fluid whose energy–momentum tensor is

$$T_{ij} = (\rho + p)u_iu_j + pg_{ij}, \tag{5}$$

where $\rho$ and $p$ denote the energy density and isotropic pressure, respectively, and the five-velocity vector satisfies $u^iu_i = -1$.
The covariant conservation law $T^{ij}_{;j} = 0$ leads to the continuity equation

$$\dot{\rho} + (\rho + p)\left(2\frac{\dot{A}}{A} + \frac{\dot{B}}{B} + \frac{\dot{C}}{C}\right) = 0 \tag{6}$$

To characterize the expansion dynamics of the anisotropic universe, we define the average scale factor as

$$a = (A^2BC)^{1/4}, \tag{7}$$

so that the spatial volume becomes

$$V = a^4 = A^2BC. \tag{8}$$

The mean Hubble parameter is

$$H = \frac{\dot{a}}{a} = \frac{1}{4}\left(2\frac{\dot{A}}{A} + \frac{\dot{B}}{B} + \frac{\dot{C}}{C}\right) \tag{9}$$

The directional Hubble parameters along the principal axes are defined by

$$H_1 = \frac{\dot{A}}{A}, \qquad H_2 = \frac{\dot{B}}{B}, \qquad H_3 = \frac{\dot{C}}{C} \tag{10}$$

The deceleration parameter is given by

$$q = -\frac{a\ddot{a}}{\dot{a}^2} \tag{11}$$

which characterizes the acceleration or deceleration of the cosmic expansion.
Substituting the metric (1) into the field equations (3) and using the perfect-fluid energy–momentum tensor (5), we obtain the independent gravitational field equations

$$\frac{\ddot{A}}{A} + \frac{\ddot{B}}{B} + \frac{\ddot{C}}{C} + \frac{\dot{A}\dot{B}}{AB} + \frac{\dot{A}\dot{C}}{AC} + \frac{\dot{B}\dot{C}}{BC} = -p + \frac{\omega}{2}\phi^m\dot{\phi}^2, \tag{12}$$

$$2\frac{\ddot{A}}{A} + \frac{\dot{A}^2}{A^2} + \frac{\ddot{C}}{C} + 2\frac{\dot{A}\dot{C}}{AC} = -p + \frac{\omega}{2}\phi^m\dot{\phi}^2, \tag{13}$$

$$2\frac{\ddot{A}}{A} + \frac{\ddot{B}}{B} + \frac{\dot{A}^2}{A^2} + 2\frac{\dot{A}\dot{B}}{AB} = -p + \frac{\omega}{2}\phi^m\dot{\phi}^2, \tag{14}$$

$$\frac{\dot{A}^2}{A^2} + 2\frac{\dot{A}\dot{B}}{AB} + 2\frac{\dot{A}\dot{C}}{AC} + \frac{\dot{B}\dot{C}}{BC} = \rho - \frac{\omega}{2}\phi^m\dot{\phi}^2, \tag{15}$$

while the scalar field equation reduces to

$$\ddot{\phi} + \dot{\phi}\left(2\frac{\dot{A}}{A} + \frac{\dot{B}}{B} + \frac{\dot{C}}{C}\right) + \frac{m}{2}\frac{\dot{\phi}^2}{\phi} = 0 \tag{16}$$

## 3. EXACT COSMOLOGICAL SOLUTIONS

The field equations (12)–(16) constitute a highly nonlinear system involving the metric potentials $A$, $B$, and $C$, the scalar field $\phi$, the energy density $\rho$, and the pressure $p$. Since the number of unknown functions exceeds the number of independent equations, an additional physically motivated condition is required to obtain exact solutions.

We adopt the hyperbolic expansion law

$$a(t) = \sinh^{\alpha}(\beta t), \qquad \alpha > 0, \quad \beta > 0, \tag{17}$$

where $\alpha$ and $\beta$ are positive constants.

Using equation (8), the corresponding spatial volume is

$$V = A^2BC = a^4 = \sinh^{4\alpha}(\beta t) \tag{18}$$

The Hubble parameter corresponding to the hyperbolic law becomes

$$H = \frac{\dot{a}}{a} = \alpha\beta \coth(\beta t) \tag{19}$$

and the deceleration parameter is

$$q = -1 + \frac{1}{\alpha}\operatorname{sech}^2(\beta t) \tag{20}$$

Equation (20) shows that the model evolves from an initially decelerating phase to a late-time accelerating epoch. In particular, $\lim\limits_{t\to\infty} q = -1$, which corresponds to a de Sitter-type accelerated expansion.

Subtracting equation (12) from equations equation (13), (14) and integrating the resulting differential equations twice, we obtain

$$\frac{A^2}{B} = l_1 \exp\left(c_1 \int a^{-4} dt\right), \tag{21}$$

$$\frac{A^2}{C} = l_2 \exp\left(c_2 \int a^{-4} dt\right), \tag{22}$$

and

$$\frac{B}{C} = l_3 \exp\left(c_3 \int a^{-4} dt\right), \tag{23}$$

where $l_1, l_2, l_3, c_1, c_2$, and $c_3$ are integration constants.

Combining the above relations with the volume condition, the metric potentials can be written as

$$A = x_1 a^{\frac{2}{3}} \exp\left(d_1 \int a^{-4} dt\right) = x_1 \sinh^{\frac{2\alpha}{3}}(\beta t) \exp\left[d_1 \int \sinh^{-4\alpha}(\beta t) dt\right], \tag{24}$$

$$B = x_2 a^{\frac{4}{3}} \exp\left(d_2 \int a^{-4} dt\right) = x_2 \sinh^{\frac{4\alpha}{3}}(\beta t) \exp\left[d_2 \int \sinh^{-4\alpha}(\beta t) dt\right], \tag{25}$$

$$C = x_3 a^{\frac{4}{3}} \exp\left(d_3 \int a^{-4} dt\right) = x_3 \sinh^{\frac{4\alpha}{3}}(\beta t) \exp\left[d_3 \int \sinh^{-4\alpha}(\beta t) dt\right] \tag{26}$$

where

$$x_1 = (l_1 l_2)^{1/6}, \qquad x_2 = \left(\frac{l_3}{l_1}\right)^{1/3}, \qquad x_3 = (l_2 l_3)^{-1/3}, \tag{27}$$

and

$$d_1 = \frac{c_1 + c_2}{6}, \qquad d_2 = \frac{c_3 - c_1}{3}, \qquad d_3 = -\frac{c_2 + c_3}{3}. \tag{28}$$

These constants satisfy the consistency conditions

$$x_1^2 x_2 x_3 = 1, \qquad d_1 + d_2 + d_3 = 0 \tag{29}$$

From equation (16) we get,

$$\phi(t) = \left[\frac{h(m+2)}{2} \int a^{-4} dt\right]^{\frac{2}{m+2}} = \left[\frac{h(m+2)}{2} \int \sinh^{-4\alpha}(\beta t)\, dt\right]^{\frac{2}{m+2}} \tag{30}$$

## 4. PHYSICAL AND KINEMATICAL PROPERTIES OF THE MODEL

Using the exact solutions obtained in the previous section, we now investigate the kinematical evolution and physical characteristics of the cosmological model.

The mean Hubble parameter corresponding to the hyperbolic expansion law is

$$H = \alpha\beta \coth(\beta t). \tag{31}$$

The expansion scalar is given by

$$\theta = 4H = 4\alpha\beta \coth(\beta t) \tag{32}$$

The directional Hubble parameters along the principal directions are obtained from the metric potentials as

$$H_x = H_y = \frac{\dot{A}}{A} = \frac{2\alpha\beta}{3} \coth(\beta t) + d_1 \sinh^{-4\alpha}(\beta t), \tag{33}$$

$$H_z = \frac{\dot{B}}{B} = \frac{4\alpha\beta}{3} \coth(\beta t) + d_2 \sinh^{-4\alpha}(\beta t), \tag{34}$$

$$H_\psi = \frac{\dot{C}}{C} = \frac{4\alpha\beta}{3} \coth(\beta t) + d_3 \sinh^{-4\alpha}(\beta t), \tag{35}$$

The shear scalar and mean anisotropy parameter is given by

$$\sigma^2 = \frac{2}{9}\alpha^2\beta^2 \coth^2(\beta t) + \frac{1}{2}\left(2d_1^2 + d_2^2 + d_3^2\right) \sinh^{-8\alpha}(\beta t) \tag{36}$$

$$\Delta = \frac{2d_1^2 + d_2^2 + d_3^2}{4\alpha^2\beta^2 \coth^2(\beta t)} \sinh^{-8\alpha}(\beta t). \tag{37}$$

Since $\lim_{t\to\infty} \sinh^{-8\alpha}(\beta t) = 0$, it follows that $\lim_{t\to\infty} \Delta = 0$, and consequently $\lim_{t\to\infty} \frac{\sigma}{\theta} = 0$. Therefore, the anisotropy gradually decreases with cosmic time and the universe approaches isotropy at late times.

The deceleration parameter corresponding to the hyperbolic expansion law is

$$q = -1 + \frac{1}{\alpha} \operatorname{sech}^2(\beta t) \tag{38}$$

At the initial epoch, $q(0) = -1 + \frac{1}{\alpha}$, while at late times $\lim_{t\to\infty} q = -1$. Hence, the model describes a universe evolving from an early decelerating phase to a late-time accelerated expansion phase approaching the de Sitter regime.

Furthermore, the average scale factor satisfies $a = \sinh^{\alpha}(\beta t)$, which implies $a \to 0$ as $t \to 0$, and $a \to \infty$ as $t \to \infty$. Therefore, the obtained cosmological model represents an expanding universe beginning with a Big-Bang-type singularity and evolving towards an accelerating and isotropic state at late times.

From equation (15) we get,

$$\rho(t) = \frac{52}{9}\alpha^2\beta^2 \coth^2(\beta t) + \left(d_1^2 + 2d_1d_2 + 2d_1d_3 + d_2d_3 + \frac{\omega h^2}{2}\right) \sinh^{-8\alpha}(\beta t) \tag{39}$$

Using equation (12) we obtain

$$\begin{aligned} p(t) = &\left(\frac{10}{3}\alpha\beta^2 - \frac{68}{9}\alpha^2\beta^2\right) \coth^2(\beta t) - \frac{10}{3}\alpha\beta^2 - \frac{4}{3}\alpha\beta d_1 \coth(\beta t) \sinh^{-4\alpha}(\beta t) \\ &+ \left[\frac{\omega h^2}{2} - \left(d_1^2 + d_1d_3 + d_3^2\right)\right] \sinh^{-8\alpha}(\beta t) \end{aligned} \tag{40}$$

The equation of state parameter is defined as

$$\omega_{de}(t) = \frac{p(t)}{\rho(t)}. \tag{41}$$

Therefore,

$$\omega_{de}(t) = \frac{\left(\frac{10}{3}\alpha\beta^2 - \frac{68}{9}\alpha^2\beta^2\right)\coth^2(\beta t) - \frac{10}{3}\alpha\beta^2 - \frac{4}{3}\alpha\beta d_1 \coth(\beta t)\sinh^{-4\alpha}(\beta t)}{\frac{52}{9}\alpha^2\beta^2\coth^2(\beta t) + \left(d_1^2 + 2d_1d_2 + 2d_1d_3 + d_2d_3 + \frac{\omega h^2}{2}\right)\sinh^{-8\alpha}(\beta t)} + \frac{\left[\frac{\omega h^2}{2} - \left(d_1^2 + d_1d_3 + d_3^2\right)\right]\sinh^{-8\alpha}(\beta t)}{\frac{52}{9}\alpha^2\beta^2\coth^2(\beta t) + \left(d_1^2 + 2d_1d_2 + 2d_1d_3 + d_2d_3 + \frac{\omega h^2}{2}\right)\sinh^{-8\alpha}(\beta t)} \tag{42}$$

At late cosmic times ($t \to \infty$), the hyperbolic functions satisfy $\coth(\beta t) \to 1$, while the terms $\sinh^{-4\alpha}(\beta t)$ and $\sinh^{-8\alpha}(\beta t)$ vanish exponentially for $\alpha > 0$. Consequently,

$$\lim_{t\to\infty} \omega_{de}(t) = -\frac{17}{13} \approx -1.308. \tag{43}$$

Since $\omega_{de} < -1$, the effective dark-energy fluid enters the phantom regime at late times. This result indicates that the universe undergoes a phase of accelerated expansion stronger than that produced by a cosmological constant ($\omega = -1$). Furthermore, the exponential decay of the anisotropic and scalar-field terms implies that their influence becomes negligible in the asymptotic future, leading to a dark-energy dominated cosmological evolution. Therefore, within the framework of the Saez–Ballester scalar–tensor theory, the present model predicts that the Universe evolves toward a stable phantom-like accelerated phase, with the late-time dynamics governed primarily by the effective dark-energy sector.

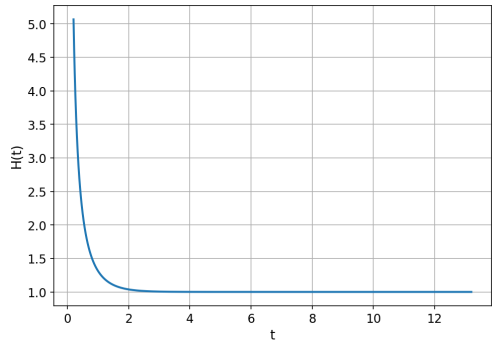


**Figure 1.** H vs t

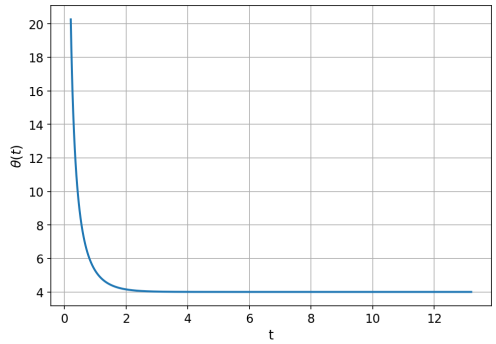


**Figure 2.** $\theta$ vs t

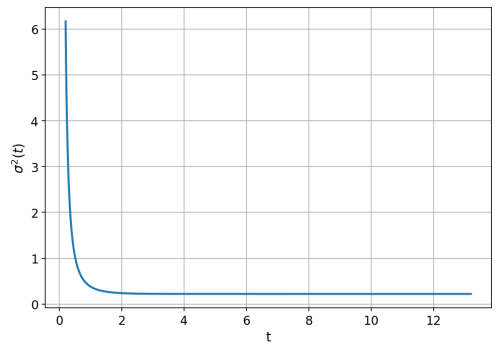


**Figure 3.** $\sigma^2$ vs t

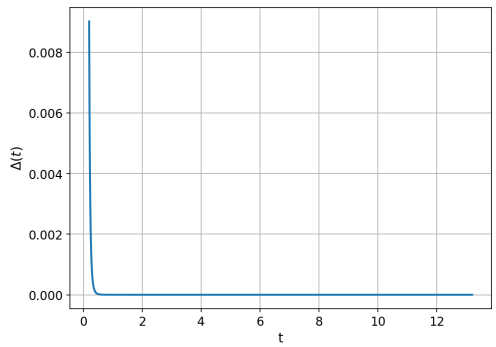


**Figure 4.** $\Delta$ vs t

For the purpose of numerical analysis and graphical illustration, we choose the parameter values $\alpha = 1.0$, $\beta = 1.0$, $d_1 = 0.001$, $d_2 = -0.0005$, $d_3 = -0.0005$, $\omega = 5.0$, $h = 1.0$, subject to the condition $d_1 + d_2 + d_3 = 0$. This set of parameters yields a physically acceptable cosmological model and is used throughout the paper to examine its evolutionary characteristics.

Figures 1–8 collectively demonstrate the evolutionary characteristics of the proposed five-dimensional anisotropic cosmological model from the early universe to the late-time accelerated epoch. The Hubble parameter $H$ and the expansion scalar $\theta$ begin with very large values near the initial singularity and decrease with cosmic time, indicating a

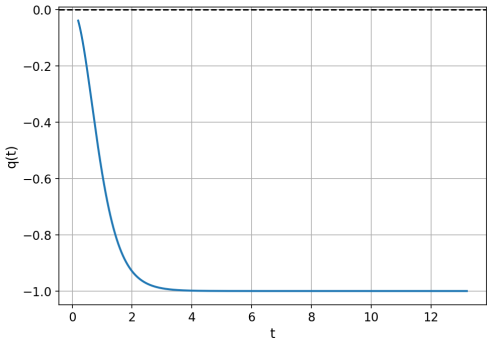


**Figure 5.** $q$ vs t

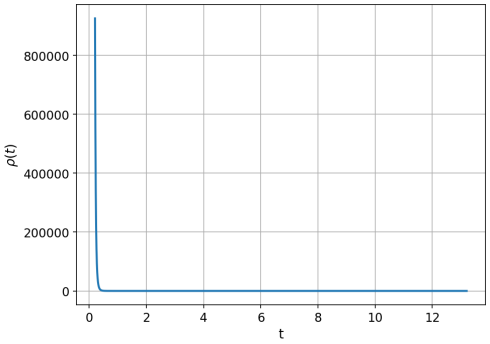


**Figure 6.** $\rho$ vs t

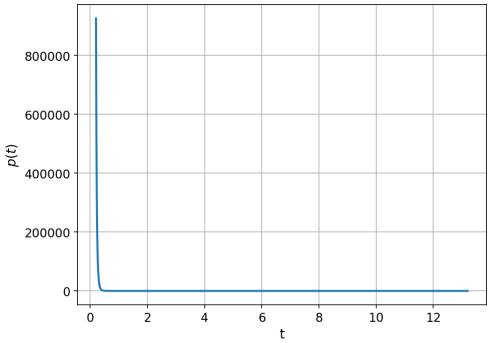


**Figure 7.** $p$ vs t

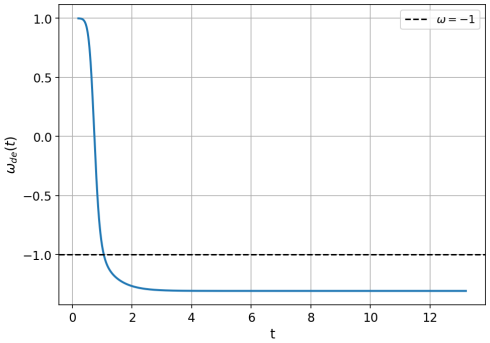


**Figure 8.** $\omega_{de}$ vs t

rapidly expanding early universe that gradually evolves toward a stable de Sitter-like expansion phase. Simultaneously, the shear scalar $\sigma^2$ and the mean anisotropy parameter $\Delta$ decrease monotonically and tend to zero at late times, demonstrating that the initial anisotropy of the universe gradually disappears and the model approaches isotropy in agreement with present cosmological observations. The deceleration parameter $q$ evolves toward the value $-1$, confirming the existence of a late-time accelerated expansion phase. The energy density $\rho$ remains positive throughout the cosmic evolution while decreasing from a very large initial value due to the continuous expansion of the universe. The pressure $p$ attains negative values during the evolution, generating the repulsive gravitational effect required to drive cosmic acceleration. Furthermore, the equation-of-state parameter $\omega_{de}$ approaches a value below $-1$, specifically $\omega_{de} \approx -1.308$, indicating that the effective dark-energy component enters the phantom regime at late times. Overall, the figures reveal that the universe evolves from an initially dense, rapidly expanding, and anisotropic state toward an isotropic, dark-energy-dominated, phantom-like accelerated phase, thereby providing a physically consistent description of the observed late-time cosmic acceleration.

## 5. ENERGY CONDITIONS

The energy conditions provide important criteria for examining the physical viability of cosmological models and the nature of the cosmic fluid driving the expansion of the Universe.

### 5.1. Null Energy Condition

The NEC requires

$$\rho + p \geq 0. \tag{44}$$

Using the above expressions, one obtains

$$\begin{aligned} \rho + p = &\left(\frac{10}{3}\alpha\beta^2 - \frac{16}{9}\alpha^2\beta^2\right)\coth^2(\beta t) - \frac{10}{3}\alpha\beta^2 \\ &- \frac{4}{3}\alpha\beta d_1 \coth(\beta t)\sinh^{-4\alpha}(\beta t) \\ &+ \left(d_1d_2 + d_1d_3 + d_2d_3 - d_3^2 + \omega h^2\right)\sinh^{-8\alpha}(\beta t) \end{aligned} \tag{45}$$

At late times ($t \to \infty$),

$$\lim_{t\to\infty}(\rho + p) = \frac{2}{9}\alpha\beta^2(15 - 8\alpha). \tag{46}$$

Hence, the NEC remains valid asymptotically for $\alpha \leq 15/8$.

### 5.2. Weak Energy Condition

The WEC requires

$$\rho \geq 0, \qquad \rho + p \geq 0 \tag{47}$$

Since the leading term in the energy density is positive,

$$\rho(t) = \frac{52}{9}\alpha^2\beta^2\coth^2(\beta t) + O\left(\sinh^{-8\alpha}(\beta t)\right), \tag{48}$$

the condition $\rho \geq 0$ is satisfied for suitable choices of the model parameters. Therefore, the validity of the WEC is determined by the sign of $\rho + p$ and coincides with the NEC at late times.

### 5.3. Strong Energy Condition

The SEC requires

$$\rho + 3p \geq 0. \tag{49}$$

For the present model,

$$\begin{aligned}\rho + 3p = &\left(10\alpha\beta^2 - \frac{152}{9}\alpha^2\beta^2\right)\coth^2(\beta t) - 10\alpha\beta^2 \\ &- 4\alpha\beta d_1\coth(\beta t)\sinh^{-4\alpha}(\beta t) \\ &+ \left(-d_1^2 + 2d_1d_2 - d_1d_3 + d_2d_3 - 3d_3^2 + 2\omega h^2\right)\sinh^{-8\alpha}(\beta t).\end{aligned} \tag{50}$$

As $t \to \infty$,

$$\lim_{t\to\infty}(\rho + 3p) = -\frac{2}{9}\alpha\beta^2(31 + 76\alpha) \tag{51}$$

Since $\alpha > 0$, it follows that

$$\rho + 3p < 0 \tag{52}$$

Therefore, the SEC is violated during the late-time evolution of the Universe. Such a violation is a characteristic feature of accelerating cosmological models and supports the observed cosmic acceleration.

### 5.4. Dominant Energy Condition

The DEC requires

$$\rho \geq 0, \qquad \rho - p \geq 0 \tag{53}$$

The quantity $\rho - p$ becomes

$$\begin{aligned}\rho - p = &\left(\frac{40}{3}\alpha^2\beta^2 - \frac{10}{3}\alpha\beta^2\right)\coth^2(\beta t) + \frac{10}{3}\alpha\beta^2 \\ &+ \frac{4}{3}\alpha\beta d_1\coth(\beta t)\sinh^{-4\alpha}(\beta t) \\ &+ \left(2d_1^2 + 2d_1d_2 + 3d_1d_3 + d_2d_3 + d_3^2\right)\sinh^{-8\alpha}(\beta t)\end{aligned} \tag{54}$$

In the asymptotic limit,

$$\lim_{t\to\infty}(\rho - p) = \frac{40}{3}\alpha^2\beta^2 > 0 \tag{55}$$

Thus, the DEC remains satisfied at late times.

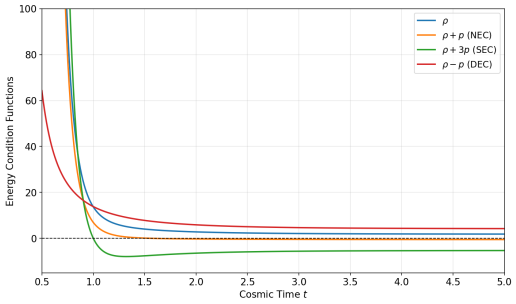


**Figure 9.** Variation of the energy density $\rho$, the null energy condition (NEC) $(\rho + p)$, the strong energy condition (SEC) $(\rho + 3p)$, and the dominant energy condition (DEC) $(\rho - p)$ with cosmic time $t$.

The above analysis shows that the energy density remains positive throughout the cosmic evolution for admissible values of the model parameters. The NEC and WEC can be satisfied depending on the value of $\alpha$, whereas the SEC is violated in the late-time epoch. The violation of the SEC indicates the presence of a repulsive gravitational effect responsible for the accelerated expansion of the Universe. Furthermore, the DEC remains valid asymptotically, ensuring that the energy flux propagates within the causal structure of spacetime. These results support the physical viability of the present cosmological model and are consistent with the phantom-like behavior of the effective dark-energy component obtained from the equation-of-state parameter.

Figure 9 illustrates the evolution of the energy density $\rho$, the Null Energy Condition (NEC) $(\rho + p)$, the Strong Energy Condition (SEC) $(\rho + 3p)$, and the Dominant Energy Condition (DEC) $(\rho - p)$ as functions of cosmic time. The figure shows that the energy density remains positive throughout the cosmic evolution, indicating the physical viability of the model and the presence of a positive effective energy content in the universe. The quantity $(\rho + p)$ remains positive during the evolution, implying that the NEC is satisfied and consequently the Weak Energy Condition (WEC) is also fulfilled. In contrast, $(\rho + 3p)$ becomes negative and remains below zero at late times, demonstrating the violation of the SEC. Such a violation is a characteristic signature of accelerated expansion, since it corresponds to the emergence of a repulsive gravitational effect capable of overcoming the attractive nature of ordinary matter. Furthermore, the quantity $(\rho - p)$ remains positive throughout the evolution, confirming the validity of the DEC and ensuring that the energy flux propagates causally within spacetime. Consequently, Figure 9 shows that the present model satisfies the NEC, WEC, and DEC, while exhibiting a violation of the SEC at late times, a feature commonly associated with an accelerating universe. This behavior is consistent with the phantom-like dark-energy nature of the model and provides strong evidence that the observed cosmic acceleration is driven by an effective repulsive dark-energy component.

## 6. STATEFINDER DIAGNOSTIC

The statefinder parameters $\{r, s\}$ are defined as

$$r = \frac{\dddot{a}}{aH^3}, \qquad s = \frac{r-1}{3\left(q - \frac{1}{2}\right)}. \tag{56}$$

Using

$$r = 1 + 3\frac{\dot{H}}{H^2} + \frac{\ddot{H}}{H^3}, \tag{57}$$

we obtain

$$r = 1 + \left(\frac{2}{\alpha^2} - \frac{3}{\alpha}\right)\mathrm{sech}^2(\beta t). \tag{58}$$

$$s = \frac{\left(\frac{2}{\alpha} - 3\right)\mathrm{sech}^2(\beta t)}{3\left[\mathrm{sech}^2(\beta t) - \frac{3\alpha}{2}\right]}. \tag{59}$$

At late times,

$$\lim_{t\to\infty} \mathrm{sech}^2(\beta t) = 0, \tag{60}$$

and consequently,

$$\lim_{t\to\infty} r = 1, \qquad \lim_{t\to\infty} s = 0. \tag{61}$$

Therefore,

$$(r, s) \to (1, 0), \tag{62}$$

which corresponds to the ΛCDM fixed point. Hence, the present model asymptotically approaches the standard cosmological constant dominated universe at late times.

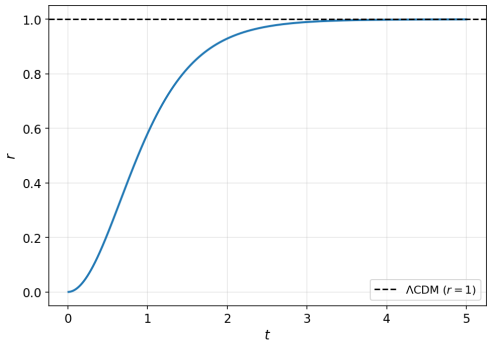


**Figure 10.** $r$ vs $t$

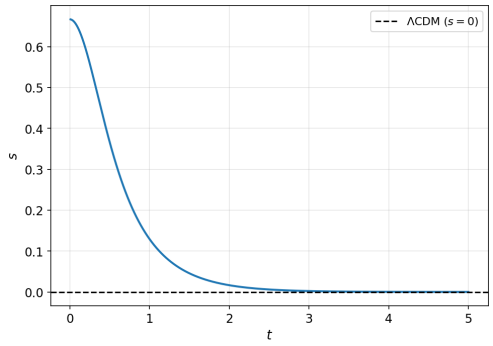


**Figure 11.** $s$ vs $t$

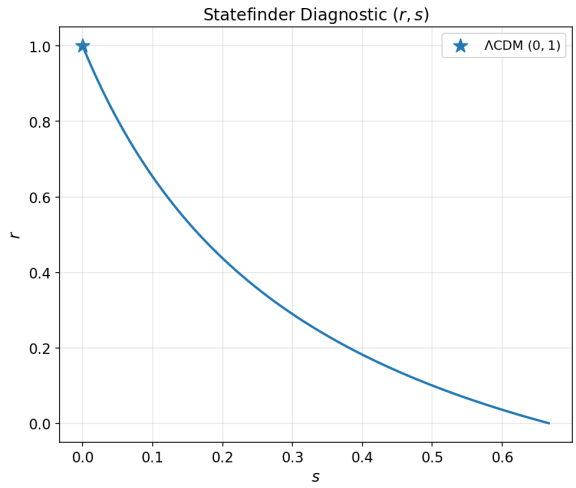


**Figure 12.** Statefinder trajectory in the $(s, r)$ plane

The evolution of the statefinder parameters is illustrated in Figs. 10–12. Figure 10 shows that the parameter $r$ increases with cosmic time and asymptotically approaches the ΛCDM value $r = 1$. Similarly, Fig. 11 demonstrates that the parameter $s$ gradually tends to zero as the universe evolves. The convergence of $r$ and $s$ to their respective ΛCDM values indicates that the present model evolves toward a cosmological-constant-dominated phase at late times.

Furthermore, the trajectory in the $(s, r)$ plane, shown in Fig. 12, approaches the fixed point $(0, 1)$ corresponding to the standard ΛCDM model. This behavior confirms that although the model may exhibit deviations from the ΛCDM scenario during the early stages of evolution, it gradually converges to the standard cosmological picture in the asymptotic future. Therefore, the statefinder diagnostic reveals that the proposed model successfully describes the late-time accelerated expansion of the universe and ultimately approaches a de Sitter-like phase.

## 7. OM DIAGNOSTIC ANALYSIS

The Om diagnostic is a useful geometrical tool for distinguishing different dark energy models and is defined as

$$Om(z) = \frac{E^2(z) - 1}{(1 + z)^3 - 1}, \tag{63}$$

where

$$E(z) = \frac{H(z)}{H_0}. \tag{64}$$

Using the scale factor

$$a = \sinh^{\alpha}(\beta t) = \frac{1}{1+z}, \tag{65}$$

we obtain

$$\sinh(\beta t) = (1+z)^{-1/\alpha}. \tag{66}$$

Since

$$H = \alpha\beta \coth(\beta t), \tag{67}$$

and

$$\coth^2(\beta t) = 1 + \sinh^{-2}(\beta t), \tag{68}$$

it follows that

$$H(z) = \alpha\beta\sqrt{1 + (1+z)^{2/\alpha}}. \tag{69}$$

At the present epoch ($z = 0$),

$$H_0 = H(0) = \alpha\beta\sqrt{2}. \tag{70}$$

Therefore,

$$E(z) = \frac{H(z)}{H_0} = \frac{\sqrt{1 + (1+z)^{2/\alpha}}}{\sqrt{2}}, \tag{71}$$

which gives

$$E^2(z) = \frac{1 + (1+z)^{2/\alpha}}{2}. \tag{72}$$

Substituting into the definition of the Om diagnostic, we obtain

$$Om(z) = \frac{\frac{1}{2}\left[(1+z)^{2/\alpha} - 1\right]}{(1+z)^3 - 1}, \tag{73}$$

or equivalently,

$$Om(z) = \frac{(1+z)^{2/\alpha} - 1}{2\left[(1+z)^3 - 1\right]}. \tag{74}$$

The behaviour of $Om(z)$ provides information about the underlying dark energy dynamics. In the ΛCDM model, $Om(z)$ remains constant and is equal to the present matter density parameter $\Omega_{m0}$. Any deviation from constancy indicates departure from the standard cosmological constant scenario.

For the present model,

$$\lim_{z\to -1} Om(z) = \frac{-1}{-2} = \frac{1}{2}, \tag{75}$$

showing that the Om parameter approaches a constant value at late times. This behaviour indicates that the model asymptotically evolves towards a de Sitter-like accelerated phase. Nevertheless, since $Om(z)$ remains redshift dependent during the cosmic evolution, the model generally differs from the standard ΛCDM cosmology except in the asymptotic future limit.

The evolution of the $Om(z)$ parameter is shown in Fig. 13. The parameter decreases monotonically with increasing redshift, indicating that it is not constant throughout the cosmic evolution. Since a constant $Om$ is a characteristic feature of the ΛCDM model, the observed redshift dependence signifies a departure from the standard cosmological constant scenario and reflects the dynamical nature of dark energy in the present model. As the universe evolves, $Om(z)$ tends toward the asymptotic value 0.5, suggesting that the model approaches a stable de Sitter-like accelerated phase at late times.

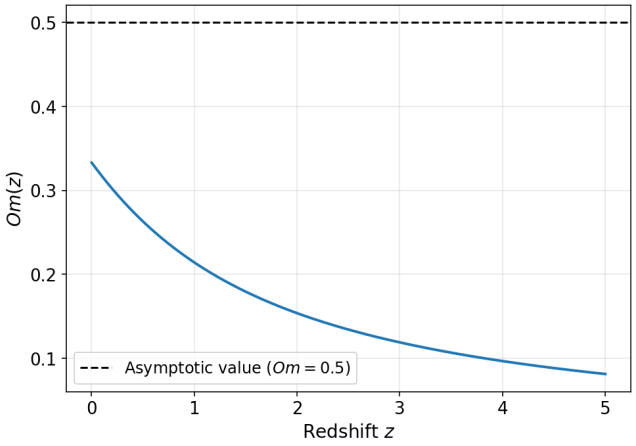


**Figure 13.** Evolution of the Om diagnostic parameter $Om(z)$ as a function of redshift $z$ for $\alpha = 1.0$.

## 8. CONCLUSIONS

In the present work, we have constructed and analyzed an exact five-dimensional Bianchi type-I cosmological model in the framework of Saez–Ballester scalar–tensor theory by adopting the hyperbolic expansion law $a(t) = \sinh^{\alpha}(\beta t)$. This choice enables the complete integration of the field equations and provides a realistic cosmological scenario capable of describing the observed accelerated expansion of the universe. The obtained solution corresponds to an expanding universe that begins with a Big-Bang-type singularity, where the spatial volume vanishes while the expansion rate becomes extremely large. The Hubble parameter and expansion scalar decrease monotonically with cosmic time and approach finite values at late times, indicating a smooth transition toward a stable accelerated epoch. The deceleration parameter evolves toward $(q = -1)$, showing that the model naturally approaches a de Sitter-like expansion phase. The anisotropic nature of the early universe is reflected through the nonvanishing shear scalar and anisotropy parameter. However, both quantities decay with cosmic time and asymptotically vanish, demonstrating that the universe evolves toward isotropy. This behaviour is consistent with current astronomical observations, which indicate a highly isotropic universe on large scales.

The physical properties of the cosmic fluid reveal that the energy density remains positive throughout the evolution, while the pressure becomes negative and generates the repulsive gravitational effect required for acceleration. The effective equation-of-state parameter evolves into the phantom region and asymptotically approaches $(\omega_{de} \approx -1.308)$, indicating that the late-time dynamics are dominated by a phantom-like dark-energy component. Consequently, the model predicts an accelerated expansion stronger than that produced by a cosmological constant. The analysis of the energy conditions further supports the physical viability of the model. The null energy condition, weak energy condition, and dominant energy condition remain satisfied for admissible parameter values, whereas the strong energy condition is violated during the late-time evolution. Such a violation is a characteristic feature of accelerating cosmologies and confirms the existence of an effective repulsive gravitational mechanism.

To further characterize the model, statefinder and Om diagnostics were employed. The statefinder parameters converge to the fixed point $\{r, s\} = (1, 0)$, showing that the model asymptotically approaches the standard $(\Lambda)$CDM cosmology. The Om diagnostic remains redshift dependent during the cosmic evolution, indicating deviations from the standard cosmological-constant scenario, although it tends to a constant value in the asymptotic future. These diagnostics demonstrate that the model can successfully reproduce the observed late-time acceleration while retaining distinctive dynamical features. Therefore, the proposed five-dimensional Saez–Ballester cosmological model provides a mathematically consistent and physically viable description of the universe, successfully explaining the transition from an initially anisotropic state to an isotropic, phantom-dark-energy-dominated accelerated phase.

## ORCID

**Jagat Daimary**, https://orcid.org/0000-0002-8723-8876; **Rajshekhar Roy Baruah**, https://orcid.org/0000-0002-5961-9540

## REFERENCES

[1] A.G. Riess, A.V. Filippenko, P. Challis, A. Clocchiatti, A. Diercks, P.M. Garnavich, *et al.*, "Observational Evidence from Supernovae for an Accelerating Universe and a Cosmological Constant," The Astronomical Journal, **116**, 1009–1038 (1998). https://doi.org/10.1086/300499

[2] S. Perlmutter, G. Aldering, G. Goldhaber, R.A. Knop, P. Nugent, P.G. Castro, *et al.*, "Measurements of Ω and Λ from 42 High-Redshift Supernovae," The Astrophysical Journal, **517**, 565–586 (1999). https://doi.org/10.1086/307221

[3] N. Aghanim, Y. Akrami, M. Ashdown, J. Aumont, C. Baccigalupi, M. Ballardini, *et al*., (Planck Collaboration), "Planck 2018 Results. VI. Cosmological Parameters," Astronomy and Astrophysics, **641**, A6 (2020). https://doi.org/10.1051/0004-6361/201833910

[4] S. Weinberg, "The Cosmological Constant Problem," Reviews of Modern Physics, **61**, 1–23 (1989). https://doi.org/10.1103/RevModPhys.61.1

[5] E.J. Copeland, M. Sami, and S. Tsujikawa, "Dynamics of Dark Energy," International Journal of Modern Physics D, **15**, 1753–1936 (2006). https://doi.org/10.1142/S021827180600942X

[6] T. Clifton, P.G. Ferreira, A. Padilla, and C. Skordis, "Modified Gravity and Cosmology," Physics Reports, **513**, 1–189 (2012). https://doi.org/10.1016/j.physrep.2012.01.001

[7] S. Capozziello, and M. De Laurentis, "Extended Theories of Gravity," Physics Reports, **509**, 167–321 (2011). https://doi.org/10.1016/j.physrep.2011.09.003

[8] T. Harko, F.S.N. Lobo, S. Nojiri, and S.D. Odintsov, "$f(R,T)$ Gravity," Physical Review D, **84**, 024020 (2011). https://doi.org/10.1103/PhysRevD.84.024020

[9] E.V. Linder, "Einstein's Other Gravity and the Acceleration of the Universe," Physical Review D, **81**, 127301 (2010). https://doi.org/10.1103/PhysRevD.81.127301

[10] S. Nojiri, S.D. Odintsov, and V.K. Oikonomou, "Unifying Inflation with Dark Energy in Modified Gravity," Physics of the Dark Universe, **29**, 100602 (2020). https://doi.org/10.1016/j.dark.2020.100602

[11] D. Saez and V.J. Ballester, "A Simple Coupling with Cosmological Implications," Physics Letters A, **113**, 467–470 (1986). https://doi.org/10.1016/0375-9601(86)90121-0

[12] C.P. Singh, and P. Kumar, "Bianchi-V string cosmology with power law expansion in f (R, T) gravity," The European Physical Journal Plus, **129**, 19 (2014). https://doi.org/10.1140/epjp/i2014-14194-y

[13] A. Pradhan, H. Amirhashchi, and H. Zainuddin, "An interacting and non-interacting two-fluid scenario for dark energy in FRW universe with constant deceleration parameter," Astrophysics and Space Science, **333**, 343–350 (2011). https://doi.org/10.1007/s10509-011-0626-9

[14] V.U.M. Rao, D.C. Papa Rao, and D.R.K. Reddy, "Five dimensional FRW cosmological models in a scalar-tensor theory of gravitation," Astrophysics and Space Science, **357(2):164**, 1–5 (2015). https://doi.org/10.1007/s10509-015-2378-4

[15] Ö. Akarsu, and C.B. Kilinc, "Bianchi Type-III Models with Anisotropic Dark Energy," General Relativity and Gravitation, **42**, 763–775 (2010). http://dx.doi.org/10.1007/s10714-009-0878-7

[16] G.F.R. Ellis, and M.A.H. MacCallum, "A Class of Homogeneous Cosmological Models," Communications in Mathematical Physics, **12**, 108–141 (1969). https://doi.org/10.1007/BF01645908

[17] C.B. Collins, and S.W. Hawking, "Why is the Universe Isotropic?" Astrophysical Journal, **180**, 317–334 (1973). https://doi.org/10.1086/151965

[18] C.W. Misner, "The Isotropy of the Universe," Astrophysical Journal, **151**, 431–457 (1968). https://doi.org/10.1086/149448

[19] A.M. Al-Haysah, and A.H. Hasmani, "Higher dimensional Bianchi type-I string cosmological model in f(R) theory of gravity," Heliyon, **7(08063)**, 1–4 (2021). https://doi.org/10.1016/j.heliyon.2021.e08063

[20] B. Saha, "Anisotropic Cosmological Models with Perfect Fluid and Dark Energy," Chinese Journal of Physics, **43**, 1035–1043 (2005). https://inspirehep.net/literature/667268

[21] T. Kaluza, "On the Unity Problem of Physics," Sitzungsber. Preuss. Akad. Wiss. Berlin (Mathematical Physics), 966–972 (1921).

[22] O. Klein, "Quantum Theory and Five-Dimensional Theory of Relativity," Journal of Physics , **37**, 895–906 (1926). https://doi.org/10.1007/BF01397481

[23] J.M. Overduin and P.S. Wesson, "Kaluza–Klein Gravity," Physics Reports, **283**, 303–378 (1997). https://doi.org/10.1016/S0370-1573(96)00046-4

[24] P.S. Wesson, "An Embedding for General Relativity with Variable Rest Mass," General Relativity and Gravitation, **16(2)**, 193–103 (1984). https://doi.org/10.1007/BF00762447

[25] R. Maartens and K. Koyama, "Brane-World Gravity," Living Reviews in Relativity, **13**, 5 (2010). https://doi.org/10.12942/lrr-2010-5

[26] D. Langlois, "Brane Cosmology: An Introduction," Progress of Theoretical Physics Supplement, **148** (2003) 181–212, https://doi.org/10.1143/PTPS.148.181

[27] G. Kofinas, E. N. Saridakis and J.-Q. Xia, "Cosmological solutions and observational constraints on five-dimensional braneworld cosmology with gravitating Nambu-Goto matching conditions," Phys. Rev. D, **90**, 084049 (2014). https://doi:10.1103/PhysRevD.90.084049

[28] Z. Davari et al., "Observational constraints on FLRW, Bianchi type I and V brane models," *Phys. Dark Univ.* **46** (2024) 101591. https://doi:10.1016/j.dark.2024.101591

[29] J. G. Lee, E. G. Adelberger, T. S. Cook, S. M. Fleischer, and B. R. Heckel, "New test of the gravitational $1/r^2$ law at separations down to 52 $\mu$m," Physical Review Letters, **124**, 101101 (2020). https://doi.org/10.1103/physrevlett.124.101101

[30] N. Sasankan, M. R. Gangopadhyay, G. J. Mathews, and M. Kusakabe, "New observational limits on dark radiation in braneworld cosmology," Physical Review D, **95**, 083516 (2017). https://doi.org/10.1103/physrevd.95.083516

[31] G. Satyanarayana, T. Vinutha, Y. Sobhanbabu, B. Srinivasu, P.J. Prasuna, and M. P. Raju, "Anisotropic Cosmological Model in a Modified Theory of Gravitation," East European Journal of Physics, (1), 357-366 (2025). https://doi.org/10.26565/2312-4334-2025-1-44

## ПРИСКОРЕННЯ П'ЯТИВИМІРНОЇ КОСМОЛОГІЇ Б'ЯНКІ ТИПУ I В ТЕОРІЇ САЕЗА-БАЛЛЕСТЕРА З ГІПЕРБОЛІЧНИМ РОЗШИРЕННЯМ

**Джагат Даймарі**[1], **Раджшехар Рой Баруах**[2]

[1]*Кафедра математики, Коледж Г'янпіт Степен, Нікаші, Бакса, Ассам - 781372, Індія*

[2]*Кафедра математичних наук, Університет Бодоленда, Кокрайхар, Ассам - 783370, Індія*

Ми представляємо п'ятивимірну анізотропну космологічну модель Б'янкі типу I в скалярно-тензорній теорії Саез-Баллестера, що використовує закон гіперболічного розкладання $a(t) = \sinh^{\alpha}(\beta t)$. Отримано точні розв'язки рівнянь поля та досліджено їх космологічну поведінку. Модель еволюціонує від початкового сингулярного стану до пізньої прискореної фази, зі зменшенням анізотропії та асимптотично досягнутою ізотропізацією. Параметр уповільнення наближається до $(q = -1)$, тоді як $(\omega_{de} \approx -1.308)$ вказує на фантомну поведінку темної енергії. Умови нульової, слабкої та домінуючої енергії залишаються виконаними, тоді як умова сильної енергії порушується, що підтверджує спостережуване космічне прискорення. Крім того, метод визначення стану та діагностика Om показують, що модель асимптотично наближається до сценарію ΛCDM.

**Ключові слова:** *теорія Саеза-Баллестера; Всесвіт Біанкі I типу; космологія вищих вимірів; гіперболічний закон розширення; темна енергія; космічне прискорення*

East European Journal of Physics. 3. 212–227 (2026)
DOI: 10.26565/2312-4334-2026-3-17 ISSN 2312-4334

# UNIFIED SYMMETRY CLASSIFICATION, CONSERVATION LAWS AND SOLITON DYNAMICS FOR A CLASS OF VARIABLE-COEFFICIENT HIGHER-ORDER NONLINEAR EVOLUTION EQUATIONS

**Suares Clovis Oukouomi Noutchie***
*School of Mathematical and Statistical Sciences, North-West University, Vanderbijlpark Campus, Vanderbijlpark, South Africa*
**Corresponding Author e-mail: clovis.oukouominoutchie@nwu.ac.za*
Received June 10, 2026; revised August 18, 2026; accepted August 21, 2026

Variable-coefficient higher-order nonlinear evolution equations constitute an important class of mathematical models for the description of nonlinear dispersive wave propagation in inhomogeneous media, including shallow water flows, plasmas, optical systems and elastic structures. This paper develops a unified analytical framework for a broad family of such equations incorporating nonlinear convection, third-order dispersion, fifth-order dispersion, BBM-type mixed dispersion and nonlinear dispersive modulation. Admissible equivalence transformations are first constructed and used to reduce the general class, under non-vanishing fifth-order dispersion, to a canonical normalized form. The normalization yields a simplified group-classification problem by establishing an explicit compatibility condition for the temporal component of every admitted Lie point symmetry. Complete Lie symmetry classifications are obtained for the kernel, power-law, exponential and constant-coefficient subclasses, followed by the construction of optimal systems and similarity reductions. Conservation laws are derived from the conservative structure of the governing equation, including a universal mass invariant and a regularized energy conservation law for an important canonical subclass. Furthermore, an exact bright-soliton solution is derived for the constant-coefficient equation, rigorously verified by direct substitution, and employed to validate numerical simulations. The proposed framework unifies equivalence transformations, Lie symmetry analysis, conservation laws, similarity reductions and soliton dynamics within a single parameterized setting, providing a systematic methodology for the analytical investigation of higher-order nonlinear dispersive wave equations.

**Keywords:** *Lie symmetry analysis; Equivalence transformations; Variable-coefficient nonlinear evolution equations; Conservation laws; Higher-order dispersive waves; Fifth-order dispersion; Similarity reductions; Soliton dynamics*

## 1. INTRODUCTION

Nonlinear evolution equations occupy a central position in modern mathematical physics because they provide fundamental models for the propagation, interaction and modulation of nonlinear waves in fluids, plasmas, nonlinear optics, elastic media, Bose–Einstein condensates and other dispersive systems. The interaction between nonlinear effects and dispersion gives rise to a rich variety of coherent structures, including solitary waves, compactons, dispersive shock waves and solitons, whose mathematical analysis has stimulated the development of numerous analytical techniques over the past five decades. Classical models such as the Korteweg–de Vries (KdV), modified KdV, Benjamin–Bona–Mahony (BBM) and Kawahara equations have consequently become canonical nonlinear evolution equations for investigating nonlinear wave propagation and have served as testing grounds for symmetry analysis, inverse scattering, perturbation theory and exact solution methods [1–4, 6–13].

Although constant-coefficient models have provided valuable theoretical insight, many realistic physical systems evolve in non-homogeneous environments where material properties, external forcing, bottom topography or background media vary in space or time. Examples include shallow-water flows over variable bathymetry, nonlinear optical pulse propagation in inhomogeneous fibres, plasma waves in slowly varying magnetic fields and elastic media with variable constitutive parameters. Such phenomena naturally lead to variable-coefficient nonlinear evolution equations whose analytical behaviour is considerably richer than that of their constant-coefficient counterparts. The presence of variable coefficients often modifies the admissible symmetry structure, influences the existence of conservation laws and affects the qualitative behaviour of travelling-wave solutions. Consequently, the systematic investigation of variable-coefficient nonlinear evolution equations has become an active area of research in mathematical physics [23, 26, 29].

Among the most powerful analytical tools available for the investigation of nonlinear differential equations is the Lie group method. Since the pioneering work of Sophus Lie and its subsequent mathematical development by Ovsiannikov, Bluman, Kumei and Olver, Lie symmetry analysis has provided a unified methodology for identifying continuous symmetry groups, constructing invariant solutions, reducing partial differential equations to ordinary differential equations and classifying differential equations according to their admitted symmetry algebras [1–4]. Equally important are admissible equivalence transformations, which identify analytically equivalent members within parameterized classes of differential equations and frequently reduce complicated classification problems to substantially simpler canonical forms. The combination of equivalence transformations and Lie symmetry analysis has therefore become an indispensable framework for complete group classifications.

***Cite as:*** S.C. Oukouomi Noutchie, East Eur. J. Phys. 3, 212 (2026), https://doi.org/10.26565/2312-4334-2026-3-17

Conservation laws constitute another fundamental component of the mathematical analysis of nonlinear evolution equations because they describe physically meaningful invariant quantities such as mass, momentum and energy while simultaneously providing analytical and numerical consistency checks. The classical variational approach introduced by Noether remains one of the cornerstones of conservation-law theory, whereas more recent developments involving multiplier methods, nonlinear self-adjointness and symbolic computation have considerably extended the applicability of conservation-law analysis to non-variational systems [5, 16, 19, 25, 27]. In parallel, the construction of exact travelling-wave solutions and soliton families continues to play a central role in understanding nonlinear dispersive phenomena. Techniques based on Hirota's direct method, inverse scattering, Lie reductions and ansatz methods have produced a wide spectrum of exact solutions for nonlinear evolution equations, thereby providing benchmark solutions for both theoretical investigations and numerical algorithms [6, 7].

Recent years have witnessed renewed interest in combining symmetry analysis, conservation laws and exact solutions for increasingly sophisticated nonlinear evolution equations. Significant progress has been reported for generalized KdV equations, Kawahara–KP systems, Boussinesq-type equations, variable-coefficient KdV equations, KdV–Burgers models, Hirota-type equations and fractional nonlinear evolution equations through the application of Lie symmetries, optimal systems, nonlinear self-adjointness, conservation-law multipliers and exact solution techniques [9–15, 17–22, 24, 28, 29]. Nevertheless, much of the existing literature remains equation-specific. In many studies a single nonlinear evolution equation is selected and analysed independently, with symmetry classification, conservation laws and exact coherent structures derived separately for that individual model. Comparatively less attention has been devoted to the development of unified analytical frameworks capable of treating broad parameterized classes of higher-order variable-coefficient nonlinear evolution equations while simultaneously integrating equivalence transformations, complete Lie classifications, optimal systems, conservation laws and verified solitary-wave solutions.

Motivated by these observations, the present work develops a unified analytical framework for the class

$$\begin{aligned}\mathcal{E}(\alpha,\beta,\gamma,\delta,\eta,p,q):\quad & u_t+\alpha(t)u^p u_x+\beta(t)u_{xxx}+\gamma(t)u_{xxxxx}\\ & +\delta(t)u_{xxt}+\eta(t)(u^q u_{xx})_x=0,\end{aligned}\tag{1}$$

where $p, q > 0$ and the coefficient functions are assumed to be sufficiently smooth. The objective is not to introduce a new nonlinear evolution equation, since the class contains several well-known models as special cases, but rather to develop a systematic analytical framework that unifies admissible equivalence transformations, canonical normalization, complete Lie symmetry classification, optimal systems, conservation laws, similarity reductions and exact soliton solutions within a single parameterized setting.

The principal contributions of this work may be summarized as follows. First, admissible equivalence transformations are derived and employed to normalize the fifth-order dispersive coefficient, thereby reducing the general class to a canonical form. Second, a complete Lie symmetry classification of the canonical class is established, including the kernel algebra together with the principal symmetry extensions corresponding to the power-law, exponential and constant-coefficient subclasses. Third, optimal systems of one-dimensional subalgebras and associated similarity reductions are constructed. Fourth, conservation laws are derived from the conservative structure of the governing equation, including a universal mass conservation law and a regularized energy conservation law for an important canonical subclass. Fifth, an exact bright-soliton solution of the constant-coefficient canonical equation is obtained, rigorously verified and employed for numerical validation. Collectively, these results provide a unified methodology for the analytical investigation of higher-order variable-coefficient nonlinear evolution equations and establish explicit connections between symmetry analysis, conservation laws and nonlinear wave dynamics.

The remainder of the paper is organized as follows. Section 2 introduces the governing class and its structural properties. Section 3 derives the admissible equivalence transformations and canonical normalization. Section 4 discusses reductions to several classical models. Section 5 presents the complete Lie symmetry classification, while Section 6 develops optimal systems and similarity reductions. Conservation laws and nonlinear self-adjointness are investigated in Section 7. Exact bright-soliton solutions and numerical validation are presented in Sections 8 and 9, respectively. The principal findings are discussed in Section 10, followed by concluding remarks in Section 11.

## 2. A CLASS OF VARIABLE-COEFFICIENT HIGHER-ORDER NONLINEAR EVOLUTION EQUATIONS

We consider the parameterized class of nonlinear evolution equations

$$\mathcal{E}(\alpha,\beta,\gamma,\delta,\eta,p,q):\quad u_t+\alpha(t)u^p u_x+\beta(t)u_{xxx}+\gamma(t)u_{xxxxx}+\delta(t)u_{xxt}+\eta(t)(u^q u_{xx})_x=0,\tag{2}$$

defined either on the real line $\mathbb{R}$ under sufficiently rapid decay conditions or on a periodic spatial domain. Here $u = u(x,t)$ denotes the wave profile, while the coefficient functions

$$\alpha(t),\ \beta(t),\ \gamma(t),\ \delta(t),\ \eta(t)$$

are assumed to be continuously differentiable on a time interval $I \subset \mathbb{R}$.

Equation (2) provides a unified framework encompassing several important classes of nonlinear dispersive wave equations arising in mathematical physics. The nonlinear convective term $\alpha(t)u^p u_x$ generalizes the nonlinear transport

mechanism encountered in generalized KdV-type equations, whereas $\beta(t)u_{xxx}$ represents the classical third-order dispersive correction responsible for balancing nonlinear steepening and generating solitary-wave propagation. The fifth-order dispersive contribution $\gamma(t)u_{xxxxx}$ extends the model to the Kawahara regime, where higher-order dispersion becomes significant in weakly dispersive media. The mixed derivative $\delta(t)u_{xxt}$ introduces BBM-type regularization, improving the dispersive properties of the equation and modifying the linear dispersion relation. Finally, the nonlinear dispersive term $\eta(t)(u^q u_{xx})_x$ models amplitude-dependent dispersion and provides additional nonlinear coupling between wave amplitude and curvature.

Writing the nonlinear dispersive contribution in conservative form is advantageous for both analytical and structural reasons. Indeed,

$$(u^q u_{xx})_x = u^q u_{xxx} + q u^{q-1} u_x u_{xx}, \tag{3}$$

showing explicitly that the model combines higher-order linear dispersion with nonlinear dispersive interactions. The conservative representation also simplifies the derivation of conservation laws and facilitates the application of multiplier methods and nonlinear self-adjointness.

Equation (2) itself possesses a natural conservation form. Introducing the flux

$$\mathcal{F} = \frac{\alpha(t)}{p+1}u^{p+1} + \beta(t)u_{xx} + \gamma(t)u_{xxxx} + \delta(t)u_{xt} + \eta(t)u^q u_{xx}, \tag{4}$$

the governing equation may be written compactly as

$$D_t u + D_x \mathcal{F} = 0, \tag{5}$$

where $D_t$ and $D_x$ denote the total derivative operators with respect to $t$ and $x$, respectively. Consequently, under periodic boundary conditions or sufficiently rapid spatial decay,

$$\frac{d}{dt}\int_\Omega u(x,t)\,dx = 0,$$

so that the total mass constitutes a universal conserved quantity for every member of the class. This intrinsic conservative structure provides the foundation for the conservation-law analysis carried out later in the paper.

Throughout this work we assume

$$\alpha, \beta, \gamma, \delta, \eta \in C^1(I), \qquad p, q > 0, \tag{6}$$

which guarantees the regularity required for the symmetry analysis and the admissible equivalence transformations developed in subsequent sections. Particular attention is devoted to the case

$$\gamma(t) \neq 0,$$

since the presence of a non-vanishing fifth-order dispersive coefficient characterizes the genuinely higher-order regime and gives rise to the richest admissible symmetry structure. Lower-order reductions obtained by setting selected coefficients equal to zero are discussed separately in Section 4, where connections with several classical nonlinear evolution equations are established.

## 3. EQUIVALENCE TRANSFORMATIONS AND CANONICAL NORMALIZATION

A fundamental step in the group classification of parameterized classes of differential equations is the determination of their admissible equivalence transformations. Such transformations preserve the differential structure of the governing equations while modifying the coefficient functions, thereby identifying analytically equivalent members of the class. Their principal advantage is that they reduce the number of essentially distinct equations that must be considered during the subsequent symmetry classification.

To determine the equivalence group of the class (2), we consider invertible point transformations of the form

$$\tilde{t} = T(t), \qquad \tilde{x} = \lambda x + \mu, \qquad \tilde{u} = \kappa u, \tag{7}$$

where

$$T_t \lambda \kappa \neq 0, \tag{8}$$

and $\lambda, \mu, \kappa$ are constants.

The restriction to constant spatial translations and amplitude scalings is not merely a simplifying assumption. Allowing $\lambda$, $\mu$ or $\kappa$ to depend explicitly on time introduces additional first-order or zeroth-order differential terms through the chain rule, destroying the differential structure of the class. Consequently, transformations of the form (7) constitute the maximal admissible point transformations preserving (2).

Application of the chain rule yields

$$u_t = \kappa^{-1} T_t \tilde{u}_{\tilde{t}}, \qquad u_x = \kappa^{-1} \lambda \tilde{u}_{\tilde{x}}, \tag{9}$$

together with

$$u_{xxx} = \kappa^{-1} \lambda^3 \tilde{u}_{\tilde{x}\tilde{x}\tilde{x}}, \qquad u_{xxxxx} = \kappa^{-1} \lambda^5 \tilde{u}_{\tilde{x}^5}, \qquad u_{xxt} = \kappa^{-1} \lambda^2 T_t \tilde{u}_{\tilde{x}\tilde{x}\tilde{t}}. \tag{10}$$

Substituting these expressions into (2) and dividing by the coefficient of $\tilde{u}_{\tilde{t}}$ preserves the differential structure of the equation while transforming the coefficient functions according to

$$\tilde{\alpha}(\tilde{t}) = \frac{\lambda}{T_t} \kappa^{-p} \alpha(t), \qquad \tilde{\beta}(\tilde{t}) = \frac{\lambda^3}{T_t} \beta(t), \tag{11}$$

$$\tilde{\gamma}(\tilde{t}) = \frac{\lambda^5}{T_t} \gamma(t), \qquad \tilde{\delta}(\tilde{t}) = \lambda^2 \delta(t), \tag{12}$$

$$\tilde{\eta}(\tilde{t}) = \frac{\lambda^3}{T_t} \kappa^{-q} \eta(t), \tag{13}$$

whereas the nonlinear exponents $p$ and $q$ remain invariant under the equivalence group.

**Theorem 3.1.** *The class $\mathcal{E}(\alpha, \beta, \gamma, \delta, \eta, p, q)$ is invariant under the equivalence transformations* (7)*, with the coefficient functions transforming according to* (11)–(13)*. Furthermore, if $\gamma(t) \neq 0$, every member of the class is equivalent to one satisfying*

$$\tilde{\gamma} = 1.$$

*Proof.* The transformation formulas follow directly from repeated application of the chain rule. Substituting the transformed derivatives into (2) and comparing the coefficients of the independent differential monomials

$$u^p u_x, \; u_{xxx}, \; u_{xxxxx}, \; u_{xxt}, \; (u^q u_{xx})_x$$

immediately yields (11)–(13). When $\gamma(t) \neq 0$, choosing

$$T_t = \lambda^5 \gamma(t)$$

gives

$$\tilde{\gamma} = \frac{\lambda^5}{T_t} \gamma(t) = 1,$$

thereby reducing every equation in the class to a canonical representative. □

The preceding theorem demonstrates that the fifth-order dispersive coefficient does not represent an essential functional degree of freedom. Consequently, without loss of generality, the subsequent Lie symmetry analysis may be performed for the canonical normalized class

$$u_t + \alpha(t) u^p u_x + \beta(t) u_{xxx} + u_{xxxxx} + \delta(t) u_{xxt} + \eta(t) (u^q u_{xx})_x = 0, \tag{14}$$

which is analytically equivalent to every member of the original class with $\gamma(t) \neq 0$.

## 4. REDUCTION TO CLASSICAL MODELS

An important feature of the class (2) is that it unifies several well-established nonlinear evolution equations within a single parameterized framework. Consequently, the analytical results developed in the subsequent sections simultaneously apply to a broad family of nonlinear dispersive wave models rather than to a single equation. The reductions presented below also illustrate the modelling flexibility of the proposed class and clarify the physical significance of the various coefficient functions.

Different choices of the coefficient functions recover several classical nonlinear evolution equations that have been extensively investigated in mathematical physics. In particular, setting

$$\gamma = \delta = \eta = 0$$

reduces (2) to the variable-coefficient generalized Korteweg–de Vries (KdV) equation

$$u_t + \alpha(t) u^p u_x + \beta(t) u_{xxx} = 0.$$

For the special choice $p = 1$ together with constant coefficients, this further reduces to the classical KdV equation, whereas $p = 2$ yields a variable-coefficient modified KdV (mKdV)-type equation.

**Table 1.** Representative reductions of the general variable-coefficient class to well-known nonlinear evolution equations.

| Reduced model | Parameter restrictions | Governing equation |
|---|---|---|
| Generalized KdV | $\gamma = \delta = \eta = 0$ | $u_t + \alpha u^p u_x + \beta u_{xxx} = 0$ |
| Modified KdV | $p = 2,\ \gamma = \delta = \eta = 0$ | $u_t + \alpha u^2 u_x + \beta u_{xxx} = 0$ |
| Generalized Kawahara | $\delta = \eta = 0$ | $u_t + \alpha u^p u_x + \beta u_{xxx} + \gamma u_{xxxxx} = 0$ |
| Generalized BBM | $\gamma = \eta = 0$ | $u_t + \alpha u^p u_x + \beta u_{xxx} + \delta u_{xxt} = 0$ |
| Canonical fifth-order class | $\gamma = 1$ | Equation (14) |

If

$$\delta = \eta = 0, \qquad \gamma \neq 0,$$

the governing equation becomes a generalized Kawahara-type model containing both third- and fifth-order dispersive effects. On the other hand, imposing

$$\gamma = \eta = 0$$

produces a BBM-type regularized equation in which the mixed derivative $u_{xxt}$ modifies the dispersive behaviour while preserving the nonlinear convective mechanism.

Finally, by means of the equivalence transformations established in Section 3, every equation satisfying $\gamma(t) \neq 0$ may be transformed to the canonical normalized form (14). Consequently, the complete Lie symmetry classification derived in the subsequent sections applies to an entire equivalence class of fifth-order variable-coefficient nonlinear evolution equations rather than to a single representative equation.

The principal reductions of the general class are summarized in Table 1.

## 5. COMPLETE LIE SYMMETRY CLASSIFICATION

The canonical normalized equation derived in the previous section is now classified with respect to its admitted Lie point symmetries. Since the fifth-order dispersive coefficient has been normalized through the admissible equivalence transformations, the resulting determining equations are considerably simpler than those for the original variable-coefficient class. Consequently, the complete group-classification problem may be carried out without loss of generality on the canonical representative (14).

Following the classical Lie group approach [1–4], we consider the general infinitesimal generator

$$X = \xi(x,t,u)\partial_x + \tau(x,t,u)\partial_t + \phi(x,t,u)\partial_u. \tag{15}$$

According to the infinitesimal invariance criterion, the fifth prolongation of $X$ must satisfy

$$\mathrm{pr}^{(5)} X(\Delta)\Big|_{\Delta=0} = 0, \tag{16}$$

where $\Delta$ denotes the left-hand side of the canonical equation (14).

Expanding the fifth prolongation and splitting with respect to the linearly independent differential monomials yields the determining equations. The first set immediately gives

$$\tau = \tau(t), \qquad \xi = \lambda x + \xi_0, \qquad \phi = \rho u, \tag{17}$$

where $\lambda$, $\xi_0$ and $\rho$ are constants.

A noteworthy consequence of the canonical normalization is that the fifth-order dispersive term immediately imposes the compatibility condition

$$\frac{d\tau}{dt} = 5\lambda, \tag{18}$$

which integrates to

$$\tau(t) = 5\lambda t + \tau_0, \tag{19}$$

where $\tau_0$ is an arbitrary constant.

The remaining determining equations reduce to

$$\tau\frac{\alpha'}{\alpha} + p\rho + 4\lambda = 0, \tag{20}$$

$$\tau\frac{\beta'}{\beta} + 2\lambda = 0, \tag{21}$$

$$\tau\frac{\delta'}{\delta} - 2\lambda = 0, \tag{22}$$

$$\tau\frac{\eta'}{\eta} + q\rho + 2\lambda = 0. \tag{23}$$

**Theorem 5.1.** *Every Lie point symmetry generator admitted by the canonical class* (14) *is of the form*

$$X = (\lambda x + \xi_0)\partial_x + (5\lambda t + \tau_0)\partial_t + \rho u \partial_u, \tag{24}$$

*where the constants $\lambda$, $\tau_0$, $\xi_0$ and $\rho$ satisfy the determining equations* (20)–(23). *For arbitrary coefficient functions, the kernel Lie algebra is*

$$\mathfrak{g}^{\cap} = \langle \partial_x \rangle. \tag{25}$$

*Proof.* The determining equations obtained from the infinitesimal invariance criterion (16) immediately imply the infinitesimal structure (17). The normalization of the fifth-order dispersive coefficient yields the compatibility condition (18), from which (19) follows directly. Substituting these expressions into the remaining determining equations produces (20)–(23). For arbitrary coefficient functions these equations admit only the translational symmetry $\partial_x$, establishing the kernel algebra. Additional symmetry extensions arise only for particular functional forms of the coefficient functions, which are classified below. □

**Remark 5.2.** *The compatibility condition* (18) *is a direct consequence of the canonical normalization performed in Section 3. Without eliminating the arbitrary fifth-order coefficient through admissible equivalence transformations, the determining equations would retain an additional functional degree of freedom, making the complete group-classification problem substantially more complicated. Canonical normalization is therefore an essential analytical step rather than merely a technical simplification.*

The first nontrivial symmetry extension arises when the coefficient functions possess power-law dependence,

$$\alpha = \alpha_0 t^{a_1}, \qquad \beta = \beta_0 t^{a_2}, \qquad \delta = \delta_0 t^{a_3}, \qquad \eta = \eta_0 t^{a_4}, \tag{26}$$

where $\alpha_0$, $\beta_0$, $\delta_0$ and $\eta_0$ are nonzero constants. Choosing

$$\tau = t$$

gives

$$\lambda = \frac{1}{5},$$

and hence the additional symmetry generator

$$X_P = t\partial_t + \frac{1}{5}x\partial_x + \rho u \partial_u. \tag{27}$$

The determining equations then require

$$a_1 = -p\rho - \frac{4}{5}, \qquad a_2 = -\frac{2}{5}, \qquad a_3 = \frac{2}{5}, \qquad a_4 = -q\rho - \frac{2}{5}. \tag{28}$$

A second symmetry extension is obtained for exponential coefficient functions. Choosing

$$\tau = 1$$

forces

$$\lambda = 0$$

through the compatibility condition (18), yielding

$$X_E = \partial_t + \rho u \partial_u. \tag{29}$$

The admissible coefficient functions are

$$\alpha = \alpha_0 e^{-p\rho t}, \qquad \beta = \beta_0, \qquad \delta = \delta_0, \qquad \eta = \eta_0 e^{-q\rho t}. \tag{30}$$

Finally, if all coefficient functions are constant, the determining equations admit the two-dimensional translation algebra

$$\mathfrak{g}_C = \langle \partial_x, \partial_t \rangle. \tag{31}$$

The resulting hierarchy of symmetry extensions is summarized in Figure 1.

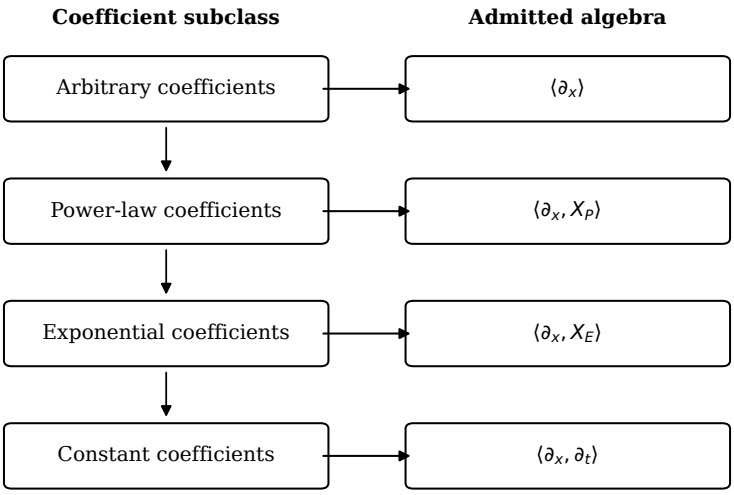


**Figure 1.** Hierarchy of Lie symmetry extensions admitted by the canonical variable-coefficient class.

## 6. OPTIMAL SYSTEMS AND SIMILARITY REDUCTIONS

Having determined the complete Lie symmetry classification of the canonical class, we now construct optimal systems of one-dimensional subalgebras and derive the corresponding similarity reductions. These reductions transform the governing partial differential equation into ordinary differential equations, thereby providing the foundation for the analytical construction of invariant solutions and travelling-wave structures.

For the power-law subclass, the admitted Lie algebra is

$$\mathfrak{g}_P = \langle X_1, X_P \rangle,$$

where

$$X_1 = \partial_x, \qquad X_P = t\partial_t + \frac{1}{5}x\partial_x + \rho u\partial_u.$$

Since

$$[X_1, X_P] = \frac{1}{5}X_1, \tag{32}$$

the adjoint representation shows that every one-dimensional subalgebra is equivalent to one generated by either

$$\langle X_1 \rangle \quad \text{or} \quad \langle X_P \rangle.$$

These therefore constitute an optimal system of one-dimensional subalgebras.

The reduction associated with the translational symmetry $X_1$ is immediate. The invariants satisfy

$$u = U(t),$$

and substitution into (14) gives

$$U'(t) = 0,$$

showing that the only invariant solutions generated by $X_1$ are spatially homogeneous steady states.

The nontrivial reduction is obtained from the scaling generator $X_P$. The characteristic equations

$$\frac{dt}{t} = \frac{dx}{x/5} = \frac{du}{\rho u} \tag{33}$$

yield the similarity variables

$$z = xt^{-1/5}, \qquad u = t^{\rho}U(z). \tag{34}$$

Substitution into the canonical equation produces the reduced fifth-order ordinary differential equation

$$\rho U - \frac{1}{5}zU' + \alpha_0 U^p U' + \beta_0 U''' + U^{(5)}$$

$$+\delta_0\left[\left(\rho-\frac{2}{5}\right)U''-\frac{1}{5}zU'''\right]+\eta_0(U^qU'')'=0, \tag{35}$$

which governs the self-similar solutions admitted by the power-law subclass.

For the exponential subclass, the admitted symmetry generator is

$$X_E=\partial_t+\rho u\partial_u.$$

Its invariants are

$$z=x, \qquad u=e^{\rho t}U(z), \tag{36}$$

leading to the autonomous reduced equation

$$\rho U+\alpha_0U^pU'+\beta_0U'''+U^{(5)}+\delta_0\rho U''+\eta_0(U^qU'')'=0. \tag{37}$$

Finally, for the constant-coefficient canonical equation, translational invariance in both space and time naturally suggests the travelling-wave ansatz

$$z=x-vt, \qquad u(x,t)=U(z),$$

where $v$ denotes the wave speed. After one integration under localized boundary conditions, the governing equation reduces to

$$U^{(4)}+(\beta-\delta v+\eta U^q)U''-vU+\frac{\alpha}{p+1}U^{p+1}=0, \tag{38}$$

which serves as the principal equation for the construction of solitary-wave solutions in Section 8.

The three reductions obtained above illustrate the different classes of invariant solutions admitted by the canonical equation. In particular, the travelling-wave reduction (38) provides the analytical framework for the bright-soliton solutions derived subsequently, while the self-similar reductions characterize scale-invariant and exponentially evolving wave structures.

## 7. CONSERVATION LAWS AND NONLINEAR SELF-ADJOINTNESS

Conservation laws constitute one of the fundamental structural properties of nonlinear evolution equations. Besides expressing physically meaningful invariant quantities, they provide valuable analytical information concerning the qualitative behaviour of solutions and furnish useful consistency checks for numerical simulations. Owing to its conservative formulation, the canonical equation naturally admits a hierarchy of conservation laws, the most fundamental of which are derived below.

The canonical equation may be written in divergence form as

$$D_tu+D_x\mathcal{F}=0, \tag{39}$$

where

$$\mathcal{F}=\frac{\alpha(t)}{p+1}u^{p+1}+\beta(t)u_{xx}+u_{xxxx}+\delta(t)u_{xt}+\eta(t)u^qu_{xx}. \tag{40}$$

Consequently,

$$C_1^t=u, \qquad C_1^x=\mathcal{F}, \tag{41}$$

defines the universal mass conservation law for every member of the canonical class.

**Proposition 7.1.** *Under periodic boundary conditions or sufficiently rapid spatial decay, the total mass*

$$M(t)=\int_\Omega u(x,t)\,dx \tag{42}$$

*is conserved; that is,*

$$\frac{dM}{dt}=0. \tag{43}$$

*Proof.* Integrating the divergence equation (39) over the spatial domain and applying either periodicity or decay at infinity eliminates the boundary flux, yielding

$$\frac{d}{dt}\int_\Omega u(x,t)\,dx=0.$$

□

The existence of this conservation law follows directly from the divergence structure of the governing equation and is independent of the particular choice of coefficient functions.

A second conservation law is obtained by multiplying the canonical equation by $u$. After straightforward integration by parts one obtains

$$D_t C_2^t + D_x C_2^x = -\frac{\delta'(t)}{2} u_x^2 + \eta(t)(q+1) u^q u_x u_{xx}, \tag{44}$$

where

$$C_2^t = \frac{1}{2} u^2 - \frac{\delta(t)}{2} u_x^2, \tag{45}$$

and

$$\begin{aligned} C_2^x = {} & \frac{\alpha(t)}{p+2} u^{p+2} + \beta(t) \left( u u_{xx} - \frac{1}{2} u_x^2 \right) \\ & + u u_{xxxx} - u_x u_{xxx} + \frac{1}{2} u_{xx}^2 + \delta(t) u u_{xt} + \eta(t) u^{q+1} u_{xx}. \end{aligned} \tag{46}$$

Unlike the mass conservation law, the corresponding energy balance contains source terms generated by the temporal variation of the BBM coefficient and by the nonlinear dispersive contribution. Consequently, a genuine energy conservation law exists only for suitable subclasses of the canonical equation.

**Proposition 7.2.** *If*

$$\delta(t) = \delta_0, \qquad \eta(t) = 0,$$

*then the functional*

$$E(t) = \int_\Omega \left( \frac{1}{2} u^2 - \frac{\delta_0}{2} u_x^2 \right) dx \tag{47}$$

*is conserved.*

*Proof.* Under the assumptions $\delta'(t) = 0$ and $\eta(t) = 0$, the right-hand side of (44) vanishes identically. Integration over the spatial domain therefore gives

$$\frac{dE}{dt} = 0,$$

establishing conservation of the regularized energy. □

The preceding result shows that the BBM-type regularization preserves an energy invariant provided its coefficient remains constant, whereas temporal variations of the regularization parameter or nonlinear dispersive modulation generate additional source terms in the energy balance.

Finally, we briefly examine nonlinear self-adjointness. For the constant-coefficient conservative subclass, consider the formal Lagrangian

$$\mathcal{L} = v\Delta, \tag{48}$$

where $\Delta$ denotes the left-hand side of the canonical equation. Since

$$\Delta = D_t u + D_x \mathcal{F}$$

is itself a total divergence, the adjoint equation coincides with the original equation under the substitution

$$v = 1.$$

Hence the conservative subclass is formally nonlinearly self-adjoint in the sense of Ibragimov. This property provides an alternative route to the construction of conservation laws and further confirms the intrinsic conservative structure of the governing equation.

**Remark 7.3.** *The universal mass conservation law, the regularized energy balance and the nonlinear self-adjointness established above complement the Lie symmetry classification obtained in the previous sections. Together they provide the structural foundation for the exact travelling-wave solutions and numerical validation presented subsequently.*

## 8. EXACT TRAVELLING-WAVE AND SOLITON DYNAMICS

The travelling-wave reduction derived in Section 6 provides a natural framework for constructing localized coherent structures of the constant-coefficient canonical equation. In this section we restrict attention to the physically important case

$$p = q = 1,$$

for which the travelling-wave equation (38) becomes

$$U^{(4)} + (\beta - \delta v + \eta U)U'' - vU + \frac{\alpha}{2}U^2 = 0. \tag{49}$$

Motivated by the classical solitary-wave solutions of KdV-type equations, we seek localized solutions of the form

$$U(z) = A\,\mathrm{sech}^2(kz), \tag{50}$$

where $A > 0$ denotes the wave amplitude and $k > 0$ is the inverse width of the pulse.

Substituting the ansatz (50) into (49), evaluating the derivatives explicitly and collecting the linearly independent powers of $\mathrm{sech}(kz)$ gives the algebraic compatibility conditions

$$16k^4 + 4(\beta - \delta v)k^2 - v = 0, \tag{51}$$

$$-120k^4 - 6(\beta - \delta v)k^2 + \frac{\alpha A}{2} + 4\eta A k^2 = 0, \tag{52}$$

$$120k^4 - 6\eta A k^2 = 0. \tag{53}$$

The third equation immediately determines the wave amplitude,

$$A = \frac{20k^2}{\eta}, \tag{54}$$

provided $\eta \neq 0$.

Similarly, solving (51) for the wave speed gives

$$v = \frac{16k^4 + 4\beta k^2}{1 + 4\delta k^2}, \tag{55}$$

while substitution of (54) and (55) into (52) produces the remaining compatibility condition

$$-40k^2 + \frac{10\alpha}{\eta} - 6(\beta - \delta v) = 0. \tag{56}$$

**Theorem 8.1.** *Suppose the parameters satisfy the compatibility condition* (56) *with* $\eta \neq 0$. *Then the constant-coefficient canonical equation admits the exact travelling-wave solution*

$$u(x,t) = \frac{20k^2}{\eta}\,\mathrm{sech}^2\big(k(x - vt)\big), \tag{57}$$

*where the wave speed is given by* (55).

*Proof.* The result follows directly from the substitution of the ansatz (50) into (49). Equations (51)–(53) are obtained by equating the coefficients of the independent powers of $\mathrm{sech}(kz)$. Solving these algebraic equations yields (54), (55) and (56), which guarantee that the profile (57) satisfies the travelling-wave equation identically. □

The solution (57) represents a bright solitary wave whose amplitude is proportional to $k^2/\eta$, while its propagation speed depends on the combined effects of the third-order dispersion, the BBM-type regularization and the fifth-order dispersive balance. Consequently, both the dispersive coefficients and the nonlinear dispersive modulation influence the shape and velocity of the solitary wave.

**Remark 8.2.** *The bright-soliton solution derived above serves two complementary purposes. First, it provides an explicit invariant solution generated by the travelling-wave reduction obtained in Section 6. Second, it furnishes an exact benchmark for assessing the accuracy of the numerical simulations presented in the following section, thereby linking the analytical and computational components of the paper.*

## 9. NUMERICAL VALIDATION

The exact bright-soliton solution obtained in the previous section provides an ideal benchmark for assessing the accuracy of the proposed analytical framework. In particular, the numerical experiments are designed to verify three principal theoretical predictions: the preservation of the solitary-wave profile during propagation, the dependence of the wave dynamics on the dispersive parameters, and the conservation of the total mass.

For numerical illustration, we consider the compatible parameter set

$$k = \frac{1}{2}, \qquad \beta = 1, \qquad \delta = -0.1, \qquad \eta = 1, \qquad \alpha = \frac{26}{15}, \tag{58}$$

which satisfies the compatibility conditions derived in Section 8. The corresponding analytical solution has amplitude and wave speed

$$A = 5, \qquad v = \frac{20}{9}, \tag{59}$$

and therefore takes the explicit form

$$u(x,t) = 5\,\mathrm{sech}^2\left[\frac{1}{2}\left(x - \frac{20}{9}t\right)\right]. \tag{60}$$

The total mass associated with the analytical solution is

$$M(t) = \int_{-\infty}^{\infty} u(x,t)\,dx = \frac{2A}{k} = 20, \tag{61}$$

which provides an exact invariant against which the numerical computations may be compared.

The governing equation is solved numerically using a Fourier pseudo-spectral discretization in space combined with time integration on a sufficiently large periodic computational domain so that boundary effects remain negligible throughout the simulation. Spatial derivatives are evaluated spectrally, while the mixed dispersive term is treated through the Fourier multiplier

$$1 - \delta\kappa^2,$$

which remains strictly positive for $\delta < 0$. The spectral approximation therefore preserves the high-order accuracy required for the fifth-order dispersive dynamics while avoiding spurious boundary reflections.

Figure 2 summarizes the overall analytical and computational procedure adopted throughout the paper. Starting from the general variable-coefficient model, admissible equivalence transformations reduce the governing equation to a canonical form, after which Lie symmetry analysis, optimal systems and conservation laws provide the analytical foundation for the construction of exact travelling-wave solutions. The final stage consists of numerical validation against the analytical soliton.

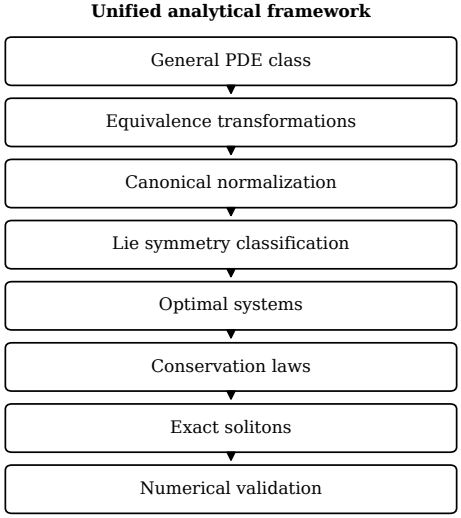


**Figure 2.** Overall workflow of the unified analytical framework, illustrating the progression from the general variable-coefficient model through equivalence transformations, Lie symmetry classification, conservation laws and similarity reductions to exact solutions and numerical validation.

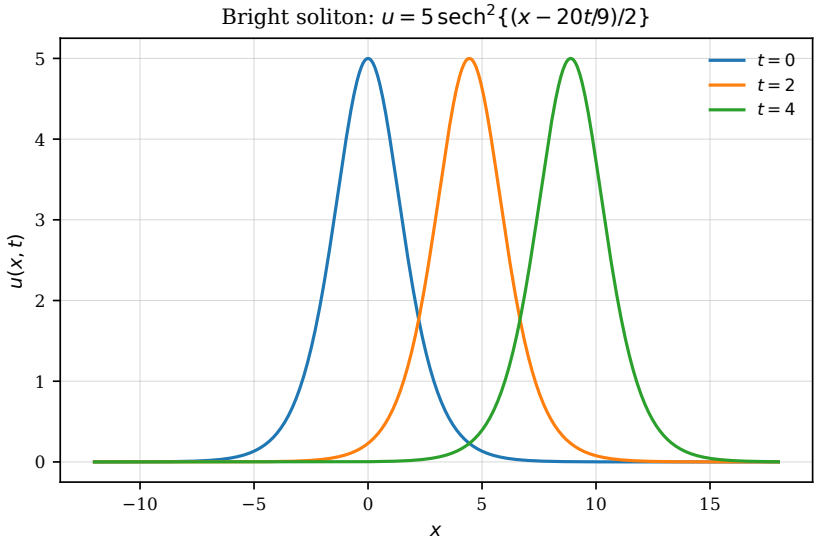


**Figure 3.** Propagation of the verified bright-soliton solution at representative times. The numerical solution remains in excellent agreement with the analytical profile, confirming the stability of the travelling-wave solution.

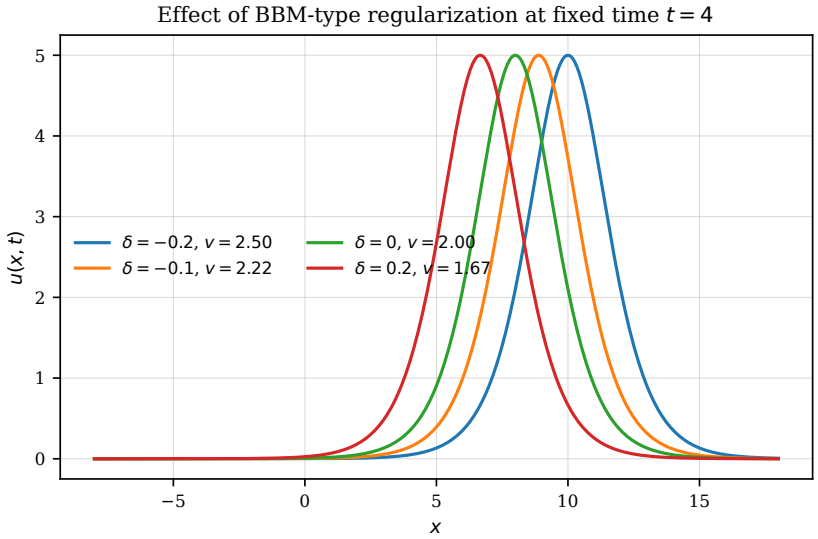


**Figure 4.** Influence of the BBM-type regularization coefficient $\delta$ on the propagation of the solitary wave. Increasing the regularization modifies the wave speed while preserving the localized structure.

Figure 3 illustrates the propagation of the exact bright soliton at several representative times. The numerical and analytical profiles remain indistinguishable throughout the computation, demonstrating that the solitary wave propagates without appreciable distortion and confirming the correctness of the travelling-wave solution derived in Section 8.

The influence of the BBM-type regularization parameter is illustrated in Figure 4. Increasing the magnitude of $\delta$ primarily affects the propagation speed through the velocity relation (55) while preserving the localized structure of the solitary wave. This behaviour is fully consistent with the analytical travelling-wave analysis.

Figure 5 illustrates the influence of the nonlinear dispersive coefficient $\eta$. As predicted by the analytical expression (54), the parameter $\eta$ directly controls the wave amplitude through

$$A = \frac{20k^2}{\eta},$$

showing that stronger nonlinear dispersive modulation reduces the amplitude of the localized wave while preserving its characteristic $\mathrm{sech}^2$ profile.

Finally, Figure 6 presents the numerical evolution of the conserved mass. Throughout the computation the numerical

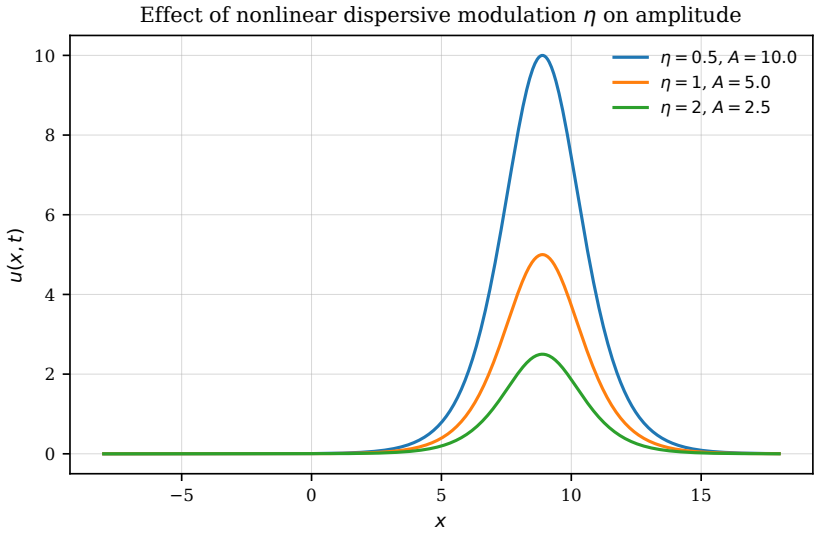


**Figure 5.** Influence of the nonlinear dispersive coefficient $\eta$ on the bright-soliton amplitude. The numerical behaviour agrees with the analytical relation $A = 20k^2/\eta$.

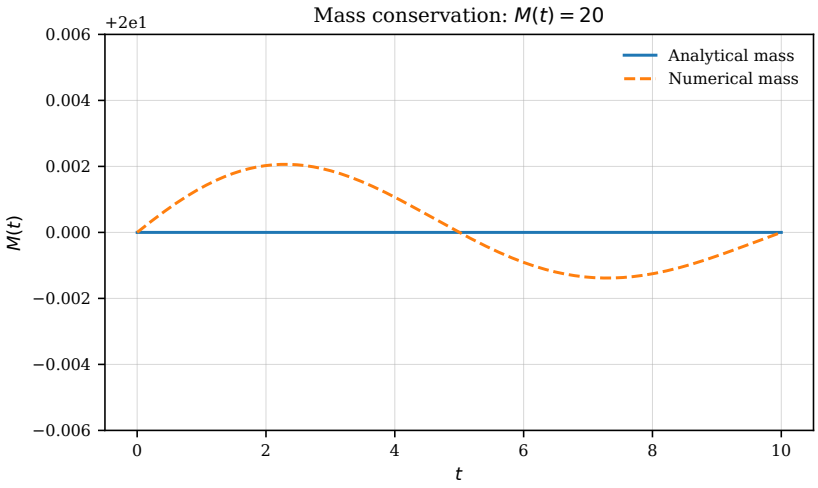


**Figure 6.** Numerical verification of the universal mass conservation law. The computed mass remains constant throughout the simulation and agrees with the exact analytical value $M = 20$.

value remains essentially constant and coincides with the exact analytical value

$$M = 20,$$

thereby confirming the universal mass conservation law established in Section 7 and demonstrating the consistency of the numerical implementation.

## 10. DISCUSSION

The present work develops a unified analytical framework for a broad class of variable-coefficient higher-order nonlinear evolution equations incorporating nonlinear convection, third-order dispersion, fifth-order dispersion, BBM-type mixed dispersion and nonlinear dispersive modulation. Rather than proposing an entirely new nonlinear evolution equation, the principal contribution lies in demonstrating that several classical dispersive wave models may be treated within a common mathematical framework through the combined use of admissible equivalence transformations, Lie symmetry analysis, conservation laws, similarity reductions and exact travelling-wave solutions.

A central result of the paper is the determination of the admissible equivalence group together with the canonical normalization of the fifth-order dispersive coefficient. This normalization substantially simplifies the complete group-classification problem by removing one arbitrary functional degree of freedom while preserving the analytical equivalence

of the original class. In particular, the compatibility condition

$$\frac{d\tau}{dt} = 5\lambda$$

emerges naturally from the normalized fifth-order term and governs the admissible temporal component of every Lie point symmetry. Consequently, the kernel algebra together with the power-law, exponential and constant-coefficient symmetry extensions are obtained in a systematic and unified manner.

The conservation-law analysis further illustrates the structural richness of the proposed class. The divergence form of the governing equation guarantees the existence of a universal mass conservation law independently of the particular coefficient functions. By contrast, the regularized energy balance reveals that temporal variations of the BBM-type regularization coefficient and nonlinear dispersive modulation introduce additional source terms that generally prevent energy conservation. This distinction has a natural physical interpretation: while the total wave mass remains invariant, nonlinear dispersive effects may redistribute energy between amplitude and curvature modes, thereby modifying the evolution of localized structures.

The exact bright-soliton solution derived for the constant-coefficient canonical equation demonstrates the effectiveness of the symmetry-based reduction procedure. The analytical expressions obtained for the wave amplitude and propagation speed explicitly reveal the roles played by the higher-order dispersive parameters. In particular, the BBM-type regularization parameter $\delta$ modifies the wave velocity through the denominator

$$1 + 4\delta k^2,$$

whereas the nonlinear dispersive coefficient $\eta$ controls the soliton amplitude through the inverse proportionality

$$A = \frac{20k^2}{\eta}.$$

These analytical predictions are fully consistent with the numerical experiments, which confirm stable propagation of the localized wave, the predicted parameter dependence and the preservation of the universal mass invariant.

From a broader perspective, the proposed framework illustrates the effectiveness of combining equivalence transformations with Lie symmetry analysis for the investigation of parameterized families of nonlinear evolution equations. Much of the existing literature focuses on individual equations or narrowly defined subclasses, whereas the present approach establishes a unified methodology capable of simultaneously treating several important higher-order dispersive models. The resulting symmetry classifications, conservation laws and travelling-wave reductions therefore extend a number of existing analytical results within a single coherent framework.

The present study nevertheless has certain limitations. The exact travelling-wave analysis has been restricted to bright solitary waves associated with the constant-coefficient canonical equation, while the conservation-law analysis has focused primarily on mass and regularized energy invariants. Furthermore, only classical Lie point symmetries have been considered. These restrictions were adopted deliberately in order to establish a complete and rigorous analytical foundation before addressing more sophisticated integrability structures.

## 11. CONCLUSIONS

This paper has developed a unified analytical framework for a broad class of variable-coefficient higher-order nonlinear evolution equations incorporating nonlinear convection, third-order dispersion, fifth-order dispersion, BBM-type mixed dispersion and nonlinear dispersive modulation. Rather than focusing on a single nonlinear evolution equation, the proposed framework provides a systematic methodology for analysing an entire family of higher-order dispersive wave models within a common mathematical setting.

The analysis began with the derivation of the admissible equivalence group, which was subsequently employed to normalize the fifth-order dispersive coefficient and reduce the general class to a canonical representative. This normalization proved to be a key analytical step, substantially simplifying the complete group-classification problem while preserving the equivalence structure of the original class. The canonical equation was then subjected to a complete Lie symmetry classification, yielding the kernel algebra together with the principal symmetry extensions associated with the power-law, exponential and constant-coefficient subclasses. Optimal systems of one-dimensional subalgebras and the corresponding similarity reductions were constructed, providing systematic reductions of the governing partial differential equation to ordinary differential equations.

The conservative structure of the canonical equation was further exploited to derive universal mass conservation together with a regularized energy conservation law for an important conservative subclass. The analysis also demonstrated the nonlinear self-adjointness of the constant-coefficient conservative model, thereby providing an alternative structural interpretation of the derived conservation laws.

A principal outcome of the paper is the construction of an exact bright-soliton solution for the constant-coefficient canonical equation. Explicit analytical expressions for the wave amplitude and propagation speed were obtained, revealing the influence of the higher-order dispersive mechanisms on solitary-wave dynamics. The analytical solution was rigorously

verified through direct substitution and subsequently employed as a benchmark for numerical simulations. The numerical experiments confirmed stable soliton propagation, the predicted dependence of the wave profile on the dispersive parameters and the preservation of the universal mass invariant, thereby providing strong agreement between the analytical and computational results.

Collectively, the results demonstrate that admissible equivalence transformations, Lie symmetry analysis, conservation laws, similarity reductions and exact travelling-wave solutions may be integrated into a single coherent analytical framework for higher-order variable-coefficient nonlinear evolution equations. The methodology developed here is sufficiently general to encompass several classical dispersive wave models while simultaneously providing new structural insights into their symmetry properties and conservation mechanisms.

Several natural extensions of the present work remain open. These include the investigation of generalized and nonlocal symmetries, higher-order conservation laws, Hamiltonian and bi-Hamiltonian structures, recursion operators, Darboux and Bäcklund transformations, integrable reductions, multi-soliton interactions and the stability of coherent structures. Such developments would further deepen the mathematical understanding of higher-order nonlinear evolution equations and broaden the range of physical applications accessible through the unified framework established in this paper.

## Acknowledgements

The author acknowledges institutional research support from North-West University. No external funding was received for this study.

## ORCID

**Suares Clovis Oukouomi Noutchie**, https://orcid.org/0000-0003-4662-8007

## REFERENCES

[1] P. J. Olver, *Applications of Lie Groups to Differential Equations*, 2nd ed. (Springer, New York, 1993).

[2] G. W. Bluman, and S. Kumei, *Symmetries and Differential Equations*, (Springer, Berlin, 1989).

[3] N. H. Ibragimov, *Transformation Groups Applied to Mathematical Physics*, (Reidel, Dordrecht, 1985).

[4] L. V. Ovsiannikov, *Group Analysis of Differential Equations*, (Academic Press, New York, 1982).

[5] E. Noether, Invariante Variationsprobleme, in: *Nachrichten von der Gesellschaft der Wissenschaften zu Göttingen, Mathematisch-Physikalische Klasse*, pp. 235–257 (1918).

[6] R. Hirota, *The Direct Method in Soliton Theory* (Cambridge University Press, Cambridge, 2004).

[7] M. J. Ablowitz, and P. A. Clarkson, *Solitons, Nonlinear Evolution Equations and Inverse Scattering* (Cambridge University Press, Cambridge, 1991).

[8] H. Schamel, and S. Bujarbarua, "Analytical double layers," Phys. Fluids, **26**, 190–193 (1983). https://doi.org/10.1063/1.864006

[9] H. Schamel, "Weak double layers: Existence, stability, evidence," Z. Naturforsch. A, **38**, 1170–1183 (1983). https://doi.org/10.1515/zna-1983-1102

[10] H. Schamel, and V. I. Maslov, "Adiabatic growth of electron holes in current-carrying plasmas," Phys. Scr. **T50**, 42 (1994). https://doi.org/10.1088/0031-8949/1994/T50/006

[11] V. I. Maslov, and H. Schamel, "Growing electron holes in drifting plasmas," Phys. Lett. A, **178**, 171–174 (1993). https://doi.org/10.1016/0375-9601(93)90746-M

[12] H. Schamel, and V. I. Maslov, "Langmuir wave contraction caused by electron holes," Phys. Scr. **T82**, 122 (1999). https://doi.org/10.1238/Physica.Topical.082a00122

[13] V. I. Maslov, "Electron beam excitation of a potential well in a magnetized plasma waveguide," Phys. Lett. A, **165**, 63–68 (1992). https://doi.org/10.1016/0375-9601(92)91055-V

[14] A. P. Márquez, M. L. Gandarias, and S. C. Anco, "Conservation laws, symmetries, and line solitons of a Kawahara–KP equation," Journal of Computational and Applied Mathematics, **436**, 115412 (2023). https://doi.org/10.1016/j.cam.2023.115412

[15] A. P. Márquez, T. M. Garrido, C. M. Khalique, and M. L. Gandarias, "Symmetries, conservation laws, and line soliton solutions of a two-dimensional generalized KdV equation with $p$-power," Discrete and Continuous Dynamical Systems Series S, **18**, 1024–1035 (2025). https://doi.org/10.3934/dcdss.2024130

[16] W. Hereman, "Symbolic computation of conservation laws of nonlinear partial differential equations in multi-dimensions," International Journal of Quantum Chemistry, **106**, 278–299 (2006). https://doi.org/10.1002/qua.20727

[17] F. Afzal, and A. A. Lupas, "Lie Symmetry Analysis, Optimal Systems and Physical Interpretation of Solutions for the KdV-Burgers Equation," Symmetry, **17**, 1981 (2025). https://doi.org/10.3390/sym17111981

[18] S. T. R. Rizvi, et al., "Lie symmetry analysis, conservation laws and soliton solutions by complete discrimination system for polynomial approach of Landau Ginzburg Higgs equation along with its stability analysis," Optik, **300**, 171675 (2024). https://doi.org/10.1016/j.ijleo.2024.171675

[19] A. Hussain, M. K. Zia, K. S. Nisar, V. Vijayakumar, and I. Khan, "Lie analysis, conserved vectors, nonlinear self-adjoint classification and exact solutions of generalized $(N + 1)$-dimensional nonlinear Boussinesq equation," AIMS Mathematics, **7**, 13139–13168 (2022). https://doi.org/10.3934/math.2022725

[20] S. Kumar, et al., "Lie symmetries, modulation instability, conservation laws, and the dynamic waveform patterns of several invariant solutions to a (2+1)-dimensional Hirota bilinear equation," Discrete and Continuous Dynamical Systems - Series S, **18**, 1054–1074 (2025). https://doi.org/10.3934/dcdss.2024136

[21] S. O. Mbusi, A. R. Adem, and B. Muatjetjeja, "Lie symmetry analysis, multiple exp-function method and conservation laws for the (2+1)-dimensional Boussinesq equation," Optical and Quantum Electronics, **56**, 670 (2024). https://doi.org/10.1007/s11082-024-06339-1

[22] F. S. Costa, J. C. A. Soares, J. V. C. Sousa, R. R. Luz, and J. A. R. Santos, "Lie point symmetries and conservation laws to fractional $\zeta(t)$-KdV equation," International Journal of Theoretical Physics, **65**, 11 (2026). https://doi.org/10.1007/s10773-025-06221-0

[23] S. Miao, et al., "An Analysis of the Lie Symmetry and Conservation Law of a Variable-Coefficient Generalized Calogero–Bogoyavlenskii–Schiff Equation in Nonlinear Optics and Plasma Physics," Mathematics, **12**, 3619 (2024). https://doi.org/10.3390/math12223619

[24] M. Junaid-U-Rehman, G. Kudra, and J. Awrejcewicz, "Conservation laws, solitary wave solutions, and Lie analysis for the nonlinear chains of atoms," Scientific Reports, **13**, 11537 (2023). https://doi.org/10.1038/s41598-023-38658-w

[25] H. Almusawa, and A. Jhangeer, "Nonlinear self-adjointness, conserved quantities and Lie symmetry of dust size distribution on a shock wave in quantum dusty plasma," Communications in Nonlinear Science and Numerical Simulation, **114**, 106660 (2022). https://doi.org/10.1016/j.cnsns.2022.106660

[26] M. A. Kawser, M. A. Akbar, and M. A. Khan, "Exploring variable coefficient models: Insights into nonlinear wave behavior and soliton solutions in physical systems," Results in Physics, **56**, 107242 (2024). https://doi.org/10.1016/j.rinp.2023.107242

[27] H. Wang Z. Zou, and X. Shen, "Lie symmetry analysis, self-adjointness and conservation law for a type of nonlinear equation," Mathematics, **9**, 1313 (2021). https://doi.org/10.3390/math9121313

[28] E. Yaşar, and E. Yaşar, "Exact wave solutions and local conservation laws of a third-order Boussinesq system," Discrete and Continuous Dynamical Systems - Series S, **18**, 1075–1092 (2025). https://doi.org/10.3934/dcdss.2024148

[29] M. Kumar, S. Anand, and D. V. Tanwar, "Lie symmetries, solitary wave solutions, and conservation laws of coupled KdV–mKdV equation for internal gravity waves," Mathematical Methods in the Applied Sciences, **47**, 6909–6927 (2024). https://doi.org/10.1002/mma.9949

## ЄДИНЕНА КЛАСИФІКАЦІЯ СИМЕТРІЇ, ЗАКОНИ ЗБЕРЕЖЕННЯ ТА ДИНАМІКА СОЛІТОНІВ ДЛЯ КЛАСУ НЕЛІНІЙНИХ ЕВОЛЮЦІЙНИХ РІВНЯНЬ ВИЩОГО ПОРЯДКУ ЗІ ЗМІННИМ КОЕФІЦІЄНТОМ

**Суарес Кловіс Оукуомі Ноучі**

*Школа математичних та статистичних наук, Північно-Західний університет, кампус Вандербейлпарк, Вандербейлпарк, Південна Африка*

Нелінійні еволюційні рівняння вищого порядку зі змінним коефіцієнтом становлять важливий клас математичних моделей для опису поширення нелінійних дисперсійних хвиль у неоднорідних середовищах, включаючи потоки мілководдя, плазму, оптичні системи та пружні структури. У цій статті розроблено єдину аналітичну основу для широкого сімейства таких рівнянь, що включають нелінійну конвекцію, дисперсію третього порядку, дисперсію п'ятого порядку, змішану дисперсію типу BBM та нелінійну дисперсійну модуляцію. Спочатку побудовано допустимі перетворення еквівалентності та використано їх для зведення загального класу за умови ненульової дисперсії п'ятого порядку до канонічної нормалізованої форми. Нормалізація призводить до спрощеної задачі групової класифікації шляхом встановлення явної умови сумісності для часової складової кожної допустимої симетрії точки Лі. Отримано повні класифікації симетрії Лі для підкласів ядра, степеневого закону, експоненціального закону та закону з постійним коефіцієнтом, після чого побудовано оптимальні системи та редукції подібності. Закони збереження виведені з консервативної структури рівняння, що визначає, включаючи універсальний інваріант маси та регуляризований закон збереження енергії для важливого канонічного підкласу. Крім того, отримано точний розв'язок яскравого солітона для рівняння з постійним коефіцієнтом, який ретельно перевірено прямою підстановкою та використано для перевірки числових симуляцій. Запропонована структура об'єднує перетворення еквівалентності, аналіз симетрії Лі, закони збереження, редукції подібності та динаміку солітонів в межах однієї параметризованої системи, забезпечуючи систематичну методологію для аналітичного дослідження нелінійних дисперсійних хвильових рівнянь вищого порядку.

**Ключові слова:** *аналіз симетрії Лі; перетворення еквівалентності; нелінійні еволюційні рівняння зі змінним коефіцієнтом; закони збереження; дисперсійні хвилі вищого порядку; дисперсія п'ятого порядку; редукції подібності; динаміка солітонів*

East European Journal of Physics. 3. 228–238 (2026)
DOI: 10.26565/2312-4334-2026-3-18 ISSN 2312-4334

# PARTICLES WITH INTERNAL DEGREES OF FREEDOM

**Kostyantyn M. Kulyk**[1*], **Maryna A. Ratner**[1], **Volodymyr V. Yanovsky**[1,2]
[1]*Institute for Single Crystals, NAS Ukraine, 60 Nauky Ave., Kharkov, 61072, Ukraine*
[2]*V. N. Karazin Kharkiv National University, 4 Svobody Sq., Kharkiv, 61022, Ukraine*
[*]*Corresponding Author e-mail: koskul@isc.kharkov.ua*
Received June 15, 2026; revised August 12, 2026; accepted August 21, 2026

A development of a structurally complex particle concept to the case of general interaction potentials between its components is proposed. A structurally complex particle is defined by the restricted problem of N+1 bodies of different masses, which is reduced to the N body problem. Based on the Lagrangian description, a Hamiltonian formalism is formulated and the resulting first integrals of motion are discussed. The absence of equipartition among the degrees of freedom is demonstrated. Using the virial theorem, it is proved that the energy of internal degrees of freedom does not exceed a certain fraction of the initial energy, depending on the ratio of the masses of internal particles to the mass of the shell. An exactly integrable case of a one-dimensional particle with two internal degrees of freedom is considered. The oscillation frequencies of such a structurally complex particle are determined by their masses and the mass of the shell. The energy distribution over them is not uniform. Universal relations are obtained for the distribution of the kinetic and potential energies of internal particles, which are independent of the choice of initial conditions. These relations provide more detailed information about the energy distribution than the virial relations.

**Keywords:** *Structurally complex particle; Internal degrees of freedom; Equations of motion; Virial relations*

## 1. INTRODUCTION

Small particles are often thought of as structureless point particles. This is one of the abstractions widely used in physics. It would seem that such a representation remains fairly reliable if one studies particle properties on scales significantly exceeding its size. In fact, in many cases this is not true. The presence of internal degrees of freedom manifests itself even on observation scales significantly exceeding the particle size. For example, when a structurally complex particle is reflected from a perfectly elastic barrier, a "violation" of the energy conservation law occurs for a supposedly point particle. The reason for this is related to the possibility of transferring the energy of internal degrees of freedom to a translation motion of a structurally complex particle, which can lead to an increase in the particle's velocity after reflection [1]. Naturally, if the internal degrees of freedom are taken into account, the conservation laws for energy and momentum are satisfied in this case. Moreover, in a number of cases, the properties of particles that depend on their internal structure and size are of interest. Such particles can no longer be considered as point ones, and their structure, i.e. internal degrees of freedom can affect virtually all relevant processes m and lead to unusual behavior. Of particular interest are particles with a small number of internal degrees of freedom, when partucle's properties depend essentially on this number. Such cases are interesting because thermodynamic laws are not applicable there. It should be emphasized that systems with a finite number of internal degrees of freedom demonstrate both pecularities of dynamic behavior [1,3], and clear manifestations of statistical anomalies [2]. Nanopeapods [5–8] and rotaxanes [9, 10] (see Fig.1) can be cited as real objects that fully correspond to one-dimensional structurally complex particles. In principle, the nature of such objects has a deeper meaning. If we consider a small particle of a medium, it typically contains quasiparticles of certain types. It's easy to see that the motion of quasiparticles in such a particle is accompanied by their reflection from the boundary of the medium. This leads to the transfer of momentum and energy to the particle itself and its surface, which corresponds to the model of a structurally complex particle. This provides a more general example of structurally complex particles.

Another type of an object with internal degrees of freedom was proposed quite a long time ago [15] and led to one of the popular models of polymer physics. Such a complex particle consists of beads connected in series by harmonic interaction in a chain. In the model, the beads experience strong friction and inertial forces in this case are insignificant. Examples of the implementation of this simple model in polymer physics are quite numerous [11–13]. The main method used for such systems consists in the use of Langevin equations (see, for example, [14]).

Another popular model of polymer molecules corresponds to a chain of rigid links connected by hinges [16]. The mechanical response of an individual polymer chain can be obtained by measuring the end-to-end length as a function of the applied force. Idealized models of individual chains, such as the freely jointed chain model, allow one to quantify these physical phenomena. It is important to note that experiments on stretching individual molecules of arbitrary length required the study of the statistical mechanics of small systems. In these cases, the thermodynamic limit is not satisfied; different macroscopic boundary conditions, corresponding to different ensembles of statistical mechanics, yield different force-displacement curves. A more comprehensive approach to approximating the mechanical response of individual chains with free joints required taking into account link extensions [17]. Among these models, exactly solvable ones

***Cite as:*** K.M. Kulik, M.A. Ratner, V.V. Yanovsky, East Eur. J. Phys. 3, 228 (2026), https://doi.org/10.26565/2312-4334-2026-3-18

have been discovered that correspond to special cases of harmonic bond potentials [18, 19]. In a certain sense, this is the opposite case to the structurally complex particles under consideration. Inertnal forces play a primary role in the behavior of structurally complex particles.

Nanodevices inevitably require internal degrees of freedom to function, which enable the device to perform certain actions. Examples of such nanodevices are currently quite numerous (see, for example, [20–23]) and are closely linked to the rapidly developing field of active particle physics [24]. Therefore, the development of the theory of structurally complex particles holds promise for the creation of new nanodevices.

Most results for particles with internal degrees of freedom have been obtained within the framework of the generalized billiard formalism [1]. This formalism considres perfectly elastic collisions between any components of a structurally complex particle. A model of a structurally complex particle can be represented as a shell of mass $M$ within which $N$ particles of different masses and possibly sizes move. In a certain sense, this reduces to the restricted problem of $N + 1$-bodies. The billiard formalism is useful for describing kinematic and dynamic properties of structurally complex particles with a small number of internal degrees of freedom. As the number of degrees of freedom increases, their properties of such particles can be studied using computer simulation. However, in some cases, such an idealization may not be realized. Therefore, this paper proposes a more general formalism that will allow us to consider the general case of potential interactions between the components of a structurally complex particle. In the proposed simple model of a particle with internal degrees of freedom, the interaction potential of the particles with the shell and with each other can be chosen in any suitable form. The most general kinematic and dynamic properties of such a particle are studied. It is shown that this problem of $N + 1$ bodies can be reduced to the problem of $N$ bodies or to the behavior of only internal particles. The behavior of a structurally complex particle or shell is determined by the sum of the displacements of its internal particles. Lagrangian and Hamiltonian equations of motion for internal particles are derived, and the emergence of additional conservation laws is demonstrated. An analysis of the general equations of motion reveals the absence of equipartition among internal degrees of freedom for different particle masses. Using a modification of virial relations, it is shown that the energy of internal degrees of freedom cannot exceed a certain fraction of the initial energy, which depends on the ratio of the masses of the internal particles to the mass of the shell. These results indicate the emergence of unusual statistical properties of internal particles in their statistical description. As an example, a simple integrable case of a shell with two internal particles is considered. Exact solutions were obtained and universal patterns of energy distribution among individual components of a structurally complex particle were established.

## 2. DYNAMICS OF PARTICLES WITH INTERNAL DEGREES OF FREEDOM

Let us consider the Lagrangian description of a particle with $N$ internal degrees of freedom. The model of such a system consists of a spherical shell with mass M with internal particles of various masses $m_\alpha$. We will number internal particles with Greek indices $\alpha = 1, ..., N$. Let the internal particles interact with the shell and with each other. The potential energy of the interaction of the internal degrees of freedom with the shell is denoted by $U$, and between themselves by $V$. Let us denote the shell center position as $\vec{R}$, and the coordinates of the internal particles as $\vec{x}_\alpha$. Latin indices are reserved for the numbering of vector coordinates. Then the Lagrangian of such a system takes the form

$$\mathcal{L} = \frac{M\dot{\vec{R}}^2}{2} + \sum_{\alpha=1}^{N} \frac{m_\alpha \dot{\vec{x}}_\alpha^2}{2} - \sum_{\alpha=1}^{N} U(\vec{R} - \vec{x}_\alpha) - \sum_{\alpha,\beta}^{N} V(\vec{x}_\alpha - \vec{x}_\beta) \tag{1}$$

Here vector $\vec{R}$ plays the role composite particle's coordinate, i.e. the position of the spherical shell center, while $\dot{\vec{R}}$ is the composite particle's velocity. The role of the potential energy of the interaction of the internal degrees of freedom with each other, $V(\vec{x}_\alpha - \vec{x}_\beta)$ , actually boils down to the appearance of chaos and the redistribution of energy between them. In a certain sense, the role of this interaction is not very significant. The same processes are carried out due to the interaction of internal particles with the shell. The choice of potential energy $V$ can be dictated by the physics of the system and the simplicity of the calculation. Let's dwell on the potential energy $U(\vec{R} - \vec{x}_\alpha)$ of the interaction of internal particles with the shell. The simplest choice of such a potential corresponds to local interactions or absolutely elastic collisions of internal particles and the shell. Such a potential is determined by an unlimited barrier of circular shape, $U(\vec{R} - \vec{x}_\alpha) = U_0\delta(R_0^2 - |\vec{R} - \vec{x}_\alpha|^2)$ , where $R_0$ the radius of the spherical shell or the size of the particle. In fact, such a potential corresponds to a cylindrical potential well (see Fig.2). In general, the potential can be more complicated, but preserving its symmetry, we will preserve its dependence on coordinates $|\vec{R} - \vec{x}_\alpha|^2$. The transition to coordinates $\vec{Q} = \sqrt{M}\vec{R}, \vec{y}_\alpha = \sqrt{m_\alpha}\vec{x}_\alpha$ transforms the Lagrangian (1) into the form

$$\mathcal{L} = \frac{\dot{\vec{Q}}^2}{2} + \sum_{\alpha=1}^{N} \frac{\dot{\vec{y}}_\alpha^2}{2} - U\left(\frac{\vec{Q}}{\sqrt{M}} - \frac{\vec{y}_1}{\sqrt{m_1}}, ..., \frac{\vec{Q}}{\sqrt{M}} - \frac{\vec{y}_M}{\sqrt{m_N}}\right) -$$

$$- \sum_{\alpha,\beta}^{N} V\left(\frac{\vec{y}_\alpha}{\sqrt{m_\alpha}} - \frac{\vec{y}_\beta}{\sqrt{m_\beta}}\right) \tag{2}$$

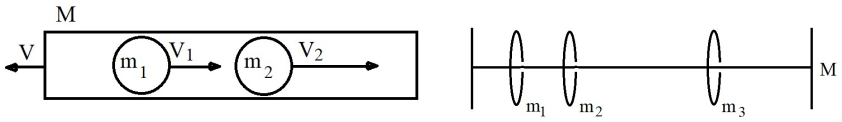


**Figure 1.** Type of one-dimensional particle with internal degrees of freedom. On the right, there is shown the equivalent model in the form of a chemical compound with topological bonds — rotaxanes.

Where $U\left(\frac{\vec{Q}}{\sqrt{M}} - \frac{\vec{y}_1}{\sqrt{m_1}}, ..., \frac{\vec{Q}}{\sqrt{M}} - \frac{\vec{y}_M}{\sqrt{m_N}}\right) = \sum_{\alpha=1}^{N} U(\frac{\vec{Q}}{\sqrt{M}} - \frac{\vec{y}_\alpha}{\sqrt{m_\alpha}})$.

It is easy see that, via introducing $3(N+1)$-dimensional configurational space, this Lagrangian can be considered as the Lagrangian of one particle of unit mass moving in a potential well in $3(N+1)$-dimensional space. In a certain sense, it can be considered as a generalization of the billiard formalism for the case of arbitrary interaction potentials.

Returning to the Lagrangian (1) we note that the limit $M \to \infty$ corresponds to a classical gas of a finite number of particles in a spherical vessel. Even this classical case demonstrates unusual statistical properties [2], which differ from the known ones associated with Boltzmann distributions. Of course, the potential $U(\vec{R}-\vec{x}_\alpha)$ may also have other dependences on the coordinates in general case. The Lagrangian (1) completely determines the general dynamics of a particle with internal degrees of freedom. The equations of motion of all $N+1$ components of the particle arise as Lagrange equations from the variational principle of the least action.

Naturally, the total energy, angular momentum, and total momentum of such a closed system are preserved. Taking into account the conservation of momentum, it is convenient to switch to a frame of reference associated with the center of mass.

$$M\vec{R} + \sum_{\alpha=1}^{N} m_\alpha \vec{x}_\alpha = 0 \tag{3}$$

In this reference system, the position of the particle is determined by the internal degrees of freedom coordinates as

$$\vec{R} = -\frac{\sum_\alpha^N m_\alpha \vec{x}_\alpha}{M} \tag{4}$$

Let's move on to the new coordinates of the internal particles, which correspond to their positions relative to the center of the shell

$$\vec{q}_\alpha = \vec{R} - \vec{x}_\alpha \tag{5}$$

In the new coordinates, the position of the particle is determined as

$$\vec{R} = \frac{\sum_\alpha^N m_\alpha \vec{q}_\alpha}{M_s} \tag{6}$$

Where $M_s = M + \sum_\alpha^N m_\alpha$ is the total mass of the particle. In a certain sense, the shell's position is determined by the sum of the "trajectories" of the internal degrees of freedom at each moment of time. The statistical properties of this sum differ from the statistical properties of the trajectories of a Brownian particle due to the shell's constraints on the quantities that make up the sum. Using this relation, we exclude the collective coordinate $\vec{R}$ from the Lagrangian (1) and obtain

$$\mathcal{L} = \frac{1}{2}\sum_{\alpha=1}^{N} m_\alpha \dot{\vec{q}}_\alpha^{\,2} - \frac{1}{2M_s}\left(\sum_{\alpha=1}^{N} m_\alpha \dot{\vec{q}}_\alpha\right)^2 - \\ - \sum_{\alpha=1}^{N} U(\vec{q}_\alpha) - \sum_{\alpha,\beta}^{N} V(\vec{q}_\alpha - \vec{q}_\beta) \tag{7}$$

First of all, it is important to note that now a complete description of a particle with internal degrees of freedom is achieved by a system of a smaller number of objects of different masses. In other words, the problem of $N+1$ bodies is reduced to the problem of $N$ bodies. The shell coordinate is determined according to the equation (6). The explicit form of the equations of motion can be obtained from the variational principle as Lagrange's equations

$$\frac{d}{dt}\frac{\partial \mathcal{L}}{\partial \dot{q}_{\alpha i}} - \frac{\partial \mathcal{L}}{\partial q_{\alpha i}} = 0 \tag{8}$$

Using Lagrangian (7), we obtain a system of equations of motion for internal degrees of freedom

$$m_\alpha \ddot{q}_{\alpha i} - \frac{m_\alpha}{M_s}\sum_{\beta}^{N} m_\beta \ddot{q}_{\beta i} = -\frac{\partial U(\vec{q}_\alpha)}{\partial q_{\alpha i}} - \sum_{\beta} \frac{\partial V(\vec{q}_\alpha - \vec{q}_\beta)}{\partial q_{\alpha i}} \tag{9}$$

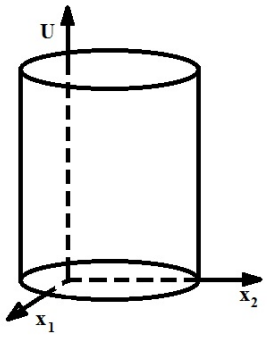


**Figure 2.** The form of a cylindrical potential well in two dimensional case; in three dimensional case, the cylinder's base is sphere $S^3$.

This system of equations fully describes the dynamic properties of a particle with internal degrees of freedom. It is easy to notice some differences from the usual equations of particles in a potential well. Already from these equations it is possible to understand the presence of two limiting cases in the system: $\frac{m_\alpha}{M} \gg 1$ and $\frac{m_\alpha}{M} \ll 1$. In the second limiting case, the system is close to the system of a finite number of particles in a potential well. In fact, the value of the second contribution in the left part of Eq.(9) is a measure of difference from this canonical physical case. Each of the Eq. (9) includes accelerations of all internal particles. They can be reduced to Newton's equations, via solving this linear equation system (9) with respect to accelerations

$$m_\alpha \ddot{\vec{q}}_{\alpha i} = \vec{F}_\alpha + \frac{m_\alpha}{M} \sum_{\beta=1}^{N} \vec{F}_\beta \tag{10}$$

Here we use the notation $\vec{F}_\alpha = -\frac{\partial U(\vec{q}_\alpha)}{\partial \vec{q}_\alpha} - \sum_{\beta=1}^{N} \frac{\partial V(\vec{q}_\alpha - \vec{q}_\beta)}{\partial \vec{q}_{\alpha i}}$ to reduce the cumbersomeness of notation. In this form, the dynamic equations correspond to the motion of interacting particles in a more complex potential well. It is important to note that the position of this potential well is independent of time. Returning to the behavior of a structurally complex particle, we note that relation (6) resembles the formation of a Brownian trajectory by summing successive jumps. However, the nature of this relation is different and is related to the sum of instantaneous jumps. In other words, the first distintion lies in the execution of not one, but multiple steps per unit time. The number of steps is determined by the number of internal degrees of freedom. The change in the shell's position over time can be estimated

$$\vec{R}(t + \Delta t) \approx \frac{\sum_\alpha^N m_\alpha \vec{q}_\alpha(t)}{M_s} + \frac{\sum_\alpha^N m_\alpha \dot{\vec{q}}_\alpha(t)}{M_s} \Delta t \tag{11}$$

Thus, the jump in the particle's position over time $\Delta t$ is determined by the sum of $m_\alpha \dot{\vec{q}}_\alpha$ internal particles and effectively determines the Brownian jump of the entire particle. However, the magnitude of the possible changes in the particle's position is limited by the inequalities

$$\frac{\min \left| \sum_\alpha^N m_\alpha \vec{q}_\alpha \right|}{M_s} \leq \left| \vec{R} \right| \leq \frac{\max \left| \sum_\alpha^N m_\alpha \vec{q}_\alpha \right|}{M_s}$$

Here the length of the vector is indicated by straight brackets |...|. The minimum and maximum values of these amounts are easy to estimate. The minimum is reached when all internal particles are located in the center of the shell and the relative deviations $\vec{q}_\alpha = 0$, and the maximum is reached when they are all close to an arbitrary point on the shell boundary, with a radius $R_0$. From this we obtain $0 \leq \left| \vec{R} \right| \leq \frac{R_0 \sum_\alpha^N m_\alpha}{M_s}$. This leads to the second distinction from Brownian motion. This is the presence of an a priori limitation on deviations from the particle's initial position. Some other features of the dynamic equations (10) will be discussed in the following sections.

## 3. HAMILTONIAN EQUATIONS OF MOTION

We now turn to the Hamiltonian formalism, which has a number of advantages. In addition to its clarity and exceptional geometric representations, these include advantage of finding exact solutions. It simplifies the transition to quantum mechanics and is useful in the statistical description of physical systems. The transition from the Lagrangian to the Hamiltonian formalism is achieved by performing a Legendre transformation [25, 26]. To do this, we define the generalized momenta according to

$$\vec{p}_\alpha = \frac{\partial L}{\partial \dot{\vec{q}}_\alpha} \tag{12}$$

Using the form of the Lagrangian (7) we obtain the relation

$$\vec{p}_\alpha = m_\alpha \dot{\vec{q}}_\alpha - \frac{m_\alpha \sum_{\beta=1}^{N} m_\beta \dot{\vec{q}}_\beta}{M_s} \tag{13}$$

Using this equation we obtain the dependence of velocities on momenta

$$m_\alpha \dot{\vec{q}}_\alpha = \vec{p}_\alpha + \frac{m_\alpha}{M} \sum_{\beta=1}^{N} \vec{p}_\beta \tag{14}$$

Now we perform the Legendre transformation of the Lagrange function with respect to velocities. Using the dependence (14) we define the Hamilton function as

$$H = \left( \sum \vec{p}_\alpha \dot{\vec{q}}_\alpha - L \right) \Big|_{\dot{\vec{q}}_\alpha = \frac{\vec{p}_\alpha}{m_\alpha} + \frac{1}{M} \sum_\beta \vec{p}_\beta} \tag{15}$$

After simple transformations we obtain the Hamiltonian in the form

$$H = \frac{1}{2} \sum_{\alpha}^{N} \frac{\vec{p}_\alpha^{\,2}}{m_\alpha} + \frac{(\sum_\alpha \vec{p}_\alpha)^2}{2M} + \sum_{\alpha}^{N} U(\vec{q}_\alpha) + \sum_{\alpha<\beta}^{N} V(\vec{q}_\alpha - \vec{q}_\beta) \tag{16}$$

The equations of motion in the Hamiltonian formalism have the form

$$\begin{aligned} \frac{d\vec{p}_\alpha}{dt} &= -\frac{\partial H}{\partial \vec{q}_\alpha} \\ \frac{d\vec{q}_\alpha}{dt} &= \frac{\partial H}{\partial \vec{p}_\alpha} \end{aligned} \tag{17}$$

Using the resulting Hamiltonian, we obtain the equation of motion.

$$\begin{aligned} \frac{d}{dt}\vec{p}_\alpha(t) &= -\frac{\partial}{\partial \vec{q}_\alpha} U(\vec{q}_\alpha) - \frac{\partial}{\partial \vec{q}_\alpha} \sum_\beta V(\vec{q}_\alpha - \vec{q}_\beta) \\ \frac{d}{dt}\vec{q}_\alpha(t) &= \frac{p_\alpha}{m_\alpha} + \frac{\sum_\beta p_\beta}{M} \end{aligned} \tag{18}$$

This system of $6N$ first-order equations determines the dynamics of internal degrees of freedom in the Hamiltonian approach. The first equation for the change in momentum coincides with the equation for interacting particles in a potential well. The distinction in the second equation, as expected, disappears in the limiting case of an infinitely heavy shell $M \to \infty$. This leads us to the classical system of a gas of a finite number of particles in a spherical potential.

Returning to the form of Hamiltonian (16) we note the absence of time dependence. In this case $H$ is the first integral of Hamiltonian equations (18). It is interesting to note that this conservation law differs from the conservation law of energy for a particle with internal degrees of freedom. Thus, for a particle with internal degrees of freedom, an additional conservation law arises. The presence of an additional conservation law is of great importance not only for dynamic properties but also it introduces significant changes to statistical theory. Thus, when obtaining a microcanonical distribution, a homogeneous distribution will be achieved not on the surface of constant energy, but at its intersection with the surface of constancy of an additional invariant. This radically affects the type of equilibrium distribution functions (see, for example [2]).

## 4. A SPECIAL CASE OF COLLISIONLESS INTERNAL DEGREES OF FREEDOM

Let us consider in more detail a simple case of interaction between internal particles and the shell in the absence of interactions of particles with each other. In this case, Lagrangian (7) is simplified and takes the form

$$\mathcal{L} = \frac{1}{2} \sum_{\alpha=1}^{N} m_\alpha \dot{\vec{q}}_\alpha^{\,2} - \frac{1}{2M_s} \left( \sum_{\alpha=1}^{N} m_\alpha \dot{\vec{q}}_\alpha \right)^2 - \sum_{\alpha=1}^{N} U(\vec{q}_\alpha) \tag{19}$$

It's easy to notice the presence of cyclic coordinates and, consequently, additional conservation laws. Thus, cyclic coordinates are the angular variables of rotation relative to the center of the potential $U(\vec{q}_\alpha)$ This is due to its symmetry and dependence only on the lengths of the vectors $|\vec{q}_\alpha|$. Moving on to spherical coordinates, we obtain

$$\mathcal{L} = \frac{1}{2} \sum_{\alpha=1}^{N} m_\alpha (\dot{q}_\alpha^{\,2} + q_\alpha^2 \dot{\theta}_\alpha^2 + q_\alpha^2 \sin(\theta_\alpha)^2 \dot{\varphi}_\alpha^2) -$$

$$-\frac{1}{2M_s}\left(\sum_{\alpha=1}^{N} m_\alpha(\dot{q}_\alpha\vec{r}_0 + q_\alpha\dot{\theta}_\alpha\vec{\theta}_0 + q_\alpha\sin(\theta_\alpha)\dot{\varphi}_\alpha\vec{\varphi}_0)\right)^2 - \tag{20}$$

$$-\sum_{\alpha=1}^{N} U(q_\alpha)$$

Where $\vec{q}_0, \vec{\theta}_0, \vec{\varphi}_0$ are the corresponding unit vectors. The cyclicity of coordinates $\varphi_\alpha$ results in the conservation of the following quantities:

$$I_\alpha = m_\alpha q_\alpha^2 \sin^2(\theta_\alpha)\dot{\varphi}_\alpha -$$

$$-\frac{1}{M_s} m_\alpha q_\alpha \sin(\theta_\alpha)\left(\sum_{\beta=1}^{N} m_\beta q_\beta \sin(\theta_\beta)\dot{\varphi}_\beta\right) \tag{21}$$

Naturally, their sum is also conserved. Note that from these relations one can explicitly find the velocities of cyclic variables in the form $\dot{\varphi}_\alpha = f_\alpha(q_\alpha, \sin(\theta_\alpha), I_\alpha)$ for given values of the conserved quantities. Using the Routh method (see, for example, [27]) ]), one can eliminate cyclic coordinates and their velocities by introducing the Routh function.

$$R(q_1, ..., q_N; \theta_1, ..., \theta_N; \dot{q}_1, ..., \dot{q}_N; \dot{\theta}_1, ..., \dot{\theta}_N; I) =$$

$$= \mathcal{L} - \sum_{\alpha=1}^{N} I_\alpha\dot{\varphi}_\alpha|_{\dot{\varphi}_\alpha = f_\alpha(q_\alpha, \sin(\theta_\alpha), I_\alpha)} \tag{22}$$

As a result, we obtain a reduced Lagrangian system, the Lagrangian $R$, of which depends on $2N$ coordinates (and their velocities) for fixed values of the invariants. It should be noted that the Routh function in our case is found explicitly and is not presented only due to the cumbersome nature of its notation. Thus, the number of equations of motion is reduced to $2N$. It is expected that other conservation laws are also satisfied due to the initial symmetry of the potential energy. Their search is significantly more difficult. However, one additional invariant can be easily found. To do this, it suffices to note that the Lagrangian of the reduced system (22) does not depend explicitly on time. This means that the energy of the reduced system is conserved and provides another additional invariant, using which we can again reduce the number of dynamic equations. In this way, we can achieve a significant reduction in the number of dynamic equations for describing the internal degrees of freedom of a structurally complex particle.

## 5. ENERGY DISTRIBUTION

Let's return to Lagrangian (19) and consider the general properties of the internal degrees of freedom. We will be interested in the distribution of kinetic and potential energy between the components of the system. Lagrangian (19) contains two contributions. One is a quadratic function of the velocities, which we denote by $T$. This function has a degree of homogeneity of 2 with respect to velocities. It should be noted that this contribution does not coincide with the kinetic energy. The second contribution is the sum of potential energies that depend only on the coordinates. The potential energies transform in a specific way under coordinate transformations. Indeed, it is easy to verify that, when changing coordinates $\vec{q}_\alpha \to \lambda\vec{q}_\alpha$ the potential energy $U(\vec{q}_\alpha) = U_0\theta(|\vec{q}_\alpha|^2 - R_0^2)$ transforms, taking into account $R_0 \to \lambda R_0$ as $U(\vec{q}_\alpha) = U_0\theta(\lambda(|\vec{q}_\alpha|^2 - R_0{}^2)) = U(\vec{q}_\alpha)$ for $\lambda > 0$. In a more general case, as noted earlier, other potentials can be used, for example, those with a different degree of homogeneity $\kappa$. (Let the potential energy transform under rescaling as $U(\lambda\vec{q}_\alpha) = \lambda^\kappa U(\vec{q}_\alpha)$.Then it is a homogeneous function of the coordinates of degree $\kappa$. In these cases, Clausius, quite long ago, derived general relations between kinetic and potential energy, which are known as the virial theorem. Using the properties of homogeneity, we obtain for the part depending on the speed according to Euler's theorem on homogeneous functions

$$2T = \sum_{\alpha=1}^{N} \dot{\vec{q}}_\alpha \frac{\partial T}{\partial \dot{\vec{q}}_\alpha} \tag{23}$$

The right side of this equality, using the definition of generalized momentum (see (12), (13)) can be written as

$$2T = \frac{d}{dt}\sum_{\alpha=1}^{N} \vec{p}_\alpha\vec{q}_\alpha - \sum_{\alpha=1}^{N} \vec{q}_\alpha\dot{\vec{p}}_\alpha \equiv \frac{d}{dt}\sum_{\alpha=1}^{N} \vec{p}_\alpha\vec{q}_\alpha + \sum_{\alpha=1}^{N} \vec{q}_\alpha\frac{\partial U}{\vec{q}_\alpha} \tag{24}$$

It should be emphasized that, due to energy conservation and the restriction of coordinates of particles in a potential well, momenta and coordinates are bounded functions of time. To obtain virial relations, we use time averaging, which is denoted by angle brackets. $\langle ... \rangle = \lim_{T\to\infty} \frac{1}{T}\int_0^T ...dt$. Averaging the previous ratio over time, we obtain

$$2\langle T\rangle = \left\langle \sum_{\alpha=1}^{N} \vec{q}_\alpha\frac{\partial U}{\vec{q}_\alpha} \right\rangle \tag{25}$$

Taking into account Euler's theorem for homogeneous functions, we obtain the virial theorem

$$2\langle T\rangle = \kappa\langle U\rangle \tag{26}$$

For the case under consideration, this relationship can be written as,

$$2\left\langle \frac{1}{2}\sum_{\alpha=1}^{N} m_\alpha \dot{\vec{q}}_\alpha^{\,2}\right\rangle - 2\left\langle \frac{1}{2M_s}\left(\sum_{\alpha=1}^{N} m_\alpha \dot{\vec{q}}_\alpha\right)^2\right\rangle = \kappa\langle U\rangle \tag{27}$$

The first term on the left coincides with the kinetic energy of the particles, while the second one is more complex. Now, using conservation of energy, we find what fraction of the initial energy is concentrated in potential energy.

$$\left\langle \frac{1}{2}\sum_{\alpha=1}^{N} m_\alpha \dot{\vec{q}}_\alpha^{\,2}\right\rangle - \frac{1}{2M_s}\left\langle\left(\sum_{\alpha=1}^{N} m_\alpha \dot{\vec{q}}_\alpha\right)^2\right\rangle + \langle U\rangle = E_0 \tag{28}$$

By excluding the average of the square of the sum from the relation (26) we obtain

$$\langle U\rangle = \frac{2E_0}{2+\kappa} \tag{29}$$

which exactly coincides with the initial energy fraction in a conventional system of particles in a potential well. However, estimating the fraction of the kinetic energy of the particles is difficult due to the presence of an additional contribution. Eliminating the potential energy from relation (27) we obtain

$$\left\langle \frac{1}{2}\sum_{\alpha=1}^{N} m_\alpha \dot{\vec{q}}_\alpha^{\,2}\right\rangle - \left\langle \frac{1}{2M_s}\left(\sum_{\alpha=1}^{N} m_\alpha \dot{\vec{q}}_\alpha\right)^2\right\rangle = \frac{\kappa E_0}{2+\kappa} \tag{30}$$

Then, to determine the proportion of the initial energy that goes to kinetic energy, we use an estimate of the second contribution in terms of kinetic energy. For this, we use the Cauchy-Bunyakovsky inequality $(\sum_{\alpha=1}^{N} a_\alpha b_\alpha)^2 \le \sum_{\alpha=1}^{N} a_\alpha^2 \sum_{\alpha=1}^{N} b_\alpha^2$. Let us write down the following relation

$$\left(\sum_{\alpha=1}^{N} m_\alpha \dot{\vec{q}}_\alpha\right)^2 \equiv \left(\sum_{\alpha=1}^{N} \sqrt{m_\alpha}\sqrt{m_\alpha}\dot{\vec{q}}_\alpha\right)^2 \le$$

$$\le \sum_{\alpha=1}^{N} m_\alpha \cdot \sum_{\alpha=1}^{N} m_\alpha \dot{\vec{q}}_\alpha^{\,2} \tag{31}$$

Denoting the mass of internal degrees of freedom as $M_{in} = \sum_{\alpha=1}^{N} m_\alpha$ we obtain

$$\left(\sum_{\alpha=1}^{N} m_\alpha \dot{\vec{q}}_\alpha\right)^2 \le M_{in}\sum_{\alpha=1}^{N} m_\alpha \dot{\vec{q}}_\alpha^{\,2} \tag{32}$$

This relation sets a limit to the kinetic energy fraction for the internal degrees of freedom in the total energy $E_0$

$$\left\langle \frac{1}{2}\sum_{\alpha=1}^{N} m_\alpha \dot{\vec{q}}_\alpha^{\,2}\right\rangle \le \frac{\kappa E_0 M_s}{(2+\kappa)M} \tag{33}$$

The distinction from the usual case is that the fraction of kinetic energy depends on the ratio of the shell mass to the total mass of the particles. Thus, the kinetic energy of the internal particles cannot exceed a certain fraction of the total energy, which is determined by the ratio of the mass of the entire particle to the shell mass.

## 6. TWO INTERNAL DEGREES OF FREEDOM

We present an exact solution of the Lagrangian equations for the internal degrees of freedom, obtained using Lagrangian (19) for the one-dimensional case with two internal particles. For simplicity, we choose the potential of particle interaction with the shell as $U(q) = \frac{k}{2}q^2$. The exact solution to this system of equations can be found easily:

$$q_1(t) = \cos\left(\frac{\omega_1 t}{2}\right)c_1 - \sin\left(\frac{\omega_1 t}{2}\right)c_2 +$$

$$+\cos\left(\frac{\omega_2 t}{2}\right)c_3 - \sin\left(\frac{\omega_2 t}{2}\right)c_4 \tag{34}$$

$$q_2(t) = \frac{M(m_1-m_2)+\eta}{2m_1m_2}\left\{\cos\left(\frac{\omega_1 t}{2}\right)c_1 - \sin\left(\frac{\omega_1 t}{2}\right)c_2\right\} +$$
$$+\frac{M(m_1-m_2)-\eta}{2m_1m_2}\left\{\cos\left(\frac{\omega_2 t}{2}\right)c_3 - \sin\left(\frac{\omega_2 t}{2}\right)c_4\right\} + \tag{35}$$

Where the vibration frequencies are determined by the masses of the internal particles and the shell

$$\omega_1 = \frac{\sqrt{(m_1M + m_2M + 2m_1m_2 + \eta)k}}{\sqrt{m_1m_2M}}$$

$$\omega_2 = \frac{\sqrt{(m_1M + m_2M + 2m_1m_2 - \eta)k}}{\sqrt{m_1m_2M}}$$

$$\eta = \sqrt{M^2m_1^2 - 2M^2m_1m_2 + M^2m_2^2 + 4m_1^2m_2^2}$$

Let's pay attention to the complex dependence of frequencies on the masses of the shell and internal particles. According to relation (6), these frequencies should manifest themselves in the behavior of the shell and, consequently, the structurally complex particle. Thus, it becomes possible to determine the properties of the internal particles and, consequently, its internal structure based on observed particle behavior. Direct observation of the internal structure of such a particle can usually be complicated by both technical reasons and the appearance of additional external influences that alter its behavior.

All other constants are determined by the initial conditions and the masses of the components of the structurally complex particle. Thus, the constants included in solution (34), (35) have the following form.

$$c_1 = q_1(0)\frac{\eta + M(m_2-m_1)}{2\eta} + q_2(0)\frac{m_1m_2}{\eta}$$

$$c_2 = -\dot{q}_1(0)\frac{\eta + M(m_2-m_1)}{2\omega_1\eta} - \dot{q}_2(0)\frac{m_1m_2}{\omega_1\eta}$$

$$c_3 = q_1(0)\frac{\eta + M(m_1-m_2)}{2\eta} - q_2(0)\frac{m_1m_2}{\eta}$$

$$c_4 = -\dot{q}_1(0)\frac{(\eta + M(m_1-m_2))}{\omega_2\eta} + \dot{q}_2(0)\frac{m_1m_2}{\omega_2\eta}$$

The existence of exact solutions makes it possible to directly calculate the energy distribution even among the components of internal degrees of freedom without appealing to virial relations. Moreover, the relations for the energies of individual components cannot be derived from virial relations.

We present the average values of potential and kinetic energies for each internal particle, obtained by directly averaging the corresponding exact quantities over time.

$$\langle U_1\rangle = \frac{1}{2}(c_1^2 + c_2^2 + c_3^2 + c_4^2)$$

$$\langle U_2\rangle = \frac{1}{2(2m_1m_2)^2}((c_1^2 + c_2^2 + c_3^2 + c_4^2)(\eta^2 + M^2(m_1-m_2)^2)+$$
$$+(c_1^2 + c_2^2 - c_3^2 - c_4^2)2M(m_1-m_2)\eta)$$

$$\langle E_1\rangle = (c_1^2 + c_2^2 + c_3^2 + c_4^2)\frac{M(m_1+m_2)+2m_1m_2}{4Mm_2}+$$
$$+(c_1^2 + c_2^2 - c_3^2 - c_4^2)\frac{\eta}{4Mm_2}$$

$$\langle E_2\rangle = \frac{1}{4m_1^2m_2^2M}\left\{(c_1^2 + c_2^2 + c_3^2 + c_4^2)(M^2(M+m_2)(m_1-m_2)+\right.$$
$$+Mm_1m_2^2(3m_1-m_2) + 2m_1^2m_2^3) +$$
$$\left.+ (c_1^2 + c_2^2 - c_3^2 - c_4^2)\eta(M(m_1-m_2)(M+m_2) + m_1m_2^2)\right\}$$

The first two equations allow us to express the initial data $(c_1^2 + c_2^2 + c_3^2 + c_4^2)$ and $(c_1^2 + c_2^2 - c_3^2 - c_4^2)$ the potential energies of the internal particles, and after substituting them into the equations for $E_1$, $E_2$ we obtain

$$\langle E_1 \rangle = \langle U_1 \rangle \frac{1}{2Mm_2} \left( M(m_1 + m_2) + \right.$$
$$\left. + 2m_1 m_2 - \frac{\eta^2 M^2 (m_1 - m_2)^2}{2M(m_1 - m_2)} \right) + \langle U_2 \rangle \frac{8m_1^2 m_2}{4M^2(m_1 - m_2)}$$
$$\langle E_2 \rangle = \langle U_1 \rangle B_1 + \langle U_2 \rangle B_2 \tag{36}$$

Where coefficients $B_1$ and $B_2$ depend on the masses only as

$$B_1 = \frac{(2 + m_2 - m_1)(m_1 - m_2)^2 M^4}{4m_1^2 m_2^2 M^2 (m_1 - m_2)} +$$
$$+ \frac{m_2 (2 + m_2 - m_1)(m_1 - m_2)^2 M^3}{4m_1^2 m_2^2 M^2 (m_1 - m_2)} +$$
$$+ \frac{\left(5m_1^2 m_2^2 - m_2^3 m_1 - \eta^2\right)(m_1 - m_2) M^2}{4m_1^2 m_2^2 M^2 (m_1 - m_2)} +$$
$$+ \frac{\left(4m_1^3 m_2^3 - 4m_1^2 m_2^4 - \eta^2 m_1 m_2 + \eta^2 m_2^2\right) M - m_1 m_2^2 \eta^2}{4m_1^2 m_2^2 M^2 (m_1 - m_2)}$$
$$B_2 = \frac{(m_1 - M) m_2^2 + (m_1 - M) M m_2 + M^2 m_1}{M^2 (m_I - m_2)}$$

When deriving these relations (36) it was assumed that $m_1 \neq m_2$. In the special case of equality of these masses, all relations are significantly simplified. Thus, the kinetic energy of an internal particle is composed of certain fractions of the potential energies of the components. Let us note, that these relations are independent of the initial conditions and, in this sense, are universal. The existence of these relations can be understood by considering the exchange of energies between internal particles through their interaction with the shell. Such relations cannot be derived from virial relations. In fact, this means that the distribution over the degrees of freedom is non-uniform and is determined by the masses of the internal particles.

## 7. DISCUSSION AND CONCLUSIONS

A generalization of the structurally complex particle is proposed for interaction potentials more general than perfectly elastic collisions. It is shown that the structurally complex particle is defined by a restricted problem of bodies of different masses. This system can be described as a system of bodies in certain coordinates. For this system of bodies, a Hamiltonian formalism is formulated, and the resulting first integrals of motion are discussed. The achieved advantage, in addition to reducing the number of variables, is that the system moves in a potential well that is at rest. This circumstance significantly simplifies the numerical solution of such systems,as well as, for the case of a small number of internal degrees of freedom, the search for exact analytical solutions. An analysis of the general properties leads to proof of the absence of equipartition among the degrees of freedom and, consequently, to an anomalous energy distribution among them. Using the virial theorem, it is proven that the energy of the internal degrees of freedom does not exceed a certain fraction of the initial energy, which depends on the ratio of the masses of the internal particles to the mass of the shell. This circumstance allows us to expect unusual energy distributions of such particles in statistical theory. This should be expected given the occurrence of additional integrals of motion and the finite number of particles. An exactly integrable case of a one-dimensional particle with two internal degrees of freedom is considered. The oscillation frequencies of the internal particles are determined by their masses and the mass of the shell. The energy distribution among them is non-uniform. Universal relations for the distribution of the kinetic and potential energies of internal particles are obtained, independent of the choice of initial conditions. These relations provide more detailed information about the energy distribution than virial relations. In the following research, it is planned to consider the effect of increasing the number of internal particles on the behavior of structurally complex particles.

### Acknowledgment

This work was supported by the National Research Foundation of Ukraine, grant number 2025.07/0030.

### ORCID

**Kostyantyn M. Kulyk**, https://orcid.org/0000-0007-0283-0584; **Maryna A. Ratner**, https://orcid.org/0000-0002-7755-017X; **Volodymyr V. Yanovsky**, https://orcid.org/0000-0003-0461-749X

## REFERENCES


[1] V. V. Yanovsky, and A. V. Tur, *Particles with internal degrees of freedom, Problems of Theoretical Physics*, Scientific Works, issue 2, (V. N. Karazin Kharkiv National University, 2016).

[2] D.M. Naplekov, and V.V. Yanovsky, "Distribution of energy in the ideal gas that lacks equipartition," Scientific Reports, **13**, 3427 (2023). https://doi.org/10.1038/s41598-023-30636-6

[3] S.V. Slipushenko, A.V. Tur, and V.V. Yanovsky, "Scattering of particles with internal degrees of freedom," Journal of Experimental and Theoretical Physics, **117**(2), 274-292 (2013). https://doi.org/10.1134/S1063776113080207

[4] Ratner M. A., Tur A. V., and Yanovsky V. V., "Peculiarities of nanoparticle reflection from a barrier," Journal of Computational and Theoretical Nanoscience, **12**, 589-594 (2015). https://doi.org/10.1166/jctn.2015.3771

[5] B. W. Smith, M. Monthioux, and D. E. Luzzi, "Encapsulated C60 in carbon nanotubes," Nature, **396**, 323-324 (1998). https://doi.org/10.1038/24521

[6] M. Monthioux, "Filling single-wall carbon nanotubes," Carbon, **40**(10), 1809-1823 (2002). https://doi.org/10.1016/S0008-6223(02)00102-1

[7] M. Yudasaka, K. Ajima, K. Suenaga, T. Ichihashi, A. Hashimoto, and S. Iijima, "Nano-extraction and nano-condensation for C60 incorporation into single-wall carbon nanotubes in liquid phases," Chemical Phys. Lett. **380**, 42-46 (2003). https://doi.org/10.1016/j.cplett.2003.08.095

[8] S. Rols, J. Cambedouzou, M. Chorro, H. Schober, V. Agafonov, P. Launois, V. Davydov, et al., "How Confinement Affects the Dynamics of C60 in Carbon Nanopeapods," Phys. Rev. Lett. **101**, 065507 (2008). https://doi.org/10.1103/PhysRevLett.101.065507

[9] Gottfried Schill, *Catenanes, rotaxanes and knots*, (Academic Press, 1971).

[10] I. T. Harrison, , and S. Harrison, "Synthesis of a stable complex of a macrocycle and a threaded chain," J. Am. Chem. Soc. **89**(22), 5723-5724 (1967). https://doi.org/10.1021/ja00998a052

[11] T.T. Perkins, D.E. Smith, R.G.Larson, and S.Chu, "Single polymer dynamics in an elongational flow," Science, **286**, 83 (1995). https://doi.org/10.1126/science.276.5321.2016

[12] S.R. Quake, H. Babcock, and S. Chu, "The dynamics of partially extended single molecules of DNA," Nature, **388**(6638), 151-154 (1997). https://doi.org/10.1038/40588

[13] D. Wirtz, "Direct Measurement of the Transport Properties of a Single DNA Molecule," Phys. Rev. Lett. **75**, 2436 (1995). https://doi.org/10.1103/PhysRevLett.75.2436

[14] A. Blumen, "Anomalous diffusion of particles with internal degrees of freedom," Philosophical Magazine Part B, **81**(9), 1021-1031 (2001). http://dx.doi.org/10.1080/13642810108205788

[15] P.E. Rouse, Jr., "A Theory of the Linear Viscoelastic Properties of Dilute Solutions of Coiling Polymers," J. Chem. Phys. **21**, 1272-1280 (1953). https://doi.org/10.1063/1.1699180

[16] P.J. Flory, *Statistical Mechanics of Chain Molecules*, (Interscience, 1969).

[17] M.R. Buche, and M. N. Silberstein, "Chain breaking in the statistical mechanical constitutive theory of polymer networks," Journal of the Mechanics and Physics of Solids, **156**, 104593 (2021). https://doi.org/10.1016/j.jmps.2021.104593

[18] N. Balabaev, and T.Khazanovich, "Extension of chains composed of freely joined elastic segments," Russian Journal of Physical Chemistry B, **3**, 242 (2009).

[19] F. Manca, S. Giordano, P. L. Palla, R. Zucca, F. Cleri, and L. Colombo, "Elasticity of flexible and semiflexible polymers with extensible bonds in the Gibbs and Helmholtz ensembles," The Journal of Chemical Physics, **136**, 154906 (2012). https://doi.org/10.1063/1.4704607

[20] M. Schliwa, and G. Woehlke, "Molecular motors, Nature," **422**, 759-765 (2003). https://doi.org/10.1038/nature01601

[21] H. C. Berg, and R. A. Anderson, "Bacteria swim by rotating their flagellar filaments," Nature, **245**, 380-382 (1973). https://doi.org/10.1038/245380a0

[22] Z. Sadjadi, M. R. Shaebani, H. Rieger, and L. Santen, "Persistent- random- walk approach to anomalous transport of self- propelled particles," Phys. Rev. E, **91**, 062715 (2015). https://doi.org/10.1103/PhysRevE.91.062715

[23] D. Chowdhury, "Stochastic mechano- chemical kinetics of molecular motors: a multidisciplinary enterprise from a physicist's perspective," Phys. Rep. 529, 1-197, (2013). https://doi.org/10.1016/j.physrep.2013.03.005

[24] *Active Matter*, edited by S. Tibbits, (The MIT Press, 2017). https://doi.org/10.7551/mitpress/11236.001.0001

[25] V.I. Arnold, *Mathematical Methods of Classical Mechanics. Graduate Texts in Mathematics*, vol. 60, 2nd ed., (Springer, 1989). https://doi.org/10.1007/978-1-4757-2063-1.

[26] J.R. Taylor, *Title Classical Mechanics*, (University Science Books, 2005).

[27] E.T. Whittaker, *A Treatise on the Analytical Dynamics of Particles and Rigid Bodies*, (Cambridge University Press, 1999).


## ЧАСТИНКИ З ВНУТРІШНІМИ СТУПЕНЯМИ СВОБОДИ


**К.М. Кулик**[1], **М.А. Ратнер**[2], **В.В. Яновський**[1,2]

[1]*Інститут монокристалів, Національна Академія Наук України пр. Науки 60, 61072 Харків, Україна*

[2]*Харківський національний університет імені В.Н. Каразіна майдан Свободи, 4, 61022, Харків, Україна*

Запропоновано узагальнену концепції структурно складної частинки на випадок загальних потенціалів взаємодії між її компонентами. Структурно складна частинка визначається обмеженою задачею N+1 тіл різної маси, яка зводиться до задачі N тіл. На основі лагранжіанського опису формулюється гамільтонів формалізм та обговорюються отримані перші інтеграли руху. Демонструється відсутність рівномірного розподілу між ступенями свободи. Використовуючи теорему віріала, доведено, що енергія внутрішніх ступенів свободи не перевищує певної частки початкової енергії, яка залежить від відношення мас внутрішніх частинок до маси оболонки. Розглянуто точно інтегрований випадок одновимірної частинки з двома внутрішніми ступенями свободи. Частоти коливань такої структурно складної частинки визначаються її масами та масою оболонки. Розподіл енергії по них не є рівномірним. Отримано універсальні співвідношення для розподілу кінетичної та потенційної енергій внутрішніх частинок, які не залежать від вибору початкових умов. Ці співвідношення надають детальнішу інформацію про розподіл енергії, ніж віріальні співвідношення.

**Ключові слова:** *структурно складна частинка; внутрішні ступені свободи; рівняння руху; віріальні співвідношення*

East European Journal of Physics. 3. 239–250 (2026)
DOI: 10.26565/2312-4334-2026-3-19 ISSN 2312-4334

# EMERGENCE OF NEGATIVE DISPERSION OF ELECTROMAGNETIC WAVES IN A SOLID-STATE STRUCTURE CONTAINING A PLASMA-LIKE MEDIUM AND PLASMONIC METASURFACES

**Yu.O. Averkov***, **O.Yu. Averkov**, **N.N. Beletskii**
*O. Ya. Usikov Institute for Radiophysics and Electronics of the National Academy of Sciences of Ukraine, 12, Acad. Proskura Str., Kharkiv, 61085, Ukraine*
**Corresponding Author e-mail: yuriyaverkov@gmail.com*
Received May 12, 2026; revised August 21, 2026; accepted August 26, 2026

This study provides a detailed theoretical and numerical account of the dispersion properties of *p*-polarized electromagnetic waves in a complex multilayered solid-state structure. The system under investigation is a six-layer stack featuring two isotropic plasmonic metasurfaces, separated by dielectric spacers and supported by a semi-infinite plasma-like substrate—either a heavily doped semiconductor or a metal. By combining the transfer-matrix formalism with Maxwell's equations and rigorous boundary conditions, we derive exact dispersion relations for both surface and bulk-surface eigenmodes. Our numerical results point to a cascaded hybridization process between the fundamental metasurface resonances and the surface plasmon-polariton (SPP) modes inherent to the substrate. A particularly significant finding is that adjusting the effective oscillator strengths of the metasurfaces triggers a pronounced dispersion asymmetry. This occurs when one metasurface exhibits a capacitive response while the other becomes effectively inductive. Such an electrodynamic imbalance leads to an anomalous negative frequency dispersion regime characterized by the propagation of backward waves. Furthermore, we demonstrate that modifying the dielectric environment or swapping the semiconductor substrate for a metallic one shifts the regions of resonant interaction, offering a versatile means of controlling the spectral intervals of mode splitting. These findings establish a solid theoretical groundwork for the design of tunable nanophotonic devices and the generation of distributed internal feedback, which is essential for the emergence of absolute electromagnetic wave instabilities in beam-coupled systems.

**Keywords:** *Plasmonic metasurface; Hybrid surface wave; Bulk-surface wave; Negative dispersion; Semiconductor substrate; Mode hybridization*

## 1. INTRODUCTION

The progress of modern nanophotonics and optoelectronics is largely driven by the search for new ways to manipulate electromagnetic waves at subwavelength scales. In this context, two-dimensional metamaterials—widely known as metasurfaces—have emerged as a focal point of research due to their ability to exhibit electrodynamic properties far beyond those of naturally occurring media [1]. Among these, plasmonic metasurfaces are of particular interest. They offer a versatile toolkit for wave tailoring, supporting extreme field localization, selective routing of surface modes, and fine-tuning of the local density of states. Extensive studies have already uncovered a range of anomalous phenomena linked to their frequency dispersion. It is now a well-recognized fact that these architectures can host tightly confined hybrid electromagnetic states. Typically, the resulting eigenspectrum splits into branches representing hybrid transverse electric (TE) and transverse magnetic (TM) waves [2, 3]. Furthermore, such systems can trigger optical topological transitions, where the isofrequency contours undergo a dynamic transformation from closed ellipses to open hyperbolic curves as the frequency shifts [4]. Accurately modeling these effects requires a precise determination of the effective surface conductivity, often done by merging near-field and far-field characterization methods [5]. A promising direction lies in integrating anisotropic metasurfaces with natural 2D materials like graphene or black phosphorus, or embedding them into multilayered solid-state stacks. For instance, doped 2D layers can support highly directional hyperbolic plasmons, which are easily tuned via electrical gating [6]. It is also worth noting that strong field confinement often arises at the physical boundaries of these anisotropic structures [7]. When multiple metasurfaces are stacked, the interaction between their eigenmodes becomes quite complex. Some theoretical models even compare these coupled modes to Feynman paths in electron transport theory [8]. To evaluate such layered systems, the transfer-matrix formalism remains one of the most reliable and direct analytical tools [9].

Recent research has significantly broadened the known spectrum of guided states. Notable examples include analytical models for anisotropic polarizabilities at arbitrary incidence [10], self-collimated surface-wave steering through equifrequency contour design [11], and the discovery of hybrid waves in twisted metasurfaces [12]. Simultaneously, work on hyperbolic shear metasurfaces [13] and antihyperbolic surface states [14] has opened new routes for controlling mode topology and axial dispersion. Other studies have demonstrated that even isotropic metasurfaces can produce a scattering-free plasmonic Brewster effect for *p*-polarized waves across a wide range of angles [15]. The strong anisotropy and tunability of these platforms allow for a variety of specialized effects, from near-perfect photon spin selectivity [16] and chiral sensing [17] to quantum-nanophotonic effects in hyperbolic media [18]. Furthermore, the high confinement

***Cite as:*** Yu.O. Averkov, O.Yu. Averkov, N.N. Beletskii, East Eur. J. Phys. 3, 239 (2026), https://doi.org/10.26565/2312-4334-2026-3-19

of surface plasmons enables these systems to exert significant transverse optical forces on nearby nanoparticles [19] or to facilitate directional radiative heat transfer [20]. Practical applications also extend to multiband polarization converters [21], multifunctional polaritonic structures [22], and Babinet-invertible metasurfaces enabling transmission-reflection and helicity switching [23, 24]. However, despite these advances, there is still a lack of comprehensive electrodynamic models for certain asymmetric hybrid architectures. A prime example is a structure where a dielectric layer is placed between a plasmonic metasurface and a semi-infinite plasma-like substrate (such as a metal or semiconductor).

In this paper, we conduct a rigorous theoretical and numerical study of the dispersion properties in such a configuration. Our goal is to identify the conditions for strong wave localization and to analyze the frequency splitting of coupled surface modes in solid-state structures incorporating isotropic plasmonic metasurfaces.

## 2. PROBLEM STATEMENT

### 2.1. Main equations and boundary conditions

The physical system under investigation represents a planar, multi-layered solid-state structure. The uppermost region consists of a semi-infinite dielectric superstrate characterized by a permittivity $\varepsilon_1$, which bounds the primary plasmonic metasurface. A dielectric spacer of thickness $d_1$ and permittivity $\varepsilon_2$ separates this top conductive sheet from a secondary plasmonic metasurface. Beneath this lower structured interface lies another dielectric layer, having a thickness $d_2$ and permittivity $\varepsilon_3$, which bridges the gap to a semi-infinite plasma-like bulk substrate, typically realized as a highly doped semiconductor or a metal. We orient the $z$-axis normal to the layer interfaces, defining its positive direction to point into the

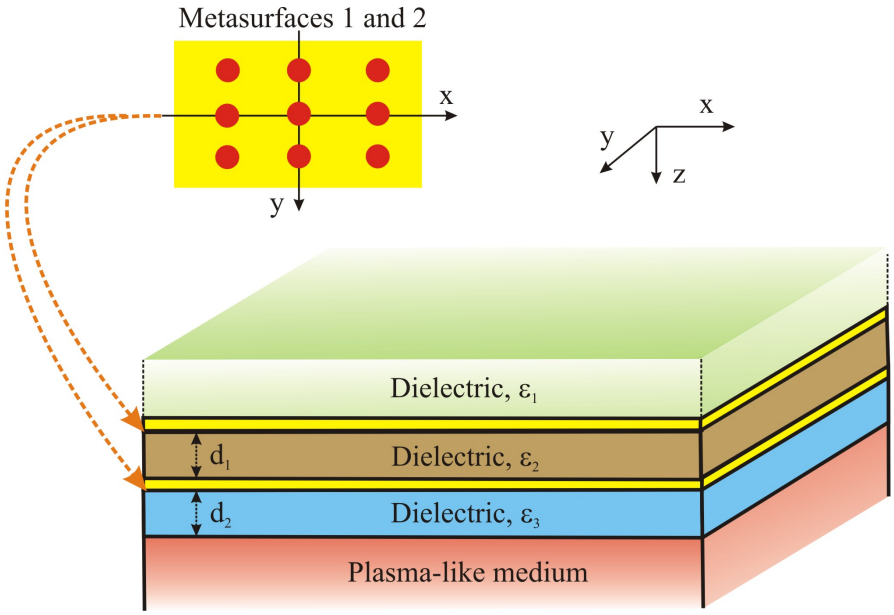


**Figure 1.** Geometry of the structure.

depth of the plasma-like medium (see Fig. 1). The top metasurface is located precisely at the $z = 0$ plane, while the bottom metasurface is positioned at $z = d_1$. From a physical standpoint, such metasurfaces are typically fabricated as periodic lattices of highly conducting, ultra-thin elements—such as metallic strips or disks. Given that both the thickness of these inclusions and the array periodicity are vastly smaller than the operational wavelength, out-of-plane spatial dispersion becomes entirely negligible. This scale separation permits us to model the electrodynamic behavior of both structured interfaces using macroscopic, isotropic effective surface conductivities, denoted here as $\sigma_1$ and $\sigma_2$.

The overall field dynamics within this multi-layered geometry are rigorously governed by Maxwell's equations:

$$\nabla \times \mathbf{H}(\mathbf{r}, t) = \frac{1}{c}\frac{\partial \mathbf{D}(\mathbf{r}, t)}{\partial t} + \frac{4\pi}{c}\mathbf{j}(\mathbf{r}, t), \tag{1}$$

$$\nabla \times \mathbf{E}(\mathbf{r}, t) = -\frac{1}{c}\frac{\partial \mathbf{B}(\mathbf{r}, t)}{\partial t}, \tag{2}$$

$$\nabla \cdot \mathbf{D}(\mathbf{r}, t) = 0, \tag{3}$$

$$\nabla \cdot \mathbf{B}(\mathbf{r}, t) = 0. \tag{4}$$

In these expressions, $c$ represents the vacuum speed of light. The variables $\mathbf{E}(\mathbf{r}, t)$, $\mathbf{H}(\mathbf{r}, t)$, and $\mathbf{B}(\mathbf{r}, t)$ correspond to the electric field, magnetic field, and magnetic induction vectors, respectively. Because all constituent layers are assumed to be non-magnetic ($\mu = 1$), the magnetic induction and magnetic fields are strictly equivalent in the Gaussian system, yielding $\mathbf{B}(\mathbf{r}, t) = \mathbf{H}(\mathbf{r}, t)$. The vector $\mathbf{D}(\mathbf{r}, t)$ defines the electric displacement. Additionally, the complete current density within

the system is purely planar, taking the form $\mathbf{j}(\mathbf{r},t) = (\mathbf{j}_\tau(\mathbf{r},t), 0)$. This transverse current distribution is mathematically pinned to the patterned interfaces using the Dirac delta function, $\delta(z)$, and can be expanded as $\mathbf{j}_\tau(\mathbf{r},t) = \mathbf{j}_{\tau 1}(\boldsymbol{\rho},t)\delta(z) + \mathbf{j}_{\tau 2}(\boldsymbol{\rho},t)\delta(z-d_1)$, with $\boldsymbol{\rho} = (x,y,0)$ acting as the in-plane position vector.

To analyze the system, we decompose the electromagnetic fields into Fourier integrals of the form [25]:

$$\mathbf{E}(\mathbf{r},t) = \int_{-\infty}^{\infty}\int_{-\infty}^{\infty} \mathbf{E}(\boldsymbol{k},\omega)\exp\left[i(k_z z + \boldsymbol{\kappa}\boldsymbol{\rho} - \omega t)\right] d\boldsymbol{k}\, d\omega, \tag{5}$$

where $\omega$ stands for the angular frequency, and the total wave vector is defined as $\boldsymbol{k} = (\boldsymbol{\kappa}, k_z)$. Its in-plane transverse component is denoted by $\boldsymbol{\kappa} = (k_x, k_y, 0)$, while $k_z$ represents the normal wave number.

Furthermore, the macroscopic constitutive relations coupling the electric displacement to the electric field inherently take a non-local form:

$$D_j(\mathbf{r},t) = \int_{-\infty}^{t} \hat{\varepsilon}_{jg}(t-t')E_g(\mathbf{r},t')dt', \tag{6}$$

where the subscripts $j$ and $g$ designate the Cartesian coordinates ($x$, $y$, $z$), with summation implicitly applied over the index $g$. The integral kernel $\hat{\varepsilon}_{jg}(t-t')$ serves as the time-domain dielectric response tensor, reflecting the assumption that the electrodynamic properties of the medium are temporally homogeneous. Upon transforming to the frequency domain, this convolution reduces to a straightforward algebraic relation:

$$D_j(\boldsymbol{k},\omega) = \varepsilon_{jg}(\omega)E_g(\boldsymbol{k},\omega). \tag{7}$$

In this formulation, the frequency-domain dielectric tensor $\varepsilon_{jg}(\omega)$ is obtained directly through the Fourier transform of the temporal response kernel:

$$\varepsilon_{jg}(\omega) = \int_0^{\infty} \hat{\varepsilon}_{jg}(\tau)\exp(i\omega\tau)d\tau. \tag{8}$$

Inside the purely dielectric regions ($z < 0$, $0 < z < d_1$, and $d_1 < z < d_1 + d_2$), the material response is essentially instantaneous, which is mathematically expressed as $\hat{\varepsilon}_{ij}(\tau) = \varepsilon_m\delta_{ij}\delta(\tau)$. Here, the scalar constant $\varepsilon_m \in \{\varepsilon_1, \varepsilon_2, \varepsilon_3\}$ is assigned according to the specific layer. As a result, the spectral electric displacement reduces to a simple proportionality: $\mathbf{D}_m(\boldsymbol{k},\omega) = \varepsilon_m\mathbf{E}(\boldsymbol{k},\omega)$. In contrast, the plasma-like substrate occupying $z > d_1 + d_2$ exhibits strong temporal dispersion, leading to the relation $\mathbf{D}_4(\boldsymbol{k},\omega) = \varepsilon_4(\omega)\mathbf{E}(\boldsymbol{k},\omega)$, where

$$\varepsilon_4(\omega) = \varepsilon_0 - \frac{\omega_p^2}{\omega(\omega + i\nu)}. \tag{9}$$

In this formulation, $\varepsilon_0$ represents the high-frequency background permittivity, $\omega_p$ designates the collective plasma frequency of the free charge carriers, and $\nu$ dictates the effective collision rate responsible for intrinsic dissipative losses.

Furthermore, the macroscopic surface currents induced on the patterned interfaces are expressed as:

$$\mathbf{j}_{\tau l}(\boldsymbol{\rho},t) = \int_{-\infty}^{\infty}\int_{-\infty}^{\infty} \mathbf{j}_{\tau l}(\boldsymbol{\kappa},\omega)\exp\left[i(\boldsymbol{\kappa}\boldsymbol{\rho} - \omega t)\right] d\boldsymbol{\kappa}\, d\omega, \tag{10}$$

where $l \in \{1,2\}$ indexes the metasurfaces. In the frequency domain, we use:

$$\mathbf{j}_{\tau l}(\boldsymbol{\kappa},\omega) = \sigma_l(\omega)\,\mathbf{E}_\tau(\boldsymbol{\kappa},\omega). \tag{11}$$

Here, the term $\sigma_l(\omega)$ represents the frequency-domain effective surface conductivity of the $l$-th metasurface, which is mathematically modeled as:

$$\sigma_l(\omega) = \frac{c}{4\pi}\left(\sigma_{\infty l} + \frac{iA_l\omega}{\omega^2 - \Omega_l^2 + i\gamma_l\omega}\right). \tag{12}$$

Here, $\sigma_{\infty l}$ represents the background conductivity arising from deep electronic band transitions ($\mathrm{Re}\,\sigma_{\infty l} = 0$). The amplitude coefficient $A_l$ is determined by the particular subwavelength geometry of the $l$-th metasurface ($\mathrm{Im}\,A_l = 0$). Additionally, $\Omega_l$ denotes the fundamental resonance frequency of the structured layer, while $\gamma_l$ accounts for the resonance broadening caused by ohmic dissipation and radiation scattering. To focus strictly on the underlying dispersion topology, we hereafter neglect all dissipative mechanisms within both the patterned interfaces and the plasma-like substrate, explicitly setting $\gamma_1 = \gamma_2 = 0$ and $\nu = 0$.

To rigorously extract the dispersion characteristics, we enforce the standard electromagnetic boundary matching at the three primary interfaces ($z = 0$, $z = d_1$, and $z = d_1 + d_2$). At the metasurface planes located at $z = 0$ and $z = d_1$,

the tangential electric field remains strictly continuous. In contrast, the tangential magnetic field undergoes a discrete discontinuity driven by the localized surface currents:

$$\mathbf{n} \times \Big( \mathbf{E}_{m+1}(\mathbf{r}, t) - \mathbf{E}_m(\mathbf{r}, t) \Big) = 0, \tag{13}$$

$$\mathbf{n} \times \Big( \mathbf{H}_{m+1}(\mathbf{r}, t) - \mathbf{H}_m(\mathbf{r}, t) \Big) = \frac{4\pi}{c} \mathbf{j}_{\tau l}(\boldsymbol{\rho}, t). \tag{14}$$

In this notation, $\mathbf{n} = (0, 0, 1)$ represents the unit normal vector pointing from the $m$-th medium into the $(m+1)$-th medium, where the index $m \in \{1, 2\}$ specifies the dielectric domains immediately bounding the $l$-th metasurface. Furthermore, since the boundary separating the bottom dielectric spacer and the plasma-like substrate (located at $z = d_1 + d_2$) lacks any conducting inclusions, it cannot support free surface currents. Consequently, both the tangential electric and magnetic field components transition continuously across this final interface:

$$\mathbf{n} \times \Big( \mathbf{E}_4(\mathbf{r}, t) - \mathbf{E}_3(\mathbf{r}, t) \Big) = 0, \quad \mathbf{n} \times \Big( \mathbf{H}_4(\mathbf{r}, t) - \mathbf{H}_3(\mathbf{r}, t) \Big) = 0. \tag{15}$$

### 2.2. Dispersion relations of structure eigenwaves

To derive the dispersion relations for the $p$-polarized (transverse magnetic) eigenmodes supported by the proposed structure, we first specify the relevant electromagnetic field vectors. Under this polarization scheme, the fields exhibit the non-vanishing components $\mathbf{E}(\boldsymbol{r}, t) = (E_x(\boldsymbol{r}, t), 0, E_z(\boldsymbol{r}, t))$ and $\mathbf{H}(\boldsymbol{r}, t) = (0, H_y(\boldsymbol{r}, t), 0)$. Assuming unidirectional wave propagation strictly along the $x$-axis, the associated wave vector simplifies to $\boldsymbol{k} = (k_x, 0, k_z)$.

Applying this specific spatial field configuration requires us to adapt the general macroscopic boundary conditions across all structural interfaces. Specifically, evaluating these matching conditions at the plane containing the top metasurface ($z = 0$) yields:

$$E_{x2}(x, t)\Big|_{z=0} = E_{x1}(x, t)\Big|_{z=0}, \tag{16}$$

$$H_{y2}(x, t)\Big|_{z=0} - H_{y1}(x, t)\Big|_{z=0} = -\frac{4\pi}{c} j_{\tau 1,x}(\boldsymbol{\rho}, t)\Big|_{z=0}. \tag{17}$$

At the plane of the second metasurface ($z = d_1$):

$$E_{x3}(x, t)\Big|_{z=d_1} = E_{x2}(x, t)\Big|_{z=d_1}, \tag{18}$$

$$H_{y3}(x, t)\Big|_{z=d_1} - H_{y2}(x, t)\Big|_{z=d_1} = -\frac{4\pi}{c} j_{\tau 2,x}(\boldsymbol{\rho}, t)\Big|_{z=d_1}. \tag{19}$$

At the interface between dielectric 3 and the plasma-like medium ($z = d_1 + d_2$):

$$E_{x4}(x, t)\Big|_{z=d_1+d_2} = E_{x3}(x, t)\Big|_{z=d_1+d_2}, \tag{20}$$

$$H_{y4}(x, t)\Big|_{z=d_1+d_2} = H_{y3}(x, t)\Big|_{z=d_1+d_2}. \tag{21}$$

We first deduce the dispersion relation specific to the *surface eigenwaves* of the structure. Moving forward, the relevant spatial and frequency parameters are expressed in dimensionless form, normalized with respect to the fundamental resonant frequency of the first metasurface, $\Omega_1$:

$$\xi = \frac{\omega}{\Omega_1}, \; q = \frac{c k_x}{\Omega_1}, \; \delta_1 = \frac{d_1 \Omega_1}{c}, \; \delta_2 = \frac{d_2 \Omega_1}{c}. \tag{22}$$

The dimensionless transverse decay constants in the corresponding layers are defined as:

$$\eta_m = i \frac{c k_{zm}}{\Omega_1} = \sqrt{q^2 - \xi^2 \varepsilon_m} \quad (m = 1, 2, 3), \; \eta_4 = i \frac{c k_{z4}}{\Omega_1} = \sqrt{q^2 - \xi^2 \varepsilon_4(\xi)}. \tag{23}$$

The remaining normalized physical parameters of the materials are given by:

$$\bar{\omega}_p = \frac{\omega_p}{\Omega_1}, \; \xi_2 = \frac{\Omega_2}{\Omega_1}, \; \bar{A}_l = \frac{A_l}{\Omega_1}, \; \bar{\sigma}_{\infty l} = -\frac{4\pi i}{c} \sigma_{\infty l}, \tag{24}$$

where the index $l \in \{1, 2\}$ refers to the first and second metasurface, respectively.

In terms of these newly defined variables, the Fourier-transformed permittivity of the plasma-like medium and the effective surface conductivities reduce to the following expressions:

$$\varepsilon_4(\xi) = \varepsilon_0 - \frac{\bar{\omega}_p^2}{\xi^2},\ \bar{\sigma}_1(\xi) = -\frac{4\pi i}{c}\sigma_1(\omega) = \bar{\sigma}_{\infty 1} + \frac{\bar{A}_1\xi}{\xi^2 - 1}, \tag{25}$$

$$\bar{\sigma}_2(\xi) = -\frac{4\pi i}{c}\sigma_2(\omega) = \bar{\sigma}_{\infty 2} + \frac{\bar{A}_2\xi}{\xi^2 - \xi_2^2}. \tag{26}$$

By substituting the integral representations of the fields (5) and the surface currents (10) into the boundary conditions (16)–(21), we arrive at the dispersion relation governing the *surface eigenwaves*:

$$a_1\left[\frac{b_3}{b_1} - \frac{b_4}{b_2}\exp(-2\eta_2\delta_1)\right]\exp(-2\eta_3\delta_2) + a_2\left[\frac{b_6}{b_1} - \frac{b_5}{b_2}\exp(-2\eta_2\delta_1)\right] = 0, \tag{27}$$

where

$$a_1 = \frac{\varepsilon_4}{\eta_4} - \frac{\varepsilon_3}{\eta_3},\ a_2 = \frac{\varepsilon_4}{\eta_4} + \frac{\varepsilon_3}{\eta_3}, \tag{28}$$

$$b_1 = \left(\frac{\varepsilon_1}{\eta_1} - \frac{\varepsilon_2}{\eta_2}\right)\xi - \bar{\sigma}_1(\xi),\ b_2 = \left(\frac{\varepsilon_1}{\eta_1} + \frac{\varepsilon_2}{\eta_2}\right)\xi - \bar{\sigma}_1(\xi),\ b_3 = \left(\frac{\varepsilon_3}{\eta_3} - \frac{\varepsilon_2}{\eta_2}\right)\xi + \bar{\sigma}_2(\xi), \tag{29}$$

$$b_4 = \left(\frac{\varepsilon_3}{\eta_3} + \frac{\varepsilon_2}{\eta_2}\right)\xi + \bar{\sigma}_2(\xi),\ b_5 = \left(\frac{\varepsilon_3}{\eta_3} - \frac{\varepsilon_2}{\eta_2}\right)\xi - \bar{\sigma}_2(\xi),\ b_6 = \left(\frac{\varepsilon_3}{\eta_3} + \frac{\varepsilon_2}{\eta_2}\right)\xi - \bar{\sigma}_2(\xi). \tag{30}$$

As the thickness $\delta_2$ tends toward infinity, the composite dispersion relation (27) decouples into two independent equations. These specifically describe the eigenmodes of the dielectric 3–plasma-like interface and the isolated five-layer metasurface structure (dielectric 1–metasurface 1–dielectric 2–metasurface 2–dielectric 3), respectively:

$$\frac{\varepsilon_4}{\eta_4} + \frac{\varepsilon_3}{\eta_3} = 0,\ \frac{b_6}{b_1} - \frac{b_5}{b_2}\exp(-2\eta_2\delta_1) = 0. \tag{31}$$

Next, we focus on the *bulk-surface eigenwaves*, which are characterized by fields that exhibit exponential decay (evanescence) within the top dielectric and the semiconductor substrate, while maintaining an oscillatory profile inside the internal dielectric spacers 2 and 3. This specific waveguiding regime is supported when the following phase-matching conditions are satisfied: $q^2 > \xi^2\varepsilon_1$, $q^2 > \xi^2\varepsilon_4(\xi)$, $q^2 < \xi^2\varepsilon_2$, and $q^2 < \xi^2\varepsilon_3$. We will use the following notation for the normal components of the wave vector in dielectrics 2 and 3:

$$\zeta_2 = \sqrt{\xi^2\varepsilon_2 - q^2},\quad \zeta_3 = \sqrt{\xi^2\varepsilon_3 - q^2}. \tag{32}$$

The dispersion relation governing the bulk-surface waves is derived from Eq. (27) by enforcing an oscillatory field profile within the internal dielectric spacers (layers 2 and 3). This transition is mathematically handled by substituting the transverse decay constants with their purely imaginary counterparts, $\eta_2 = -i\zeta_2$ and $\eta_3 = -i\zeta_3$. By subsequently invoking Euler's identities to recast the complex exponentials into a trigonometric form, we arrive at the following expression:

$$\begin{aligned}&\cos(\varphi_1)\left\{\xi\left(\frac{\varepsilon_3}{\zeta_3} - \frac{\varepsilon_2}{\zeta_2}\right)\left[\xi\left(\frac{\varepsilon_2}{\zeta_2}\Delta_1 - \frac{\varepsilon_1}{\eta_1}\Delta_2\right) + \bar{\sigma}_1(\xi)\Delta_2\right] - \bar{\sigma}_2(\xi)\left[\xi\left(\frac{\varepsilon_1}{\eta_1}\Delta_1 + \frac{\varepsilon_2}{\zeta_2}\Delta_2\right) - \bar{\sigma}_1(\xi)\Delta_1\right]\right\}\\ &+\cos(\varphi_2)\left\{\xi\left(\frac{\varepsilon_3}{\zeta_3} + \frac{\varepsilon_2}{\zeta_2}\right)\left[\xi\left(\frac{\varepsilon_1}{\eta_1}\Delta_3 + \frac{\varepsilon_2}{\zeta_2}\Delta_4\right) - \bar{\sigma}_1(\xi)\Delta_3\right] + \bar{\sigma}_2(\xi)\left[\xi\left(\frac{\varepsilon_1}{\eta_1}\Delta_4 - \frac{\varepsilon_2}{\zeta_2}\Delta_3\right) - \bar{\sigma}_1(\xi)\Delta_4\right]\right\} = 0,\end{aligned} \tag{33}$$

where

$$\Delta_1 = \frac{\varepsilon_4}{\eta_4} - \frac{\varepsilon_3}{\zeta_3}\tan(\varphi_1),\ \Delta_2 = \frac{\varepsilon_3}{\zeta_3} + \frac{\varepsilon_4}{\eta_4}\tan(\varphi_1),\ \Delta_3 = \frac{\varepsilon_3}{\zeta_3} - \frac{\varepsilon_4}{\eta_4}\tan(\varphi_2),\ \Delta_4 = \frac{\varepsilon_4}{\eta_4} + \frac{\varepsilon_3}{\zeta_3}\tan(\varphi_2), \tag{34}$$

$$\varphi_1 = \zeta_2\delta_1 - \zeta_3\delta_2,\ \varphi_2 = \zeta_2\delta_1 + \zeta_3\delta_2. \tag{35}$$

We also examine a specific class of *bulk-surface eigenwaves* characterized by evanescent field profiles in the vacuum cladding, the first dielectric spacer, and the plasma-like substrate, while sustaining an oscillatory behavior strictly within the third dielectric layer. These modes are supported when the in-plane wave number $q$ satisfies the phase-matching inequalities $q^2 > \xi^2\varepsilon_1$, $q^2 > \xi^2\varepsilon_2$, and $q^2 > \xi^2\varepsilon_4(\xi)$, but remains below the light line of the silica layer ($q^2 < \xi^2\varepsilon_3$). Under these conditions, the governing dispersion equation takes the following form:

$$g\frac{\varepsilon_4}{\eta_4} - f\frac{\varepsilon_3}{\zeta_3} + \left(g\frac{\varepsilon_3}{\zeta_3} + f\frac{\varepsilon_4}{\eta_4}\right)\tan(\zeta_3\delta_2) = 0, \tag{36}$$

where

$$f = -\xi\frac{\varepsilon_2}{\eta_2}\left[\frac{1}{b_1}+\frac{1}{b_2}\exp(-2\eta_2\delta_1)\right]+\bar{\sigma}_2(\xi)\left[\frac{1}{b_1}-\frac{1}{b_2}\exp(-2\eta_2\delta_1)\right], \tag{37}$$

$$g = \xi\frac{\varepsilon_3}{\zeta_3}\left[\frac{1}{b_1}-\frac{1}{b_2}\exp(-2\eta_2\delta_1)\right]. \tag{38}$$

## 3. NUMERICAL ANALYSIS OF DISPERSION RELATIONS

To numerically evaluate the dispersion profiles, we adopt the following material parameters: vacuum for the top layer ($\varepsilon_1 = 1$), Teflon for the first spacer ($\varepsilon_2 = 2.1$), fused silica for the second spacer ($\varepsilon_3 = 3.7$), and an InSb semiconductor substrate ($\varepsilon_0 = 15.68$). The normalized geometric and metasurface parameters are fixed at $\bar{\sigma}_{\infty 1} = \bar{\sigma}_{\infty 2} = 0.2$, $\bar{A}_1 = \bar{A}_2 = 0.2$, $\delta_1 = 0.3$, $\delta_2 = 0.15$, and $\xi_2 = 1.3$. In the subsequent analysis, only the dimensionless plasma frequency $\bar{\omega}_p$ and the oscillator strengths $\bar{A}_l$ will be treated as variable quantities.

Our numerical analysis relies on a fundamental physical concept: pronounced branch repulsion—typically referred to as an avoided crossing—emerges whenever the eigenfrequencies of initially non-degenerate modes approach one another. The proposed six-layer structure inherently supports three distinct resonant states: the fundamental resonance of the top metasurface ($\xi_1 = 1$), the resonance of the bottom metasurface ($\xi_2$), and the surface plasmon-polariton (SPP) supported by the boundary between the semiconductor substrate and the adjacent silica spacer. This SPP resonance is governed by the standard matching condition $\varepsilon_4 + \varepsilon_3 = 0$.

We aim to track how the overall mode spectrum reorganizes as the normalized SPP frequency, defined as $\xi_{sp} = \bar{\omega}_p/\sqrt{\varepsilon_0+\varepsilon_3}$, is systematically swept across the metasurface resonances, specifically moving from a sub-resonant regime ($\xi_{sp} < \xi_1$) to a supra-resonant one ($\xi_{sp} > \xi_2$, assuming $\xi_2 > \xi_1$).

We start by examining a scenario where the SPP frequency resides well below the resonant frequencies of both structured layers, meaning $\xi_{sp} < \xi_1 < \xi_2$. The resulting eigenspectrum under these conditions is plotted in Fig. 2, calculated for $\bar{\omega}_p = 3.5$ and identical oscillator strengths $\bar{A}_1 = \bar{A}_2 = 0.2$.

To ensure consistency across all spectra of electromagnetic waves (Figs. 2, 4–8), we use a unified labeling scheme. The straight lines denoted by 1, 2, and 3 are the light lines corresponding to the vacuum, Teflon, and silica regions, respectively. Curve 4 marks the transition boundary where the transverse decay constant inside the semiconductor vanishes ($\eta_4 = 0$). The horizontal lines 5 and 6 specify the isolated resonant frequencies of the upper ($\xi_1 = 1$) and lower ($\xi_2 = 1.3$) metasurfaces, while line 7 tracks the SPP frequency $\xi_{sp}$. Furthermore, the lower-frequency and upper-frequency dispersion branches originating from the metasurfaces are identified as curves 8, 9 and 11, 12. Finally, curve 10 specifically maps the electromagnetic state that remains largely confined to the semiconductor interface. In Fig. 9, lines 1–3 have the same meaning as in the preceding figures; line 4 corresponds to $\xi_1 = 1$, line 5 to $\xi_2 = 1.3$, and line 6 to $\xi_{sp}$. Curves 7, 8 and 10, 11 represent, respectively, the low-frequency and high-frequency branches of electromagnetic waves predominantly localized near the metasurfaces, whereas curve 9 represents an electromagnetic wave predominantly localized near the plasma-like medium.

As illustrated in Fig. 2, the dispersion branches representing the low-frequency ($\xi < 1$) modes largely confined to the two metasurfaces (curves 8 and 9) exhibit a clear avoided crossing within region B. This repulsion signifies a strong

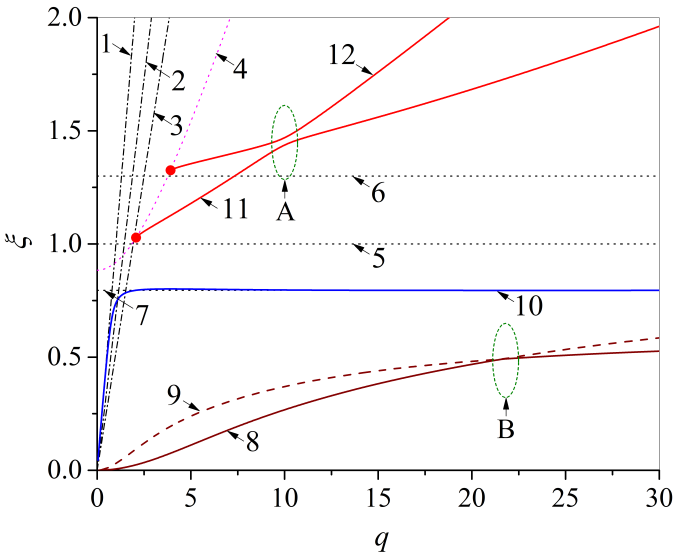


**Figure 2.** Dispersion spectrum of electromagnetic waves in the analyzed solid-state structure when $\xi_{sp} < \xi_1 < \xi_2$ (with $\bar{\omega}_p = 3.5$). The highlighted areas A and B demonstrate the pronounced resonant coupling between the underlying non-degenerate modes.

resonant coupling between the initially non-degenerate states. The higher-frequency ($\xi > 1$) metasurface modes undergo a comparable hybridization process. Specifically, in region A, dispersion curves 11 and 12—which correspond to the electromagnetic states governed by the upper and lower metasurfaces—mutually repel and diverge. Because we have set $\xi_{sp} < \xi_1 = 1$, the branch principally confined to the semiconductor substrate (curve 10) remains entirely uncoupled from the upper-frequency metasurface branches. Instead, the primary energy exchange in this high-frequency domain occurs exclusively between the two metasurfaces themselves, driving the pronounced splitting observed in region A. Notably, both curves 11 and 12 originate from the boundary defined by curve 4. At wave numbers below this threshold, the electromagnetic fields inside the semiconductor adopt an oscillatory character, precluding the existence of purely bound surface wave solutions. Furthermore, as curve 10 crosses the relevant light lines, its physical nature transitions. The segment bounded by spectral lines 1 and 2 captures a bulk-surface wave governed by Eq. (33), whereas the section between light lines 2 and 3 maps to a distinct bulk-surface state accurately described by Eq. (36).

We now turn our attention to the specific shape of curve 10 from Fig. 2 and its dependence on the structural oscillator strengths, $\bar{A}_1$ and $\bar{A}_2$. To isolate this effect, Fig. 3 plots the dispersion profile of the semiconductor-confined mode under the exact same background parameters, leaving only the conductivity amplitudes $\bar{A}_1$ and $\bar{A}_2$ as variable quantities.

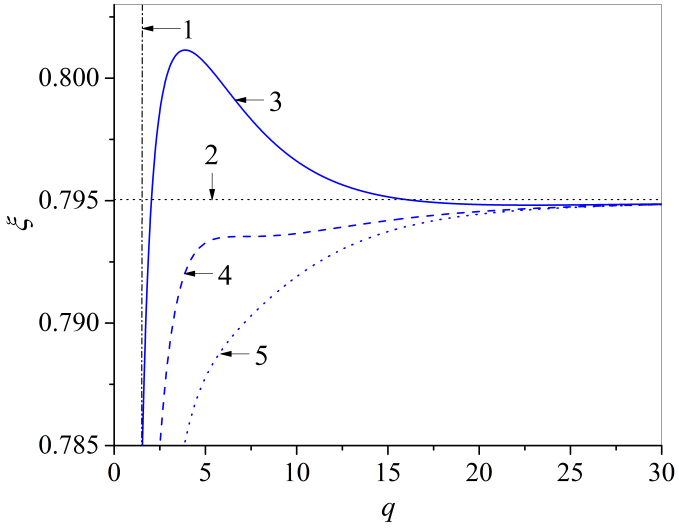


**Figure 3.** Dispersion spectrum of the electromagnetic mode confined near the plasma-like substrate. The structural parameters match those in Fig. 2, evaluated for oscillator strengths $\bar{A}_1 = \bar{A}_2 = 0.2$ (curve 3), $\bar{A}_1 = \bar{A}_2 = 0.4$ (curve 4), and $\bar{A}_1 = \bar{A}_2 = 0.6$ (curve 5). Line 1 denotes the light line in the third dielectric layer, while line 2 indicates the surface plasmon-polariton (SPP) resonance at $\xi_{sp} \approx 0.8$.

As depicted in Fig. 3, setting the oscillator strengths to $\bar{A}_1 = \bar{A}_2 = 0.2$ induces a distinct anomalous segment characterized by negative dispersion on the branch associated with the semiconductor-confined mode. Within this specific frequency band, the electrodynamic parameters satisfy the following criteria: $\varepsilon_4 < 0$, $\bar{\sigma}_1(\xi) = -4\pi i\sigma_1(\xi)/c < 0$, and $\bar{\sigma}_2(\xi) = -4\pi i\sigma_2(\xi)/c > 0$. Conversely, increasing these oscillator strengths to $\bar{A}_1 = \bar{A}_2 = 0.4$ (curve 4) or $\bar{A}_1 = \bar{A}_2 = 0.6$ (curve 5) completely eliminates the backward-wave behavior. Under these higher-strength conditions, the system enters a regime where both patterned layers share an identical reactive nature, meaning that $\varepsilon_4 < 0$, $\bar{\sigma}_1(\xi) = -4\pi i\sigma_1(\xi)/c < 0$, and crucially, $\bar{\sigma}_2(\xi) = -4\pi i\sigma_2(\xi)/c < 0$ across the entirety of curves 4 and 5.

This analysis demonstrates that for a specific subset of parameters $\bar{A}_1$ and $\bar{A}_2$, a profound electrodynamic asymmetry is established within the stack. Specifically, the top metasurface maintains a fundamentally capacitive profile ($-4\pi i\sigma_1(\xi)/c < 0$), whereas the bottom metasurface transitions to an inductive, metal-like behavior ($-4\pi i\sigma_2(\xi)/c > 0$). It is precisely this competitive capacitive-inductive feedback between the adjacent structured layers that drives the emergence of the negative-dispersion region. From a practical standpoint, the generation of such a backward-wave segment provides the internal distributed feedback necessary to support absolute instabilities when the hybrid geometry is coupled to a synchronized beam of charged particles.

Let us consider the case where the SPP frequency practically coincides with the resonance frequency of the first metasurface, i.e.,

$$\xi_{sp} \approx \xi_1 = 1 < \xi_2 = 1.3.$$

The corresponding eigenspectrum is shown in Fig. 4 for $\bar{\omega}_p = 4.4$ and $\bar{A}_1 = \bar{A}_2 = 0.2$. Due to the frequency degeneracy ($\xi_{sp} \approx \xi_1 = 1$), a regime of strong mode hybridization is achieved. This leads to a pronounced anticrossing (curve repulsion), highlighted as Region A, between curve 10, which corresponds to the mode predominantly localized near the plasma-like medium, and curve 11, the high-frequency branch predominantly associated with metasurface 1. The strong electrodynamic coupling fundamentally reorganizes the spectrum in the vicinity of $\xi = 1$. Additionally, Regions B and C indicate the secondary resonant interactions between the high-frequency and low-frequency electromagnetic waves, respectively, which are localized near the two separated metasurfaces.

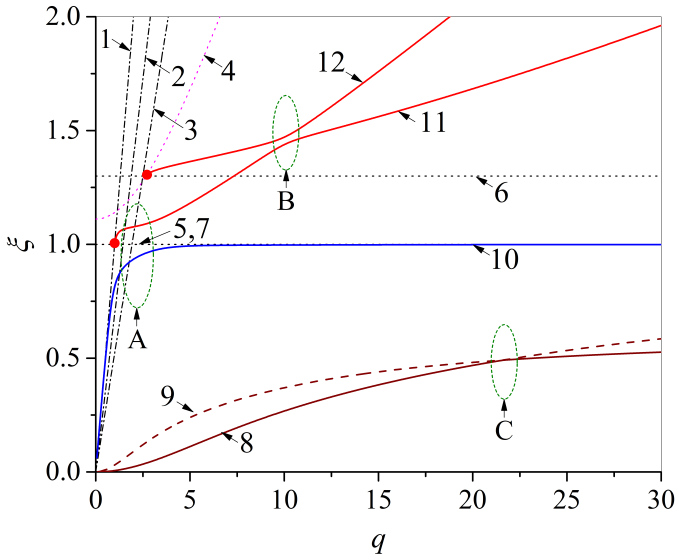


**Figure 4.** Dispersion spectrum of electromagnetic waves in the analyzed solid-state structure under the condition $\xi_{sp} \approx \xi_1 = 1 < \xi_2 = 1.3$ (where $\bar{\omega}_p = 4.4$). Region A features a substantial avoided crossing between the dispersion branch of the plasma-like medium (curve 10) and that of the primary metasurface (curve 11).

Fig. 5 demonstrates the eigenspectrum for a uniform distribution of resonances, where $\xi_1 = 1 < \xi_{sp} \approx 1.13 < \xi_2 = 1.3$ (with $\bar{\omega}_p = 5.0$).

In this regime, the system avoids giant single-point mode splitting and instead forms a characteristic "ladder" of repelling branches. The spectrum features three distinct interaction areas: Region A corresponds to the coupling of the proper high-frequency surface modes localized near both metasurfaces; Region B highlights the interaction between the branch localized near metasurface 1 and the branch predominantly localized near the plasma-like medium (curve 10); and Region C reflects the mutual coupling of the low-frequency metasurface modes. Such a sequential repulsion mechanism reveals the complex cascaded nature of the mode interactions across the entire structure. Therefore, when the SPP frequency falls between the two metasurface resonances, the spectrum undergoes a sequential reorganization. It starts with the hybridization of low-frequency modes, followed by the interaction between the plasma-like branch and the first metasurface branch, and culminates in the mutual repulsion of the high-frequency branches.

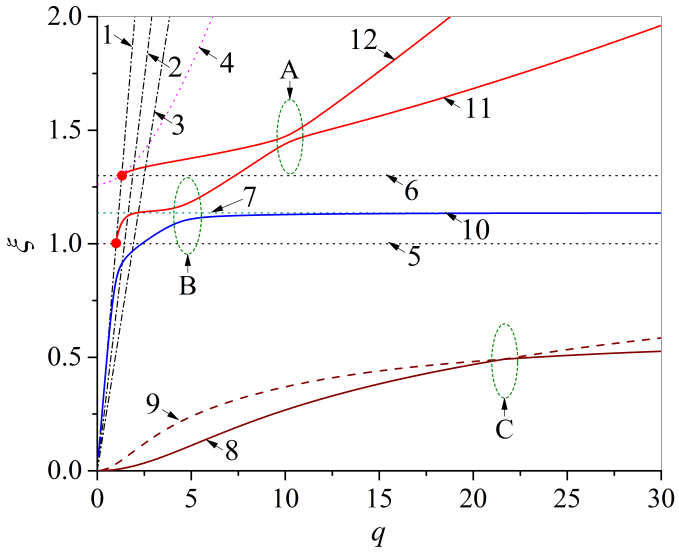


**Figure 5.** Dispersion spectrum of electromagnetic waves in the analyzed solid-state structure for an evenly spaced arrangement of resonances, taking $\xi_1 = 1 < \xi_{sp} \approx 1.13 < \xi_2 = 1.3$ ($\bar{\omega}_p = 5.0$). A distinct sequence, or "ladder," of mutually repelling dispersion branches emerges across interaction zones A, B, and C.

Ultimately, we examine the scenario where the SPP frequency nears the resonant frequency of the second metasurface, given by $\xi_1 = 1 < \xi_{sp} \approx \xi_2 = 1.3$.

Fig. 6 illustrates the resulting dispersion profile for $\bar{\omega}_p = 5.7$. Under these conditions, the primary avoided crossing moves to a higher frequency range, taking place between curve 10—representing the mode largely confined

to the plasma-like semiconductor—and curve 12, which represents the upper-frequency mode principally linked to the second metasurface. Consequently, a substantial spectral gap emerges in region C around $\xi = 1.3$. Furthermore, region A continues to capture the coupling between the two intrinsic upper-frequency metasurface modes, while region B highlights the interaction linking the plasma-like-medium branch with the branch governed by the first metasurface. In the lower-frequency spectrum, region D indicates the ongoing mutual repulsion of the bottom-tier metasurface branches. Therefore, as $\xi_{sp}$ transitions away from $\xi_1$ and closer to $\xi_2$, the primary pathway for energy hybridization shifts from the first metasurface to the second. Concurrently, the preservation of the other interaction zones clearly underscores the fundamentally multiresonant nature of this six-layer structure.

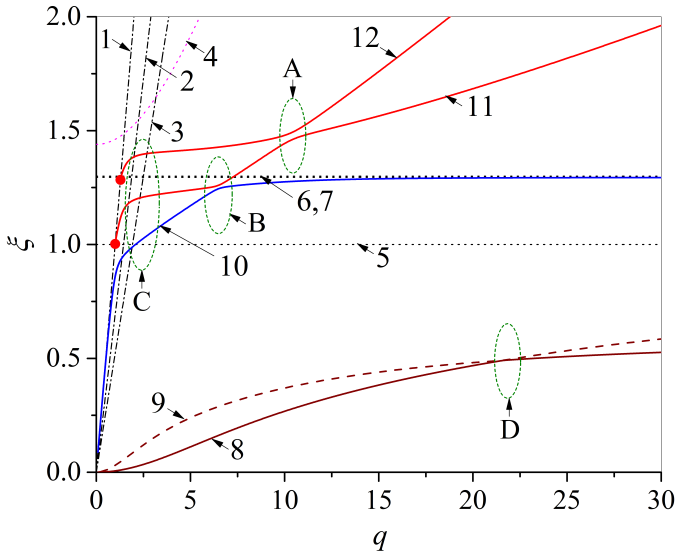


**Figure 6.** Dispersion spectrum of electromagnetic waves in the analyzed solid-state structure under the condition $\xi_1 = 1 < \xi_{sp} \approx 1.3 \approx \xi_2$ (with $\bar{\omega}_p = 5.7$). The most significant mode hybridization and splitting are localized within Region C.

To evaluate the impact of the dielectric environment, we consider the case where the fused-silica spacer is replaced by a high-index silicon layer ($\varepsilon_3 = 11.7$). As shown in Fig. 7, the increased permittivity causes the light line in the third dielectric (curve 3) to shift downward. This modification, combined with the high background permittivity of the semiconductor, reduces the SPP frequency to $\xi_{sp} \approx 0.95$. Consequently, the SPP resonance resides below the primary metasurface resonance ($\xi_{sp} < \xi_1$), which prevents the splitting of the semiconductor-localized branch (curve 10) through interaction with the metasurface modes. However, the intrinsic coupling between the two metasurfaces remains active, leading to the pronounced avoided crossing observed in Region A for the high-frequency branches.

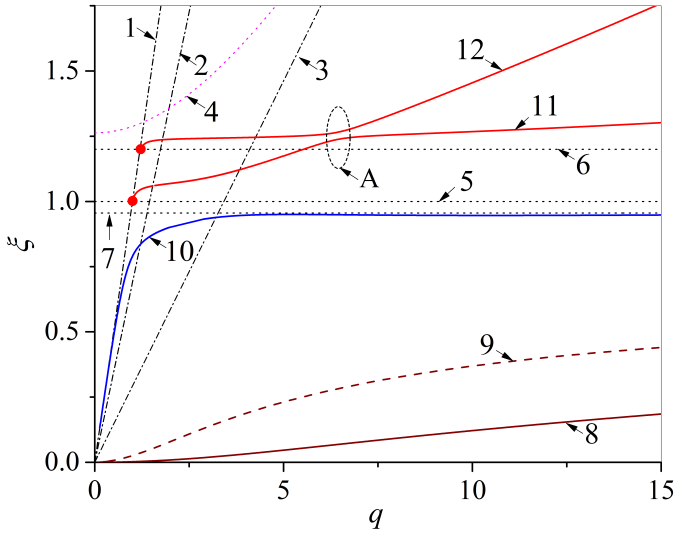


**Figure 7.** Dispersion spectrum of electromagnetic waves in the analyzed solid-state structure with a high-index dielectric spacer (silicon, $\varepsilon_3 = 11.7$) for the case $\xi_{sp} \approx 0.95 < \xi_1 = 1 < \xi_2 = 1.3$ ($\bar{\omega}_p = 5.0$). Curves 1, 2, and 3 represent light lines; curve 4 marks the boundary $\eta_4 = 0$; lines 5, 6, and 7 indicate $\xi_1$, $\xi_2$, and $\xi_{sp}$, respectively. Curves 8–12 identify the low- and high-frequency hybrid branches.

The influence of the metasurface oscillator strengths on the hybridization width is illustrated in Fig. 8. By increasing the parameters $\bar{A}_1$ and $\bar{A}_2$ from 0.2 to 0.4 while maintaining other system variables, we observe a significant expansion of the spectral gaps. The anti-crossing regions A, B, and C become notably wider. In this configuration, Region A characterizes the interaction between the upper-frequency metasurface modes, while Region B represents the coupling between the primary metasurface and the plasma-like substrate. Region C captures the repulsion between the fundamental low-frequency metasurface branches. This demonstrates that the geometric design of the conductive elements provides a robust mechanism for controlling the magnitude of mode splitting.

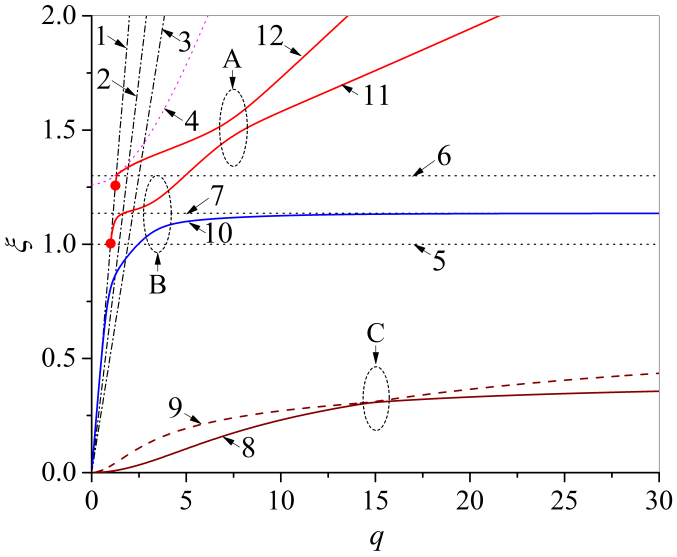


**Figure 8.** Dispersion spectrum of electromagnetic waves in the analyzed solid-state structure under strong coupling conditions, where the oscillator strengths are increased to $\bar{A}_1 = \bar{A}_2 = 0.4$ ($\bar{\omega}_p = 5.0$, $\xi_{sp} \approx 1.13$). The labeling of branches 1–12 follows the scheme established in Fig. 7.

Finally, we examine the transition from a semiconductor-like to a metal-like substrate by setting the background permittivity to $\varepsilon_0 = 1$. As seen in Fig. 9, this shift dramatically increases the SPP resonance frequency to $\xi_{sp} \approx 2.3$. A comparison between Fig. 8 and Fig. 9 reveals that the metallic nature of the substrate introduces a new interaction zone, labeled Region D, where the SPP branch of the substrate couples strongly with the mode localized near the second metasurface. Furthermore, the existing interaction regions A and B are shifted toward the higher-frequency domain. We also observe that the spectral repulsion between the low-frequency metasurface branches (Region C) is significantly enhanced compared to the semiconductor-based configuration.

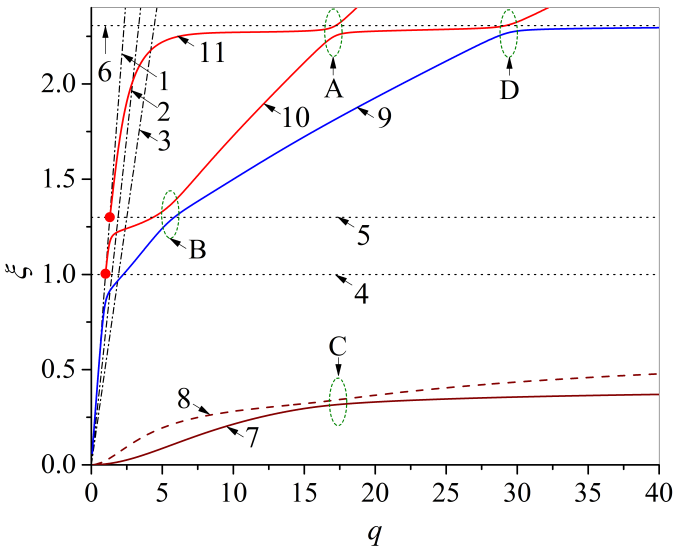


**Figure 9.** Dispersion spectrum of electromagnetic waves in the analyzed solid-state structure with a metal-like plasma medium ($\varepsilon_0 = 1$) at $\xi_{sp} \approx 2.3 > \xi_2 > \xi_1$. The parameters are $\bar{A}_1 = \bar{A}_2 = 0.4$ and $\delta_1 = \delta_2 = 0.15$. Region D highlights the additional interaction zone emerging at the SPP frequency.

## 4. DISCUSSION AND CONCLUSION

Our study presents a detailed electrodynamic account of a six-layer hybrid structure, where two isotropic plasmonic metasurfaces are integrated within dielectric spacers above a semi-infinite plasma-like medium. By analyzing the dispersion relations for $p$-polarized electromagnetic waves, we have mapped a variety of waveguiding regimes. These range from tightly confined surface states to hybrid bulk-surface modes, where the fields exhibit an oscillatory character within the internal dielectrics while maintaining evanescent decay in the cladding and substrate. Numerical results highlight the decisive role of cascaded mode hybridization in shaping the structure's response. Specifically, we found that tuning the surface plasmon-polariton (SPP) frequency of the substrate relative to the metasurfaces' inherent resonances triggers a complex topological reorganization of the eigenspectrum. The strong repulsion between initially non-degenerate states manifests as a multi-resonant "ladder" of dispersion branches. Notably, the spectral position and width of these hybridization gaps prove to be highly sensitive to both the geometric dimensions and the material parameters of the stack. One of the central findings of this work is the identification of the specific parameters necessary for a backward-wave regime. We demonstrated that by introducing an asymmetry in the effective oscillator strengths of the structured interfaces, the system can be forced into a state of competitive reactive feedback. In this specific configuration, the top metasurface remains fundamentally capacitive ($-4\pi i\sigma_1(\xi)/c < 0$), whereas the lower one transitions into a metallic, inductive state ($-4\pi i\sigma_2(\xi)/c > 0$). This electrodynamic imbalance serves as the direct physical mechanism behind the emergence of negative dispersion. From a practical standpoint, creating such intrinsic distributed feedback is essential for triggering absolute instabilities during interactions with synchronized charged-particle beams. Finally, our analysis shows that the energy exchange pathways can be fundamentally shifted by modifying the local dielectric environment or replacing the semiconductor with a metal. Such adjustments alter the critical SPP frequency, effectively pushing the primary interaction zones into higher frequency domains and broadening the spectral gaps between the lowest-order branches. This structural flexibility offers a predictable and versatile platform for managing subwavelength electromagnetic confinement, which is crucial for the next generation of active optoelectronic and nanophotonic devices.

## ORCID

**Yu.O. Averkov**, https://orcid.org/0000-0002-1169-9393; **O.Yu. Averkov**, https://orcid.org/0000-0001-6055-015X; **N.N. Beletskii**, https://orcid.org/0000-0002-3194-7251

## REFERENCES

[1] A. Ranjbar and A. Grbic, "Broadband, Multiband, and Multifunctional All-Dielectric Metasurfaces," Phys. Rev. Applied, **11**, 054066 (2019). https://doi.org/10.1103/PhysRevApplied.11.054066

[2] D. Correas-Serrano, J. S. Gomez-Diaz, A. Alvarez-Melcon, and A. Alù, "Black phosphorus plasmonics: anisotropic elliptical propagation and nonlocality-induced canalization," J. Opt. **18**, 104006 (2016). https://doi.org/10.1088/2040-8978/18/10/104006

[3] J. S. Gomez-Diaz, M. Tymchenko, and A. Alù, "Hyperbolic Plasmons and Topological Transitions Over Uniaxial Metasurfaces," Phys. Rev. Lett. **114**, 233901 (2015). https://doi.org/10.1103/PhysRevLett.114.233901

[4] A. A. High, R. C. Devlin, A. Dibos, M. Polking, D. S. Wild, J. Perczel, N. P. de Leon, M. D. Lukin, and H. Park, "Visible-frequency hyperbolic metasurface," Nature, **522**, 192–196 (2015). https://doi.org/10.1038/nature14477

[5] C. L. Holloway, E. F. Kuester, J. A. Gordon, J. O'Hara, J. Booth, and D. R. Smith, "An overview of the theory and applications of metasurfaces: The two-dimensional equivalents of metamaterials," IEEE Antennas Propag. Mag. **54**, 10–35 (2012). https://doi.org/10.1109/MAP.2012.6230714

[6] A. Nemilentsau, T. Low, and G. Hanson, "Anisotropic 2D Materials for Tunable Hyperbolic Plasmonics," Phys. Rev. Lett. **116**, 066804 (2016). https://doi.org/10.1103/PhysRevLett.116.066804

[7] P. A. D. Gonçalves, L. P. Bertelsen, S. Xiao, and N. A. Mortensen, "Hybridized Plasmons in 2D Nanoslits: From Graphene to Anisotropic 2D Materials," ACS Photonics, **4**, 2645–2652 (2017). https://doi.org/10.1021/acsphotonics.7b00558

[8] J. Sperrhake, M. Falkner, S. Fasold, T. Kaiser, and T. Pertsch, "Equivalence of reflection paths of light and Feynman paths in stacked metasurfaces," Phys. Rev. B, **102**, 245108 (2020). https://doi.org/10.1103/PhysRevB.102.245108

[9] T. Zhan, X. Shi, Y. Dai, X. Liu, and J. Zi, "Transfer matrix method for optics in graphene layers," J. Phys.: Condens. Matter, **25**, 215301 (2013). https://doi.org/10.1088/0953-8984/25/21/215301

[10] I. Allayarov, V. R. Tuz, A. Cala Lesina, and A. B. Evlyukhin, "Analytical model of metasurfaces comprising meta-atoms with anisotropic polarizabilities and for arbitrary incident angles," Phys. Rev. B, **111**, 155438 (2025). https://doi.org/10.1103/PhysRevB.111.155438

[11] S. M. Kandil, D. J. Bisharat, and D. F. Sievenpiper, "Engineering equifrequency contours of metasurfaces for self-collimated surface-wave steering," Phys. Rev. Applied, **21**, 044006 (2024). https://doi.org/10.1103/PhysRevApplied.21.044006

[12] X. Zhang, C. Bian, Z. Gong, R. Chen, T. Low, H. Chen, and X. Lin, "Hybrid surface waves in twisted anisotropic heterometasurfaces," Phys. Rev. Applied, **21**, 064034 (2024). https://doi.org/10.1103/PhysRevApplied.21.064034

[13] E. M. Renzi, E. Galiffi, X. Ni, and A. Alù, "Hyperbolic Shear Metasurfaces," Phys. Rev. Lett. **132**, 263803 (2024). https://doi.org/10.1103/PhysRevLett.132.263803

[14] C. Bian, X. Zhang, W. Ma, X. Chen, H. Chen, T. Low, and X. Lin, "Antihyperbolic surface waves on hyperbolic metasurfaces," Phys. Rev. A, **111**, 033522 (2025). https://doi.org/10.1103/PhysRevA.111.033522

[15] X. Zhang, X. Cui, T. Cai, W. Cai, T. Low, H. Chen, and X. Lin, "Scattering-free Plasmonic Brewster Effect via Metasurfaces," ACS Photonics, **12**(4), 1865–1872 (2025). https://doi.org/10.1021/acsphotonics.4c02263

[16] R. Ogier, Y. Fang, M. Käll, and M. Svedendahl, "Near-Complete Photon Spin Selectivity in a Metasurface of Anisotropic Plasmonic Antennas," Phys. Rev. X, **5**, 041019 (2015). https://doi.org/10.1103/PhysRevX.5.041019

[17] S. Droulias and L. Bougas, "Chiral sensing with achiral anisotropic metasurfaces," Phys. Rev. B, **104**, 075412 (2021). https://doi.org/10.1103/PhysRevB.104.075412

[18] C. L. Cortes, W. Newman, S. Molesky, and Z. Jacob, "Quantum nanophotonics using hyperbolic metamaterials," J. Opt. **14**, 063001 (2012). https://doi.org/10.1088/2040-8978/14/6/063001

[19] N. K. Paul, D. Correas-Serrano, and J. S. Gomez-Diaz, "Giant lateral optical forces on Rayleigh particles near hyperbolic and extremely anisotropic metasurfaces," Phys. Rev. B, **99**, 121408(R) (2019). https://doi.org/10.1103/PhysRevB.99.121408

[20] Y. Zhang, M. Antezza, H.-L. Yi, and H.-P. Tan, "Metasurface-mediated anisotropic radiative heat transfer between nanoparticles," Phys. Rev. B, **100**, 085426 (2019). https://doi.org/10.1103/PhysRevB.100.085426

[21] B.-Q. Lin, J.-X. Guo, P. Chu, W.-J. Huo, Z. Xing, B.-G. Huang, and L. Wu, "Multiple-Band Linear-Polarization Conversion and Circular Polarization in Reflection Mode Using a Symmetric Anisotropic Metasurface," Phys. Rev. Applied, **9**, 024038 (2018). https://doi.org/10.1103/PhysRevApplied.9.024038

[22] C.P. Mavidis, A.C. Tasolamprou, E.N. Economou, C.M. Soukoulis, and M. Kafesaki, "Polaritonic cylinders as multifunctional metamaterials: Single scattering and effective medium description," Phys. Rev. B, **102**, 155310 (2020). https://doi.org/10.1103/PhysRevB.102.155310

[23] Y. Nakata, Y. Urade, K. Okimura, T. Nakanishi, F. Miyamaru, M.W. Takeda, and M. Kitano, "Anisotropic Babinet-Invertible Metasurfaces to Realize Transmission-Reflection Switching for Orthogonal Polarizations of Light," Phys. Rev. Applied, **6**, 044022 (2016). https://doi.org/10.1103/PhysRevApplied.6.044022

[24] Y. Nakata, K. Fukawa, T. Nakanishi, Y. Urade, K. Okimura, and F. Miyamaru, "Reconfigurable Terahertz Quarter-Wave Plate for Helicity Switching Based on Babinet Inversion of an Anisotropic Checkerboard Metasurface," Phys. Rev. Applied, **11**, 044008 (2019). https://doi.org/10.1103/PhysRevApplied.11.044008

[25] J. D. Jackson, *Classical Electrodynamics*, 3rd ed. (John Wiley & Sons, New York, 1999).

## ВИНИКНЕННЯ ВІД'ЄМНОЇ ДИСПЕРСІЇ ЕЛЕКТРОМАГНІТНИХ ХВИЛЬ У ТВЕРДОТІЛЬНІЙ СТРУКТУРІ, ЩО МІСТИТЬ ПЛАЗМОПОДІБНЕ СЕРЕДОВИЩЕ ТА ПЛАЗМОННІ МЕТАПОВЕРХНІ

**Ю.О. Аверков**, **О.Ю. Аверков**, **М.М. Білецький**

*Інститут радіофізики та електроніки ім. О. Я. Усикова НАН України, вул. Акад. Проскури, 12, Харків, 61085, Україна*

У цьому дослідженні представлено детальний теоретичний і чисельний аналіз дисперсійних властивостей $p$-поляризованих електромагнітних хвиль у складній багатошаровій твердотільній структурі. Досліджувана система являє собою шестишарову структуру, що містить дві ізотропні плазмонні метаповерхні, які розділені діелектричними прошарками та розташовані на напівнескінченній плазмоподібній підкладці — або сильно легованому напівпровіднику, або металі. Поєднуючи формалізм матриць переносу з рівняннями Максвелла та строгими граничними умовами, ми вивели точні дисперсійні рівняння як для поверхневих, так і для об'ємно-поверхневих мод. Наші чисельні результати вказують на процес каскадної гібридизації між фундаментальними резонансами метаповерхонь і власними поверхневими плазмон-поляритонними (ППП) модами підкладки. Особливо значущим результатом є те, що регулювання ефективних сил осциляторів метаповерхонь викликає виражену дисперсійну асиметрію. Це відбувається тоді, коли одна метаповерхня виявляє ємнісний відгук, тоді як інша стає ефективно індуктивною. Такий електродинамічний дисбаланс призводить до аномального режиму негативної частотної дисперсії, що характеризується поширенням зворотних хвиль. Крім того, ми демонструємо, що модифікація діелектричного оточення або заміна напівпровідникової підкладки на металеву зміщує області резонансної взаємодії, пропонуючи універсальний засіб керування спектральними інтервалами розщеплення мод. Ці висновки створюють міцне теоретичне підґрунтя для проєктування перебудовуваних нанофотонних пристроїв та генерації розподіленого внутрішнього зворотного зв'язку, що є необхідним для виникнення абсолютних нестійкостей електромагнітних хвиль у системах, пов'язаних із пучками заряджених частинок.

**Ключові слова:** *плазмонна метаповерхня; гібридна поверхнева хвиля; об'ємно-поверхнева хвиля; від'ємна дисперсія; напівпровідникова підкладка; гібридизація мод*

EAST EUROPEAN JOURNAL OF PHYSICS. 3. 251-268 (2026)
DOI:10.26565/2312-4334-2026-3-20 ISSN 2312-4334

# GOLD-INDUCED MAGNETISM AND THERMAL STABILITY IN SiC NANOSHEETS: DFT+U

**Sevda Rzayeva[1]*, Yuldosh Yakubov[2], Umedjon Khalilov[3,4,5], Maftun Aliyev[6], Ariel Sharon Asare[7,8]**
[1]*Azerbaijan State Oil and Industry University, 20 Azadlig Ave., AZ-1010, Baku, Azerbaijan*
[2]*Institute of General and Inorganic Chemistry, Mirzo-Ulugbek 77-a, 100170 Tashkent, Uzbekistan*
[3]*Arifov Institute of Ion-Plasma and Laser Technologies, Durmon yuli 33, 100120 Tashkent, Uzbekistan*
[4]*University of Antwerp, Groenenborgerlaan 171, Antwerp 2020, Belgium*
[5]*Engineering School, Central Asian University, Tashkent 111221, Uzbekistan*
[6]*Nakhchivan State University, Nakhchivan, Azerbaijan*
[7]*Department of Physics, University of Ghana*
[8]*Abdus Salam International Centre for Theoretical Physics (ICTP), Italy*
**Corresponding author: rzayeva.sevda@asoiu.edu.az*
Received April 12, 2026; revised June 21, 2026; accepted July 2, 2026

Gold-doped two-dimensional silicon carbide (SiC) nanosheets are investigated using spin-polarized density functional theory (DFT+U) to examine their electronic structure, induced magnetism, and thermal stability. Single (1Au@Si) and double (2Au@2Si) substitutional configurations are modeled within a 4×4 supercell to ensure reliable evaluation of intrinsic properties. Au incorporation significantly narrows the band gap while preserving the semiconducting character of the SiC nanosheet. Spin-resolved density-of-states analysis shows that Au 5d orbitals dominate the electronic states near the Fermi level. Despite nearly spin-degenerate band dispersions, Mulliken spin population analysis reveals dopant-induced magnetism mediated by neighboring carbon atoms. The 1Au@Si system exhibits a magnetic moment of ~3 $\mu_B$, while the 2Au@2Si configuration stabilizes a ferrimagnetic-like state with a total magnetic moment of ~6 μB. Within the mean-field approximation, the estimated Curie temperature is approximately 510 K, suggesting the possibility of magnetic stability above room temperature and potential applications in spintronic devices.
**Keywords:** *SiC nanosheets; Gold doping; Spintronics; Dilute magnetic semiconductors; Density functional theory; Curie temperature*

## 1. INTRODUCTION

Two-dimensional (2D) materials have emerged as one of the most compelling platforms for investigating spin-dependent phenomena at the nanoscale. Owing to strong quantum confinement effects and reduced dielectric screening, the electronic states in 2D systems exhibit exceptional sensitivity to external perturbations such as elemental doping, intrinsic defects, and applied strain [1-3]. This heightened responsiveness enables precise atomic-scale control over charge, spin, and magnetic degrees of freedom, positioning 2D materials at the forefront of next-generation spintronic and nano-electronic technologies.

Within this rapidly expanding research field, two-dimensional silicon carbide (SiC) nanosheets have attracted increasing attention as wide-band-gap semiconductors due to their exceptional thermal stability, chemical inertness, high mechanical robustness, and strong resistance to radiation-induced degradation [4,5]. Unlike many conventional 2D materials, SiC nanosheets retain their structural integrity and electronic characteristics under extreme environmental and operating conditions, making them particularly attractive for high-performance and durable device applications.

Despite these favorable properties, pristine SiC nanosheets are intrinsically non-magnetic and have relatively wide band gaps, which severely limit their direct applicability to spintronic devices that require finite spin polarization and stable long-range magnetic ordering. To overcome this intrinsic limitation, substitutional doping has been widely employed as an effective strategy, as it can induce pronounced electronic reconstruction and generate spin polarization through strong dopant–host orbital hybridization [6,7].

Although considerable research efforts have been devoted to transition-metal (3d) doping in SiC-based nanostructures, such dopants often induce strong electronic localization, clustering tendencies, or undesirable metallic behavior. These effects can adversely influence carrier mobility, magnetic stability, and overall device performance, thereby limiting their practical applicability [8-13].

In contrast, noble-metal dopants-particularly gold (Au)-offer an alternative and fundamentally distinct route for engineering the electronic and magnetic properties of low-dimensional systems. Gold is characterized by spatially extended 5d orbitals, pronounced relativistic effects, and strong spin–orbit coupling, which collectively enable substantial modification of the host electronic structure without necessarily inducing a semiconductor-to-metal transition [9, 14, 15]. Recent theoretical studies suggest that substitutional Au incorporation can introduce impurity-derived states near the band edges and promote strong hybridization with host p orbitals. Nevertheless, the microscopic origin of magnetism in Au-doped SiC nanosheets remains insufficiently understood. In particular, it is still unclear whether the induced magnetic moments are primarily localized on the Au dopants or are mediated through the surrounding Si-C lattice, with a potentially dominant contribution arising from the carbon sublattice [16].

***Cite as:*** S. Rzayeva, Y. Yakubov, U. Khalilov, M. Aliyev, A.Sh. Asare, East Eur. J. Phys. 3, 251 (2026), https://doi.org/10.26565/2312-4334-2026-3-20

Motivated by these unresolved issues, the present work provides a systematic spin-polarized first-principles investigation of Au-doped SiC nanosheets. Single (1Au@Si) and double (2Au@2Si) substitutional doping configurations are examined using a large 80-atom supercell to effectively suppress artificial dopant–dopant interactions and ensure reliable evaluation of intrinsic electronic and magnetic properties. The calculations were performed within the framework of spin-polarized density functional theory using the QuantumATK simulation platform [17], employing the LDA+U formalism to account for localized electronic states and reduce self-interaction effects [19–21].

Our calculations reveal a dual and nontrivial impact of Au incorporation on the electronic and magnetic behavior of SiC nanosheets. First, Au substitution induces a pronounced band-gap narrowing while largely preserving spin-degenerate band dispersions, thereby maintaining the semiconducting nature of the host material. Second, Au doping stabilizes a localized ferrimagnetic-like spin state that is not manifested through conventional exchange splitting in the band structure, but is instead primarily revealed by atom-resolved Mulliken spin population analysis.

Notably, the induced magnetism is found to be predominantly mediated by the carbon sublattice, which hosts sizable positive local magnetic moments. In contrast, the Au dopants and their nearest-neighbor Si atoms contribute antiparallel, compensating spin polarization. For the 1Au@Si configuration, a net magnetic moment of approximately $3\mu_B$ is obtained, whereas double Au substitution stabilizes a robust magnetic state with a total magnetic moment of about $6\mu_B$. Importantly, the 2Au@2Si system converges to essentially the same magnetic solution irrespective of whether the calculations are initialized in non-magnetic, ferromagnetic (FM), or antiferromagnetic (AFM) spin configurations. This behavior indicates that the magnetic ground state is intrinsically governed by dopant–host hybridization effects rather than by externally imposed spin ordering, a characteristic feature commonly observed in transition-metal- and noble-metal-modified semiconductors and dilute magnetic systems [6,15,16,25].

Taken together, these results establish Au-doped SiC nanosheets as a promising class of two-dimensional dilute magnetic semiconductors in which band-gap engineering and thermally robust magnetism can coexist. Such coexistence of semiconducting character and localized magnetic ordering is particularly desirable for next-generation spintronic and multifunctional nanoelectronic applications, where spin-dependent electronic transport and stable magnetic ordering are essential [2,3,9,11].

In addition to inducing robust spin polarization, Au substitution is found to stabilize a high-temperature magnetic phase in SiC nanosheets. Total-energy comparisons between non-magnetic, ferromagnetic, and antiferromagnetic configurations reveal that spin-polarized states are energetically favored, with a very small energy splitting between FM and AFM solutions, indicating near magnetic degeneracy. Mean-field estimation based on first-principles total-energy differences yields an estimated Curie temperature of approximately 510 K. Within the limitations of the mean-field approximation, this result suggests the possibility of magnetic stability above room temperature. This result demonstrates that Au-doped SiC nanosheets can simultaneously exhibit semiconducting character and thermally robust magnetism, a combination rarely achieved in two-dimensional dilute magnetic semiconductors and highly desirable for practical spintronic device applications [2,6,9,11,23].

## 2. COMPUTATIONAL METHODOLOGY

All calculations were carried out within the framework of spin-polarized density functional theory (DFT) using the linear combination of atomic orbitals (LCAO) method, as implemented in the Quantum ATK simulation package [17-18]. Spin polarization was explicitly accounted for to accurately describe dopant-induced magnetic effects and spin-dependent electronic reconstruction in SiC nanosheets.

Within the spin-polarized DFT+U formalism, the total electronic charge density was decomposed into spin-up (α) and spin-down (β) components. The spin density, defined as the difference between these two spin channels, was used to characterize the system's magnetic response and spin polarization. The corresponding relations are given by:

$$\rho(r) = \rho^{\alpha}(r) + \rho^{\beta}(r) \tag{1}$$

$$\Delta\rho(r) = \rho^{\alpha}(r) - \rho^{\beta}(r) \tag{2}$$

Here, $\rho^{\alpha}(r)$ and $\rho^{\beta}(r)$ denote the spin-up and spin-down electron densities, respectively, while $\Delta\rho(r)$ represents the spin density distribution, which provides direct insight into the origin and spatial distribution of magnetism in the doped SiC nanosheets.

Exchange-correlation effects were described within the local density approximation (LDA) using the Perdew-Zunger parameterization of the Ceperley-Alder data [20]. To reduce the self-interaction error inherent in conventional LDA calculations, the rotationally invariant Dudarev DFT+U formalism was employed. Consistent with previous theoretical studies, the effective on-site Coulomb parameters were chosen as USi = 5.0 eV for Si-3d states and UC = 4.8 eV for C-2p states. These values provide a physically reasonable description of the electronic and magnetic properties of Au-doped SiC nanosheets.

Core-valence interactions were treated by norm-conserving pseudopotentials of the Fritz Haber Institute (FHI) type [18]. The valence electronic states of all constituent elements (Si, C, and Au) were expanded using a double-zeta polarized (DZP) numerical atomic orbital basis set, providing a reliable and balanced description of both the light host atoms and the heavy Au dopants [20].

Electronic occupations were determined using the Fermi–Dirac distribution with an electronic temperature of 300 K to ensure numerical stability and smooth convergence of the self-consistent field cycles. A real-space density mesh cutoff of 75 Hartree was employed, which was found to be sufficient to achieve well-converged total energies and charge density distributions for all studied configurations.

Brillouin-zone integrations were performed using a Monkhorst-Pack k-point mesh of 3x3x1, which provides a suitable compromise between numerical accuracy and computational efficiency for the employed supercell size [22]. The two-dimensional SiC nanosheet was modeled using a 4×4 hexagonal supercell containing 80 atoms (40 Si and 40 C). A vacuum region of at least 15 Å was introduced perpendicular to the nanosheet plane to suppress spurious interactions between periodically repeated images.

Substitutional Au doping was realized by replacing Si atoms, considering both the single-dopant 1Au@1Si configuration (≈1.25 at.%) and the double-dopant 2Au@2Si configuration (≈2.50 at.%). The dopant concentration was defined relative to the total number of atoms in the supercell [21]. For the 2Au@2Si system, spin-unconstrained as well as ferromagnetic (FM) and antiferromagnetic (AFM) initial spin configurations were explicitly examined to evaluate the stability and robustness of the magnetic ground state. All atomic structures were fully optimized using a conjugate-gradient algorithm until the residual forces on each atom were reduced below 0.01eV $Å^{-1}$ and the total energy convergence criterion reached 10-5eV. Spin-resolved band structures were calculated along the Γ–Z direction, with the Fermi level set to 0eV. In addition, the total and partial densities of states (TDOS and PDOS) were evaluated to analyze dopant-induced impurity states and Au–host hybridization effects [19,20].

To elucidate the microscopic origin of magnetism in Au-doped SiC nanosheets, Mulliken spin population analysis was employed. Within this framework, the local magnetic moment associated with a given atom A is defined as the difference between its spin-up and spin-down Mulliken populations:

$$\mu_A = n_A^{\alpha} - n_A^{\beta} \tag{3}$$

where $n_A^{\alpha}\ and\ n_A^{\beta}$ represent the Mulliken populations of spin-up and spin-down electrons localized on atom A, respectively. The total magnetic moment of the supercell is then obtained by summing the atomic contributions over all atoms:

$$\mu_{tot} = \sum_A \mu_A \tag{4}$$

This analysis is particularly important for the present system, as Au-doped SiC nanosheets exhibit spin-degenerate band structures while simultaneously sustaining a finite net magnetic moment. Such behavior cannot be fully resolved from band structure analysis alone. Mulliken spin population analysis enables direct identification of the dominant spin carriers and provides atom-resolved insight into the system's magnetic texture. The results suggest that the induced magnetism is predominantly localized on the carbon sublattice, whereas the Au dopants and neighboring Si atoms contribute smaller, anti-parallel spin moments that partially compensate the total magnetization. This finding highlights the crucial role of dopant–host hybridization in mediating magnetism through the surrounding lattice rather than through localized Au moments alone.

For systems with identical chemical composition, such as the 2Au@2Si configuration, the relative stability of different magnetic solutions was evaluated by comparing their total energies. The magnetic stabilization energy was defined as:

$$\Delta E_{mag} = E_{NM} - E_{FM}, \tag{5}$$

where $E_{NM}$ and $E_{FM}$ denote the total energies of the non-magnetic and ferromagnetic states, respectively. A positive value of $\Delta E_{mag}$ indicates that the ferromagnetic solution is energetically favored over the non-magnetic one.
In addition, the energy difference between antiferromagnetic and ferromagnetic configurations,

$$\Delta E_{AFM-FM} = E_{AFM} - E_{FM}, \tag{6}$$

was calculated to assess the sensitivity of the magnetic ground state to the initial spin ordering. The small energy separation observed between the FM and AFM solutions indicates a near-degeneracy of these magnetic states. Such behavior suggests that the Au-induced magnetism is not governed by rigid long-range ferromagnetic coupling but instead reflects a ferrimagnetic-like or weakly competing magnetic ordering mediated by the Si-C host lattice. This energetic proximity suggests that the dopant-induced magnetic state is largely governed by dopant–host hybridization in Au-substituted SiC nanosheets.

## 3. RESULTS AND DISCUSSION

### 3.1. Electronic structure of Au-doped SiC nanosheets

The electronic band structures of Au-doped SiC nanosheets were systematically analyzed to elucidate the influence of Au concentration on the system's electronic properties [22,23]. Two substitutional doping configurations were considered: a single Au atom substituting a Si site (SiC:1Au@1Si NS) and a double Au substitution at two Si sites (SiC:2Au@2Si NS), which serve as representative models for low and moderate dopant concentrations in two-dimensional SiC systems [24].

Spin-polarized band structures were calculated along the high-symmetry path Γ–Z of the 2D Brillouin zone, with the Fermi level aligned at 0eV, following standard electronic-structure analysis protocols for a two-dimensional Brillouin zone (2D monolayer). The corresponding results are presented in Figures 1 and 2.

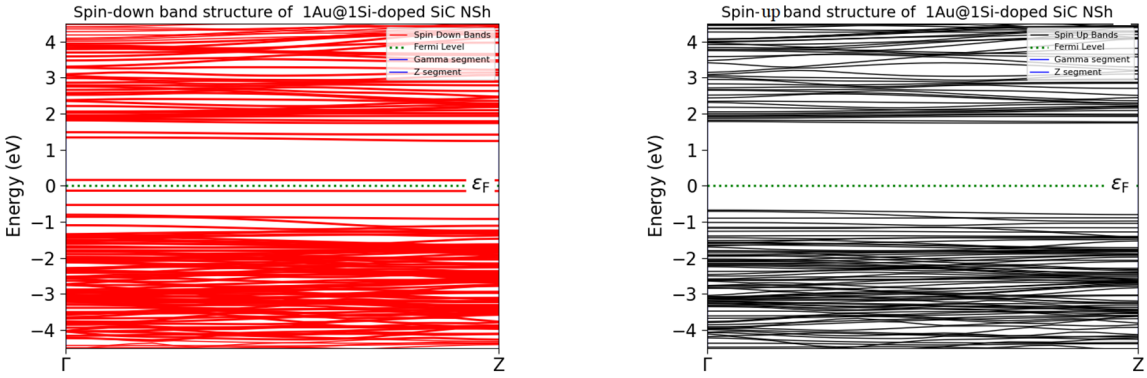


**Figure 1.** Spin-polarized electronic band structures of the 1Au@1Si-SiC nanosheet along the Γ-Z direction

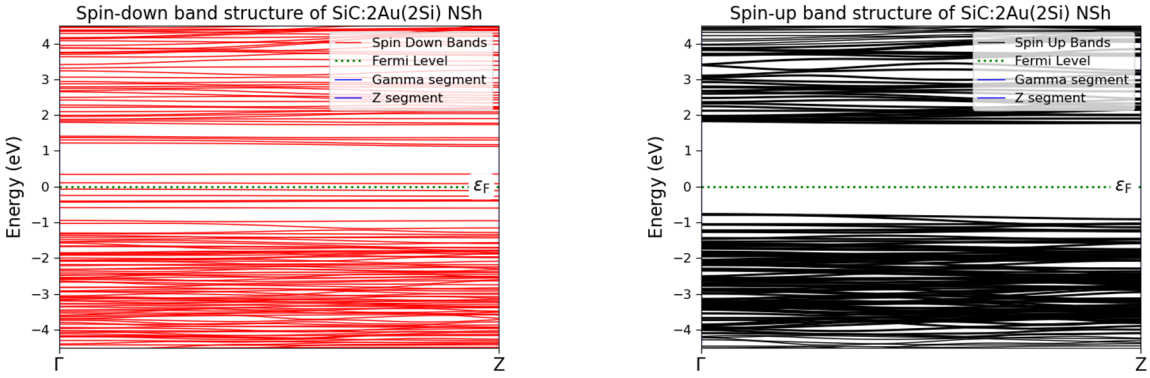


**Figure 2**. Spin-polarized electronic band structures of the SiC:2Au(2Si) nanosheet along the Γ-Z direction

As shown in Figure 1, the SiC:1Au@1Si nanosheet retains a semiconducting character in both spin-up and spin-down channels, exhibiting a narrow band gap of approximately 0.30 eV. This behavior is consistent with previous reports on noble-metal-induced band-gap modulation in wide-band-gap semiconductor systems. Upon increasing the Au concentration to the SiC:2Au@2Si configuration, a pronounced reduction of the band gap is observed, yielding values of approximately 0.18eV (direct) and 0.16eV (indirect), as summarized in Table 1.

**Table 1.** Spin-resolved band gaps and band-edge positions (VBM and CBM) for SiC:1Au@1Si and SiC:2Au@2Si nanosheets, illustrating Au-concentration-induced band gap narrowing while preserving spin degeneracy.

| System | Spin channel | Direct band gap (eV) | Indirect band gap (eV) | VBM (eV) | CBM (eV) |
|---|---|---|---|---|---|
| SiC:1Au(1Si) NS | Spin-up | 0.297 | 0.288 | -0.1389 | 0.1491 |
| | Spin-down | 0.297 | 0.288 | -0.1389 | 0.1491 |
| SiC:2Au(2Si) NS | Spin-up | 0.179 | 0.157 | -0.0738 | 0.0824 |
| | Spin-down | 0.179 | 0.157 | -0.0738 | 0.0824 |

The observed dopant-concentration-dependent band gap narrowing originates from an upward shift of the valence band maximum (VBM), accompanied by a downward shift of the conduction band minimum (CBM). This effect can be attributed to enhanced hybridization between Au-derived states and the host Si–C orbitals, which modifies the electronic structure near the Fermi level [25].

Importantly, the spin-up and spin-down band dispersions remain largely similar for both doping configurations, indicating the absence of pronounced exchange splitting at the band-dispersion level. This behavior reflects the closed-shell electronic configuration of Au and suggests that Au substitution primarily modifies the electronic structure through orbital hybridization rather than inducing strong band-resolved spin asymmetry. Nevertheless, as discussed in Section 3.2, atom-resolved spin population analysis reveals the emergence of dopant-induced magnetic moments mediated by the host lattice. Such behavior is consistent with previous first-principles studies on noble-metal-doped wide-band-gap semiconductor systems [23,24,26].

To further elucidate the effect of Au incorporation on the electronic structure, the total density of states (TDOS) was systematically analyzed for both single and double Au-doped SiC nanosheets. As shown in Figure 3, pristine SiC nanosheets exhibit a clear semiconducting gap around the Fermi level ($E_F$=0eV), which is in good agreement with previous first-principles studies on two-dimensional SiC monolayers [30].

Upon single Au substitution, impurity-induced states emerge near the valence- and conduction-band edges, leading to a pronounced enhancement of the TDOS in the vicinity of the Fermi level while preserving a finite band gap. These states mainly originate from hybridization between Au-derived orbitals and neighboring Si and C states, resulting in band-gap narrowing without altering the overall semiconducting character of the system. When the Au concentration is increased to the double-doped configuration (Figure 4), a further increase in the TDOS near EF is observed, accompanied by broader spectral features. This behavior reflects stronger Au-Au and Au-host interactions as well as enhanced electronic delocalization at higher dopant concentrations.

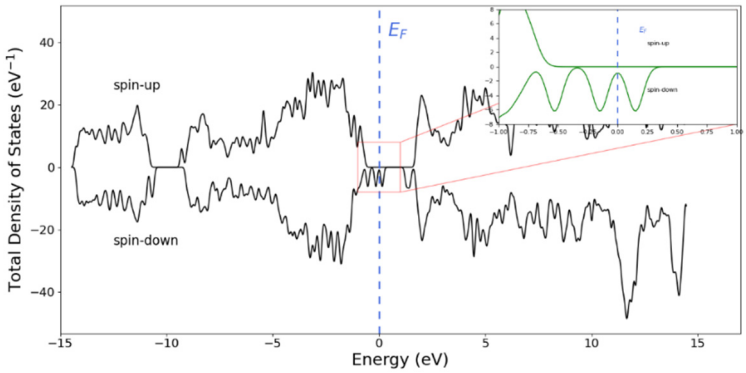


**Figure 3.** TDOS of single Au-doped SiC ($Au_1Si_{39}C_{40}$). The dashed line indicates the Fermi level (EF = 0eV).

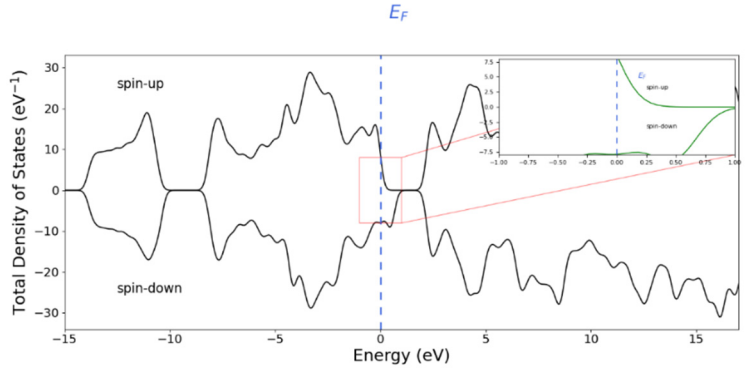


**Figure 4.** TDOS of double Au-doped SiC ($Au_2Si_{38}C_{40}$), showing enhanced states near $E_F$ compared to the single-doped case

Despite the increased density of states near the Fermi level, both Au-doped systems remain semiconducting, with no finite TDOS appearing exactly at $E_F$.

Moreover, the spin-up and spin-down TDOS curves remain largely symmetric, indicating no pronounced spin asymmetry at the TDOS level, indicating that Au incorporation modifies the electronic structure without inducing a semiconductor-to-metal transition.

Although the spin-up and spin-down TDOS curves remain largely similar over the entire energy range, enlarged DOS plots near the Fermi level reveal weak spin-dependent differences. These small asymmetries indicate that the exchange splitting is relatively weak and localized. Therefore, the finite magnetic moments obtained from Mulliken population analysis originate primarily from localized spin polarization rather than from pronounced exchange splitting throughout the entire electronic structure.

This nearly spin-degenerate electronic structure is consistent with previous first-principles investigations of noble-metal-doped semiconductors.

To identify the atomic and orbital origins of the electronic reconstruction induced by Au doping, spin-resolved partial density of states (PDOS) calculations was performed. Figure 5 shows the orbital-projected PDOS of Au in the single-Au-doped SiC nanosheet. The electronic states in the vicinity of the Fermi level are predominantly governed by Au-5d orbitals, while the contributions from Au-6s and Au-6p states are comparatively weaker and distributed over a broader energy range. The spin-up and spin-down PDOS curves remain largely similar over most of the energy range, indicating weak exchange splitting, consistent with the closed-shell electronic configuration of Au and previous first-principles studies [28,29]. However, enlarged views near the Fermi level reveal small spin-dependent differences, indicating weak local spin polarization. The Au-5d states dominate the electronic states near $E_F$ and contribute to the localized magnetic behavior.

For the double-Au-doped configuration (Figure 6), the Au-5d states become more intense and exhibit notable broadening, reflecting enhanced dopant-dopant as well as dopant-host interactions at higher Au concentration. Despite this increased electronic hybridization, spin degeneracy remains preserved, further reinforcing the conclusion that Au acts primarily as a modifier of the electronic structure rather than as a magnetic impurity in SiC nanosheets.

Although the overall exchange splitting remains relatively weak, the observed spin-dependent differences support the existence of localized magnetic polarization, consistent with the Mulliken spin population analysis.

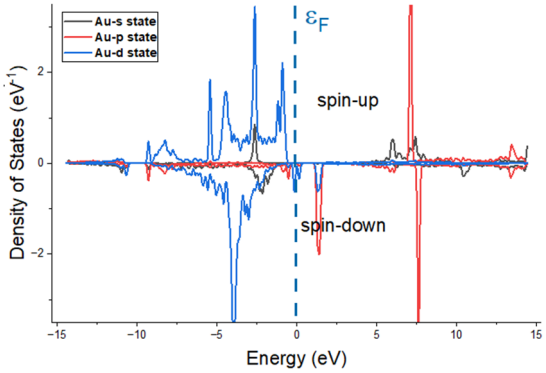


**Figure 5.** Spin-resolved PDOS of Au orbitals in single Au-doped SiC (Au1Si39C40)

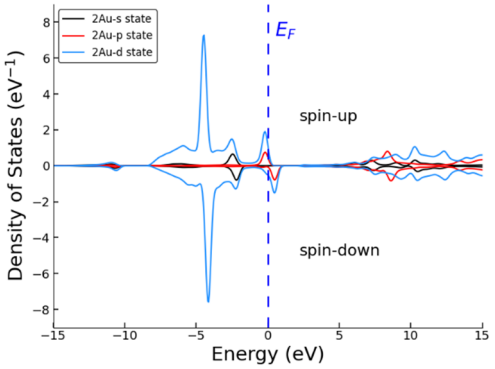


**Figure 6.** Spin-resolved PDOS of Au orbitals in double Au-doped SiC ($Au_2Si_{38}C_{40}$)

The spin-resolved partial density of states (PDOS) of host carbon atoms is presented in Figure 7. The electronic states near the valence and conduction band edges are predominantly governed by C-2p orbitals, whereas the C-2s and C-2d states contribute mainly at lower binding energies.

Although the total C-PDOS remains nearly symmetric, several carbon atoms neighboring the Au dopants exhibit substantial local magnetic moments according to the Mulliken analysis. This indicates that the induced magnetism is highly localized and cannot be fully resolved from orbital-averaged PDOS alone.

A similar trend is observed for the host silicon atoms, as shown in Figure 8. The Si–3p orbitals provide the dominant contributions to both the valence and conduction bands, while the Si–3d states exhibit only weak and broadly distributed features across the energy spectrum. The nearly symmetric spin-resolved PDOS indicates that Si atoms do not exhibit pronounced spin polarization, despite the pronounced Au-induced electronic reconstruction. These results highlight that the role of the host atoms is primarily indirect, mediated through orbital hybridization with Au states rather than through the development of substantial local magnetic moments.

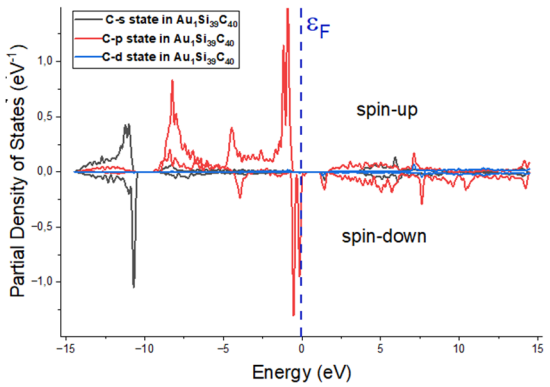


**Figure 7.** Spin-resolved partial density of states (PDOS) of C-s, C-p, and C-d orbitals for the $Au_1Si_{39}C_{40}$ system

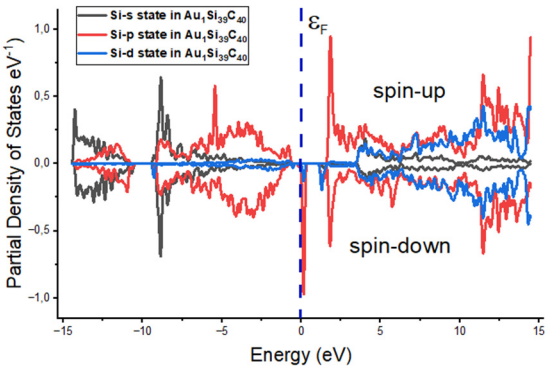


**Figure 8.** Spin-resolved partial density of states (PDOS) of Si-s, Si-p, and Si-d orbitals for the $Au_1Si_{39}C_{40}$ system

To quantitatively assess the influence of Au concentration on the electronic band gap characteristics of SiC nanosheets, the spin-resolved band gaps were systematically evaluated for pristine, single-Au-doped, and double-Au-doped configurations. Particular attention was paid to the evolution of both direct and indirect band gaps in the spin-up (↑) and spin-down (↓) channels in order to clarify whether Au incorporation induces spin asymmetry or magnetic exchange effects. Increasing Au concentration results in pronounced narrowing of both direct and indirect band gaps while preserving identical spin-up and spin-down values, demonstrating that Au enables effective band gap engineering in SiC nanosheets while preserving nearly spin-degenerate electronic states and only weak exchange splitting.

### 3.2. Magnetic Properties of Au-Doped SiC Nanosheets

#### 3.2.1. Pristine 80-Atom SiC Nanosheet: Non-Magnetic Reference State

The magnetic properties of the pristine 80-atom SiC nanosheet were first investigated using spin-polarized Mulliken population analysis to establish a reliable non-magnetic reference state. As shown in Fig. 9, the pristine system exhibits negligible spin polarization at all atomic sites, with local magnetic moments confined within $\pm 0.01\mu_B$. Silicon atoms carry very small positive magnetic moments ($\approx +0.011$-$0.012\mu_B$), whereas carbon atoms display comparably small negative moments ($\approx$ -0.010 to $-0.013\mu_B$), resulting in an almost perfect compensation between the two sublattices.

Consequently, the total Mulliken spin magnetic moment converges to approximately zero ($\Sigma_\mu \approx -0.000\mu_B$), as summarized in Table 2, confirming the absence of intrinsic magnetism in the pristine nanosheet. These extremely small residual moments fall well within the numerical uncertainty associated with Mulliken charge and spin partitioning and therefore cannot be interpreted as evidence of genuine magnetic ordering.

Further orbital-resolved analysis reveals spin-symmetric occupations of the Si s/p and C p states, with no observable exchange splitting near the Fermi level. Overall, these findings demonstrate that pristine SiC nanosheets possess a fully spin-degenerate, non-magnetic ground state, in excellent agreement with previous first-principles studies on two-dimensional SiC systems [30,31]. This non-magnetic reference state provides a robust baseline for identifying and quantitatively assessing dopant-induced magnetism upon Au substitution.

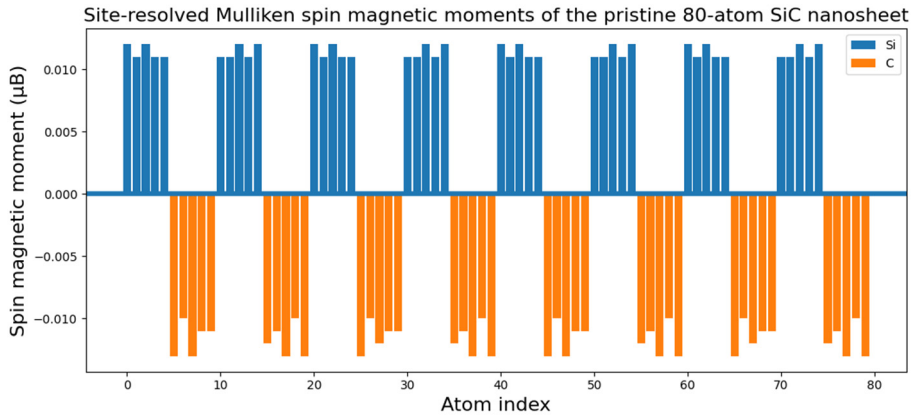


**Figure 9.** Site-resolved Mulliken spin magnetic moments of the pristine 80-atom SiC nanosheet, showing complete compensation between Si and C contributions and a vanishing net magnetic moment

**Table 2.** Element-resolved Mulliken spin magnetic moments for the pristine 80-atom SiC nanosheet

| Element | Number of atoms | Spin moment range ($\mu_B$) | Total contribution ($\mu_B$) |
|---|---|---|---|
| Si | 40 | +0.011 to +0.012 | ≈ +0.48 |
| C | 40 | -0.010 to -0.013 | ≈ -0.48 |
| Total | 80 | — | 0.000 |

### *3.2.2. Single Au Substitution: 1Au@1Si Configuration*

The substitution of a single Si atom by Au induces a pronounced magnetic response in the SiC nanosheet. The atom-resolved Mulliken spin magnetic moments shown in Fig. 10 reveal a strongly inhomogeneous and localized spin distribution, which is characteristic of induced magnetism governed by dopant–host interactions. The total magnetic moment reaches approximately 3.00 μB, indicating the emergence of a ferromagnetic-like state (Tables 3 and 4).

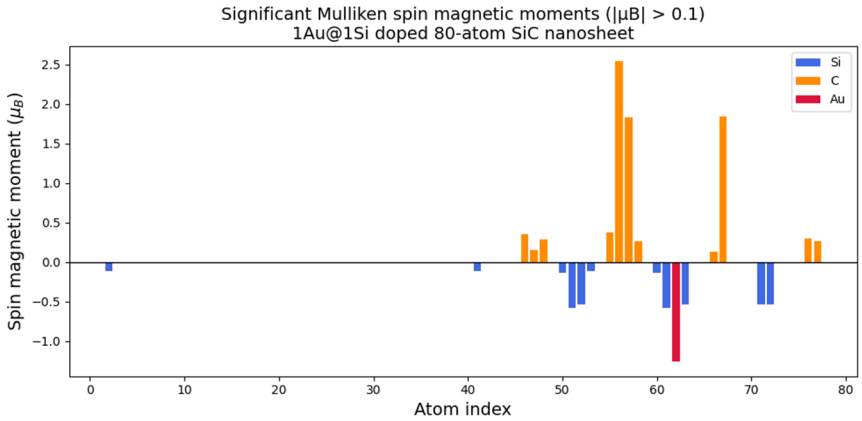


**Figure 10.** Atom-resolved Mulliken spin magnetic moments for the 1Au@1Si-doped SiC nanosheet

**Table 3.** Element-resolved Mulliken spin magnetic moments for the 1Au@1Si configuration

| Element | Number of atoms | Sum of spin moments ($\mu_B$) | Mean per atom ($\mu_B$) | Max \|moment\| ($\mu_B$) | Min ($\mu_B$) | Max ($\mu_B$) |
|---|---|---|---|---|---|---|
| C | 40 | 8.781 | 0.2195 | 2.543 | -0.011 | 2.543 |
| Si | 39 | -4.520 | -0.1159 | 0.583 | -0.583 | 0.001 |
| Au | 1 | -1.254 | -1.2540 | 1.254 | -1.254 | -1.254 |
| Total | 80 | ≈ 3.00 | | | | |

The reported total spin moment is 3.003$\mu_B$. Minor deviations on the order of $10^{-3}\mu_B$ arise from rounding of atom-resolved values.

**Table 4.** Dominant spin-carrying atoms in the 1Au@1Si configuration

| Atom index | Element | Spin moment ($\mu_B$) |
|---|---|---|
| 56 | C | +2.543 |
| 67 | C | +1.839 |
| 57 | C | +1.834 |
| 62 | Au | -1.254 |
| 51 | Si | -0.583 |
| 61 | Si | -0.581 |
| 52 | Si | -0.541 |
| 63 | Si | -0.537 |
| 71 | Si | -0.531 |
| 72 | Si | -0.531 |
| 55 | C | +0.379 |
| 46 | C | +0.348 |

Notably, the Au dopant itself carries a sizable negative local magnetic moment (−1.25 μB), whereas several neighboring carbon atoms exhibit unusually large positive moments exceeding +2.5 μB. The unusually large Mulliken moments obtained for several carbon atoms should be interpreted with caution because Mulliken populations depend on the employed basis set and population scheme.

This behavior suggests that the dominant magnetic contribution does not originate from the Au atom but is instead mediated by the surrounding carbon sublattice through strong Au–C hybridization. Such a redistribution of spin density is commonly associated with induced magnetism in doped sp-electron systems [32,33].

In contrast, silicon atoms acquire relatively small antiparallel magnetic moments, acting as a compensating magnetic background. Element-resolved analyses (Figs. 11 and 12) confirm that carbon provides the dominant positive contribution to the net magnetization, while both Si and Au contribute negatively. Atoms located far from the dopant site exhibit near-zero spin magnetic moments, confirming the localized nature of the magnetic perturbation.

These results demonstrate that even a single Au substitution is sufficient to generate robust magnetism in SiC nanosheets. Importantly, the magnetization is largely delocalized over the carbon framework rather than being confined to the heavy dopant atom, highlighting the central role of host-mediated spin polarization in Au-doped SiC systems [34,35].

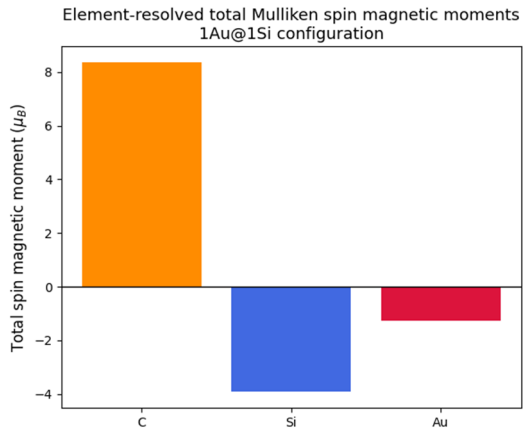


**Figure 11.** Element-resolved total Mulliken spin magnetic moments for the 1Au@1Si configuration

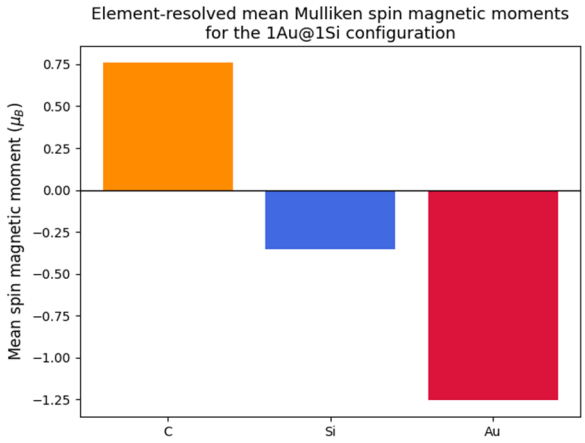


**Figure 12.** Element-resolved mean Mulliken spin magnetic moments for the 1Au@1Si-doped SiC nanosheet

### 3.2.3. Double Au Substitution: 2Au@2Si Configuration (General State)

Spin-polarized calculations for the 2Au@2Si configuration reveal a further enhancement of the magnetic response compared to the single-dopant case. As shown in Fig. 13, only a limited number of atoms exhibit significant local magnetic moments ($|\mu| > 0.1\mu_B$), indicating a highly localized yet intensified induced magnetism mechanism. The largest positive magnetic moments are predominantly localized on carbon atoms, reaching values of up to +2.41$\mu_B$, whereas silicon atoms and Au dopants exhibit negative (antiparallel) spin polarization.

Element-resolved integration (Fig. 14 and Table 5) demonstrates that carbon provides a large positive total spin magnetic moment (+19.06$\mu_B$), while silicon (−10.44μB) and gold (−2.62$\mu_B$) contribute compensating negative moments. The incomplete cancellation between these opposing sublattices results in a finite net magnetic moment of approximately 6.01$\mu_B$, confirming the stabilization of a ferrimagnetic-like ground state.

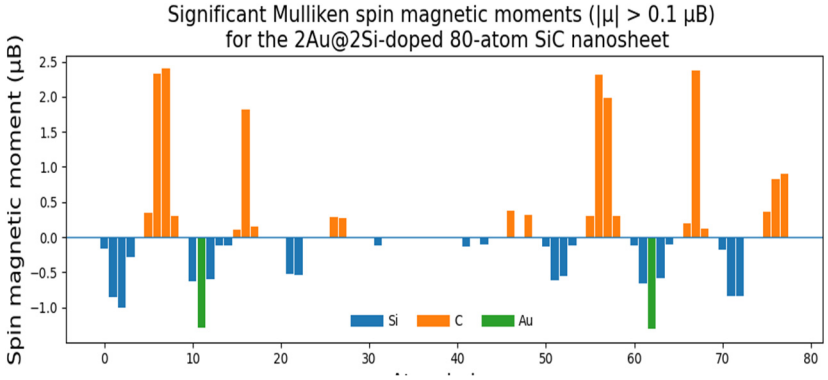


**Figure 13.** Local Mulliken spin magnetic moments for the 2Au@2Si-doped SiC nanosheet ($|\mu| > 0.1\mu_B$)

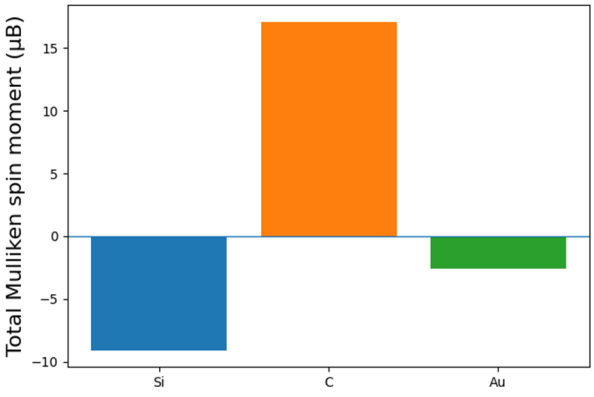


**Figure 14**. Element-resolved total Mulliken spin magnetic moments for the 2Au@2Si configura-tion

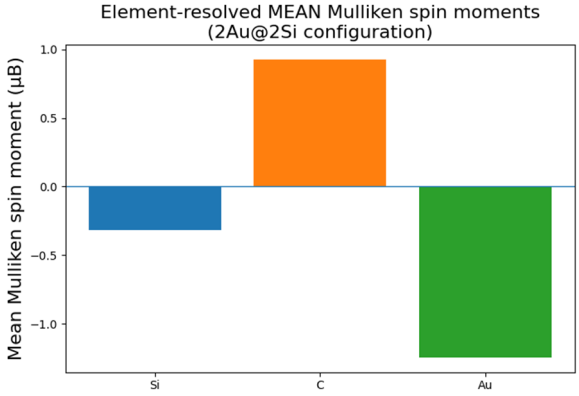


**Figure 15.** Element-resolved mean Mulliken spin magnetic moments for the 2Au@2Si-doped SiC nanosheet

**Table 5.** Element-resolved magnetic characteristics of the 2Au@2Si-doped 80-atom SiC nanosheet

| Element | Number of atoms | Total spin moment ($\mu_B$) | Mean spin moment per atom ($\mu_B$/atom) | Maximum ($\mu_B$) | Dominant spin role |
|---|---|---|---|---|---|
| C | 40 | +19.059 | +0.476 | +2.410 | Primary spin polarization carrier |
| Si | 38 | -10.437 | -0.275 | -1.005 | Antiparallel (compensating) host |
| Au | 2 | -2.616 | -1.308 | -1.319 | Dopant-induced antiparallel center |
| Total (Sum) | 80 | +6.007 | - | - | Net ferromagnetic moment |

### 3.2.4. Ferromagnetic and AFM-Initialized 2Au@2Si Configuration: Robust Carbon-Mediated Induced Ferrimagnetism and Spin-Compensation Mechanism

When the 2Au@2Si-doped 80-atom SiC nanosheet is initialized in a ferromagnetic (FM) state, the system converges to a stable spin-polarized solution with a net magnetic moment of $\Sigma\mu \approx 6.007$ μB. This behavior demonstrates that Au substitution induces an intrinsic magnetic response rather than a metastable artifact associated with the initial spin configuration (Tables 6 and 7). Atom-resolved Mulliken spin magnetic moments reveal that the magnetization is highly nonuniform and predominantly localized on a limited number of lattice sites in the vicinity of the do-pant-induced perturbation. The largest positive moments are hosted by carbon atoms (e.g., C7 ≈ +2.404 $\mu_B$, $C_{67}$ ≈ +2.372$\mu_B$, $C_6$ ≈ +2.331$\mu_B$, $C_{56}$ ≈ +2.317$\mu_B$, $C_{57}$ ≈ +1.983$\mu_B$, and $C_{16}$ ≈ +1.821$\mu_B$), as summarized in Table 10 and illustrated in Figures 16-18.

This pronounced localization on the carbon sublattice is physically consistent with a carbon-mediated induced-magnetism mechanism. Au substitution at Si sites perturbs the local bonding environment and electronic potential landscape, leading to reconstruction and spin splitting of C-p–dominated electronic states near the Fermi level. Within this mechanism, the dopant primarily acts as a spin polarizer that enables exchange-driven imbalance in the host electronic states, while the carbon sublattice becomes the principal reservoir of positive spin density. Element-resolved total moments corroborate this interpretation, showing that carbon provides the dominant positive contribution ($\Sigma\mu(C) \approx +19.057\mu_B$), whereas the silicon framework and Au dopants contribute antiparallel (negative) polarization ($\Sigma\mu(Si) \approx -10.450$ $\mu_B$ and $\Sigma\mu(Au) \approx -2.599\mu_B$), as reported in Table 7.

**Table 6.** Statistical summary of selected atom-resolved Mulliken local spin magnetic moments ($\mu_B$) for the FM-initialized 2Au@2Si-doped SiC nanosheet

| Descriptor | Local moment ($\mu_B$) | Atom(s)/index(es) | Brief comment |
|---|---|---|---|
| Au (mean) | -1.300 | Au(11)=-1.287, Au(62)=-1.312 | Au dopants align antiparallel to the net magnetization |
| $Au_1$ | -1.287 | Au(11) | Substitutional Au at Si site |
| $Au_2$ | -1.312 | Au(62) | Substitutional Au at Si site |
| C (maximum) | +2.404 | C(7) | Strong Au-C hybridization, dominant spin polarization |
| C (high values) | +2.372, +2.331, +2.317, +1.983, +1.821 | C(67), C(6), C(56), C(57), C(16) | Majority of magnetization localized on the C sublattice |
| Si (largest \|μ\|) | -0.998 | Si(2) | Si sublattice provides compensating (antiparallel) contribution |
| Si (smallest \|μ\|) | -0.005 | Si(34) | Near-zero moment, weak spin polarization |
| Total moment (sum) | 6.007 | - | Net magnetization: FM, ferrimagnetic-like distribution |

**Table 7.** Element-resolved Mulliken spin magnetic moments for the FM 2Au@2Si–SiC nanosheet.

| Element | Number of atoms | Total spin moment ($\mu_B$) |
|---|---|---|
| C | 40 | 19.0570 |
| Si | 38 | -10.4500 |
| Au | 2 | -2.5990 |

This antiparallel partitioning is also reflected in the element-resolved mean magnetic moments (Figures 16 and 17), indicating that Si and Au atoms do not suppress the magnetization but instead participate through spin compensation. Specifically, they develop induced negative moments that partially offset the strong carbon-derived magnetization. Such a compensated spin arrangement is most appropriately described as ferromagnetic-like, since different sublattices carry oppositely oriented spin polarization whose magnitudes do not fully cancel, resulting in a finite net magnetic moment.

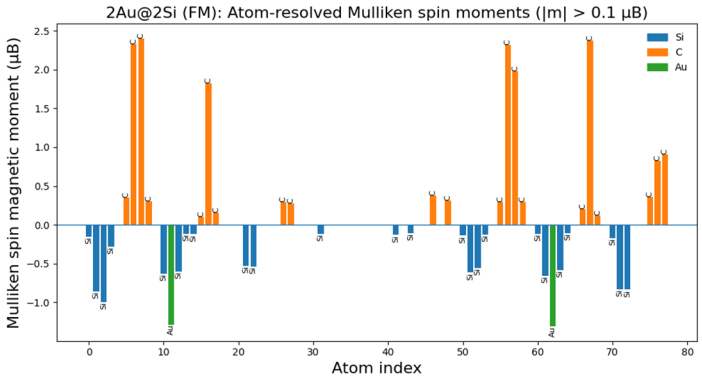


**Figure 16.** Element-resolved mean spin magnetic moments. Carbon atoms exhibit a dominant positive contribution that governs the ferromagnetic net response, while Si and Au show antiparallel (negative) polarization, providing partial compensation

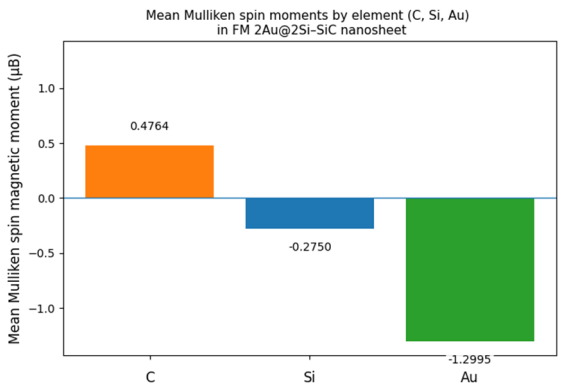


**Figure 17.** Element-resolved mean Mulliken spin magnetic moments for the FM 2Au@2Si-doped SiC nanosheet, showing positive spin polarization on C atoms and compensating negative moments on Si and Au, with Au contributing the largest negative component

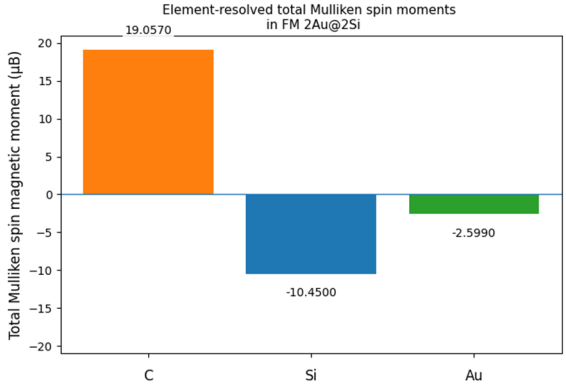


**Figure 18.** Element-resolved Mulliken spin magnetic moments for the FM 2Au@2Si configuration, showing a dominant positive contribution from the carbon sublattice and compensating anti-parallel moments on Si and Au atoms

A critical stability test is provided by the antiferromagnetic (AFM) initialization. If the magnetism were merely an imposed FM solution, an AFM initial condition would be expected to relax toward a compensated AFM state ($\Sigma\mu \rightarrow 0$) or to a qualitatively different local-moment distribution. Instead, the AFM-initialized calculation converges to essentially the same non-compensated magnetic solution with $\Sigma\mu \approx 6.007\mu_B$ (Table 8), demonstrating that the magnetic ground state is robust against the initial magnetic ordering and is dictated by intrinsic dopant–host interactions.

**Table 8.** Element-wise summary of Mulliken magnetic moments for the AFM 2Au@2Si–SiC nanosheet

| Element | Number of atoms (N) | Total magnetic moment, $\Sigma\mu$ ($\mu_B$) | Mean magnetic moment, $\langle\mu\rangle$ ($\mu_B$/atom) | Mean $\lvert\mu\rvert$ ($\mu_B$/atom) | Minimum $\mu$ ($\mu_B$) | Maximum $\mu$ ($\mu_B$) |
|---|---|---|---|---|---|---|
| Au | 2 | −2.596 | −1.298 | 1.298 | −1.310 | −1.286 |
| C | 40 | +19.055 | +0.476 | 0.477 | −0.003 | +2.397 |
| Si | 38 | −10.452 | −0.275 | 0.275 | −0.997 | −0.005 |
| Total | 80 | +6.007 | — | — | — | — |

Atom-resolved AFM moments (Figure 19 and Table 9) confirm that the largest positive moments remain localized on carbon sites (maximum ≈+2.397$\mu_B$ on C7, followed by ≈ +2.374 $\mu_B$ on $C_{67}$ and ≈+2.335$\mu_B$ on $C_6$), while both Au dopants retain sizeable antiparallel moments ($Au_{11}$ ≈-1.286 $\mu_B$ and $Au_{62}$ ≈ -1.310$\mu_B$). Silicon atoms again act as distributed compensating centers, with the largest magnitude observed at Si2 (≈-0.997$\mu_B$).

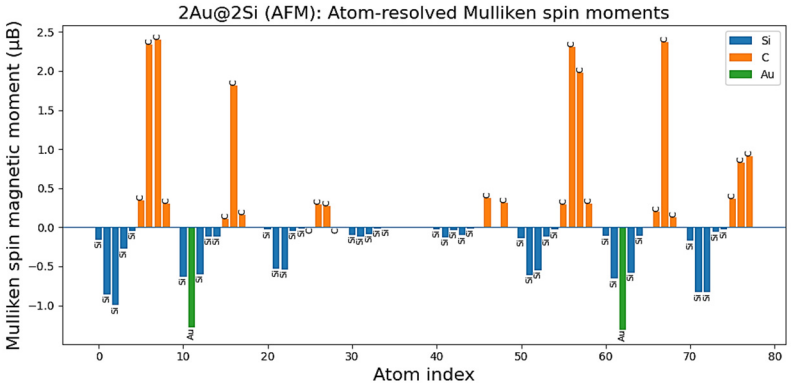


**Figure 19.** Atom-resolved Mulliken spin magnetic moments for the AFM-initialized 2Au@2Si–SiC nanosheet

**Table 9.** Statistical summary of selected atom-resolved Mulliken local spin magnetic moments (μB) for the AFM-initialized 2Au@2Si-doped SiC nanosheet

| Descriptor | Local moment ($\mu_B$) | Atom(s)/index(es) | Brief comment |
|---|---|---|---|
| Au (mean) | -1.298 | Au(11) = -1.286, Au(62) = -1.310 | Au dopants polarize in an antiparallel direction |
| $Au_1$ | -1.286 | Au(11) | Substitutional Au at a Si site |
| $Au_2$ | -1.310 | Au(62) | Substitutional Au at a Si site |
| C (maximum) | +2.397 | C(7) | Strong Au–C hybridization, dominant spin polarization |
| C (high values) | +2.374, +2.335, +2.313, +1.980, +1.819 | C(67), C(6), C(56), C(57), C(16) | Majority of the magnetization is localized on the carbon sublattice |
| Si (largest $\lvert\mu\rvert$) | −0.997 | Si(2) | Si sublattice provides compensating (antiparallel) contribution |
| Si (smallest $\lvert\mu\rvert$) | −0.005 | Si(34) | Near-zero moment, weak spin polarization |
| Total moment (sum) | 6.007 | — | Finite net magnetic moment (based on total sum) |

Element-resolved decomposition in the AFM state (Figures 20-21 and Table 9) quantitatively reproduces the FM partitioning: $\Sigma\mu$(C) ≈+19.055 $\mu_B$, $\Sigma\mu$(Si) ≈-10.452 $\mu_B$, and $\Sigma\mu$(Au) ≈-2.596$\mu_B$, yielding the same net magnetic moment through incomplete sublattice cancellation.

This unified physical picture is reinforced by the comparative summary across the General, FM, and AFM solutions (Figure 22 and Table 10). The consistency of (i) the mean local moment on Au atoms (≈ -1.30μB), (ii) the maximum local moments on carbon atoms (≈+2.40$\mu_B$), (iii) the ex-trema of Si moments (largest $\lvert\mu\rvert$ ≈ -1.0μB and smallest ≈ -0.005μB), and (iv) the total magnetic moment $\Sigma\mu \approx 6.0\mu_B$ demonstrates that the magnetization is not confined to the dopant sites but is redistributed over the SiC lattice with a dominant carbon character.

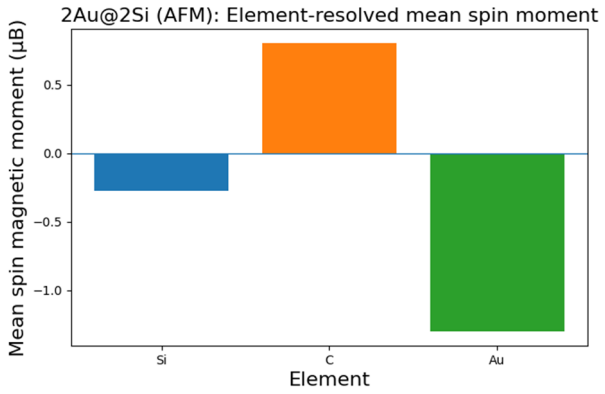


**Figure 20.** Element-resolved total Mulliken spin magnetic moments ($\mu_B$): carbon provides a positive contribution, while silicon and gold contribute to compensating negative moments

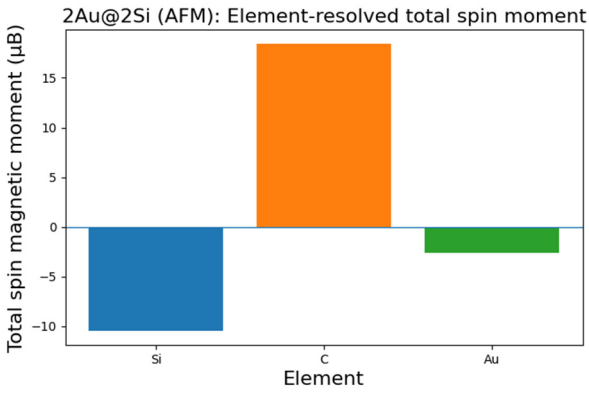


**Figure 21.** Element-resolved mean Mulliken spin magnetic moments (AFM state)

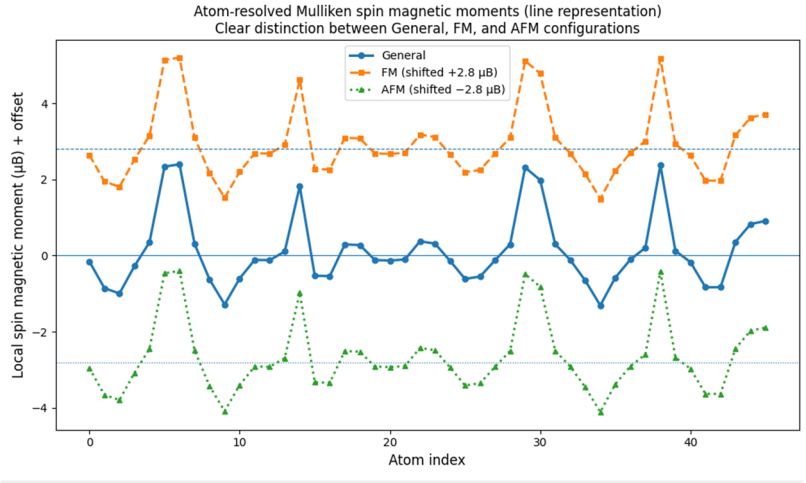


**Figure 22.** Atom-resolved Mulliken spin magnetic moments of the 2Au@2Si-doped SiC nanosheet comparing the general, FM, and AFM configurations

**Table 10.** Unified comparison of Mulliken spin magnetic moments for the 2Au@2Si–doped SiC nanosheet under General, FM, and AFM configurations

| Quantity /Descriptor | General configuration | FM configuration | AFM configuration | Physical interpretation |
|---|---|---|---|---|
| Au (mean local moment, $\mu_B$) | -1.298 | -1.300 | -1.298 | Au dopants consistently show antiparallel polarization |
| Au1(μB) | -1.286 ($Au_{11}$) | -1.287 ($Au_{11}$) | -1.286 ($Au_{11}$) | Substitutional Au at Si site |
| Au2(μB) | -1.310 ($Au_{62}$) | -1.312 ($Au_{62}$) | -1.310 ($Au_{62}$) | Substitutional Au at Si site |
| C (maximum local moment, $\mu_B$) | +2.410 (C7) | +2.404 ($C_7$) | +2.397 ($C_7$) | Strong Au-C hybridization, dominant spin polarization |
| C (other high local moments, $\mu_B$) | +2.383, +2.331, +2.316, +1.998, +1.828 | +2.372, +2.331, +2.317, +1.983, +1.821 | +2.374, +2.335, +2.313, +1.980, +1.819 | Spin density mainly localized on selected C atoms |
| Si (largest) | μ | ($\mu_B$) | -1.005 ($Si_2$) | -0.998 ($Si_2$) |
| Si (smallest | μ | ($\mu_B$) | -0.005 ($Si_{34}$) | -0.005 ($Si_{34}$) |
| Total moment Σμ ($\mu_B$) | ≈ 6.007 | 6.007 | 6.007 | Robust net magnetic moment |
| Magnetic character | Ferrimagnetic-like | FM / ferrimagnetic-like | AFM-initialized → ferrimagnetic | Ground state is insensitive to initial spin ordering |

From a spintronics perspective, this behavior is particularly advantageous. A robust, nonzero net magnetic moment that is insensitive to the initial spin configuration implies a stable magnetic response under perturbations, while the carbon-dominated spin polarization suggests that transport-relevant electronic states may acquire significant spin

selectivity through host-state exchange splitting. Overall, the FM/AFM convergence behavior, together with the element-wise compensation pattern, provides strong evidence that Au substitution at Si sites stabilizes a carbon-driven, compensated ferrimagnetic-like magnetic ground state in SiC nanosheets, governed by induced spin polarization and dopant–host hybridization effects (Figures 16–21; Tables 5–9; Figure 22; Table 10) [30–44].

### 3.3. Curie Temperature Estimation and Magnetic Stability of Au-Doped SiC Nanosheets

In this section, the magnetic stability and Curie temperature–related characteristics of pristine and Au-substituted SiC nanosheets are systematically investigated within a first-principles framework. Spin-polarized density functional theory (DFT) calculations combined with Mulliken spin population analysis were employed to examine five representative configurations: pristine SiC nanosheet, single Au substitution at a Si site (1Au@1Si), double Au substitution at two Si sites (2Au@2Si) in the non-magnetic (NM) state, as well as ferromagnetic (FM) and antiferromagnetic (AFM) initializations of the same 2Au@2Si composition. This strategy enables a consistent assessment of dopant-induced magnetism and the energetic preference among different magnetic states under identical computational conditions.

The total energies of all configurations were calculated using the same computational parameters. For accurate total-energy comparisons, the electronic smearing was reduced to a very small value to minimize entropy-related contributions while maintaining numerical stability (Table 11). These energies form the basis for analyzing magnetic ordering and estimating the Curie temperature.

**Table 11.** Total energies of pristine and Au-substituted SiC nanosheets calculated under identical conditions for non-magnetic (NM), ferromagnetic (FM), and antiferromagnetic (AFM) states of the 2Au@2Si configuration

| Configuration | Total energy (eV) |
|---|---|
| Pristine SiC nanosheet | -13295.45214 |
| 1Au1Si | -14484.79843 |
| 2Au(2Si) | -15514.21941 |
| FM_2Au(2Si) | -15514.28516 |
| AFM_2Au(2Si) | -15514.28677 |

It should be noted that direct comparison of absolute total energies between pristine, 1Au@1Si, and 2Au@2Si systems is not physically meaningful due to their different atomic compositions; such comparisons require a formation-energy analysis. In contrast, for the same 2Au@2Si composition, direct comparison among NM, FM, and AFM solutions is valid and allows reliable evaluation of magnetic stability [45].

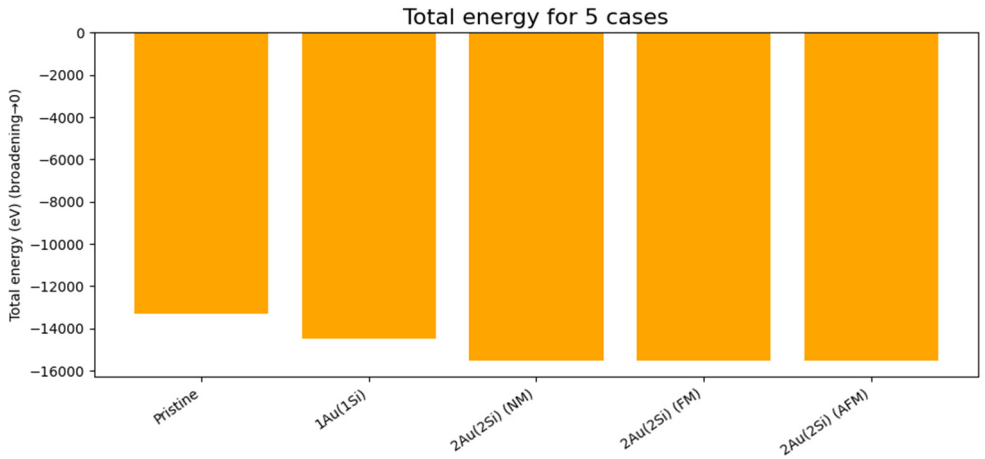


**Figure 23.** Total energy comparison for pristine SiC, 1Au@Si, and 2Au@2Si configurations in non-magnetic (NM), ferromagnetic (FM), and antiferromagnetic (AFM) states, showing energetic preference of magnetic solutions over the NM state for 2Au@2Si.

As summarized in Table 11 and illustrated in Figure 23, both magnetic solutions are significantly more stable than the non-magnetic reference state. The AFM initialization yields the lowest total energy, followed very closely by the FM state, establishing the energetic hierarchy

$$E_{AFM} < E_{FM} \ll E_{NM}$$

This result indicates that spin polarization provides a substantial stabilization of the Au-doped system, while the precise spin alignment plays a secondary role.

The energy gain associated with the onset of magnetism, which quantifies the stabilization of the magnetic phase, is defined as

$$\Delta E_{mag} = E_{NM} - E_{FM} \tag{7}$$

yielding $\Delta E_{mag} = 0.06575\text{meV}$. Furthermore, the energy difference between the AFM and FM configurations,

$$\Delta E_{AFM-FM} = E_{AFM} - E_{FM} \approx -1.61 \text{ meV} \tag{8}$$

is extremely small, indicating a near degeneracy between these two magnetic states (Figure 24). Such a small exchange energy suggests weak magnetic coupling and implies that the magnetic ground state is only weakly sensitive to the relative spin alignment, with the dominant driving force being the overall energy lowering due to spin polarization [46-48].

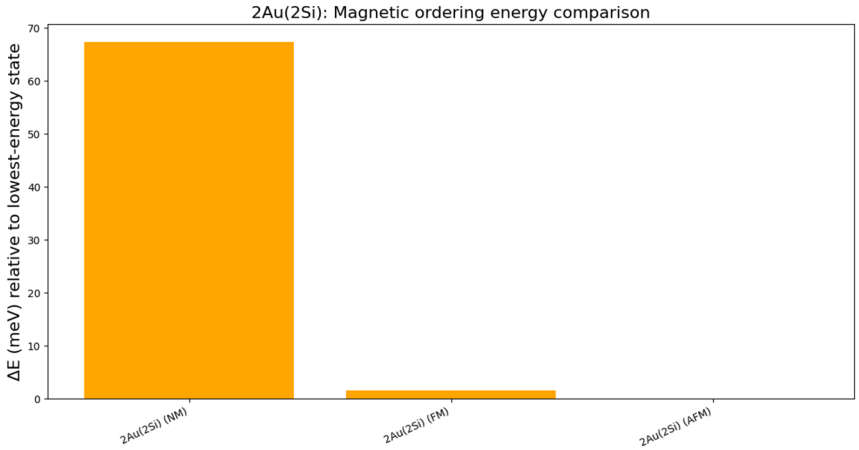


**Figure 24.** Relative energy differences (ΔE, meV) between NM, FM, and AFM states for the 2Au@2Si system, showing a small FM-AFM splitting (~1-2meV) indicative of near-degenerate magnetic orderings

The Curie temperature ($T_C$), which characterizes the thermal transition from a spin-polarized magnetic phase to a spin-degenerate paramagnetic state, was estimated using the mean-field approximation (MFA). This approach is widely adopted in first-principles studies of low-dimensional magnetic systems due to its conceptual simplicity and ability to provide qualitative trends in magnetic ordering temperatures [49, 50]. Within the MFA framework, the Curie temperature is directly related to the magnetic stabilization energy according to

$$k_B T_C^{MFA} \approx \frac{2}{3}\Delta E_{mag}. \tag{9}$$

Where $k_B$=8.617×10$^{-5}$ eV/K is the Boltzmann constant and $\Delta E_{mag}$ represents the energy gain due to spin polarization. Using the calculated magnetic stabilization energy $\Delta E_{mag} = 0.06575$ eV for the 2Au@2Si configuration, the Curie temperature is estimated as

$$T_C^{MFA} = \frac{2}{3}\frac{0.06575}{8.617\times10^{-5}} \approx 5.1 \cdot 10^2 K.$$

Thus, the MFA-estimated Curie temperature of the Au-doped SiC nanosheet is approximately 510 K.

It should be emphasized that the present Curie temperature represents a mean-field approximation (MFA) estimate. The MFA neglects thermal spin fluctuations and spin-wave excitations, which are known to reduce the actual magnetic ordering temperature, particularly in low-dimensional and two-dimensional magnetic systems. Therefore, the calculated Tc value should be regarded as an approximate upper-limit estimate that reflects the tendency toward magnetic ordering rather than an exact prediction of the experimental Curie temperature.

The total-energy comparison for the five investigated configurations is summarized in Figure 23, which clearly shows that magnetic solutions for the same 2Au@2Si composition are energetically favored over the non-magnetic reference state. Furthermore, Figure 24 highlights the relative energy differences between the NM, FM, and AFM states for the 2Au@2Si system. The very small AFM–FM energy splitting (≈1-2 meV) indicates near degeneracy between different magnetic orderings, implying weak exchange interactions but a robust stabilization against the non-magnetic state.

A comparison of the estimated Curie temperature of the present Au-doped SiC nanosheet with previously reported transition-metal-doped SiC-based low-dimensional systems is provided in Table 12. Notably, the predicted $T_C$ of approximately 510K exceeds those reported for V-, Fe-, and Mn-doped SiC nanostructures calculated using similar DFT-based MFA approaches [50]. This comparison highlights the effectiveness of Au substitution in stabilizing thermally robust magnetism in two-dimensional SiC systems.

**Table 12.** *Comparison of Curie temperatures of transition-metal–doped SiC-based low-dimensional systems calculated using DFT-based mean-field approximations, highlighting the highest estimated Curie temperature for the present Au-doped SiC nanosheet.*

| System | Method | Tc (K) | Reference |
|---|---|---|---|
| V-doped SiC nanotube | DFT+U (MFA) | 420 | Physica E 158 (2024) 115641 |
| Fe-doped SiC nanosheet | DFT+U (MFA) | 460 | Materials Science in Semiconductor Processing 197 (2025) 109702 |
| Mn-doped SiC nanosheet | DFT (MFA) | 380 | Journal of Magnetism and Magnetic Materials *530* (2021) 167926 |
| Au-doped SiC nanosheet (this work) | DFT+U (MFA) | ≈ 510 | Present work |

The dependence of the Curie temperature on the magnetic stabilization energy is illustrated in Figure 25, which shows the linear relationship between $T_C$ and ΔEmag within the MFA framework.

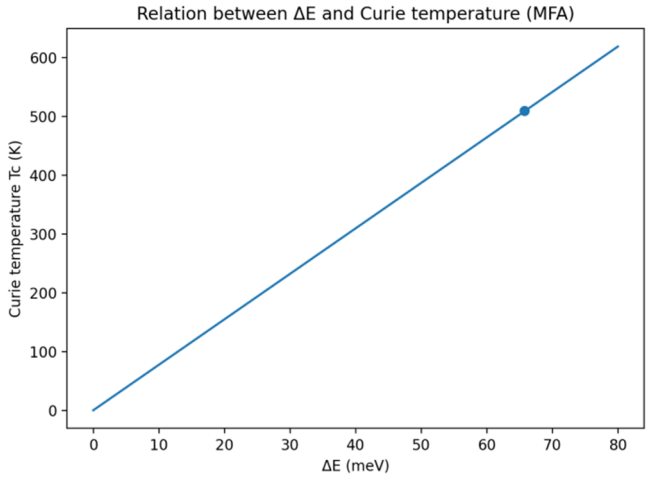


**Figure 25.** Mean-field-approximation (MFA) Curie temperature Tc as a function of the NM–FM energy difference ΔE, illustrating the estimated magnetic ordering temperature of the Au-doped SiC nanosheet.

The corresponding temperature dependence of the normalized magnetization is constructed using the standard mean-field expression

$$\frac{M(T)}{M_0} = \left(1 - \frac{T}{T_C}\right)^{1/2}, \quad T < T_C, \tag{10}$$

as shown in Figure 26.

While pristine SiC and the non-magnetic reference configuration exhibit vanishing magnetization over the entire temperature range, the 2Au@2Si system retains a finite magnetization up to approximately $T_C$≈510K, confirming the thermal robustness of the dopant-induced magnetic state.

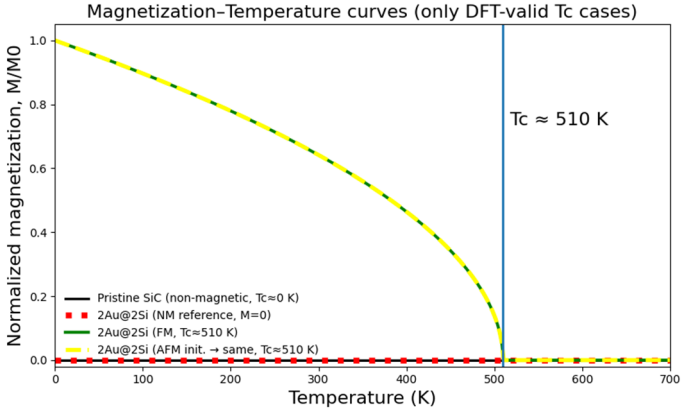


**Figure 26.** MFA-calculated normalized magnetization (M/M0) for 2Au@2Si, showing finite magnetization up to the estimated Tc ≈ 510 K within the mean-field approximation

Overall, the combined Mulliken spin population analysis, total-energy stability assessment, and MFA-based Curie temperature estimation consistently demonstrate that double Au substitution at Si sites stabilizes a robust high-temperature magnetic phase in SiC nanosheets. Importantly, the magnetism is predominantly mediated by dopant-induced electronic reconstruction within the carbon sublattice rather than by localized magnetic moments on the Au atoms

themselves. The MFA-estimated Curie temperature suggests the possibility of magnetic ordering above room temperature. However, more sophisticated approaches beyond the mean-field approximation would be required to quantitatively predict the experimental Curie temperature.

## 4. CONCLUSIONS

In summary, a comprehensive spin-polarized first-principles investigation has been carried out to elucidate the electronic structure, magnetic behavior, and thermal stability of Au-doped two-dimensional SiC nanosheets. Single (1Au@Si) and double (2Au@2Si) substitutional doping configurations were systematically examined in a large supercell framework to minimize artificial dopant–dopant interactions and ensure a reliable assessment of intrinsic properties.

The results demonstrate that Au substitution provides an effective route for band-gap engineering in SiC nanosheets, leading to pronounced band-gap narrowing while preserving spin-degenerate band dispersions and the overall semiconducting character of the host material. Orbital-resolved density-of-states analysis reveals that the electronic reconstruction near the Fermi level is dominated by Au 5d states, with comparatively minor contributions from Au 6s and 6p orbitals.

Despite the absence of exchange splitting in the band structure, Mulliken spin population analysis uncovers robust dopant-induced magnetism mediated predominantly by the carbon sublattice. In the 1Au@Si configuration, a net magnetic moment of approximately 3 μB is stabilized, whereas double Au substitution gives rise to a ferrimagnetic-like ground state with a total magnetic moment of about 6 μB. Importantly, the magnetic solution is found to be insensitive to the initial spin configuration, as ferromagnetic and antiferromagnetic initializations converge to nearly identical magnetic states, highlighting the intrinsic and robust nature of the induced magnetism.

Total-energy comparisons confirm that spin-polarized states are energetically favored over the non-magnetic reference, with a very small energy difference between ferromagnetic and antiferromagnetic solutions. Mean-field estimation based on first-principles total-energy differences yields an estimated Curie temperature of approximately 510 K for the 2Au@2Si configuration. Since the mean-field approximation neglects thermal spin fluctuations, this value should be regarded as an approximate upper-limit estimate, suggesting the possibility of magnetic ordering above room temperature.

Overall, the present study establishes Au-doped SiC nanosheets as a promising class of two-dimensional dilute magnetic semiconductors in which band-gap tunability and the possibility of high-temperature magnetic ordering coexist.

The carbon-mediated nature of the induced magnetism, combined with the preservation of semiconducting behavior, highlights the strong potential of these systems for future spintronic and multifunctional nano-electronic applications.

## Declarations

**Ethics approval and consent to participate**
Not applicable

**Consent for publication**
Not applicable.

**Funding**
This research did not receive any specific grant from funding agencies in the public, commercial, or not-for-profit sectors.

**Acknowledgements**
The authors gratefully acknowledge the computational resources and academic support provided by Azerbaijan State Oil and Industry University. The authors also acknowledge the Arifov Institute of Ion-Plasma and Laser Technologies (Uzbekistan) for institutional collaboration and scientific support.

**Availability of data and materials**
The datasets generated and analyzed during the current study are available from the corresponding author upon reasonable request.

**Competing interests**
The authors declare that they have no competing interests.

**Authors' contributions**
Sevda Rzayeva conceived and designed the study, performed the DFT simulations, analyzed the electronic and magnetic properties, and drafted the manuscript.
Yuldosh Yakubov contributed to the conceptual development, provided expertise on nanostructures, and reviewed the manuscript.
Umedjon Khalilov contributed to the scientific discussion, interpretation of the results, and critical revision of the manuscript.
All authors read and approved the final manuscript.

## ORCID

**Sevda Rzayeva,** https://orcid.org/0009-0006-9747-3972; **Umedjon Khalilov,** https://orcid.org/0000-0003-3841-1895

## REFERENCES

[1] A.K. Geim, and I.V. Grigorieva, "Van der Waals heterostructures," Nature, **499**, 419–425 (2013). https://doi.org/10.1038/nature12385
[2] S.A. Wolf, D.D. Awschalom, R.A. Buhrman, *et al*., "Spintronics: A spin-based electronics vision for the future," Science, **294**, 1488–1495 (2001). https://doi.org/10.1126/science.1065389
[3] D. Pesin, and A.H. MacDonald, "Spintronics and pseudospintronics in graphene and topological insulators," Nat. Mater. **11**, 409-416 (2012). https://doi.org/10.1038/nmat3305

[4] S. Chabi, and K. Kadel, "Two-Dimensional Silicon Carbide: Emerging Direct Band Gap Semiconductor," Nanomaterials, **10**, 2226 (2020). https://doi.org/10.3390/nano10112226
[5] R. Madar, "Materials science: silicon carbide in contention," Nature, **430**(7003), 974-975 (2004). https://doi.org/10.1038/430974a
[6] H. Ohno, Making nonmagnetic semiconductors ferromagnetic, Science **281**, 951–956 (1998). https://doi.org/10.1126/science.281.5379.951
[7] S. Sanvito, "Molecular spintronics," Chem. Soc. Rev. **40**, 3336-3355 (2011). https://doi.org/10.1039/c1cs15047b
[8] W. Chen, Q. Chen, J. Zhang, *et al*., "Electronic and magnetic properties of transition-metal-doped monolayer $B_2S_2$ within the GGA + U framework," RSC Adv. **14**, 3390–3399 (2024). https://doi.org/10.1039/D3RA08472H
[9] C. Gong, L. Li, Z. Li, *et al*., "Discovery of intrinsic ferromagnetism in two-dimensional van der Waals crystals," Nature, **546**, 265–269 (2017). https://doi.org/10.1038/nature22060
[10] V.N. Jafarova, S.S. Rzayeva, S. Popa, *et al*., Prediction of electronic, magnetic, and structural stability characteristics in Al- and Ga-doped single-walled SiC nanotubes: An ab initio study, Phys. Chem. Chem. Phys. **27**, 25980–26010 (2025). https://doi.org/10.1039/D5CP03523F
[11] S. Rzayeva, V.N. Jafarova, and D.D. Roy, "First-principles prediction of ferromagnetism and Curie temperature for transition-metal-doped (6,0) SiC nanotubes," Mater. Sci. Semicond. Process, **197**, 109702 (2025). https://doi.org/10.1016/j.mssp.2025.109702
[12] V.N. Jafarova, S.S. Rzayeva, V.I. Eminova, *et al*., "Theoretical investigation of electronic and magnetic characteristics of ZnSe substituted and co-substituted with transition metals," Int. J. Mod. Phys. B, **39**, 2550201 (2025). https://doi.org/10.1142/S0217979225502017
[13] V.N. Jafarova, S. S. Rzayeva, U. Abdurahmanova *et al*., "Spintronic potential of ZnSe doped with 3d transition metals: Insights from first-principles calculations," Indian J. Phys. (2025). https://doi.org/10.1007/s12648-025-03794-8
[14] M. Kurpas, P.E. Faria Junior, M. Gmitra, and J. Fabian, "Spin–orbit coupling in elemental two-dimensional materials," Phys. Rev. B, **100**, 125422 (2019). https://doi.org/10.1103/PhysRevB.100.125422
[15] J. He, G. Liu, C. Zhang, and G. Zhang, "Electronic structure and magnetic properties of noble metal (Rh, Ru, Pd, Ag) adsorbed vacancy-defective arsenene: A first-principles study," Int. J. Quantum Chem. **123**, e27197 (2023). https://doi.org/10.1002/qua.27197
[16] Q.J. Wang, Q.H. Tan, and Y.K. Liu, "Magnetic properties in carbon-doped In2O3: A density functional theory investigation," Physica B: Condensed Matter, **450**, 54–57 (2014). https://doi.org/10.1016/j.physb.2014.05.033
[17] S. Smidstrup, T. Markussen, P. Vancraeyveld, *et al*., "QuantumATK: An integrated platform of electronic and atomic-scale modelling tools, J. Phys.: Condens. Matter, **32**, (2020) 015901. https://doi.org/10.1088/1361-648X/ab4007
[18] O. Gunnarsson, and B.I. Lundqvist, "Exchange and correlation in atoms, molecules, and solids by the spin-density-functional formalism," Phys. Rev. B, **13**, 4274–4298 (1976). https://doi.org/10.1103/PhysRevB.13.4274
[19] J. P. Perdew, and A. Zunger, "Self-interaction correction to density-functional approximations for many-electron systems," Phys. Rev. B, **23**, 5048–5079 (1981). https://doi.org/10.1103/PhysRevB.23.5048
[20] J. Junquera, Ó. Paz, D. Sánchez-Portal, and E. Artacho, "Numerical atomic orbitals for density functional calculations," Phys. Rev. B, **64**, 235111 (2001). https://doi.org/10.1103/PhysRevB.64.235111
[21] G. Kresse, and J. Furthmüller, "Efficient iterative schemes for ab initio total-energy calculations using a plane-wave basis set," Phys. Rev. B, **54**, 11169–11186 (1996). https://doi.org/10.1103/PhysRevB.54.11169
[22] Y. Ding, Y. Wang, J. Ni, *et al*., "First principles study of structural, elastic, and electronic properties of graphene-like $MX_2$ (M = Si, Ge; X = C, Si)," Physica B: Condensed Matter, **406**, 2254–2260 (2011). https://doi.org/10.1016/j.physb.2011.03.012
[23] H. Zhang, Y. Ma, and Z. Chen, "Stability and electronic properties of two-dimensional silicon carbide sheets," Solid State Commun. **151**, 1641–1645 (2011). https://doi.org/10.1016/j.ssc.2011.08.028
[24] H. Sahin, S. Cahangirov, M. Topsakal, and S. Ciraci, "Monolayer honeycomb structures of group-IV elements and III–V binary compounds," Phys. Rev. B, **80**, 155453 (2009). https://doi.org/10.1103/PhysRevB.80.155453
[25] K. Dolui, I. Rungger, and S. Sanvito, "Origin of the doping asymmetry in two-dimensional materials," Phys. Rev. B, **87**, 165402 (2013). https://doi.org/10.1103/PhysRevB.87.165402
[26] X. Yang, Y. Shen, J. Liu, X. Meng, X. Gao, L. Lv, M. Zhou, Y. Zhang, Y. Zheng, and Z. Zhou, "Electronic and optical properties of a novel two-dimensional semiconductor material $TlPt_2S_3$: A first-principles study," Phys. Chem. Chem. Phys. 24, 7642–7652 (2022). https://doi.org/10.1039/D1CP05918A
[27] Z. Zhang, X. Liu, J. Yu, *et al*., "Tunable electronic and magnetic properties of two-dimensional materials and their one-declensional derivatives," WIREs Comput. Mol. Sci. **6**, e1251 (2016). https://doi.org/10.1002/wcms.1251
[28] Y. Li, Z. Zhou, S. Zhang, and Z. Chen, "$MoS_2$ nanoribbons: high stability and unusual electronic and magnetic properties," J. Am. Chem. Soc. **130**, 16739–16744 (2008). https://doi.org/10.1021/ja805545x
[29] V.N. Jafarova and S. Rzayeva, "The effect of doping on the electronic and magnetic properties of GaN nanotubes: A preliminary study within the framework of LDA and LDA+U methods," Journal of the Faculty of Engineering and Architecture of Gazi University, **40** (4), 2627–2634 (2025). https://doi.org/10.17341/gazimmfd.1625213
[30] R.S. Mulliken, "Electronic population analysis on LCAO–MO molecular wave functions. I," J. Chem. Phys. **23**, 1833–1840 (1955). https://doi.org/10.1063/1.1740588
[31] J.P. Perdew, K. Burke, and M. Ernzerhof, "Generalized gradient approximation made simple," Phys. Rev. Lett. **77**, 3865–3868 (1996). https://doi.org/10.1103/PhysRevLett.77.3865
[32] S. Chabi, and K. Kadel, "Two-dimensional Silicon carbide: emerging direct band gap semiconductor," Nanomaterials, **10**, 2226 (2020). https://doi.org/10.3390/nano10112226
[33] S. Chabi, Z. Guler, A. Brearley, *et al*., "The creation of true two-dimensional silicon carbide," Nanomaterials, **11**, 1799 (2021). https://doi.org/10.3390/nano11071799
[34] Z. Shi, Z. Zhang, A. Kutana, and B.I. Yakobson, "Predicting two-dimensional silicon carbide monolayers," ACS Nano, **9**, 9802-9809 (2015). https://doi.org/10.1021/acsnano.5b02753

[35] R. Katoch, and S. Jain, "Magnetic Properties of 2D Materials," in: *Emerging Two Dimensional Materials and Applications*, (CRC Press, 2022), pp. 95–122. https://doi.org/10.1201/9781003247890-6
[36] M. Luo, Y.H. Shen, and T.L. Yin, "Ab initio study of electronic and magnetic properties in TM-doped SiC, Physica E: Low-dimensional Systems and Nanostructures," **85**, 280–284 (2017). https://doi.org/10.1016/j.physe.2016.08.028
[37] L. Jiang, Y. Dong and Z. Cui, "Adsorption of metal atoms (including Au) on SiC monolayer: electronic and magnetic properties from DFT," Inorganics, **11**, 240 (2023). https://doi.org/10.3390/inorganics11060240
[38] L. Zhang, and Z. Cui, "First-Principles Study of Metal Impurities in Silicon Carbide: Structural, Magnetic, and Electronic Properties," Front. Mater. **9**, 956675 (2022). https://doi.org/10.3389/fmats.2022.956675
[39] O.V. Yazyev, and L. Helm, "Defect-induced magnetism in graphene," Phys. Rev. B, **75**, 125408 (2007). https://doi.org/10.1103/PhysRevB.75.125408
[40] R.R. Nair, I.-L. Tsai, M. Sepioni, *et al*., "Dual origin of defect magnetism in graphene and its reversible switching by doping," Nat. Commun. **4**, 2010 (2013). https://doi.org/10.1038/ncomms3010
[41] J. Hernández-Tecorralco, L. Meza-Montes, M. E. Cifuentes-Quintal, *et al*., "Understanding the sp magnetizm in substitutionally doped graphene: a first-principles study," Phys. Rev. B, **105**, 224425 (2022). https://doi.org/10.1103/PhysRevB.105.224425
[42] M. Houmad, O. Dakir, H. Benzidi, *et al*., "Magnetic behavior of Mn-doped SiC nanosheet," Int. J. Mod. Phys. B, **31**, 1750163 (2017). https://doi.org/10.1142/S0217979217501636
[43] X. He, T. He, Z. Wang, and M. Zhao, "Neutral vacancy-defect-induced magnetism in SiC mono-layer," Physica E, **42**, 2451-2454 (2010). https://doi.org/10.1016/j.physe.2010.06.010
[44] Q. Wei, Y. Yang, G. Yang, and X. Peng, "New stable two-dimensional silicon carbide nanosheets," J. Alloys Compd. **868**, 159201 (2021). https://doi.org/10.1016/j.jallcom.2021.159201, arXiv: arXiv.2012.07841
[45] J. Hafner, "Ab-initio simulations of materials using VASP: Density-Functional theory and Beyond," J. Comput. Chem. **29**, 2044-2078 (2008). https://doi.org/10.1002/jcc.21057
[46] M. Pajda, J. Kudrnovský, I. Turek, *et al*., "Ab initio calculations of exchange interactions, spin-wave stiffness, and Curie temperatures of Fe, Co, and Ni," Phys. Rev. B, **64**, 174402 (2001). https://doi.org/10.1103/PhysRevB.64.174402
[47] S. Rusz, L. Bergqvist, J. Kudrnovský, and I. Turek, "Exchange interactions and Curie temperatures of diluted magnetic systems," Phys. Rev. B, **73**, 214412 (2006). https://doi.org/10.1103/PhysRevB.73.214412
[48] K. Sato, L. Bergqvist, J. Kudrnovský, *et al*., "First-principles theory of dilute magnetic semiconductors," Rev. Mod. Phys. **82**, 1633–1690 (2010). https://doi.org/10.1103/RevModPhys.82.1633
[49] M. Pajda, J. Kudrnovský, I. Turek, *et al*., "Ab initio calculations of exchange interactions, spin-wave stiffness constants and Curie temperatures of Fe, Co and Ni," Phys. Rev. B, **64**, 174402 (2001). https://doi.org/10.1103/PhysRevB.64.174402
[50] S. Rusz, L. Bergqvist, J. Kudrnovský, and I. Turek, "Exchange interactions and Curie temperatures in $Ni_{2-x}MnSb$ alloys: First-principles study," Phys. Rev. B, **73**, 214412 (2006). https://doi.org/10.1103/PhysRevB.73.214412

## ЗОЛОТО-ІНДУКОВАНИЙ МАГНЕТИЗМ ТА ТЕРМІЧНА СТАБІЛЬНІСТЬ У НАНОЛИСТАХ SiC: DFT+U

**Севда Рзаєва[1], Юлдош Якубов[2], Умеджон Халілов[3,4,5], Мафтун Алієв[6], Аріель Шарон Асаре[7,8]**
*[1]Азербайджанський державний університет нафти та промисловості, проспект Азадлиг, 20, AZ-1010, Баку, Азербайджан*
*[2]Інститут загальної та неорганічної хімії, Мірзо-Улугбек 77-а, 100170 Ташкент, Узбекистан*
*[3]Інститут іонно-плазмових та лазерних технологій ім. Аріфова, Дурмон юлі 33, 100120 Ташкент, Узбекистан*
*[4]Антверпенський університет, Грюненборгерлан 171, Антверпен 2020, Бельгія*
*[5]Інженерна школа, Центральноазіатський університет, Ташкент 111221, Узбекистан*
*[6]Нахчиванський державний університет, Нахчиван, Азербайджан*
*[7]Кафедра фізики, Університет Гани*
*[8]Міжнародний центр теоретичної фізики імені Абдуса Салама (ICTP), Італія*

Двовимірні нанолисти карбіду кремнію (SiC), леговані золотом, досліджуються за допомогою теорії спін-поляризованої густини (DFT+U) для вивчення їхньої електронної структури, індукованого магнетизму та термічної стабільності. Одинарні (1Au@Si) та подвійні (2Au@2Si) конфігурації заміщення моделюються в суперкомірці 4×4 для забезпечення надійної оцінки власних властивостей. Включення Au значно звужує ширину забороненої зони, зберігаючи при цьому напівпровідниковий характер нанолиста SiC. Аналіз густини станів зі спіновим розрізненням показує, що 5d-орбіталі Au домінують в електронних станах поблизу рівня Фермі. Незважаючи на майже спін-вироджені дисперсії зон, аналіз спінової популяції Маллікена виявляє індукований легуючими речовинами магнетизм, опосередкований сусідніми атомами вуглецю. Система 1Au@Si демонструє магнітний момент ~3 μB, тоді як конфігурація 2Au@2Si стабілізує феримагнітний стан із загальним магнітним моментом ~6 μB. У наближенні середнього поля оцінена температура Кюрі становить приблизно 510 K, що свідчить про можливість магнітної стабільності вище кімнатної температури та потенційне застосування в спінтронічних пристроях.

**Ключові слова:** *нанолисти SiC; легування золотом; спінтроніка; розбавлені магнітні напівпровідники; теорія функціоналу густини; температура Кюрі*